

DEVELOPMENT OF KINETIC MODEL FOR INDUSTRIAL ETHYLENE OXIDE CATALYST BY USING MODEL-TARGETED EXPERIMENTATION APPROACH

**A Thesis Submitted to
the Graduate School of Engineering and Sciences of
İzmir Institute of Technology
in Partial Fulfillment of the Requirements for the Degree of**

MASTER OF SCIENCE

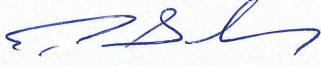
in Chemical Engineering

**by
Şahin SARRAFİ**

**July 2019
İZMİR**

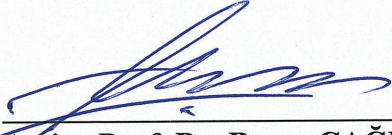
We approve the thesis of **Şahin SARRAFİ**

Examining Committee Members:



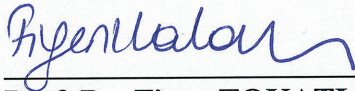
Prof. Dr. Erol ŞEKER

Department of Chemical Engineering, İzmir Institute of Technology



Assist. Prof. Dr. Başar ÇAĞLAR

Department of Energy System Engineering, Yaşar University



Prof. Dr. Figen TOKATLI

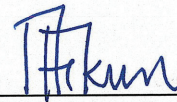
Department of Food Engineering, İzmir Institute of Technology

16 July 2019



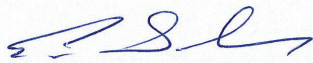
Prof. Dr. Erol ŞEKER

Supervisor, Department of
Chemical Engineering,
İzmir Institute of Technology



Prof. Dr. Yaman ARKUN

Co-Supervisor, Department of
Chemical and Biological Engineering,
Koç University



Prof. Dr. Erol ŞEKER

Head of the Department of
Chemical Engineering

Prof. Dr. Aysun SOFUOĞLU

Dean of the Graduate School of
Engineering and Sciences

ACKNOWLEDGMENTS

First and foremost, I would like to express my sincere gratitude to my research advisor Prof. Erol Şeker and my co-advisor Prof. Yaman Arkun for providing invaluable guidance throughout this project. Moreover, I would like to thank Prof. Ahmet Kerim Avcı for his consultancy during the course of this project and mentorship that urged me to complete it in a timely manner. I also extend my special thanks to Petkim Petrochemical Co. and all my dear colleagues working there.

I am indebted to the precious support of Prof. Costas Pantelides in writing the TÜBİTAK (Türkiye Bilimsel ve Teknolojik Araştırma Kurumu) project (No: 3150906) within the scope of 1501-TÜBİTAK Industrial R&D Projects Grant Program. I will never forget his patience and his ability to teach rather complicated subjects in easy ways to understand. It was nearly impossible to fulfill the grant application without his endless support.

I cannot express enough thanks to both Dr. Stepan Spatenka and Mayank Patel from Process Systems Enterprise. The completion of this project could not have been accomplished without their technical support. I wish peace and happiness onto them and their families.

I am extremely grateful to my dear friend Yaşar Serkan Kabak for his unlimited support during the course of the project. I could not have completed the project without him. He is one of the most dedicated persons I have known throughout my life. May all good fortune and prosperity find him in the rest of his business life.

I am incapable of giving enough gratitude and love to my beloved wife, Bircan Sarrafi, whose understanding and patience has made me more determined and perseverant in my research. Her presence has offered me peace, which has led me to move forward with each step. She is a special gift from heaven and I love her; today and always!

Finally, I would like to give special thanks to my sister-in-law, Ümmügülsüm Altuğ, for her inexhaustible energy to help my wife and my son, which helped me aliquot more time to work on my project. I will never forget her affectionate and unrequited assistance.

ABSTRACT

DEVELOPMENT OF KINETIC MODEL FOR INDUSTRIAL ETHYLENE OXIDE CATALYST BY USING MODEL-TARGETED EXPERIMENTATION APPROACH

Ethylene oxide (EO) is produced via selective oxidation of ethylene with oxygen using a Ag supported on α -Al₂O₃ catalyst. The ethylene epoxidation reaction is desired, whereas the ethylene and EO combustion reactions are not. Proposed study is aimed at developing a tailor-made kinetic model in order for making use in the industrial ethylene oxide reactors which are of paramount importance from the viewpoint of process economics and the greenhouse gas (GHG) induced various environmental exposures. With aging of the catalyst, the trade-off between selectivity and productivity becomes gradually more prominent. Along with the compensation of loss of active sites under the favor of increasing of the temperature, catalyst still provides sustainable commercial yields at the expense of excess feedstock consumption which in turns leads to boost GHG emissions by releasing more carbon dioxide (CO₂) into the atmosphere. To maintain catalyst activity for a longest period possible, controlling process variables more preciously with a robust model is very demanding issue throughout the last two decades. Within the scope of this thesis, model-targeted experimentation approach was used assisting by gPROMS software in determining intrinsic kinetics of the commercial catalyst in use through integral reactor coupled with gas chromatography. During the course of the kinetic experiments, the effect of VCM used as a promoter together with inhibiting effects of product gases such as CO₂ and EO were also investigated and included into the kinetic model to be derived.

ÖZET

MODEL-BAZLI DENEYSEL YAKLAŞIM İLE ENDÜSTRİYEL ETİLEN OKSİT KATALİZÖRÜ İÇİN KİNETİK MODEL GELİŞTİRİLMESİ

Etilen oksit (EO), α -Al₂O₃ destekli gümüş katalizörü kullanarak etilenin oksijen ile seçici oksidasyon tepkimesi sonucunda üretilir. Etilenin epoksidasyonu istenilen tepkimeyken, etilen ve etilen oksitin yanması istenmeyen yan reaksiyonlardır. Öne sürülen bu çalışma, çeşitli çevresel maruziyetleri tetikleyen sera gazının oluşumu ve fabrika süreç ekonomisi açılarından büyük öneme sahip endüstriyel etilen oksit reaktörlerinde kullanılacak ihtiyaca özel bir kinetik model geliştirilmesine yöneliktir. Katalizörün yaşlanması ile beraber, seçicilik ya da verimlilik faktörlerinden birinden ödün vermek kaçınılmaz hale gelir. Katalizör deaktivasyonu ile kaybedilen aktif noktaların sebebiyet vereceği üretkenlik kaybı sıcaklığın artırılması ile önlenir ancak bu da fazla hammadde kullanımına ve atmosfere daha çok karbon dioksit salınarak sera gazı emisyonlarının artışına neden olur. Son 20 yıllık zaman periyodunda, katalizör aktivitesini mümkün olan en uzun süreye çıkartabilmek için dayanıklı bir model kullanarak proses değişkenlerinin kontrolü çok rağbet gören bir araştırma konusu haline gelmiştir. Bu tez kapsamında, gaz kromatografiye bağlı integral reaktör içeren bir deney sistemi yardımıyla ticari etilen oksit katalizörünün özgün kinetikleri gPROMS yazılımında uygulanan model-tabanlı deneysel yaklaşım ile bulunmuştur. Kinetik deneyler sürecisince, reaksiyon düzenleyici olarak kullanılan VCM gazının etkisi ile tepkimeler sonucu oluşan karbon dioksit ve etilen oksit gazlarının engelleyici etkileri de geliştirilen kinetik modelde kullanmak üzere incelenmiştir.

To my beloved wife and son

TABLE OF CONTENTS

LIST OF TABLES	ix
LIST OF FIGURES	x
LIST OF SYMBOLS	xiv
LIST OF ABBREVIATIONS	xx
CHAPTER 1. INTRODUCTION.....	1
CHAPTER 2. LITERATURE REVIEW	4
2.1 Process and Reaction Mechanism Overview	4
2.2 Kinetic Models in Ethylene Oxide Production.....	15
2.3 Reactor Modeling in Ethylene Oxide Production.....	21
CHAPTER 3. MATERIAL AND METHODS	29
3.1 Materials	29
3.2 Experimental Set-up for Catalyst Testing	30
3.3 Techniques Used in Catalyst Characterization.....	38
3.4 Modeling Environment.....	39
3.5 Experimental Design Approaches.....	45
CHAPTER 4. RESULTS AND DISCUSSION	50
4.1 Characterization Results for Ethylene Oxide Catalyst	50

4.2 Preliminary Kinetic Experiments.....	63
4.3 Design of Experiments	81
4.4 Data Reconciliation and Experimental Analysis	84
4.5 Parameter Estimation and Kinetic Model Discrimination	91
4.6 Lab-Rig Reactor Modeling	105
 CHAPTER 5. CONCLUSION	 119
 REFERENCES	 121
 APPENDICES	
APPENDIX A. GC CALIBRATION RESULTS	135
APPENDIX B. CALCULATION OF PLUG FLOW CRITERIA AND MASS TRANSFER LIMITATIONS.....	138
APPENDIX C. EXPERIMENTAL DOMAIN AND EXPERIMENTAL DESIGN CONSIDERATIONS.....	143
APPENDIX D. SAMPLE CALCULATIONS FOR MOLAR-BASED DATA RECONCILIATION.....	154
APPENDIX E. FIGURES UPON RECONCILED EXPERIMENTAL DATA	160
APPENDIX F. TESTED KINETIC MODEL CANDIDATES, EXPERIMENTS USED IN PARAMETER ESTIMATION STEPS AND STATISTICAL EVALUATION FOR BEST-FITTED MODEL ..	170
APPENDIX G. CHANGES IN REACTION RATES AND COMPOSITIONS ALONG THE BED	182

LIST OF TABLES

<u>Table</u>	<u>Page</u>
Table 2.1. Popular kinetic models for EO production process in the literature.....	17
Table 3.1. Information about lab-rig reactor and catalyst bed properties.....	33
Table 3.2. Events of GC valves.	34
Table 3.3. Validity range of reactor inlet components.	47
Table 3.4. Factor variables used in D-Optimal Design in Modde Pro.....	48
Table 4.1. Elemental analysis of the catalyst.....	52
Table 4.2. Results of the Hanawalt Index based on Powder Diffraction File (PDF).....	52
Table 4.3. Helium pycnometer results for pellet and powder samples.....	56
Table 4.4. Experimental conditions for the second stability test at constant VCM.....	76
Table 4.5. Experimental conditions with/without CO ₂ co-feed experiments.....	80
Table 4.6. Error analysis based on standard experiment between catalyst loadings.	87
Table 4.7. Variance models in gPROMS	92
Table 4.8. Variance models and parameters that are used in parameter estimations.	94
Table 4.9. Control and measured variable for experimental entities in gPROMS.	95
Table 4.10. Results of the model discrimination at the first stage.....	103
Table 4.11. Results of the model discrimination at the second stage.	103
Table B.1. Some of the important properties of the feed gases.	138
Table B.2. Interphase (external) mass transfer limitation experiments.	141
Table B.3. Intraphase (internal) mass transfer limitation experiments.....	142
Table C.1. Experiments that are used for kinetic model determination	144
Table C.2. Range values of industrial ethylene oxide reactor taken from different operational periods (SOR and EOR).	152
Table C.3. Optimal design summary and performance criteria.	153
Table F.1. All kinetic model candidates used in model discrimination steps.....	171
Table F.2. Experiments used for parameter estimations in step 1.	174
Table F.3. Experiments used for parameter estimations in step 2.	175
Table F.4. Experiments used for parameter estimations in step 3.	177
Table F.5. Parameter estimation results of the best-fitted kinetic model (Westerterp et al. _model (1))......	178

LIST OF FIGURES

<u>Figure</u>	<u>Page</u>
Figure 2.1. The structure of the ethylene oxide molecule .	4
Figure 2.2. Ethylene oxide consumption (ktpa) in 2016.....	5
Figure 2.3. Non-catalytic (top) and catalytic (below) process routes for ethylene oxide production	6
Figure 2.4. Electrophilic impact of lattice structure upon the reaction mechanism.	7
Figure 2.5. Risky and non-risky regions for different mode of EO reactor operations concerning flammability notion.	10
Figure 2.6. Multitubular reactor with steam cooling.	11
Figure 2.7. General representation for the trajectory of the recycle loop gas (Site 0: Battery limit; Site 1: Reactor site; Site 2: EO absorber and stripper; Site 3: Compression and purging; Site 4: CO ₂ absorber and stripper).	13
Figure 2.8. Eley-Rideal (top) and Langmuir-Hinshelwood (below) mechanisms.....	15
Figure 2.9. General overview of the modeling concept for ethylene oxide reactor	22
Figure 2.10. Modeling strategies of the fixed bed-reactor	24
Figure 2.11. Representation of white box, grey box and black box modeling	28
Figure 3.1. Catalyst bed scheme for lab-rig reactor.....	31
Figure 3.2. Experimental set-up.....	32
Figure 3.3. Configuration and replacement positions of GC valves (#1 and #2) during a trial(a) t=0, 0.5, 5.0 and 25.0 min; (b) t=0.01 min; (c) t=2.0 and 16.0 min.	35
Figure 3.4. Sample chromatogram.....	36
Figure 3.5. Catalyst and inert pellet specifications for the lab-rig reactor model.....	38
Figure 3.6. Workflow of model-targeted experimentation in gPROMS	41
Figure 4.1. SEM image of fresh Ag/Al ₂ O ₃ catalyst pellet.	51
Figure 4.2. Pore size scale related with measurement technique.....	53
Figure 4.3. Multipoint BET analysis of the pellet.	54
Figure 4.4. Full adsorption-desorption curve of the pellet by using nitrogen adsorption.	55
Figure 4.5. Intrusion-extrusion curve of the pellet obtained from mercury porosimetry at 40.000 psi (275.8 MPa).....	57

<u>Figure</u>	<u>Page</u>
Figure 4.6. Pore size distribution of the pellet taken from mercury porosimetry.....	58
Figure 4.7. Catalyst deactivation pattern visualization by using PCA and SVR.....	62
Figure 4.8. Temperatures from reactor mid-section ($x = 0$) at steady-state conditions.	65
Figure 4.9. Concentration profile through the film.....	69
Figure 4.10. Influence of flow rate on conversion at a constant space velocity	69
Figure 4.11. Influence of catalyst particle diameter on conversion at a constant space velocity.	70
Figure 4.12. Conversion patterns with respect to VCM step changes during stability test.	71
Figure 4.13. Catalyst bed temperature pattern with respect to VCM step changes during stability test.	72
Figure 4.14. Product concentration patterns with respect to VCM step changes during stability test.	74
Figure 4.15. Conversion patterns at constant VCM with activated and non-activated catalyst during stability test.	74
Figure 4.16. Catalyst bed temperatures at constant VCM with activated and non-activated catalyst during stability test.	75
Figure 4.17. Product concentrations at constant VCM with activated and non-activated catalyst during stability test.	75
Figure 4.18. EO selectivities during the course of the catalyst stability tests obtained for each hour.	76
Figure 4.19. Conversion patterns at discrete furnace set temperatures (220°C-230°C-240°C) during the course of the experiments with/without CO ₂ obtained for each hour.....	78
Figure 4.20. Catalyst bed temperatures at discrete furnace set temperatures (220°C-230°C-240°C) during the course of the experiments with/without CO ₂ obtained for each hour.....	78
Figure 4.21. Product concentrations at discrete furnace set temperatures (220°C-230°C-240°C) during the course of the experiments with/without CO ₂ obtained for each hour.....	79

<u>Figure</u>	<u>Page</u>
Figure 4.22. EO selectivities at discrete furnace set temperatures (220°C-230°C-240°C) during the course of the experiments with/without CO ₂ obtained for each hour.....	79
Figure 4.23. Lab-rig reactor system model in gPROMS Process Builder.....	106
Figure 4.24. Diffusion specifications for lab-rig reactor.	107
Figure 4.25. Coolant specifications for lab-rig reactor.	108
Figure 4.26. General settings in Catalyst_pellets_section_1D.	110
Figure 4.27. Heat transfer parameter specifications in lab-rig reactor model.	113
Figure 4.28. Flow resistance and fluid-to-solid heat and mass transfer specifications.	116
Figure A.1. Calibration curve for ethylene.	135
Figure A.2. Calibration curve for oxygen.....	135
Figure A.3. Calibration curve for carbon dioxide.....	136
Figure A.4. Calibration curve for ethylene oxide.	136
Figure A.5. Calibration curve for methane.	137
Figure E.1. Changes in ethylene and oxygen conversions (a) and EO/CO ₂ selectivity (b) at two different catalyst amounts (0.1 and 0.2g) and three different C ₂ H ₄ /O ₂ ratios (2.94, 3.94 and 4.95).....	160
Figure E.2. Changes in ethylene and oxygen conversions at two different temperatures (219 and 250°C) and C ₂ H ₄ /O ₂ ratios (2.71, 4.95 and 8.40)..	161
Figure E.3. Changes in ethylene and oxygen conversions at three different inlet CO ₂ feed molar concentrations (1.58, 3.11 and 4.64%) with different temperatures of 219 °C (a), 237 °C (b), and 250 °C (c).....	162
Figure E.4. Changes in EO/CO ₂ selectivity at three different molar inlet concentrations of CO ₂ feed (1.58, 3.11 and 4.64%) with different temperatures of 219, 237, and 250 °C.....	163
Figure E.5. Changes in ethylene and oxygen conversions at five different inlet concentrations of VCM feed (0, 3.75, 7.5, 11.25 and 15.0 ppmv) with different temperatures of 219 °C (a), 237 °C (b), and 250 °C (c).....	164
Figure E.6. Changes in EO/CO ₂ selectivity at five different inlet concentrations of VCM feed (0, 3.75, 7.5, 11.25 and 15.0 ppmv) with different temperatures of 219, 237 °C and 250 °C (c).....	165
Figure E.7. Changes in ethylene and oxygen conversions (a) and EO/CO ₂ selectivity (b) at five different total flow rates (65, 70, 75, 80 and 85 sccm).	166

<u>Figure</u>	<u>Page</u>
Figure E.8. Changes in ethylene and oxygen conversions (a) and EO/CO ₂ selectivity (b) at five same center point experiments executed different times at the same catalyst loading (#4).	167
Figure E.9. Changes in ethylene and oxygen conversions (a) and EO/CO ₂ selectivity (b) at six different reactor pressures (0, 2, 4, 6, 8 and 10 barg).	168
Figure E.10. Changes in ethylene oxide conversion at five different temperatures (237, 245, 255, 265 and 275°C).	169
Figure F.1. Parity chart of reactor outlet ethylene composition for Westerterp et al._model (1).	180
Figure F.2. Parity chart of reactor outlet oxygen composition for Westerterp et al._model (1).	180
Figure F.3. Parity chart of reactor outlet CO ₂ composition for Westerterp et al._model (1).	181
Figure F.4. Parity chart of reactor outlet EO composition for Westerterp et al._model (1).	181
Figure G.1. Change in main reaction rate along with the catalyst bed in the axial direction.	182
Figure G.2. Change in side reaction_1 rate along with the catalyst bed in the axial direction.	182
Figure G.3. Change in side reaction_2 rate along with the catalyst bed in the axial direction.	183
Figure G.4. Change in bed temperature along with the catalyst bed in the axial direction.	183
Figure G.5. Change in ethylene concentration along with the catalyst bed in the axial direction.	184
Figure G.6. Change in oxygen concentration along with the catalyst bed in the axial direction.	184
Figure G.7. Change in carbon dioxide concentration along with the catalyst bed in the axial direction.	185
Figure G.8. Change in ethylene oxide concentration along with the catalyst bed in the axial direction.	185

LIST OF SYMBOLS

a_{ci}	Value of $a_i(T)$ at $T=T_c$
a_i	RKS equation of state parameter which is function of temperature and sphericity of the molecules (acentric factor)
a_j	Catalyst activity in j^{th} reaction
a_{tol}	Absolute error tolerance
a_v	Specific surface area per unit volume of catalyst bed (m^2m^{-3})
A	Cross-sectional area of the reactor tube (m^2)
A_{BET}	Specific BET surface area (m^2g^{-1})
A_f	User-specified adjustable factors for laminar flow term of the pressure drop equation
A_α	User-specified adjustable factors for dynamic term of the effective bed
B	Set of variance model parameters
B_f	User-specified adjustable factors for turbulent flow term of the pressure drop equation
Bi_d	Biot number for Dixon correlation
Bi_h	Biot heat number
C_i	Concentration of species i in the reactor ($mol\ m^{-3}$)
$C_{i,s}$	Concentration of species i in the solid (catalyst) phase of the reactor ($mol\ m^{-3}$)
$C_{p,Ag}$	Heat capacity of the pure silver ($J\ kg^{-1}K^{-1}$)
$C_{p,cor}$	Heat capacity of the corundum (Al_2O_3) ($J\ kg^{-1}K^{-1}$)
$C_{p,f}$	Heat capacity of the fluid phase in the reactor ($J\ kg^{-1}K^{-1}$)
$C_{p,pellet}$	Heat capacity of the pellet ($J\ kg^{-1}K^{-1}$)
CBE_k	Carbon balance error in the k^{th} iteration
CF_k	Correction factor for data reconciliation in the k^{th} iteration
d_{mean}	Average pore size diameter (nm)
dn_{doi}	D-space values (interatomic spacing) in the order of degree of intensity (doi)
d_p	Particle diameter of the catalyst or inert material (μm)
d_{pl}	Equivalent pellet diameter of a sphere with the same surface area (cm)
d_t	Inner tube diameter (hydraulic diameter) of the reactor (cm)

D_e	Effective mass diffusivity of the fluid ($\text{m}^2 \text{s}^{-1}$)
E_{ADS}	Adsorption activation energy (J mol^{-1})
E_d	Deactivation energy (J mol^{-1})
f	Friction factor
G'	Mass flux ($\text{kg m}^{-2} \text{s}^{-1}$)
h_c	Heat transfer coefficient of the coolant ($\text{W K}^{-1} \text{m}^{-2}$)
h_f	Heat transfer coefficient of the fluid ($\text{W K}^{-1} \text{m}^{-2}$)
i	Species (component) index
I/I_1	Relative intensity
j	Reaction index
j_D	Colburn j-factor for mass transfer
j_H	Colburn j-factor for heat transfer
k	Iteration index used in data reconciliation
k_{d0}	Pre-exponential deactivation kinetic constant
k_d	Deactivation kinetic constant
k_{eff}	Effective thermal conductivity of the pellet ($\text{W m}^{-1} \text{K}^{-1}$)
$k_{f,i}$	Fluid to solid mass transfer coefficient for the i^{th} component ($\text{m}^3 \text{m}^{-2} \text{s}^{-1}$)
k_{fp}	Thermal conductivity of filler particles (silver) ($\text{W m}^{-1} \text{K}^{-1}$)
k_m	Thermal conductivity of composite matrix (corundum) ($\text{W m}^{-1} \text{K}^{-1}$)
k_{pc}	Permeability coefficient
k_{ref}	Kinetic rate constant at reference temperature
K	Kozeny constant
$K_{\text{ADS_TREF}}$	Adsorption kinetic constant at reference temperature (250°C)
l	Experiment index used in parameter estimation
L	Catalyst bed length (m)
$L_{c,\text{particle}}$	Characteristic length of the solid particle (m)
$L_{h,\text{laminar}}$	Hydrodynamic entrance region (m)
LD_{50}	Lethal Dose, 50%
LC_{50}	Lethal Concentration, 50%
m	Variable index used in parameter estimation
$m_{c,b}$	Total catalyst mixture (inert + catalyst) mass in the bed (g)
m_i	Measured outlet GC concentration of i^{th} component (mol%)
M	Total # of reactions

MW_i	Molecular weight of i^{th} component (g/mol)
n	Differential variable index in the solver
n_{doi}	Degree of intensity in d-space values
n_j	Reaction order of j^{th} reaction used in the kinetic models of Westerterp et al. (model 1 and 1a)
n_{RMSE}	Total number of experiments in use for RMSE calculation
n_{se}	Number of experiments used for standard error calculation
N_d	Number of differential variables in the problem
N_{meas}	Total number of measurements taken during all the experiments
NE	Number of experiments performed
NM_{lm}	Number of measurements of the m^{th} variable in the l^{th} experiment
Nu_p	Nusselt number for fluid-solid heat transfer
Nu_w^f	Nusselt number for bed-wall heat transfer – dynamic term
NV_l	Number of variables measured in the l^{th} experiment
P_{Hg}	Applied pressure for the liquid mercury to enter a pore (MPa)
p_i	Predicted outlet GC concentration of i^{th} component (mol%)
$P(\text{N}_2)/P_0(\text{N}_2)$	Relative pressure of nitrogen
Pe_r	Peclet number for radial mass transfer
Pe_z	Peclet number in the axial direction
Pr	Prandtl number for the fluid phase
Q_{in}^i	Inlet volumetric flow rate of i^{th} component (sccm)
Q_T	Total flow rate of the reactor (sccm)
Q_T'	Temperature compensated total flow rate of the reactor (sccm)
r/L	Ratio of tube radius to catalyst length
r_i	Rate of formation of the i^{th} component ($\text{mol kg-cat}^{-1} \text{s}^{-1}$)
r_j	Rate of j^{th} reaction ($\text{mol kg-cat}^{-1} \text{s}^{-1}$)
r_K	Kelvin radius of the pore (nm)
r_{tol}	Relative error tolerance
r_{Washburn}	Radius of the pore where mercury intrudes (nm)
R	Gas constant (8.314×10^7 ergs/deg/mol)
R_{fluid}	Heat resistance on the surface ($\text{m}^2 \text{K W}^{-1}$)
R_{solid}	Heat resistance inside the solid ($\text{m}^2 \text{K W}^{-1}$)
Re_p	Reynolds number for packed bed

$Re_{p,p}$	Reynolds number for packed bed (calculated for establishing plug flow criteria)
Sc	Schmidt number for the fluid phase
Sh_p	Sherwood number for packed bed
t	Measurement index used in parameter estimation
T	Catalyst bed temperature ($^{\circ}C$)
T_{∞}	Ambient temperature ($^{\circ}C$)
$T_b(N_2)$	Boiling point of nitrogen (77 K)
$T_{c,i}$	Critical temperature of i^{th} component ($^{\circ}C$)
T_m	Melting temperature of the support material in the catalyst ($^{\circ}C$)
T_r	Reduced temperature (T/T_c) ($^{\circ}C$)
T_{ref}	Reference temperature for reparameterized version of Arrhenius equation ($^{\circ}C$)
T_s	Catalyst (solid) temperature ($^{\circ}C$)
U	Overall heat transfer coefficient ($W K^{-1} m^{-2}$)
$V_{c,p}$	Total catalyst mixture (inert + catalyst) volume in the bed (cm^3)
$V_m(N_2)$	Molar volume of liquid nitrogen ($34.7 cm^3/mol$)
V_{mp}	Total specific pore volume (from mercury porosimetry) (m^3/g)
x_i	mole fraction of i^{th} gas component
$X(i)$	Conversion of the i^{th} component (%) (ethylene, oxygen or ethylene oxide)
X_{in}^i	Inlet molar concentration of the i^{th} component (%)
X_{outk}^i	Outlet molar concentration of the i^{th} component in the k^{th} iteration (%)
y_i	Mass fraction of the i^{th} component
z	Axial direction along the bed (m)
z_{lmt}	t^{th} predicted (model) value of variable m in experiment l
\tilde{z}_{lmt}	t^{th} measured value of variable m in experiment l
z_{mp}	Model prediction in maximum likelihood estimation
α	Variance model parameter for linear variance model
α_0	Activity of the catalyst at Start-of-Run
α_{∞}	Terminal activity of the catalyst or activity of the catalyst at End-of-Run
α_j	Reaction order for the nominator of j^{th} reaction in the kinetic model of Salmi et al.

α_{st}	Statistical significance level
α_w^0	Overall effective bed-wall heat transfer coefficient, with respect to center bed temperature ($\text{W K}^{-1}\text{m}^{-2}$)
α_{ws}^e	Overall effective bed-wall heat transfer coefficient (used in 1D bed models) ($\text{W K}^{-1}\text{m}^{-2}$)
α_{ws0}^e	Static term of the effective bed-wall heat transfer coefficient ($\text{W K}^{-1}\text{m}^{-2}$)
$\alpha_{ws,d}^e$	Dynamic term of the effective bed-wall heat transfer coefficient ($\text{W K}^{-1}\text{m}^{-2}$)
β	Variance model parameter for linear variance model
β_j	Reaction order for the denominator of j^{th} reaction in the kinetic model of Salmi et al.
γ	Variance model parameter for heteroscedastic variance model
$\gamma(\text{N}_2)$	Surface tension of nitrogen at its boiling point (8.85 ergs/cm^2 at 77K)
γ_{Hg}	Surface tension of mercury (480 mNm^{-1})
γ_{sf}	Pore shape factor
ε	Non-zero constant in variance model
ε_b	Bed void fraction
$\varepsilon_{b,p}$	Bed porosity (calculated for establishing plug flow criteria)
$\varepsilon_{l,n}$	Solver's estimate for the local error in the i^{th} differential variable
ε_p	Particle porosity (from mercury porosimetry)
ε_{sf}	Exponent of pore shape factor (1 for cylindrical shape)
η	Effectiveness factor
θ_{beam}	Incidence angle of the X-ray beam (2θ)
θ_{Hg}	Contact angle of mercury on the surface of a solid sample (140°)
$\theta_{s,m}$	Set of model parameters to be estimated
κ_i	RKS equation of state parameter which is function of sphericity of the molecules (acentric factor)
λ_f	Thermal conductivity of the fluid phase ($\text{W m}^{-1} \text{K}^{-1}$)
λ_s	Thermal conductivity of the solid phase ($\text{W m}^{-1} \text{K}^{-1}$)
λ_{rs}^e	Effective bed heat conductivity ($\text{W m}^{-1} \text{K}^{-1}$)
λ_{rs0}^e	Static term of the effective bed heat conductivity ($\text{W m}^{-1} \text{K}^{-1}$)
$\lambda_{rs,d}^e$	Dynamic term of the effective bed heat conductivity ($\text{W m}^{-1} \text{K}^{-1}$)
Λ_n	Current value of the n^{th} differential variable

μ_f	Dynamic viscosity of the fluid (Pa.s)
$\mu_{f,p}$	Mixture viscosity of the reaction mixture (calculated for establishing plug flow criteria) (Pa.s)
μ_i	Viscosity of the i^{th} reactor inlet species (used for establishing plug flow criteria) (Pa.s)
$\rho_b(i)$	Bulk density of a material (kg/m^3)
ρ_f	Density of the fluid phase (kg/m^3)
$\rho_{f,p}$	Mixture density of the inlet reaction mixture (calculated for establishing plug flow criteria) (kg/m^3)
ρ_i	Density of the i^{th} reactor inlet species (used for establishing plug flow criteria) (g/cm^3)
ρ_{mp}	Pellet bulk density (from mercury porosimetry) (g/cm^3)
$\rho_p(i)$	Particle density of a material (kg/m^3)
ρ_s	Density of the solid (catalyst) phase (kg/m^3)
$\rho_{s,p}$	Catalyst mixture density (calculated for establishing plug flow criteria) (g/cm^3)
σ_{ex}	Standard deviation of each experiment
σ_{lmt}^2	Variance of the t^{th} measurement of variable m in experiment l
$\Delta H_{rxn,j}$	Heat of reaction of j^{th} reaction (J mol^{-1})
ΔP	Pressure drop along the bed (Pa)
τ	Tortuosity
v_f	Superficial velocity of the fluid phase (m s^{-1})
$v_{f,p}$	Superficial velocity of the fluid phase (calculated for establishing plug flow criteria) (m s^{-1})
$v_{i,s}$	Interstitial velocity (cm s^{-1})
ϕ_{cat}	Volumetric fraction of the catalyst
ϕ_{fp}	Volume fraction of the filler particles in the composite material
Φ	Objective function of the parameter estimation function
ω	Variance model parameter
ω_i	Acentric factor of i^{th} component

LIST OF ABBREVIATIONS

1D	One Dimensional
2D	Two Dimensional
AC	Allyl Chloride
ACM	Aspen Custom Modeler
AML: FBCR	Advanced Model Library for Fixed-Bed Catalytic Reactors
ANN	Artificial Neural Network
ASCII	American Standard Code for Information Interchange
BET	Brunauer-Emmett-Teller
BJH	Barrett-Joyner-Halenda
BPR	Back Pressure Regulator
CCD	Central Composite Design
CPU	Central Processing Unit
CRVM	Constant Relative Variance Model
CSTR	Continuous Stirred Tank Reactor
DAE	Differential-Algebraic Equations
DAEBDF	Differential-Algebraic Equations Backward Differentiation Formulae
DCE	1,2-dichloroethane (same as EDC)
DEG	Diethylene Glycol
Det.	Determinant
DFT	Density Functional Theory
DGM	Dusty Gas Model
DIPPR	Design Institute for Physical Properties
DoE	Desing of Experiments
D-Optimal	Determinant-optimal
DR	Data Reconciliation
DSC	Differential Scanning Calorimetry
EC	Ethyl Chloride
EDAX	Energy Dispersive X-Ray Analysis
EDC	Ethylene Dichloride (same as DCE)
EO	Ethylene Oxide
EO/EG	Ethylene Oxide/Ethylene Glycol

EOR	End of Run
EoS	Equation of State
EPC	Electro-Pneumatic Control
E-R	Eley-Rideal
ESEM	Environmental Scanning Electron Microscope
FEG	Field Emission Gun
fp	Filler particle in the pellet
GA	Genetic Algorithms
GC	Gas Chromatography
GHG	Greenhouse Gases
GHSV	Gas Hourly Space Velocity
gPROMS	g eneral P rocess M odeling S ystem
HK	Harvath-Kawazoe
HMI	Human-Machine Interphase
ID	Internal Diameter
IEA GHG	International Energy Agency Greenhouse Gases
I-factor	Inhibitor factor
IGM	Ideal Gas Model
JDC	Joint Design Criterion
ktpa	kilo tonnes per annum
LFA	Laser Flash Analysis
L-H	Langmuir-Hinshelwood
LSVR	Linear Support Vector Machine Regression
LVM	Linear Variance Model
MbDoE	Model-based Desing of Experiments
Mbps	Megabits per second
MC	Methyl chloride
MCP	Multi-layer Perceptron
MEG	Monoethylene Glycol
MFC	Mass Flow Controller
MINLP	Mixed Integer Nonlinear Programming
MLE	Maximum Likelihood Estimation
MOO	Multi-objective Optimization

mp	Mercury Porosimetry
NLPSQP	Nonlinear Sequential Quadratic Programming
Norm.	Normalized
OAERAP	Outer Approximation Equality Relaxation Augmented Penalty
OD	Outer Diameter
OFAT	One-factor at a time
OLE	Ordinary Least-square Estimation
OMC	Oxametallacycle
pc	Permeability coefficient
PCA	Principal Component Analysis
PDF	Powder Diffraction File
PEG	Polyethylene Glycols
PI	Pressure Indicator
PID	Proportional-Integral-Derivative
PLC	Programmable Logic Control
PLOT	Porous Layer Open Tubular
PR	Peng Robinson
RBFN	Radial Basis Function Network
RKS	Redlich-Kwong-Soave
RMSE	Root Mean Square Error
RRate	Reaction Rate
S/SL	Split/Splitless
sccm	standard cubic centimeter
SE	Standard Error of Mean
SEM	Scanning Electron Microscopy
SEP	Solid Electrolyte Potentiometer
sf	Shape factor
SiC	Silicon Carbide
SOR	Start of Run
SP	Set Point
SQP	Sequential Quadratic Programming
ST	Space Time
SVR	Support Vector Machines

TCD	Thermal Conductivity Detector
TEG	Triethylene Glycol
TI	Temperature Indicator
TIC	Temperature Indicator Controller
TR	Taylor Ratio
VCM	Vinyl Chloride Monomer
XRD	X-Ray Diffraction
XRF	X-Ray Fluorescence Spectrometer

CHAPTER 1

INTRODUCTION

Solid-catalyzed gas reactions play a crucial role in the chemical industry. Most of the chemical industrial processes are founded on the heterogeneous catalysts. The most massive amount of produced chemical is ethylene with 113 million tonnes. In petrochemical industry, diversification of the petrochemical product range commence with the ethylene production as a consequence of steam cracking of hydrocarbons (e.g., naphtha, ethane, propane, butane and gas oil) which is the non-catalyzed process [1-3].

Ethylene oxide (EO) is the one of the pillar of the bulk chemicals and the 14th most produced commodity chemical with around 29 million tonnes all over the World. It has the growing demand in the market due to the wide range of the important end-use products such as ethylene glycols, polyethylene glycols, ethylene glycol ethers, ethanol amines, polyols, ethoxylates and their derivatives [2, 4].

Production of ethylene oxide is performed either direct (ethylene-rich condition) or air oxidation (ethylene-lean condition). Direct oxidation is much more favorable owing to guarantee more selectivity, less downtime and feedstock savings. The dominant reactions in the process are partial oxidation of ethylene and total oxidation of ethylene. The consecutive combustion is also likely to occur as a result of oxidizing the ethylene oxide [5].

Urged on by the precise temperature control and catalytic kinetic mechanisms, the process is tend to be more selective for partial oxidation rather than total oxidation of ethylene. By virtue of the fact that the heat generated by the total oxidation reaction is an order of magnitude greater than partial oxidation. In other words, the total oxidation products is strongly favorable by chemical equilibrium, it is therefore inevitable that the use of selective catalytic process is of paramount important for the yield of ethylene oxide [6-7].

Another important factor on selectivity is addition of promoters and inhibitors. Promoters, added by the catalyst vendor during the manufacturing of the catalyst, are the compounds of alkali, alkaline earth metals and silane. The inhibitors whose responsibility belongs to the catalyst end-users (i.e. ethylene oxide plant supervisors),

are chlorine compounds such as vinyl chloride, 1,2-dichloroethane (DCE) and ethyl chloride. Both of them are functioning in the regularization of catalyst lattice surface [8-9].

Selective oxidation is provided by the utilization of Ag/ α -Al₂O₃ catalyst in the multitubular fixed-bed reactor. For the sake of the avoidance of any tendency from partial to total oxidation, catalyst should have a low surface area (<1 m²/g) and slightly porous characteristics. This allows the reactants for a short residence time in the catalyst bed. Commercial EO catalyst has a silver content in the range between 10-35%. Seeing that the silver catalyst is very expensive and on top of that, it is not recommended to regenerate. Thus, catalyst life which is about 2-5 years, is very pivotal touchstone for both financial and process aspects [5, 10].

Even though the multitubular reactors in EO production are reckoned to be non-adiabatic in chemical engineering design concept, these are deemed to be isothermal reactors. It is because the operational strategy is to maintain the isothermicity in the reactor in order to achieve essential selectivity target [11].

All EO reactor operating strategies are serving at the same purpose, which is to maximize the EO production as much as close to the maximum EO selectivity limit within a guaranteed catalyst life by playing with reactor temperature and feed inhibitor concentration, while pursuing the product quality specification. The type of plant design (i.e. direct/air oxidation), catalyst life and the fidelity of the advanced process control systems in the vicinity of the reactor are the key game changers on EO production [5, 11-12].

From the environmental perspective of the view, EO plants in the world have a 1.5-2% cumulative contribution to CO₂ emission. Almost 9-10 million tonnes CO₂ per year in total are venting to the atmosphere after CO₂ absorption units. According to the International Energy Agency Greenhouse Gases (IEA GHG), the average CO₂ emission of every EO plant is 150,000 tonnes per year. Notwithstanding tiny percentage at first glance, the detrimental effect of EO plants on GHG is the gospel truth [2].

Process plants in the petrochemical industry have some certain technological limits which means that the breakthrough innovations rarely occur. In this sense, the main motivation for researchers upon EO process is to leave no stone unturned for boosting selectivity and catalyst efficiency with the avoidance of compromising the feedstock and energy costs under such cumbersome industrial evolution. Over and above, process intensifications based on significant retrofit in process units, by and

large, are regarded as costly, risky and time-consuming solutions. For this reason, intensification in process control systems are more preferable in all aspects without making any concessions in respect of safety, energy-efficiency and environmental considerations [12-13].

In this study, the principle objective is to construct a kinetic model tailored for the commercial catalyst in use in the industrial ethylene oxide reactor by using model-targeted experimentation in gPROMS. To attain this objective, experiments that are designed particularly for the industrial process were conducted in contemplation of discovering the kinetic model intrinsic to the commercial catalyst in use.

CHAPTER 2

LITERATURE REVIEW

2.1 Process and Reaction Mechanism Overview

Among the petrochemical intermediates, ethylene oxide has an exclusive position in the sense that it reaches out a broad range of end products and their derivatives. In addition to this, the production process of ethylene oxide is engulfed by the many different engineering aspects and heuristics.

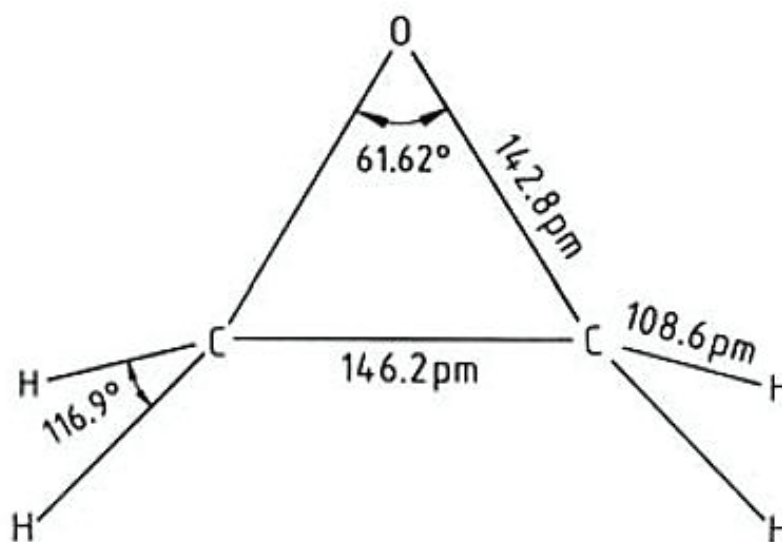


Figure 2.1. The structure of the ethylene oxide molecule (Source: [14]).

By virtue of the overwhelming ring strain in the C-O-C angle of 61.62° in Figure 2.1, ethylene oxide becomes easily reactive in consequence of the ring-opening reaction. The toxicity coupled with reactivity make ethylene oxide hazardous compound. LD_{50} and LC_{50} (for 4h hours) values of this compound are 330 mg/kg and 1460 ml/m³ in the rats, respectively. That's why, safe handling and processing of ethylene oxide are of great importance [14-15].

The first discovery of the ethylene oxide was made by Wurtz in 1859 from liquid phase oxidation of ethylene chlorohydrin and aqueous potassium hydroxide. The current technology which is direct oxidation of ethylene and ethylene oxide in presence of silver catalyst was founded by Lefort in 1931. However, transformation of the technology from chlorohydrin process to direct oxidation of the ethylene oxide continued for 10 years [14-15].

Ethylene oxide is the second most produced ethylene-based commercial intermediate [19]. Generally, it is used as captive product in other words ethylene oxide is converted to other products immediately where it is produced. According to the market report in 2017 [16], the annual production of ethylene oxide was about 29 million tonnes in 2016. Most of the related end-products produced by ethylene oxide are ethylene glycol (MEG, DEG and TEG), ethoxylates, ethanolamines, polyols and polyethylene glycols. In Figure 2.2, the end-product range of the ethylene oxide is represented as the portion of the total production (ktpa) in 2016 [4, 14-16].

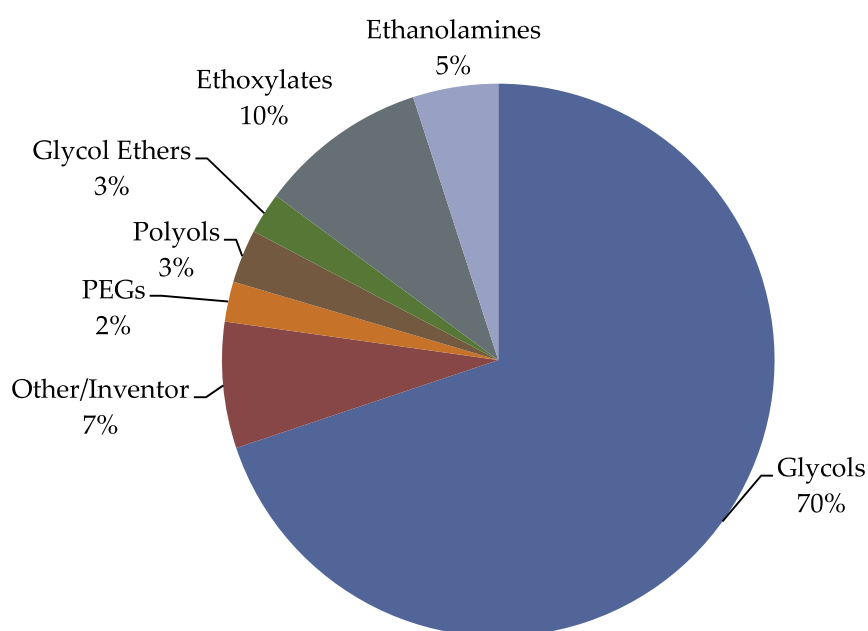


Figure 2.2. Ethylene oxide consumption (ktpa) in 2016 (Source: Adapted from [16]).

There are mainly two routes to obtain ethylene oxide as shown in Figure 2.3 One is epichlorohydrine process which is non-catalytic route. This process gives rise to massive amount of waste of salts and consumption of chlorine compounds. For this

reason, it is totally superseded by the catalytic process which is provided by Ag/ α -Al₂O₃ catalyst. In catalytic process, selective oxidation is the essential reaction for feasible and eco-friendly production of the ethylene oxide. However, the total oxidation which is undesired reaction inevitably occurs [14-15].

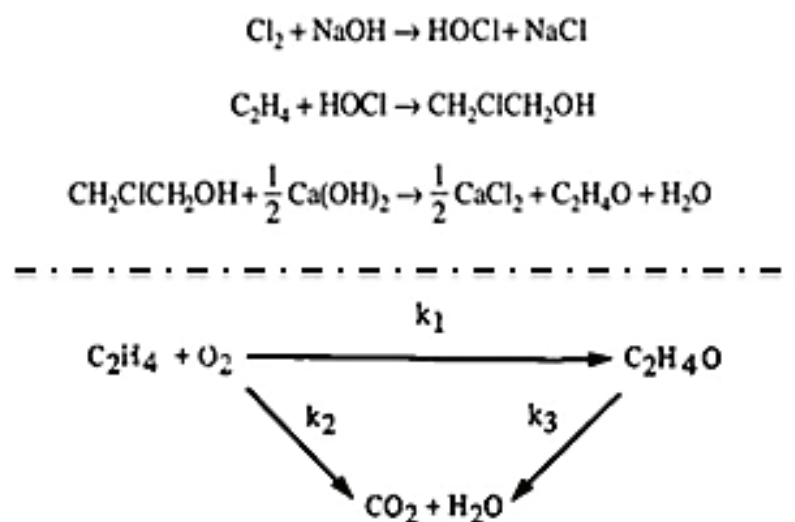


Figure 2.3. Non-catalytic (top) and catalytic (below) process routes for ethylene oxide production (Source: Adapted from [17-18]).

The recent production technology of ethylene oxide is centered on the direct oxidation that is supplied by either oxygen-based or air-based paths. The main dissimilarities of these processes are ethylene to oxygen ratio and ethylene conversion. In air-based process, ethylene to oxygen ratio is between 1:1 to 1:2 and ethylene conversion is in the range between 20-65 [5], whereas the mole ratio of these two reactants and ethylene conversion are about 3:1 to 4:1 and 7-15%, respectively. The main advantage of the oxygen-based process over the air-based process is to achieve higher selectivities [19].

The advances in catalytic process pave the way for making many enhancements in the first stage of the technology in Lefort's decade in which the selectivity was about 50%. At the present, the situation has come to the recent level where the selectivity reached out to 90% by the additional effects of the inhibitors, promoters and effective silver distribution [14-15, 21].

The underlying phenomenon that determines the proceeding of the reaction is the way of absorption of the oxygen in active silver sites of the catalyst. There are three types of oxygen adsorption patterns in the silver: Atomic oxygen, molecular oxygen and subsurface oxygen. It is not most recently that molecular oxygen considered to be responsible for the formation of ethylene oxide. This brought about a fallacy that the theoretical maximum selectivity is 85.7%. However, throughout the last three decades, it is noteworthy that the value of 90% selectivity is approachable in the ethylene oxide production process.

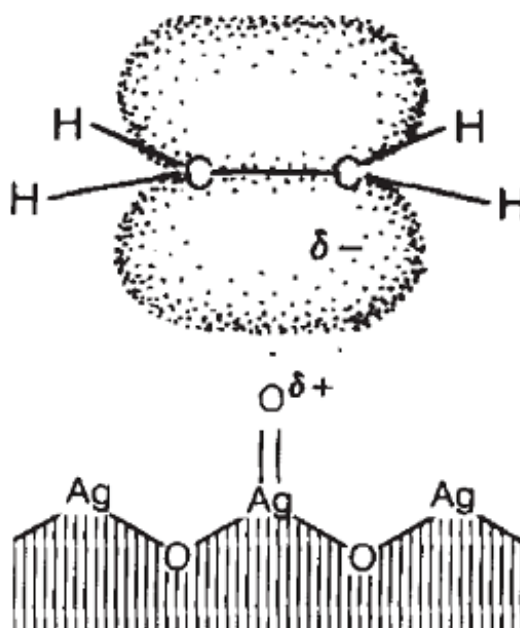


Figure 2.4. Electrophilic impact of lattice structure upon the reaction mechanism
(Source: [20]).

Although there is no any consensus upon which mechanisms favor the ethylene oxide reaction even for now, the majority of the recent studies show that the atomic oxygen is responsible for both reactions (k_1 and k_2). Moreover the subsurface oxygen concentration has an important influence on the future attitude of adsorbed atomic oxygen. Large number of subsurface oxygen competes more strongly with the atomic oxygen for silver electrons. As shown in Figure 2.4, This allows the atomic oxygen to have more powerful attraction towards the higher electron-densed region of the ethylene molecule with π bonds which culminates in ethylene oxide. That is to say, the

effect of the subsurface oxygen serves as electron-affinity boosting agent for the atomic oxygen [5, 15, 22-23].

The positive effect of the chlorine compounds was inadvertently discovered in a plant in France. Like the subsurface oxygen, these compounds such as vinyl chloride monomer (VCM), 1,2-dichloroethane (DCE) and ethyl chloride enhance the surface dipole moment of atomic oxygen species owing to its electronegative nature. These molecules could be also seeped into the surface because of the lower cohesive energy of the silver molecules. Electron affinity is the desirable feature for selectivity. Hence, Cl is preferred rather than other halogen promoters [5, 17]. The chemisorption ability of the active sites of the silver is independent on the surface structure, which in turn makes partial oxidation of ethene structure-insensitive. Most majority of the heterogeneous reactions are structure-insensitive, in other words, Taylor ratio (TR) which refers to the fraction of the active sites to the total sites is equal to 1. This phenomenon is stated as facile reaction whereas the opposite one is named as the demanding reaction. As a consequence of this situation, the steric effect of the catalyst is negligible for the ethylene oxide reaction [24-25].

New researches reveal that chlorine additives prevent the surface from the formation of oxametallacycle (OMC) which gives rise to acetaldehyde formation. OMC is formed by the reason of the ethylene adsorption on an oxygen vacancy [26]. Another microkinetic study performed by Stoltze et al. shows that OMC formation is the rate controlling of the process. Two essential branching elementary reactions rule over the selectivity. The first is the dissociation of the oxygen which plays crucial role in ethylene-rich process and the second is the surface reaction between oxygen and ethylene ending with OMC which has a conclusive action in oxygen-rich process [27].

It is also used some promoters in the commercial silver catalysts such as alkaline salts and silane during the course of the catalyst preparations. Unlike inhibitors, the kinetic mechanisms are not directly affected by the promoters. It has, nonetheless, a blocking impact by neutralizing the acid sites that makes room for the isomerization reaction of ethylene oxide to acetaldehyde. Another important contribution of the promoters is that they thwart the migration of the active surface sites which in turn maintain surface stability and procrastinate thermal degradation of the catalyst [5, 14-15].

The regeneration (regen) of the surface sites is the crucial action that is done by the catalyst. In ideal case, the regen cycles last forever but this is impossible in practice

because of the deactivation of the catalyst, put differently, sintering of the catalyst. In ethylene oxide process, the deactivation mechanism hinges on the coalescence and collision of active materials (i.e. silver) by the migration over the catalyst. This ends up with the discernible crystalline growth during the course of the aging process that could be determined by SEM and XRD analysis [28-29]. Boskovic et al.[30] investigated the deactivation of a commercial catalyst in the ethylene oxide process at a constant temperature and oxygen concentration increase and their findings show that 260°C is the inflection temperature for the rate production pattern of ethylene oxide. After 260°C, at high O₂ concentration, CO₂ production rate exceeds that of EO. Another important fact from their study was that increasing the temperature causes to the growth in Ag particles. This is a most compelling evidence that catalyst activity is strongly related to the degree of agglomeration of Ag particles.

As has been noted, the sintering is the function of the temperature. At high surface temperatures, migration of particles is likely to happen. Tamman and Hüttig temperatures are useful semi-empirical indicators that give a feeling to the catalyst designers whether the support material is the most appropriate candidate for operating conditions of desired process. For α -Al₂O₃ (corundum), Tamman and Hüttig temperatures are 1159K and 695K, respectively. Tamman temperature at which the atoms from bulk becomes mobile, is the half of the melting temperature (T_m) of the support whereas the Hüttig temperature at which the atoms at defects starts to exhibit mobility, is the three tenths of T_m [5]. This alludes to the fact that sintering will not occur at a fast rate and the support material is reasonable for ethylene oxide reactor operation in terms of temperature which is in the range between 240-260°C throughout the catalyst life. Catalyst changeover decision is determined by the key economical parameters such as feedstock and energy consumption based on the unit production of the main indicative commercial product.

As long as the journey of the catalyst from the loading to the change-over, the sintering takes place gradually. To meet the ethylene oxide production rate at a certain feasible region, the loss of surface of the active sites through agglomeration is compensated by increasing the temperature. This operation strategy is applicable until the maximum temperature could not violate the flammability safety limit which is dependent on temperature, composition and pressure. The operation region that is acceptable for the flammability notion changes with respect to the mode of feed oxygen in the operation as is apparent in Figure 2.5.

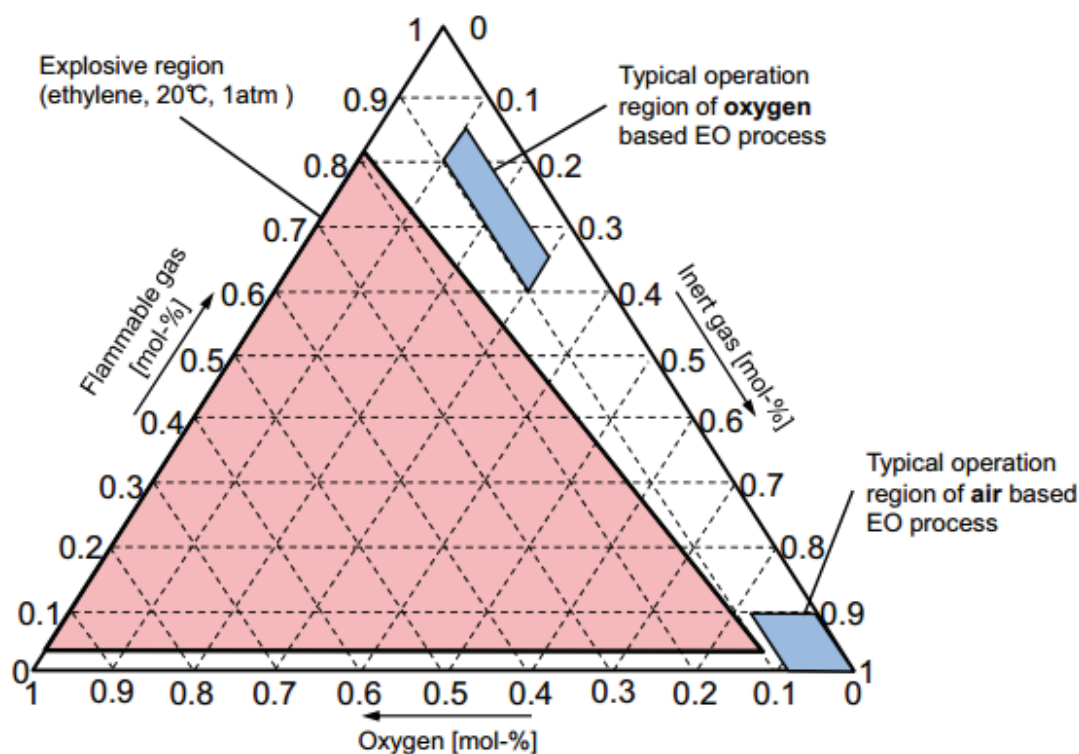


Figure 2.5. Risky and non-risky regions for different mode of EO reactor operations concerning flammability notion (Source: [31]).

Activity distribution is also very determinative in selectivity for catalyst manufacturers. The fundamental idea behind optimal catalyst distribution is to seek out the optimum deposition conditions of active material inside the pellet so that the maximum performance with regard to intraparticle mass and heat transfer could be notched up. A great deal of effort is performed for which activity distribution is better representative pattern for catalyst selectivity. The optimal catalyst distribution with surface Dirac-delta function shows that the selectivity improves with DCE levels (0.7-1.5 ppm) and besides that the reactor runaway behaviour could be diminished by the use of Dirac catalysts. However, in practice, manufacturing such a catalyst with Dirac-type distribution is not viable to produce, step-type catalyst having the same behaviour with Dirac-type could be prepared using impregnation methods, instead. The study of Morbidelli et al. demonstrates that unevenly active material distribution in the support matrix for ethylene oxide catalysts is more fruitful in the sense of selectivity and yield rather than uniform distribution [21, 32].

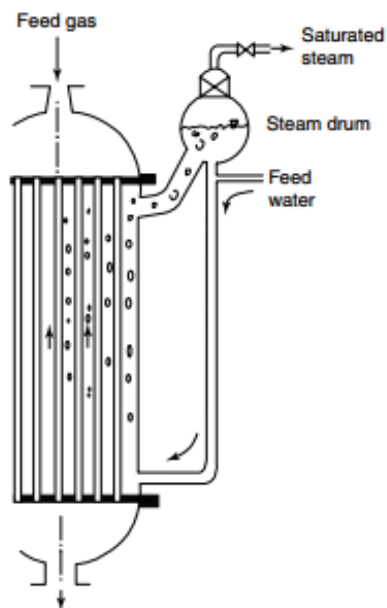


Figure 2.6. Multitubular reactor with steam cooling (Source: [5]).

Many heuristics and mode of actions both for the air and oxygen-based direct oxidation processes are similar. Reaction takes place inside the multi-tubular fixed bed reactor tubes (Figure 2.6) with a diameter of about 20-40 mm. The range of diameter is critical for the ease of the heat transfer to the coolant medium. Coolant medium could be changed from the design of the steam generation unit operations. Generally steam or organic heat transfer fluid are used. Heat of reaction of partial oxidation (105.2 kJ/mol) is much more lower than total oxidation (1419 kJ/mol). Therefore, heat transfer management is of great importance in order to take advantage of this massive exothermicity coming from the total combustion in terms of the process economics by decreasing the overall steam consumption of the plant. This is achieved by the pressure regulated coolant system which is designed to keep the tube-side temperature zones at a certain limits. Heat removal is carried out through two ways. The first is sensible heat of the process with output stream, the second is by means of the heat transfer to the steam generation units via coolant media.

The decision of change-over the catalyst is a trade-off between the steam generation and yield of commercial end products. Steam costs are not only intrinsic to the company but also strongly dependent on the national circumstances based on the electricity and natural gas production prices and sources. That is to say, there is no general acceptance with the life span even for the same type catalyst. In brief, it depends

on the corparative feasibility and besides its country as well. As long as the catalyst is getting on in years, with the strategy of maintaining the production at constant level, coolant temperature is increased which eventuates in diminishing the selectivity because of the fact that the activation energy of complete oxidation is 16.8 kJ/mol whereas the partial oxidation is 15.2 kJ/mol. The portion of the topmost reaction rate for both reactions is the vicinity of the entrance of the tubes owing to the highest partial pressure of the inlet components. Ideally, the difference between the peak and the lowest temperatures should be less than 30-40°C for the preservation of the reactor stability [5, 14-15].

Another point to consider is the operating pressure which is directly related to process economics. It is not that the reason of keeping the process at high operating pressures is about equilibrium considerations. Needless to say that, the formation of ethylene oxide is totally founded on the catalytic reaction principles. The heat generation could be easily directed to the wall side towards coolant medium by the help of the higher volumetric flow rate. For this reason, this situation makes high operating pressure conditions necessary for the sake of the avoidance of the pressure drop in terms of the total fluid energy conservation (i.e. Bernoulli law). The best operating range is between 1 to 2 MPa [7, 33].

Low ethylene conversion per pass is desirable for oxygen-based process while the conversion is much higher for decreasing the amount of ethylene in purge gas stream. The recent technologies are based on oxygen-based direct oxidation because of the high selectivity based process economics. To attain low ethylene conversion and prevent the reactor from high pressure drops, the space velocity is extremely important issue. The best practice of the space velocity for the oxygen-based process is about 3000-4500 1/hr [14-15].

In ethylene oxide process, the pathway of the recycle gas stream is significant to fully understand the material balance of the system. As can be depicted in Figure 2.7, in oxygen-based ethylene oxide process, the trajectory of the recycle gas in the closed-loop chiefly splits into five sections: Make-up (0), reaction (1), EO absorption and stripping (2), CO₂ absorption by-pass, purge and recompression (3) and lastly CO₂ absorption and stripping (4) sections. Firstly reactor products are going through the ethylene absorber and stripper unit [34]. Water is used as an absorbent for ethylene oxide because of the good polar interactions.

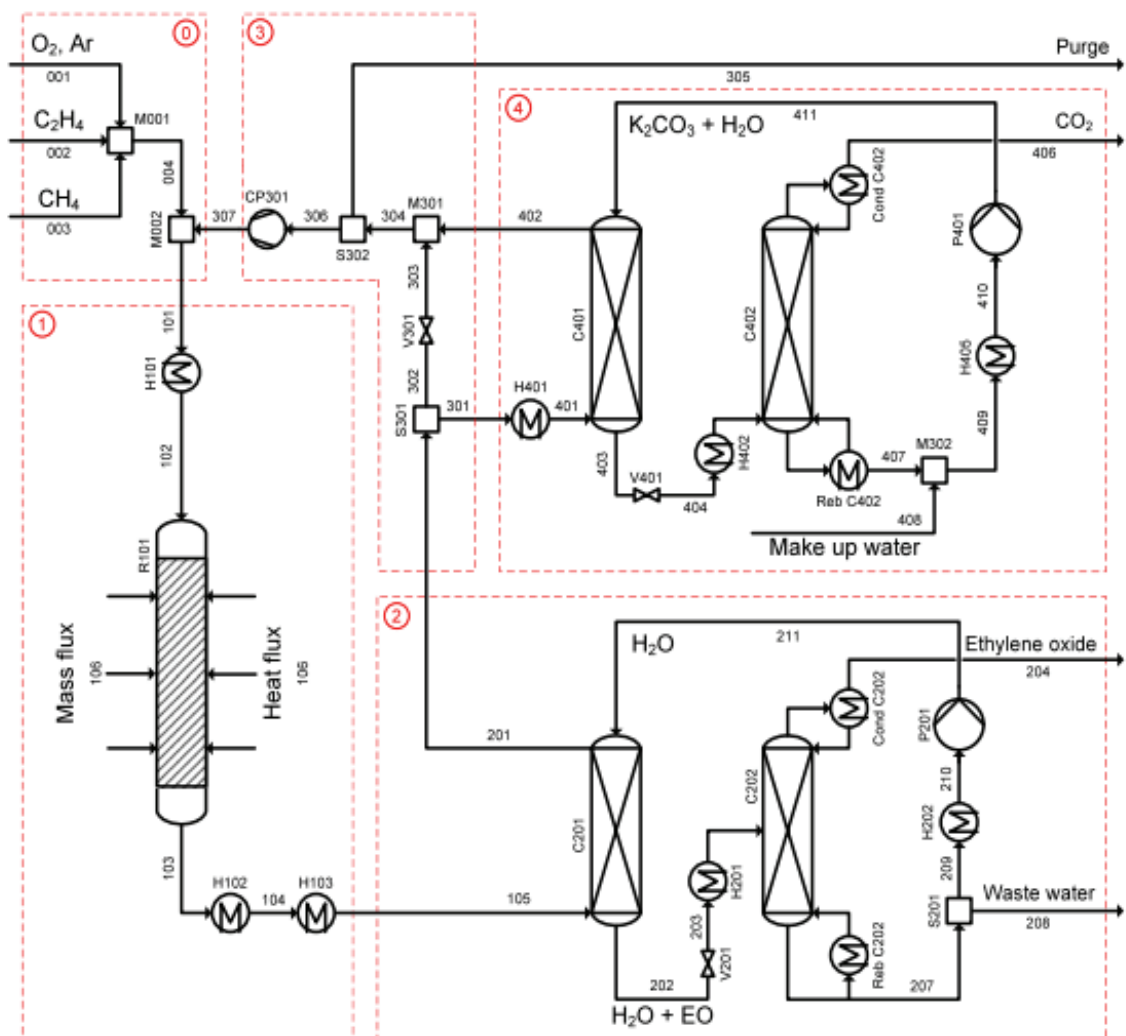


Figure 2.7. General representation for the trajectory of the recycle loop gas (Site 0: Battery limit; Site 1: Reactor site; Site 2: EO absorber and stripper; Site 3: Compression and purging; Site 4: CO_2 absorber and stripper) (Source: [34]).

Some portion of non-absorbable gas in the overhead stream of the EO absorber goes to CO₂ absorber and the rest of the portion is combined with the CO₂ absorber overhead which mostly includes inerts and ethylene and then make-up gases are added into this combined stream. Afterwards, the mixture gas, also called as the recycle gas stream are compressed so as to introduce into the reactor. During the course of this pathway, purge is essential for precluding the accumulation of inerts in the cycle.

Methane is generally preferred to use as a reactor diluent with a patented technology [35] because of many influential reasons. The most important key point is that the maximum ethylene oxide yields was obtained with methane because its improved heat transfer properties and good thermal conductivity prevent the reactor tubes from the hot spot formation which causes to generate CO₂ [36]. Besides that, its specific heat capacity is also close to the nitrogen. That's way there is no any drawback on the flammability limit. For these reasons, methane was selected as the most appropriate ballast gas for the oxygen-based ethylene oxide process. By the way, another benefit of making the purge is to remove the ethane from the loop which insinuates into the process as an impurity through the ethylene. Ethane accumulation directly causes to the reduction of the selectivity because of the fact that ethane consumes and sweeps the chlorine compounds on the catalyst surface. The effect of argon is positive because it makes available to reduce the flammability limit of the reaction. While the purge flow keeping the inerts at a certain range, ethylene and methane which are valuable regarding process economics are also inevitably purged. For that reason, membrane systems are used for the recovery of the ethylene and methane [14-15].

Regarding to the effect of the reaction products at the entrance of the reactor, there is some kind of disagreement on how severe this situation has influence on the selectivity. Because researchers have used different catalyst supports and promoters in their system so these certainly affect to the catalytic mechanism. However, according to the industrial experience and researchs, it is clearly known that CO₂ has more inhibiting effect on total combustion than partial oxidation. That is to say, it has a positive impact on the selectivity. For this reason, despite the fact that it is impossible in practice, it is untoward to make inlet CO₂ zero. All studies about the investigation on ethylene oxide effect on both reactions are on the same page that ethylene oxide inhibits more or less the partial oxidation. As regards to the presence of the water, it has an adverse effect on the selectivity even at the low concentrations of 0.2-1.4% [19, 37-39].

2.2 Kinetic Models in Ethylene Oxide Production

There are two schemed reaction mechanism (Figure 2.8) models in the literature. The first is Eley-Rideal mechanism which propose that the only-chemisorbed reactant on the active sites is molecular oxygen and consecutively reacts with ethylene in gas phase, that results in ethylene oxide production. In this model, atomic oxygen is responsible for the total combustion. The second model is based on Langmuir-Hinshelwood mechanism which puts forward that ethylene and dissociative oxygen (i.e. atomic oxygen) could be adsorbed on the vacant sites and accordingly react on the adjacent sites. In the case of this model, dissociatively adsorbed oxygen gets involved in yielding both carbon dioxide and ethylene oxide. Some previous infrared spectra[40-41] and TPR [42-43] results coupled with recent microkinetic modeling and density functional theory (DFT) studies [22, 27, 44] reject the Eley-Rideal model. The general acceptance is that the rate-determining step is the surface reaction for most studies and models.

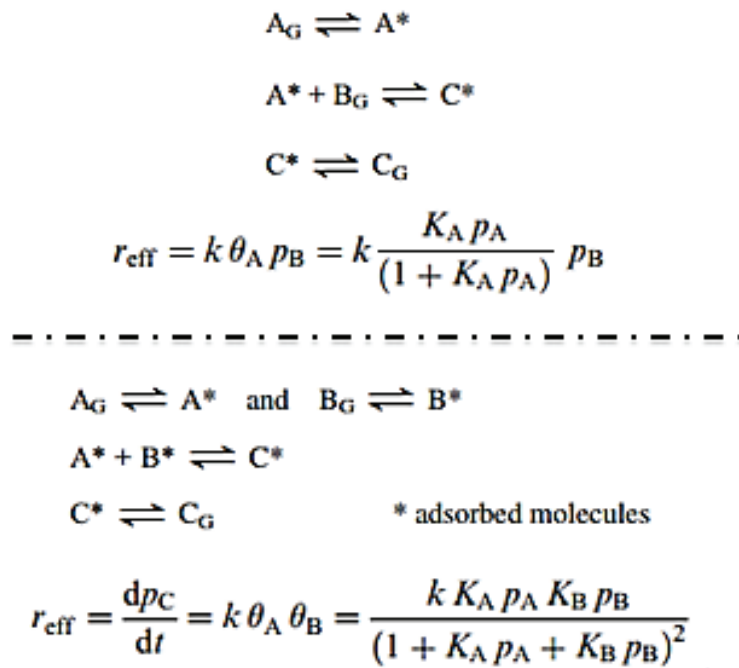


Figure 2.8. Eley-Rideal (top) and Langmuir-Hinshelwood (below) mechanisms
(Source: Adapted from [24]).

To date back, most majority of the researchers developed some empirical models from their experimental studies, with the exception of few studies conducted by first principles based on transient surface science experiments. The diversification of these empirical models in the literature are resulting from the category of catalysts in use (self-prepared or vendor-based), shape of the catalyst (fine or pellet), amount and type of the promoters and lastly different experimental conditions (ethylene-rich or oxygen-rich) [38, 45]. The most worth considering deduction from this general observation is that it should be taken all these issues into account while selecting a kinetic model from the literature for a unique process contemplating making it use for fine tuning in the modeling works.

In Table 2.1, most-cited kinetic models in the literature are summarized. This table unfolds the reality that the terms inside the nominator and denominator of any model vary with respect to the assumptions and simplifications that were taken for granted by the researchers.

According to Klugherz and Harriot, a dual-site Langmuir-Hinshelwood (L-H) mechanism is prevailing on both reaction rates, with a self-prepared catalyst in their differential reactor set-up at different feed conditions. They alleged that these reactions take place different adjacent sites of the surface location that have dissimilar bonding energies for oxygen adsorption and the concentration of active sites are determined by the oxygen partial pressure. Both primary reactants separately and all products in a lumped parameter are competing for the sites to adsorb with a wide range of ethylene and oxygen pressures and this case has shown in the model. Also, they proposed that all products (EO, CO₂ and water) inhibit the reactions [46].

Metcalf and Harriot targeted for harvesting results in the wide range of high oxygen pressure under lean-ethylene conditions with a catalyst prepared as to the similar procedure in Klugherz and Harriott study. They investigated the effects of CO₂, water, EO and dichloroethane (DCE) on the ethylene oxide and carbon dioxide reaction rates in a differential reactor in accordance with the Langmuir-Hinshelwood theory. They came up with the fact that inhibiting effects of CO₂ and water seem to be fast, reversible and not obeyed to a competitive rate law, whereas the inhibiting effects of EO and DCE appears to be slow and reversible. Lastly, they stated that the results were not completely consistent with the L-H mechanism [47].

Table 2.1. Popular kinetic models for EO production process in the literature.

Kinetic Model Expression	Reference
$r_i = \frac{k * K_E * K_O * P_E * P_O}{(1 + K_E * P_E + K_O * P_O + K_{EO} * P_{EO})^2}$	Ghazali et al. [53]
$r_1 = \frac{k_1 * P_E * P_O - k_2 * P_E * P_O * P_{DCE}^{k_7}}{1 + k_5 * P_O + k_6 * P_E} \quad r_2 = \frac{k_3 * P_E * P_O - k_4 * P_E * P_O * P_{DCE}^{k_8}}{1 + k_5 * P_O + k_6 * P_E}$	Petrov et al. [50]
$r_i = \frac{k_r^i * K_E^i * P_E * P_O^{n_i}}{1 + K_E^i * P_E + K_C^i * P_C + K_W^i * P_W + K_{EO}^i * P_{EO}}$	Westerterp et al. [58]
$r_i = \frac{k_r^i * K_E^i * K_O^i * P_E * P_O}{(1 + K_E^i * P_E + K_O^i * P_O + K_C^i * P_C + K_W^i * P_W + K_{EO}^i * P_{EO})^2}$	
$r_i = \frac{k_r^i * K_E^i * \sqrt{K_O^i * P_E * \sqrt{P_O}}}{(1 + K_E^i * P_E + \sqrt{K_O^i * P_O + K_C^i * P_C + K_W^i * P_W + K_{EO}^i * P_{EO}})^2}$	
$r_j = \frac{k_j * C_E * C_{O_2}^{\alpha_j}}{(1 + K_E * C_E + K_{O_2} * C_{O_2}^{\beta_j})^2}$	Salmi et al. [63]
$r_i = \frac{k_i * P_E * P_O^{n_i}}{(1 + K_E^i * P_E)^2}$	Lafarga et al. [23]
$r_{EO}^0 = \frac{(k_1 * \exp(-E_1/RT) * P_{ET} * P_{O_2}) * (1 + e_1 * C_{EDC})}{1 + K_1 * \exp(\Delta H_1/RT) * P_{CO_2} + K_2 * \exp(\Delta H_1/RT) * P_{O_2}^{0.5} * P_{H_2O}}$	Gu et al. [61]
$r_{CO_2}^0 = \frac{(k_2 * \exp(-E_2/RT) * P_{ET} * P_{O_2}^{0.75}) * (1 + e_2 * C_{EDC})}{1 + K_1 * \exp(\Delta H_1/RT) * P_{CO_2} + K_2 * \exp(\Delta H_1/RT) * P_{O_2}^{0.5} * P_{H_2O}}$	
$r_1^0 = \frac{k_{r1} * P_{O_2} * P_{C_2H_4}}{1 + K_1 * P_{O_2} + K_2 * P_{O_2}^{0.5} * P_{CO_2}}$	Gan et al. [60]
$r_2^0 = \frac{k_{r2} * P_{O_2}^{0.5} * P_{C_2H_4}}{1 + K_1 * P_{O_2} + K_2 * P_{O_2}^{0.5} * P_{CO_2}}$	

Petrov et al. have many sequential studies on ethylene oxide process kinetics. They used their own synthesized silver catalyst promoted by a Ca additive in a circulation flow system and the kinetic models based on the single site Eley-Rideal (E-R) mechanism with various modifications in all their works. The experimental conditions are set to wider range of feedstocks (ethylene and oxygen) and generally at oxygen-rich conditions, from lower to higher concentration. In their first study, they proposed a kinetic model at 210-290°C without inhibition effects of products and chlorine inhibitors [48]. In their second work, they included the DCE as an inhibitor and extended the model that they previously generated [49]. Ethylene oxide oxidation with and without DCE was also studied in their subsequent studies [50-51]. Also influence of the feed water was investigated with a catalyst containing 20% silver and a lots of promoters such as Li, Na, K, Mg, Ca, Ba, Mn and Fe. As a result of this study, the feed water even if at low concentration strongly affects the selectivity [39]. Another study of this team was aimed at the inhibiting effect of CO₂ by 12-33% feed concentration with the same catalyst as in the feed water study. They concluded that CO₂ inhibition is much more effective for combustion reaction than partial oxidation [37].

Ghazali et al. explored the possibility of extending the observations into the catalyst coverage and inhibition as a function of reactant and product partial pressures at low temperatures of 180-210°C, by using L-H mechanism under the various ethylene and oxygen concentration. They used a fixed bed semi-differential reactor with a catalyst containing 11.3% silver promoted by a 1% Ba and silica as a support material. They established such an outcome from their study that partial oxidation is inhibited because of not providing basis on sufficient self-cleaning conditions with the avoidance of the silver carbonates. To confirm this, unsteady-state experiments has been conducted [52].

As well as Ghazali et al., Park and Gau set up a similar reactor at a constant temperature of 160°C with a catalyst including 25% silver and 2% Ba at a broad range of ethylene and oxygen concentrations, in order to determine the deposits (alkoxides or carbonates) originated from combustion reaction at unsteady-state case and examine its influence on steady-state reaction kinetics. They used L-H mechanism as well, besides that in this case the kinetic model has a good performance of steady-state kinetics even when the catalyst is not self-cleaning. They concluded that the effect of the deposits may change with regards to the catalyst type, the nature of the promoting agents, temperature and ratio of partial pressure of the reactants. Through the chlorine coverage,

the reaction of adsorbed molecular oxygen with an adjacent free site is inhibited at high carbonate coverage and this results in increasing the selectivity at low temperatures [53].

Apart from other studies, Stoukides and Pavlou investigated the issue of excess feed ethylene oxide concentration at the temperatures 280-400°C in the CSTR and how the reaction affected by the presence of the external and mass transfer limitations, using a single site E-R mechanism. They used a pure silver catalyst with no support and promoter. The conclusion from the work is that the reaction selectivity adversely affected by the overabundance of ethylene oxide feed because of the fact that EO and ethylene compete for the same sites on the catalyst surface and ethylene oxide oxidation reaction increased. Second result is that the existence of the external mass and heat transfer limitations ends up with the significant drop in selectivity [54].

Al-Saleh et al. made a research on finding the ethylene oxidation kinetics with E-R mechanism by using Berty reactor which is a type internal recycle reactor not allowing any heat and mass transfer limitations, operating at a temperature range of 513-593K and pressure of 21.7 bar. They used a commercial silver catalyst having a 7.96 % silver load and 8.8 ppm iron promoter in oxygen-rich experimental conditions. They reported that carbon dioxide inhibits both of the reactions [55].

Westerterp and Ptasiński simplified the rate equations for both reactions in concordance with the first-order kinetics with respect to oxygen concentrations taking the basis of oxygen-lean operating conditions. They observed that it is required to decrease the coolant temperature in order to increase the selectivity with the loss of total conversion [56].

Borman and Westerterp examined the kinetics of the selective oxidation of ethylene in oxygen-rich feed conditions using an internal recycle reactor with an industrial silver catalyst by the help of utilizing the dual site L-H mechanism. They found the apparent activation energies for k_1 and k_2 reactions as 70 and 86 kJ/mol, respectively which means that increasing the temperature causes to decrease the selectivity. Another important point to mention is that higher partial pressures of CO_2 leads to an increase in selectivity of ethylene oxide, whereas higher partial pressures of EO in the feed induce diminishing the selectivity. On the other hand, water has no immense affect on the selectivity.

The last significant issue reported by Westerterp et al. is that special deactivation procedure was implemented to crack the first activity region of the catalyst. This made

easier for the transition to the high selectivity region in pursuance of outsmarting the fallacious preliminary results of the catalyst with high activity as stated in other studies. Within the context of the activation procedure, the reactor was heated to 500 K with nitrogen and 1.8% ethylene in air was introduced to the reactor at a flow rate of 0.74 g/s and a reactor pressure of 5 bar. The expected maximum lapsed time for monitoring to reach out the stability was 150h [19, 46, 57]. Same authors made a research study on epoxidation kinetics with the same reactor and inlet feed conditions (excess oxygen) at a temperature range of 181-253°C without chlorine addition. They formed a judgment that CO₂ strongly inhibits both reactions, particularly total oxidation. Ethylene oxide has a more inhibiting effect for epoxidation reaction over the other one. Regarding water, its influence of inhibition is same degree of severity for both reactions [58].

In the study of Lafarga et al., ethylene epoxidation kinetics was studied over a cesium-doped silver catalyst supported on α -Al₂O₃ pellets in a differential reactor, using a dual-site L-H mechanism under the different ethylene and oxygen concentration (3-12%) at four temperatures of 210, 230, 250 and 270°C. Activation energies are in a similar range with Westerterp et al. By the same fashion, Lafarga et al. applied an initial activation procedure for 48 h at a constant temperature of 280°C with a reaction mixture of 6% oxygen, 6% ethylene and balance argon by a 200 sccm total flow. They concluded that the selectivity of EO was increased with increase in oxygen pressure and decreased with temperature. This is unlikely to happen for other partial oxidation reactions of hydrocarbons in which increase of oxygen partial pressure gives rise to increase hydrocarbon conversion but decrease the selectivity of the desired product [23].

Gan et al. constructed two-dimensional heterogeneous model based on E-R mechanism for finding the global kinetic rate equations of ethylene oxide process in a gradientless fixed bed reactor under ethylene-rich conditions (i.e. oxygen based process) [59]. For similar conditions as Gan et al. regarding adsorption mechanism and feed conditions, Gu et al. proposed a kinetic model with EDC inhibition [60].

Hernandez et al. preferred to use microplate reactors varying the temperature from 220-300°C for the determination of the kinetics with two alternative self-preoared catalysts: Wash-coated with a silver/ α -alumina (15% silver content) and pure silver. Microreactors have the growing attention in reactor engineering due to the fact that they have much higher surface-to-volume ratio (10000-50000 m²/m³) than conventional reactors (100-1000 m²/m³), which enables effective heat removal. Two types of Langmuir-Hinshelwood mechanism were tested. The only difference between these

types is whether molecular or dissociatively adsorbed oxygen reacts with adsorbed ethylene during the course of the surface reaction that is rate-determining step in all types of the model (L-H or E-R). It was also used a pretreatment procedure for the catalyst stabilization with ethylene flow in helium followed by oxygen flow in helium. The products influence on the kinetic model is not taken into account, the feed conditions both for the ethylene and oxygen are changing from 5-25% in their study. They concluded that reaction rates of ethylene oxide and oxygen increase both with boosting ethylene and oxygen concentration [6].

Salmi et al. conducted an investigations upon ethylene oxide formation on pure silver catalyst in an isothermal microreactor, with the feed conditions of the oxygen (2-30%) and ethylene (2-25%) at a temperature of 250°C. Pretreatment of the catalyst was used with ethylene during 12h. 3 types of adsorption models are used. For the experimental data, two reasonable model from the rivals came into prominence. The first is one type of L-H with 92.4% R^2 which is the combination of atomic and molecular oxygen. The second is E-R with 95.9% R^2 which neglects the atomic oxygen effect. They drew the conclusion that the reaction order for epoxidation reaction with respect to oxygen is higher than 0.5 which demonstrates any form of oxygen play an important role in the kinetics of ethylene oxide reaction. From the point of the view of the selectivity, different kind of the oxygen takes effect on both epoxidation and total oxidation [61].

In the thesis of Ansgar Kursawe, in consideration of selectivity and conversion calculations, Langmuir-Hinshelwood mechanism was used utilizing different microchannel reactors to show their performance comparing with the fixed bed reactors. To do this, he conducted experiments with self-prepared catalyst, however in the fixed bed reactor it is used Shell 800 series commercial catalyst. Feed conditions were changed from oxygen-lean to oxygen-rich cases. Specific catalyst activation procedure with a mixture of 20% ethylene and 20% oxygen was implemented [19].

2.3 Reactor Modeling in Ethylene Oxide Production

In the literature, ethylene oxide reactor modeling studies could be categorizes into two groups as shown in Figure 2.9. The former refers to any study that performs to model lab-scale reactor aimed at different reasons such as reactor design, catalyst

performance testing, determination of parameter sensitivity and kinetic testing. The latter points out any study conducted for modeling an industrial reactor in the light of either the empirical algorithms (artificial neural networks (ANN), support vector machines (SVR), genetic algorithms (GA) or any combination of numerous machine learning algorithms) or grey-box modeling which is the integration of theoretical equations with data-driven algorithms.

The starting point to design a grey box model could be through a black-box (empirical) modeling or white-box (mechanistic) modeling. Afterwards, upon that, it is manipulated by either adding specific model equations or applying regression methods. In contemplation of predictive performance of real process data, grey-box models are more robust and reliable. For this reason, they are more favorable in the industry unless construction of these models takes much time. Complexity of the system to be modeled is by all means the most significant consideration to specify a roadmap in advance of the work.

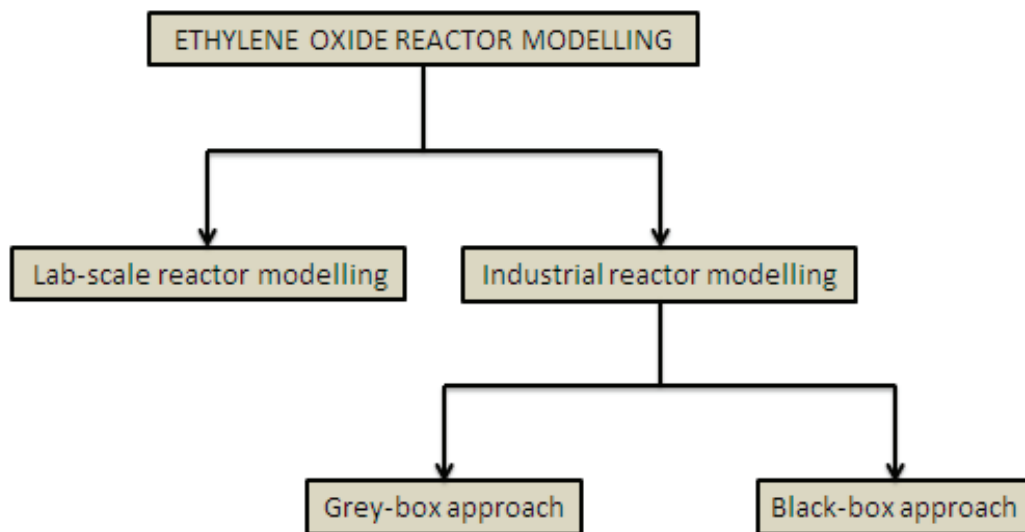


Figure 2.9. General overview of the modeling concept for ethylene oxide reactor.

Salmi et al. [62] conducted research on two novel reactor models for microreactors within the context of the lab-scale reactor modeling, using one of the best kinetic models with some simplifications that has been generated by themselves in a previous study [61]. The constructed models were based on dynamic mass balances including with the gas phases with convection, radial and axial terms coupled with the interaction between intrinsic kinetics and diffusion in the porous catalyst layer by the

help of using gPROMS software. They reported that modeling results were consistent with the experimental results.

In the thesis of Hanna Perzon [63], it was used a simple first order kinetic model in order to construct a model for the industrial ethylene oxide reactor in AkzoNobel company by using Aspen Plus software. Pre-exponential factors and activation energy values were taken from the study of Gu et al. It is concluded that kinetic parameters from the literature could be used to model the EO reactor provided that they have to adjust to the historical data. This is the way of making grey-box model that could be done by starting with mechanistic models. Ethylene oxide conversion was estimated with the percent error of 7.3%.

As part of the doctorate thesis performed by Kishor G.Gudekar, it was targeted to develop a two-dimensional heterogeneous dynamic model for ethylene oxide reactor coupled with the separation units. The kinetic model in this study has been taken from the article issued by Westerterp et al. [58]. Within the scope of the thesis, catalyst deactivation was also modeled as a nonlinear function of operating time and reactor temperature. Sequential quadratic programming (SQP) was used to solve nonlinear equations. It was reported that an optimal temperature profile is found maximizing the profit [64].

In the context of another doctorate thesis accomplished by A.A.Iordanidis [65], ethylene oxide reactor was modeled in the software package “PackSim” by using the kinetic model adopted from Westerterp and Ptasinski [56]. Author demonstrated the general roadmap of the modeling strategies of the fixed-bed reactor very well, as shown in Figure 2.10. It was reported that a rise in the range between 20-40⁰C in the reactor was observed. This points out a moderately exothermicity which was substantiated by the smooth temperature and concentration profile in the reactor. There are two important results that inferred from this study. One is that percent difference between 1D pseudo-homogeneous and 1D heterogeneous model is close to 5%. The second one is that there is no significant disparity between axial and radial models.

In the doctorate thesis of Andreas Peschel [31] and his published two articles that are related to the thesis [34, 66], air-based and oxygen-based processes were separately examined within the framework of designing the optimal ethylene oxide reactor in terms of the selectivity, energy minimization and environmental considerations. For air-based section of the study, the kinetic model constructed by Al-Saleh et al. and their catalyst specifications were used due to the fact that the highest

selectivity was obtained among the other air-based research studies. A selectivity increase of 3.25% was obtained. In the second section, oxygen-based reactor considerations was examined taking the basis of the kinetics and catalyst information from the study of Gan et al. . Feed conditions of the published studies that has been used for their kinetic paramaters and models played a crucial role in the model screening for both sections. Therefore, total running expenses for an oxygen-based EO plant having an average capacity of 10^5 EO/yr was reduced as a result of the new designed reactor.

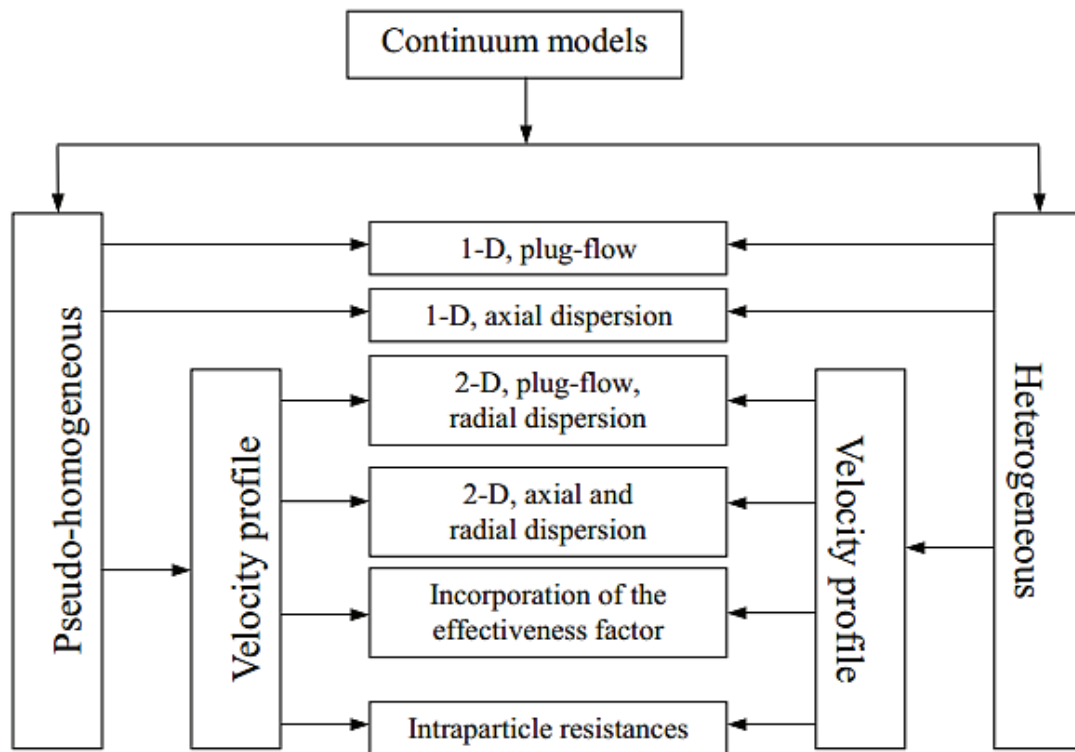


Figure 2.10. Modeling strategies of the fixed bed-reactor (Source: [65]).

Aryana et al. [67] made a research study on an oxygen-based industrial ethylene oxide reactor modeling and optimization in Huntsman Corporation. They used a kinetic model from the external source of Petrov et al. [49] in which the EDC effect was included. Catalyst deactivation was also taken into account as a nonlinear function of operating time. The structured model in this study is 1D-heterogeneous model neglecting radial dispersion of concentration and temperature in reactor tubes owing to the small radius of the tubes relative to the length ($r/L \ll 1$). Moreover, radiation term was also disregarded by reason of the fact reactor operating temperature is below 673K. The simulation result shows that EO concentration in the recycle gas loop causes to

decrease the selectivity and the influences of EDC level and oil temperature on selectivity and work rate is of great importance. As a result of steady-state optimization, EDC and ethylene concentration play an active role in the bounds. As usual, steady-state optimization results were utilized as initial conditions for dynamic optimization. Dynamic optimization outcomes demonstrated that selectivity could be enhanced by more than 2% by playing with oil temperature precisely in order to compensate catalyst activity losses during the course of the catalyst life. Besides that, optimal transition strategies from low to high capacity were defined for oil inlet temperature and oxygen concentration.

Galan et al. [68] also investigated the same industrial reactor in Huntsman Corporation as Aryana et al. [67] by using the kinetic model of Petrov et al. [49], including EDC inhibiting effect and catalyst deactivation aimed at creating a self-regulating mechanism to prevent excessive thermal excursions. They reported that increasing the inlet feed temperature results in boosting the selectivity within the constraints and this was achieved by optimizing the heat exchange of the preheater which is the combined heat exchanger. Apart from that, ratio control of ethylene to oxygen could be effective on selectivity and safety considerations according to this study. Lastly, they stated that DCE level and coolant inlet temperature are also very significant variables to be optimized continuously.

Zhou et al. studied on steady-state and dynamic optimization of oxygen-based ethylene oxide reactor taking the basis kinetic model of Gu et al. They explicitly stated that down-stream decarbonated and design limits of the recycle gas compressor coupled with the explosive envelope mainly triggered by EO and oxygen are the key constraints to be reasoned out for those who want to squeeze a benefit culminating on any EO reactor optimization study. It has not escaped the notice that it is found to have great influences of inlet EDC concentration and coolant temperature on the bed temperature and on the top of this, these effects are very acute to the degree of that they could be merely realized by dynamic optimization. Moreover, the optimal EDC level remains intact when increased of the productivity. The effects of the reaction kinetics depends on the optimization type which means that they are not so much significant in steady-state optimization because optimal values are established by physical properties of the gas mixtures and explosive limit whereas they would play a crucial role at the dynamic optimization upon finding the optimal value of EDC concentration and coolant temperature profile. Lastly, they advised that it is to be used refined kinetics by the

process historian data intrinsic to the reactor to get more approachable results to the reality because kinetics in the literature has been obtained under different circumstances such as chemical compositions, promoters in trace amounts, size of silver particles and as one might expect these are very decisive parameters on the kinetic model to be derived [45].

In the published article of Zeeshan Nawaz, it was reported that an industrial multitubular packed-bed ethylene oxide reactor was modeled by using the equation-oriented software of Aspen Custom Modeler (ACM) in order to maximize EO selectivity and production. As a kinetic model, it was used that of Petrov et al. [49] in which EDC effect also takes into consideration. As a result of the study, 1D heterogeneous reactor model was obtained which had a good match with the process data. After analyzing radial temperature profile, it was observed that this is an important indicator for hot spot determination. It is also worth mentioning in this study that the feed inlet temperature is not critical unless it is desired to control hot spots in the beginning of the tubes. On the contrary, by the designer of the reactor, the top side of the tubes serves as a preheater [8].

Vandervoort et al. examined the ethylene oxide reactor within the framework of multiobjective optimization (MOO) concept. The objectives are maximization of ethylene oxide selectivity, production and the safety factor. They used the kinetic study of Petrov et al. by using “Objective-Based Gradient Algorithm” as a first approximation and Net-Flow procedure accordingly in the Pareto domain. The results show that operating conditions were gone out of the Pareto domain by any variation in the volumetric gas flow rate or a decrease in inlet pressure, this means that it should be paid heed to control these variables in the reactor [69].

Rahimpour et al. made two research studies on grey-box modeling of oxygen-based industrial ethylene oxide reactor. In the first one [70], a 1D heterogeneous model (steady-state and dynamic) was developed by using a kinetic model of Gu et al. [60] in the presence of 3-year-deactivation term of the commercial catalyst ($\text{Ag}/\text{Al}_2\text{O}_3$). Optimum EDC level was found as 0.37-0.42 ppm by virtue of the ANN technique of Multilayer Perceptron (MLP) in Matlab software. The network has three input variables and one output variable in MLP architecture. The inputs are EDC, activation energy used in deactivation model and EO whereas the only output variable is the selectivity. The resultant model has a percent error of 5% with regard to the process historian data. It was shown that the difference between EO mole fraction of bulk and pellet phases are

both increasing with decrease of gas velocity which attributed to the chemically controlled kinetics and the mass transfer resistance of gas film around the catalyst pellets.

In the second work [71] of Rahimpour et al., they used different optimization algorithm called as differential evolution algorithm for two different optimization cases (steady-state and dynamic) in order to optimize the ethylene oxide yield. Dimensionality of the model and other conditions (cited kinetic model, reactor and process specifications) are same with the previous study. The optimization strategy is that the optimal values of four process variables (temperatures of feed and cooling water, inlet pressure, inlet molar flow rate) were determined under the steady-state conditions and afterwards these variables were used in finding the optimal temperature profile for bed and coolant side of the reactor. As a consequence of these subsequent optimization cases, there seems to be increased the EO yield by an increase of 1.726% and 4.22%, respectively.

Zahedi et al. [72] investigated into a creating a grey-box model about an industrial ethylene oxide reactor with the help of the kinetic of Gu et al. [60]. They used radial basis function network (RBFN) for building a model with some input variables (Time, C_2H_4 , O_2 , C_2H_4O , CO_2 , H_2O) and a multiplication factor of reaction rate and catalyst deactivation. In the ANN model, 109 data out of 169 were used for training and the rest of them were utilized for validation set for the confirmation of generalization capability of the network. The results show that the grey-box model is 8.437 times more accurate than the first principle model. For the calculation of white-box model, 1D heterogeneous model equations were preferred to use. General workflow of this study is represented in Figure 2.11.

Luo et al. developed a hybrid model with an integration of kinetic mechanism, reactor model and deactivation model generated by using Support Vector Regression (SVR) which is a powerful machine learning algorithm. First principle modeling part was based on 1D heterogeneous equations and included the kinetic model of Gan et al. [59]. Three input variables (Time, reactor temperature and previous reaction rate) and one output variable (deactivation rate) were used in SVR. Monthly-average data matrix over the period of 750 days were selected for comparing the results with process historian data. The result shows that the grey-box model has a percent prediction error of less than 5% [73].

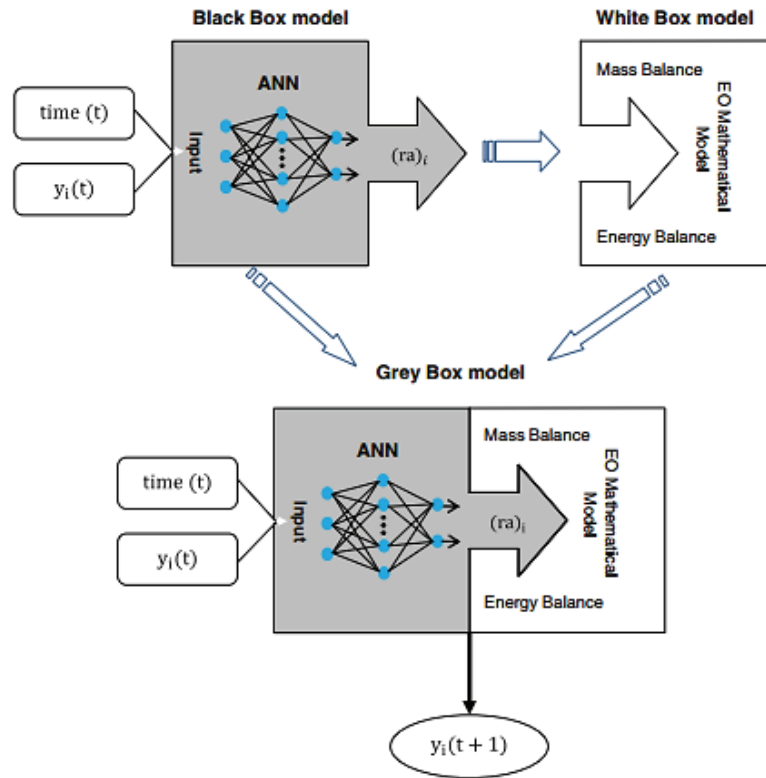


Figure 2.11. Representation of white box, grey box and black box modeling
(Source: [72]).

Apart from above-mentioned approaches (grey and white box modeling), Lahiri et al. merely used SVR-GA (Support Vector Machine-Genetic Algorithm) which is a black-box modeling technique without including any prior process knowledge such as first principle based reactor modeling equations and kinetic mechanism. SVR is adopted for making correlation between process and performance variables, whereas GA is for optimization to maximize the process performance. It was concluded that significant improvement in the EO production and selectivity was obtained thanks to the optimized solutions [74].

CHAPTER 3

MATERIAL AND METHODS

3.1 Materials

From the gas tubes that were used in catalyst testing system, oxygen ($\geq 99.999\%$), carbon dioxide (≥ 99.995) and methane (≥ 99.95), vinyl chloride monomer (5ppm, ballast gas: Helium) were purchased from Linde Gas, ethylene oxide (1.23%, ballast gas: Helium) and helium ($\geq 99.999\%$) were purchased from Habaş A.Ş and ethylene (≥ 99.97) was internally supplied from ethylene plant in Petkim. Apart from these, two different calibration gas tubes were used. One (tube#1) is oxygen free-main mixture tube including 57% methane, 25% ethylene, 13% helium, 4% carbon dioxide, 1% ethylene oxide that was purchased from Air Products was used for gas chromatography (GC) calibration. Second (tube#2) is, which was purchased from Hat Sinai A.Ş., another mixture gas including 6.5% oxygen and 2.5% carbon dioxide with nitrogen balance. The reason why oxygen is excluded from main mixture tube is to prevent ethylene oxide to be depleted by oxygen.

The commercial catalyst was taken from the EO/EG plant and detailed brand information was not allowed to share by the catalyst vendor, therefore its name and generation were both kept anonymous throughout this study. Silicon carbide in different particle sizes (38-600 μm) was procured from Saykar Ltd. and aluminum oxide (standard grade) was purchased from Sigma Aldrich. Quartz wool for supporting catalyst bed elements was procured from Terralab A.Ş. Instrument air (alternatively nitrogen) that is used for valve movements in GC and sodium hydroxide solution (50%) for neutralizing GC outlet gas were also supplied from Petkim. In case of any maintenance situation in instrument air pipeline, GC line has a flexibility to switch the gas supply to nitrogen. Lastly, activated carbon was purchased from Sel A.Ş. in an attempt to eliminate any possibility that ethylene gas includes trace amount of impurities.

3.2 Experimental Set-up for Catalyst Testing

Catalyst testing system was customized particularly for ethylene oxide reaction. As depicted in Figure 3.1, kinetic experimental system could be typically divided into three sections: Feed introduction, reactor panel and gas chromatography. In the first part, there are six feed lines (ethylene, oxygen, methane, carbon dioxide, vinyl chloride monomer/helium and ethylene oxide/helium) belonging to reaction system components along side the mass flow controllers (MFC) which were supplied from Alicat Scientific, Inc except ethylene oxide line which was purchased from Aalborg Instruments and Controls, Inc. All MFCs have an upper capacity limit of 50 sccm but that of oxygen is 20 sccm. Turndown ratios of Alicat and Aalborg MFCs are 50:1 and 40:1 respectively. Apart from these MFCs, a Bronkhorst MFC with a maximum limit of 150 sccm was mounted to provide coarse flow rate adjustment alongside the GC inlet in order to preclude the GC valve from being exposed to high pressure.

Tubing and fitting materials were purchased from Swagelok co. All tubings that are used in catalyst testing system are 1/8 in. and made of SS 316 grade material. Filters that are mounted before MFCs and have 0.5 micron element pore size are used for capturing infinitesimal amount of impurities being entrained by feed gases. Ethylene is passing through double filtering process. The former is the filter including activated carbon and the latter is metal filter. Check valves that are used for blocking reverse flow are put after MFCs and have a cracking pressure of 1 psi. Flow coefficients (cv) of all valves in the system were determined in consideration of the range of flow rate in the planned experiments which is 75 sccm on average. Gases are mixed in a nozzle and introduce into the reactor. Pressure of the reactor is monitored by a pressure transducer (PI) at the inlet of the reactor. Pressure is manually controlled by manipulating back pressure controller (BPR) settled on the downstream of the reactor.

After mixing nozzle, the mixture is pre-heated by using flexible electric heating tape (HTS/Amptek Co.) which is controlled by TIC-1 (PT-100 type sensor) and given same set point as furnace temperature (TIC-2) mounted in the middle of the reactor. Nevertheless TIC-1 and TIC-2 (Type K thermocouple) have the same set point, mixture temperature is inevitably reducing to a certain level alongside the reactor until reaches the catalyst bed and center of the heat source providing by single-zone tube furnace made of ceramic refractory (Thermcraft Inc.).

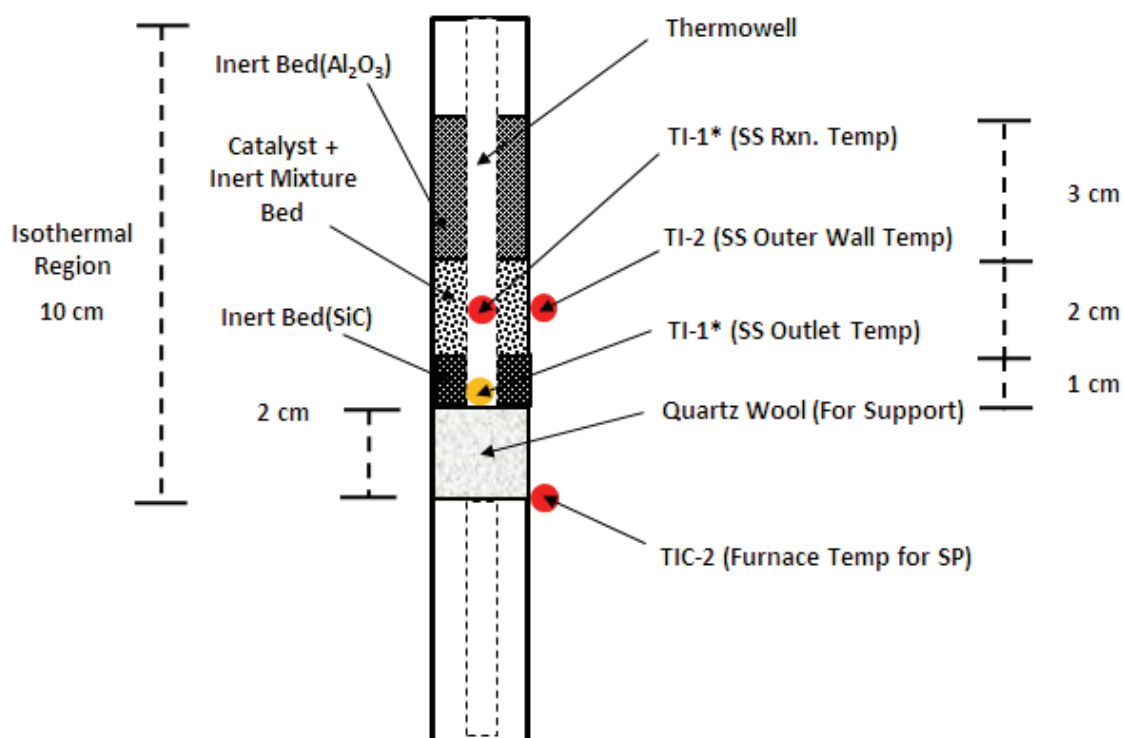


Figure 3.1. Catalyst bed scheme for lab-rig reactor.

All MFCs and reactor with furnace are mounted on the customizable panel purchased from Parr Instruments. There is no cooling jacket coupled with the reactor that is hanged on the furnace cavity.

The schematic design illustrated in the Figure 3.2 shows the enlarged section of the reactor tube middle (not the entire reactor) encompassing isothermal region. TI-1 is a thermocouple that sits directly in the thermowell inserted from the top of the reactor. It has been keeping the TI-1 at a fixed location in the center of the catalyst mixture region until the process reaches its steady state. Once steady state is reached, it is moved to the thermocouple up and down to measure bed temperatures at different heights assuming that the T-profile does not change in time after steady-state. There is an extra inert layer (SiC) below the catalytic bed so that the range of the motion of TI-1 also covers the outlet of the catalytic bed. Throughout the modeling study, TI-1 is only used for measuring center of the catalyst bed as a single point. Outlet of the reactor and other axial points of the catalyst bed were not used in the kinetic model because of the fact that 1-D axially distributed model coupled with advanced discretization methods is used in gPROMS. In this way, mass and energy balance equations are solved simultaneously in the flow direction.

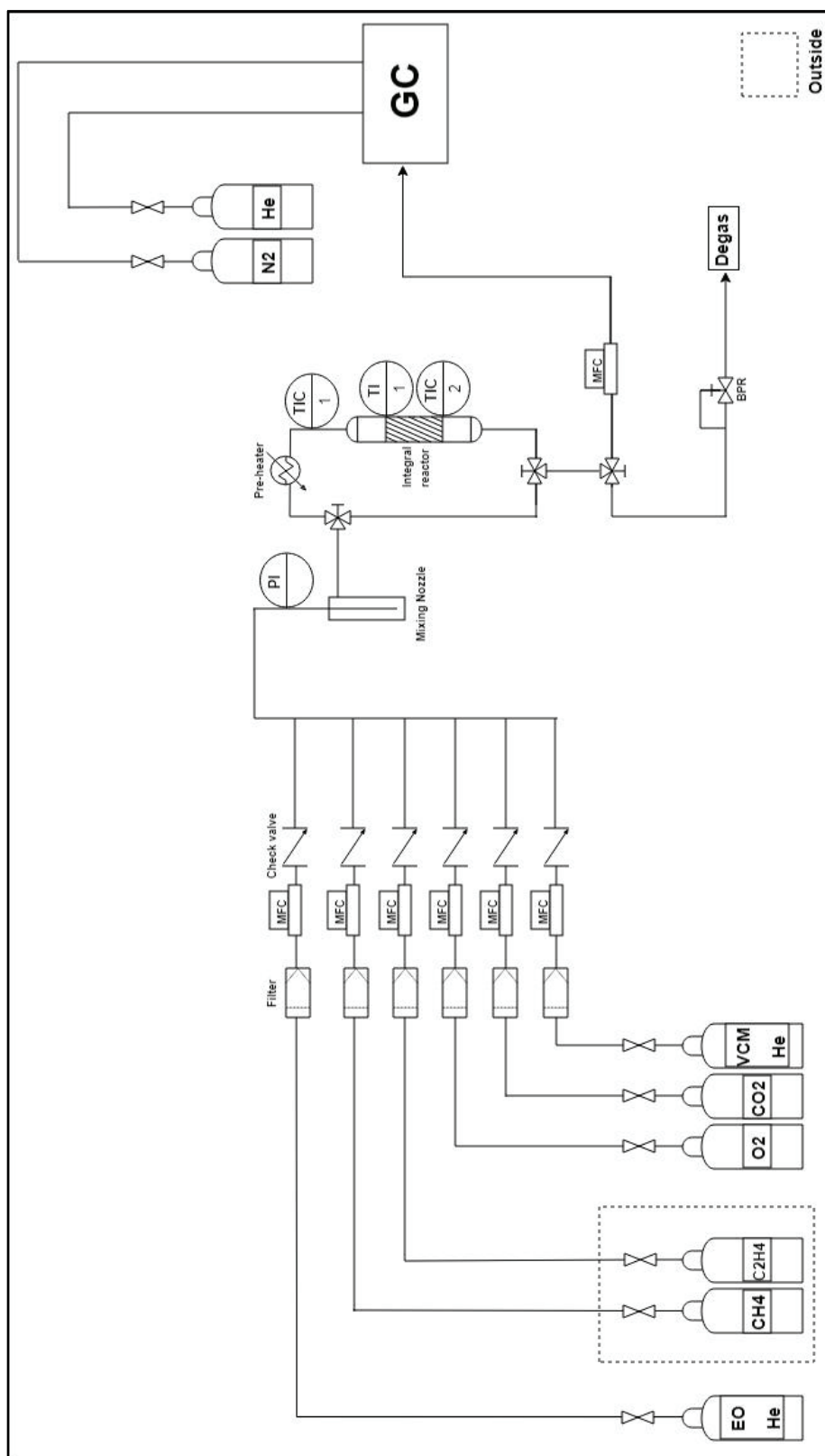


Figure 3.2. Experimental set-up.

Table 3.1. Information about lab-rig reactor and catalyst bed properties.

Reactor tube ID (cm)	0.9
Reactor tube OD (cm)	1.3
Reactor tube cross-section inner area (cm ²)	0.64
Catalyst amount (g)	0.1/0.2
Catalyst mixture amount (SiC+catalyst) (g)	2
Inert/catalyst ratio	1.9/0.9
Inert bed amount (SiC) below the catalyst bed (g)	1
Inert bed amount (Al ₂ O ₃) above the catalyst bed (g)	2
Catalyst mixture density (g/cm ³)	1.57
Inert (SiC) density (g/cm ³)	1.6
Inert (Al ₂ O ₃) density (g/cm ³)	1
Catalyst mixture bed length (cm)	2
Inert (SiC) bed length (cm)	1
Inert (Al ₂ O ₃) bed length (cm)	3
Catalyst particle size (μm)	212

In Table 3.1, all crucial information on bed properties and lab-rig reactor which is made of stainless steel material is shown. There are four types of bed section: Supporting material (quartz wool) layer, bottom inert layer (SiC), catalyst mixture layer (SiC+Catalyst) and top inert layer (Al₂O₃). From trial and error, it is found that 2 cm of quartz wool makes a sufficiently strong enough support for the catalyst and prevents permeation of the catalyst or inert particles. The intermediate inert bed serves to represent our reactor outlet conditions whereby the temperature here would be lower than in the catalyst mixture due to the absence of an exothermic reaction, but still be much warmer than farther downstream in the reactor tube due to conductive heat transfer with the catalyst mixture particles. Throughout the experiments, two different catalyst amount (0.1 and 0.2g) and inert/catalyst ratio (1.9 and 0.9) were used by keeping constant of the total catalyst mixture as 2.0g. Top section of the bed with Al₂O₃ material serves as a heat shield reducing the the excessive heat transfer between the bed and the upstream zone. The isothermal region has been determined to be an area whereby temperatures reach a maximum in the reactor tube and remain fairly constant in this region.

.Regarding to detection of the gases in kinetic studies, there are mainly two alternative pathways for analyzing the products and unconverted reactants at the outlet of the reactor in the literature. One is most commonly and traditional way that is GC [6, 23, 46-53, 55, 57, 59-61]. The other one is Solid Electrolyte Potentiometer (SEP) [54]. In this study, GC was used. Column and detector selection play a crucial role in GC. There are various kind of surrogates for columns which are easily searched by using cross-reference tables but advances in the capillary column technology provides beneficial solutions such as rapid analysis and well-shaped peak area for researchers, partially superseding packed column technology. GC (Agilent 7890B) and all GC-related parts (columns, valves etc...) were purchased from Sem Lab A.Ş within the scope of this project. Thermal conductivity detector (TCD) was chosen for gas detection. Split/splitless injection line was used with a split ratio of 10:1. Oven program was set to 40°C for 14 min then increased to 130°C as a ramping rate of 20°C/min and left 130°C for 5 min. Gas sampling loop of 0.25 ml was used. Heater temperature of valve box including sampling loop was set to 80°C. Helium fed through electro-pneumatic control valve (EPC) was used as a carrier gas. There were used two replacement valves with 6-port that are operating together. As depicted in Figure 3.3, column configuration includes three different positions with two different columns. HP-PLOT/Q that has a length, diameter and film thickness of 30 m, 0.530 µm and 40.0 µm respectively was used for the separation of carbon dioxide, ethylene and ethylene oxide whereas CP-Molsieve 5A column with a length, diameter and film thickness of 50 m, 0.530 µm and 50.0 µm respectively was used for the elution of oxygen as a permanent gas and methane.

Table 3.2. Events of GC valves.

Elapsed Time	Valve-1	Valve-2
0	OFF	OFF
0.01	ON	OFF
0.5	OFF	OFF
2	OFF	ON
5	OFF	OFF
16	OFF	ON
25	OFF	OFF

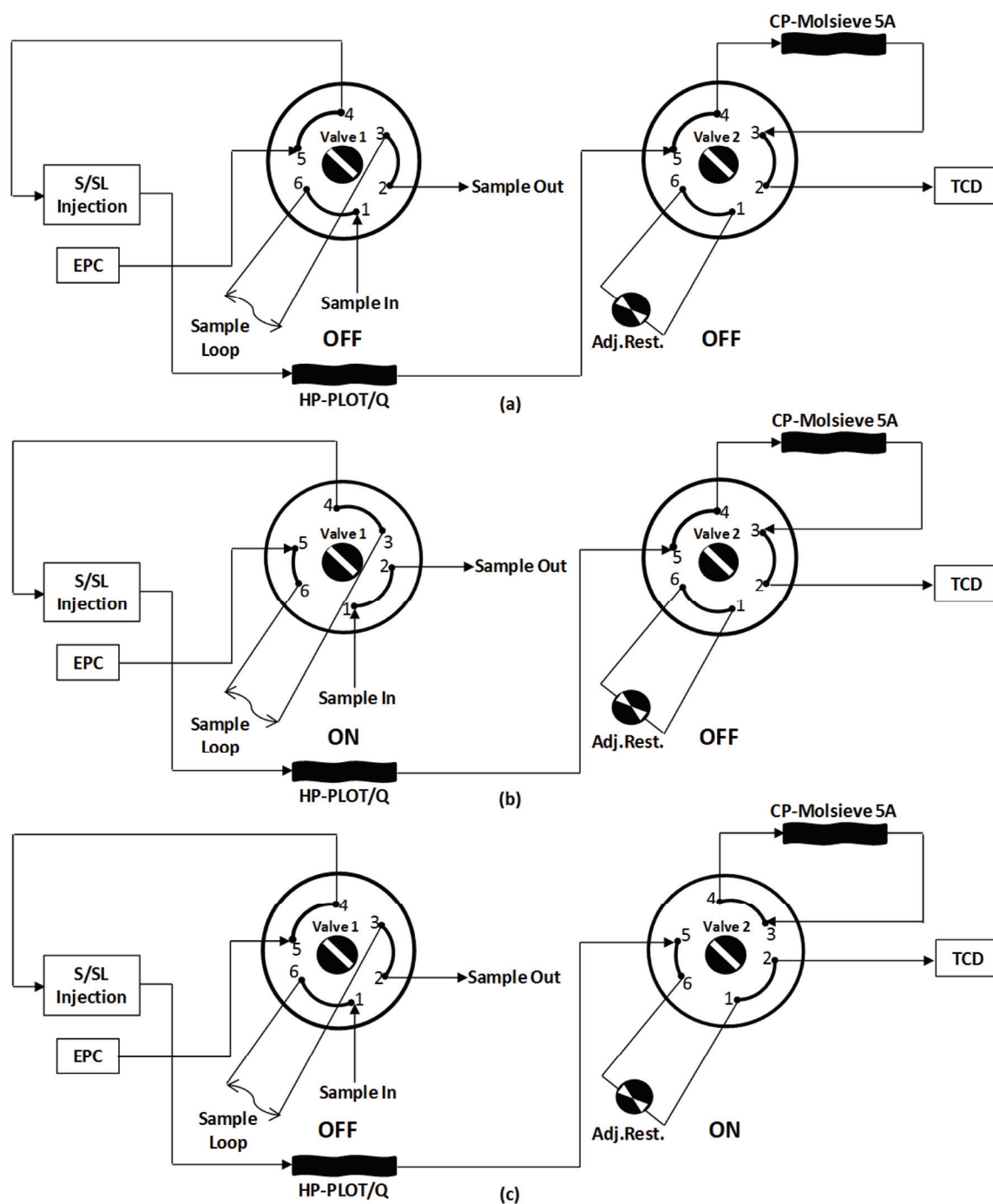


Figure 3.3. Configuration and replacement positions of GC valves (#1 and #2) during a trial(a) $t=0, 0.5, 5.0$ and 25.0 min; (b) $t=0.01$ min; (c) $t=2.0$ and 16.0 min.

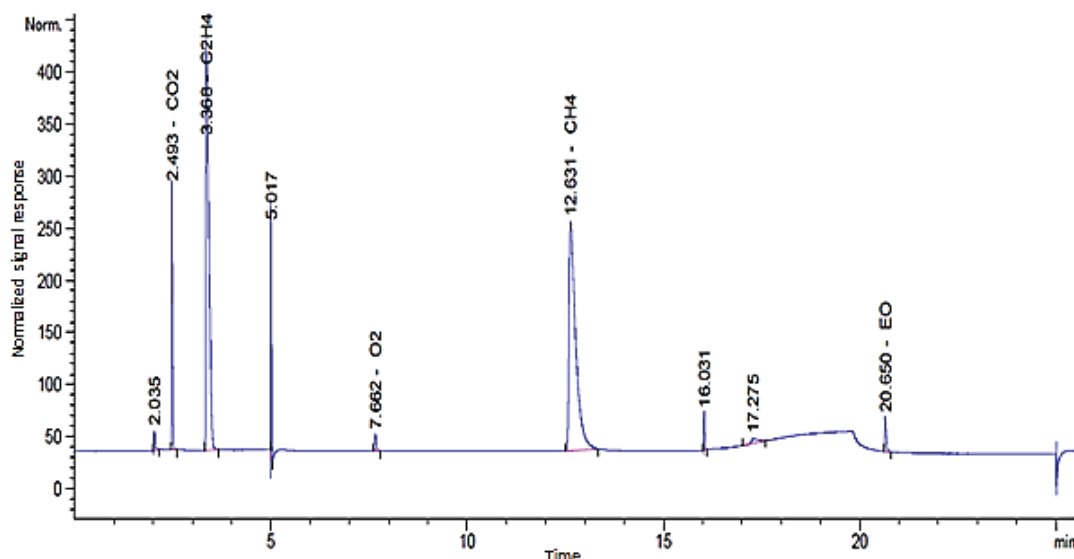


Figure 3.4. Sample chromatogram.

Mass flow controllers, temperature controllers (TIC-1 and TIC-2) coupled with temperature and pressure indicators (TI-1, TI-2 and PI) are monitored and controlled by controller panel (Unitronics V700 PLC) and HMI with remote control. RS-485 ASCII protocol is used for MFCs because of the fact that it has higher data transmission speed (up to 10-Mbps) comparing to RS-232 protocol [75]. On the other hand, TICs communicate by the help of analog input signals. PID controllers are only for TIC-1 and TIC-2. For the sake of the agile PID operation, differential term set to zero in PID tuning section. As a matter of fact, dead time is negligible due to the fact that physical distance is almost nonexistent. Therefore, there is only PI controller in the system.

Little portion of reactor outlet gases are going through gas chromatography (GC). This portion is adjusted and kept minimum by BPR coupled with MFC (Bronkhorst El-Flow) in order to minimize the pressure burden on GC valve. Most majority of the gas flow is discharging to atmosphere by means of degass line after BPR.

PLOTQ column is the new capillary version of PORAPAKQ packed column which has been using widely in epoxidation kinetic studies from past to present [19, 46, 48, 53]. Molsieve column necessitates regular bake-out procedure (300-350°C) in case of exploiting contaminants like carbon dioxide but this is not practical to carry out because of temperature upper limits of other columns co-existing in the same oven. For this reason, way-switching via adjusted restrictor is performed by using second valve

which switches on right before eluting CO₂ from PLOTQ. Therefore, adjusted restrictor was primarily used to isolate molsieve column when CO₂ comes out.

Total run length for a typical GC trial is 25 min. When adding preparation duration after each trial, this extends to 29-30 min depending on the atmospheric temperature. There are 6 valve movements excluding the position at $t=0$ as tabulated in Table. 3.2. All reaction gases are retained by related columns at $t=0.01$ min when valve#1 is on and valve#2 is off between $t=0.01$ and 0.5 min. After valve#1 is off and valve#2 is on at $t=2$ min, carbon dioxide comes first just before ethylene by means of adjusted restrictor (i.e bypassing the molsieve column). After valve#1 and valve#2 are both off at $t=5$ min, oxygen and methane are eluted around 7.5 and 12.5 min respectively. After valve#1 is off and valve#2 is on at $t=16$ min, ethylene oxide is lastly eluted just after being completed temperature ramp.

All valve movements and gas retention times are also shown in Figure 3.4 which is a typical chromatogram of a trial dealing with an experimental condition. Each unique experiment could consist of many trials until obtaining consistent results. There are four conspicuous spikes (at $t=2, 5, 16, 25$ min) resulting from valve movements in the chromatogram.

GC calibration was done by using calibration tube#1 and tube#2. In addition to this, the accuracy of the calibration curves based on each component was enhanced by performing cold experimental runs. By doing this, representative experimental conditions which include 18 cold runs were chosen in determination of calibration concentrations. For a realistic approach, spurious values of y-intercepts for all calibration curves were eliminated by setting them to zero. In the end, all points were combined component by component in obtaining the calibration regression equations (Appendix A). As it should be, all reactant and product components follow a linear range in the calibration.

Correlation coefficient of methane is showing slightly less accurate than others. However, it is not targeted to find methane concentration accurately due to the fact that methane is only used for a ballast gas as in the industrial reactor. In addition to this fact, methane is acting as an inert gas within the temperature ranges of interest (220-280°C). Therefore, it was not directly used in data reconciliation (DR) of reactor outlet gases but it has been exploited from methane concentration in calculating the percent error with respect to methane during the iterative DR approach.

3.3 Techniques Used in Catalyst Characterization

In accordance of model-targeted experimentation approach, there needs to use catalyst characterization techniques aimed at finding the unknown properties in Figure 3.5 that will be used in the lab-rig reactor model constructing in gPROMS environment (AML: FBCR). Moreover, some of the parameters (e.g., tortuosity, permeability coefficient) were found by using empirical equations in which other characterization test results were used as an input parameter.

The screenshot shows a software interface for defining catalyst pellet properties. The title bar is 'Catalyst_section (Catalyst_pellets_section_1D)'. On the left is a sidebar with tabs: General settings, Pellet, Heat transfer, Methods, Diffusion, Dynamics, and Numerics. The 'Pellet' tab is selected. The main area contains the following settings:

- Catalyst pellet type:** Whole pellet (dropdown)
- Catalyst pellet shape:** Sphere (dropdown)
- Catalyst model:** Lumped (dropdown)
- Pellet geometry:**
 - ☒ Pellet radius: 110 μm (dropdown)
- Pellet properties:**
 - ☒ Pellet bulk density: 1.48 g/cm^3 (dropdown)
 - ☒ Pellet specific heat capacity: 913.41 $\text{J kg}^{-1} \text{K}^{-1}$ (dropdown)
 - ☒ Pellet conductivity: 1 $\text{W m}^{-1} \text{K}^{-1}$ (dropdown)
 - ☒ Pellet porosity: 0.268 m^3/m^3 (dropdown)
 - ☒ Pellet emissivity: 0.8
- Inert pellet (for catalyst fraction less than 1):**
 - ☒ Inert pellet bulk density: 3160 kg/m^3
 - ☒ Inert pellet specific heat capacity: 675 J/kg-K

Figure 3.5. Catalyst and inert pellet specifications for the lab-rig reactor model.

ESEM-FEG/EDAX (Philips XL30) was used to investigate qualitatively whether there is an active coating layer on the catalyst and to observe porosity and active material (silver) distribution. X-ray diffractometer (Shimadzu XRD-6000) was used to understand crystal structure particularly for support material. In order to investigate surface area and pore size distribution, Multipoint BET (Brunauer-Emmett-Teller) method was utilized by using Autosorb-1 (Quantachrome) instrument. In addition to this, mercury porosimetry (PoreMaster 60-Quantachrome) was used in determination of total porosity, total pore volume and average pore size diameter. True density of the catalyst (pellet&powder) was found by using helium pycnometer (UltraPyc 1200e-

Quantachrome). Elemental analysis of the catalyst was determined by Sequential X-ray Fluorescence Spectrometer (ARL 9400). Disc grinder (Pulverisette 13 Classic Line) and laboratory sieve shaker (Loyka ESM 200) were used for making the catalyst ready for kinetic experimentation.

3.4 Modeling Environment

The main target in this thesis is to obtain a kinetic model that will be embedded in the industrial multitubular fixed bed reactor model. For this reason, all reasons that led us to opt for gPROMS (v1.3, General Process Modeling System) is not only dealing with kinetic modeling, multiple parameter estimation and experimentation study but also high-level modeling (i.e. industrial reactor modeling). Modeling libraries in gPROMS that were used for lab-rig reactor modeling are AML: FBCR, gML Basics, gML Flow Transportation and gML Heat Exchange.

Within the context of process simulation, softwares like Aspen Plus, HYSYS and Unisim are counting as flowsheet modeling softwares in general not in detail in a sense that they are lack of flexibility, robustness, high fidelity, comprehensive custom based modules. Besides, modeling approach (Equation-oriented and sequential-based modeling) is also very important. In the complex systems, sequential-based modeling approach are not appropriate for finding the global optimum and reaching the closest results to the reality [76]. With a consideration of these points, the most demanding softwares that preferred by chemical industry are gPROMS and Aspen Custom Modeling (ACM). There are chiefly four reasons why we felt disposed to gPROMS instead of ACM as follows:

High-fidelity in fixed-bed catalytic reactor modeling: In gPROMS software, there exists a detailed catalytic reactor modeling module called as AML: FBCR which allows the user-friendly drag-drop environment and kinetic mechanism modification by means of gPROMS language section. This module includes 1D and 2D heterogeneous models and also pellet models in which intraparticle diffusion phenomena containing advanced diffusion mechanisms such as Dusty Gas Model (DGM) takes into account. Besides that, specific catalyst information, detailed reactor and coolant geometry are requested. There are many coolant side sub-modules that could be easily integrated with the main reactor module [77-79].

Ready-to-use initialization procedure and integration with the process flowsheet units: While doing custom modeling in gRROMS, it is not need to write specific initialization procedures (including extra codes and initial guesses for each module). Custom units, for example catalytic pellet section is easily-synchronized and automatically incorporated with other flowsheet units and other custom units as well. Unique Model and Flowsheet Initialization Procedures in gPROMS allow rapid initial solution without the need for guesses in most cases. At the same time, this feature is very time-saving [76, 80-81].

Advanced parameter estimation: Extensive statistical and parameter estimation algorithms and facilities are present in gPROMS than ACM. In the case of kinetic parameter determination in an experimental rig or fine-tuning a key parameters taken form the literature playing with process historian database, the parameter estimation capabilites are of great importance. ACM has a limited statistical toolbox [81-83].

Optimization Capability, Robustness and Speed: Even if tens of decision variables (continuous and discrete) take place while making optimization, gPROMS can handle with all together and lean towards the most optimum point without being stucked in local minimum, by the help of many numeric solvers and advanced optimization algorithms such as OAERAP (outer approximation equality relaxation augmented penalty) [84]. In a study, gPROMS made a further enhancement by advanced optimization techniques resulted in increasing total annualised profit by several tens of millions [78]. Over 100.000 differential and algebraic equations could be solved in a robust and prompt manner when comparing with ACM [76, 83, 85]. In the literature, many studies report that the speed of gPROMS is considerably higher than ACM and other dynamic softwares in terms of CPU (central processing unit) [82, 86-87]. Speed and therefore elapsed time for a run is very decisive for those model that will be used for the purpose of real-time optimization.

Throughout the determination of kinetic model, model-targeted experimentation (i.e. model-centric experimentation) approach was used. This approach is based on performing experiments in order to improve the accuracy of the model rather than to improve process itself. The model is than typically used to optimize the process operation or design as illustrated in Figure 3.5. From the point of R&D perspective, this approach serves as a pathfinder particularly for early-stage process or product development [13, 88-91].

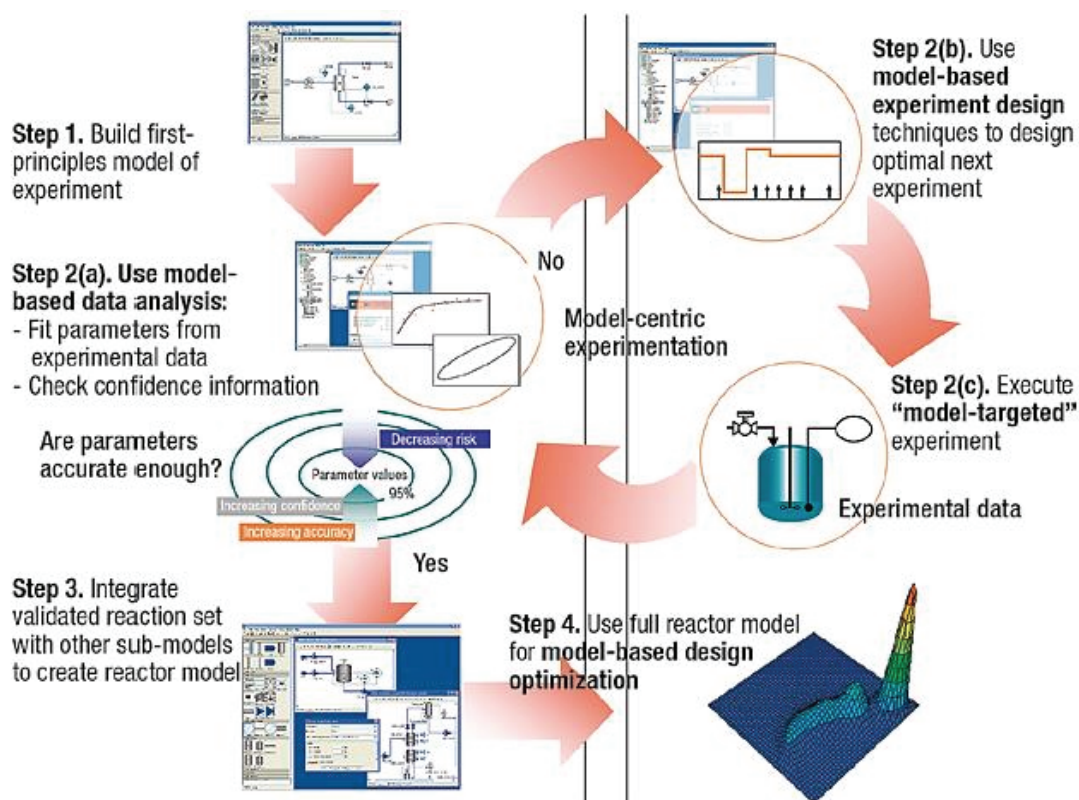


Figure 3.6. Workflow of model-targeted experimentation in gPROMS (Source: [13]).

Steps shown in Figure 3.5 are explained as below:

Constructing first-principles models for lab-rig reactor (Step 1): Lab-rig reactor (preferably small scale bench-type apparatus) in which generates kinetic data is modeled in terms of white-box modeling principles. Kinetic models and related kinetic parameters that exist in the literature are investigated and used as initial model candidates that are refined and restructured in a stepwise manner.

Model-based data analysis (Step 2a): Model parameters (kinetic constants, adsorption coefficients etc...) as well as the error caused by instruments are estimated by using advanced estimation and statistical techniques like maximum likelihood estimation. Initial accuracy and confidence intervals are determined. In this step, the approaches defined in Step 1 are also re-evaluated and consolidated.

Model-based experimental design (Step 2b): Apart from traditional design of experiment approaches (e.g factorial design), experimental plan is carried out in view of the reactor modeling principles in a way that results in creating more data-rich experimental domain with a minimum parametric uncertainty. This will also provide experimenter with optimization of time and cost of experiments.

Model-targeted experimentation (Step 2c): With these planned experiments, the execution is carried out. As a rule of thumb, it should be noted that experiments are conducted as much close to isothermal conditions as possible in order to free from temperature gradients alongside the axial direction of the reactor. This is of great importance for obtaining scale-invariant parameters which means that the conclusive model is able to predict the overall behavior regardless of the scale of the system. The cycle consisting of Steps 2a-2b-2c-2a is recursively executed until the degree of confidence for each parameter of interest is reached to a statistically significant level.

Building a high-level model and optimization (Step 3&4): Once the model is finalized, it could be integrated with high-level model which may include industrial unit operations. At this stage, some scale-variant parameters like flow coefficients or overall heat transfer coefficients could be adjusted by using real process data. No longer does it need to estimate the kinetic parameters that it is fixed at the earlier stage. The last step is to optimize the system pursuant to an objective function with regards to constraints and decision variables dealing with the overall process [13].

What makes kinetic experimentation in this study inevitable is to expand the operating window beyond the process historian database which only provides data that lies only between operating conditions throughout the catalyst life expectancy. Most of the time, the existing data would not be sufficient to modify literature-based kinetic models by using parameter estimation methods when catalyst deactivation is of concern. Besides, numerous operating points are tested in a safe manner with the help of kinetic test system irregardless of performing real perturbation test in the process. A rigorous kinetic model is always one of the pillar concepts for expert systems (e.g., real time optimization) in process control technology. For this reasons, it is decided to construct a catalyst testing system and conduct case-specific kinetic experiments in a much broader process range.

Due to the fact that model-based kinetic experimentation is used, integral reactor was chosen for the experimental rig. In this approach, the main issue is to achieve higher conversions as much closer to industrial conditions (8-10%) as possible. Reactor model could handle to solve design equations with ease unlike differential reactor in which conversion should be kept lower than industrial conditions. Nevertheless it is assumed that catalyst bed is lying on isothermal region, 1-D axial distributed model do not take it for granted that it is perfectly isothermal, even if it is close to isothermal owing to the grinded catalysts, use of inert mixture and inert beds [92-94]. Therefore, it

takes small temperature change into account by calculating mass and energy balance alongside the bed. This approach increases the accuracy of the kinetic data. The main drawbacks of differential reactor are to measure the lower amount of concentration difference between inlet and outlet of the reactor and to fail to decouple measured concentration value from instrument error. For these reasons, there are two most appropriate ways to get accurate kinetic data: Model-based approach by using integral reactor or internal recycle reactor (e.g. Berty type) preferably integrated with micro gas chromatography [95-96].

There are two main editors in gPROMS ProcessBuilder environment: *Model editor* and *process editor*. A custom model in gPROMS at least consists of three main sections. *First* is variable section. Variables are associated with variable types that exist in gML Basics interface model or alternatively defined by the user. Apart from variables, parameters do not vary with time and must be given fixed values before a simulation begins. Variables types also could be used in the definition of parameters in the gPROMS language tab. There are six types of parameters in gPROMS: Real, integer, logical, foreign_object and ordered_set [97-98].

Second is model section which includes variables, parameters and equations. Set section in which specific assigned values are given to parameters is also situated in model part. Topology section shows the way of connecting units and actively in use ports dealing with the units in the model environment. Equations section in model entity is also very critical. It could be written all types of equations such as partial, differential and algebraic. Nested functions and loop structures (e.g. for, while and within) are also available in the gPROMS language [97-98].

Third is process section in which contains all case-specific information needed for simulation. There is also set part that shows the specified values in the model windows. Assign section is the most important part of this section. In this part, some specific values are given to variables which are case-specific. These values could be estimated in parameter estimation section in the project tree. Another important part is Preset which generally referred to the stored value in “Saved Variable Sets”. In simple modeling cases, initial guesses and bounds for variables are defined in Variable Types and this could be satisfactory to solve the initialization problem. However, in more complex cases, a more flexible method is required in determination of initial guesses. Even once a set of suitable initial guesses are found, some problems may take a considerable length of time to solve. This can often be greatly reduced if the solution of

the initialisation problem is used to provide the initial guesses. This can be done in gPROMS using “Saved Variable Sets” by saving the values of all variables after the initialisation and restoring them in the Preset section in Process editor language [97-98].

gPROMS ProcessBuilder contains some customizable unit operations that could be used in a drag and drop style in the model palette specialized in terms of advanced model libraries (AML). gPROMS language, which is case-insensitive and declarative (i.e. order of equations is not important), could be used for the parts that requires custom code writing (e.g. kinetic model development). One advantage of gPROMS is that all low-level and high-level models are placed in the same project tree and they could be integrated with each others with a cross-reference feature. . In gPROMS, you can command by model windows (templates) or directly via language. Put it differently, once there needs to make a model variable customizable in the ready-to use model templates, it could be assigned by using custom codes in the process editor on the condition that same variable is unticked in the template. In the gPROMS language tabs of the editors, there are some notifications in the beginning of each part that guide the modeler in a user-friendly manner [97-98].

As a physical property software, Multiflash (6.1, Infochem/KBC Advanced Technologies plc) supplied together with gPROMS was used. All thermodynamic and transport properties are provided by Multiflash in which two databanks (INFODATA and DIPPR) are included. Once components of interest and related physical properties are defined as a separate file in Multiflash environment, this file is exported and run into gPROMS environment in the section of “Miscellaneous Files” [97, 99].

Fugacity representations with regards to temperature, pressure and composition are conducted into two methods in Multiflash: Equation of state (EOS) and activity coefficient methods. In EOS methods, thermodynamic properties of the vapor and liquid phases are calculated from EOS. In activity coefficient methods, properties of vapor phase is obtained from EOS while that of liquid phase is determined from the summation of the pure component properties to which a mixing term or an excess term has been added.. Transport properties (e.g. viscosity, thermal conductivity and surface tension) are derived from semi-empirical models. Peng Robinson (PR) and Redlich-Kwong-Soave (RKS) are the best methods in cubic equation of states and more convenient for gas processing units like in this study. As a rule of thumb, RKS is good at fugacity prediction whereas PR shows better performance in density calculations around critical conditions for gas/condensate systems [100].

3.5 Experimental Design Approaches

The experimental plan is just a prerequisite to the kinetic experimentation and will be actualized by determining the necessary input and output compositions based on the start-of-run (SOR) and end-of-run (EOR) conditions obtained from the process (Table C.2 in Appendix C). The foundation behind this classification in Table C.2 is a catalyst lifetime of five years. In the assessment step of the range study, not only reactor input conditions, but also reactor output conditions were taken into consideration in order to obtain wider operating windows for the multi-tubular fixed bed reactor. Two different methods were applied within the scope of design of experiments: Classical one-factor at a time experiments (OFAT) and D-optimal based experiments.

The primary aim of the design of experiments is to simulate recycle gas composition for the inlet of the industrial ethylene oxide reactor in the lab-rig reactor. For this reason, inlet gases are introduced into the reaction system in a component wise. Of the feed gases, methane (CH_4) is a ballast gas and carbon dioxide (CO_2) is an unwanted side product gas that is always present in the recycle gas. Because, approximately one-third of CO_2 is removed in the industrial process with the remaining two-thirds continually recycled in the reactor loop gas. Vinyl chloride monomer (VCM) has a special role in moderating the catalyst activity by increasing the selectivity towards the EO reaction. VCM is charged into the lab-rig reactor from a special gas mixture tube which includes a balance He gas amounting to a final VCM concentration of 5 ppm. In the experiments with EO-cofeed that were carried out to find EO oxidation reaction kinetics, EO was fed from a mixture tube that has a 5% EO in balance helium.

Most of the experiments that were performed are aimed at discovering partial and total oxidation reaction rates and their kinetic parameters. To do so, it was attempted to reproduce plant operations except D-optimal design. On the other hand, another important target of the experimental design is to find out EO oxidation reaction rate. Nevertheless EO inlet approximately falls in the range of 0.005-0.01% in the industrial reactor inlet, it could not be precisely estimated that how much generated EO is consumed along side the reactor bed unless EO oxidation based rate equation has been obtained experimentally. Therefore, the purpose of co-feeding EO is not to reproduce the plant operation, but to allow the reaction kinetics to evaluate rate of EO oxidation to CO_2 , which can become significant at higher temperatures.

Without having experiments with co-feeding EO, it is not possible to distinguish between ethylene oxidation to CO_2 and EO oxidation to CO_2 from the perspective of modeling. In such case, it would be assumed that all CO_2 is produced directly from ethylene, as it is done as such in most of the studies in the literature [6, 23, 38, 61, 95] by ignoring EO oxidation reaction in their set of kinetic model equations. In the set of 3&4&5 in Table C.1, there are two groups of EO experiments. The former was performed by co-feeding EO along with all the other inlet gases whereas the latter was conducted by using EO as a main source of hydrocarbon instead of ethylene. Ample amount of co-feeding EO experiments fall into the latter group on the grounds that combustion characteristic of EO starts to become prominent in an ascending order of temperatures. This provides rich information to find out activation energy for this reaction.

First of all, limitations on GC peak areas were investigated. Some limitations on the higher concentration end for each gas can be observed. Apart from few exceptional experiments with regard to inlet concentration, it is stuck to the validity range shown in Table 3.3 in all experiments. These ranges are extricated from the calibration graphs in Appendix A. Generally, this situation is only different in methane concentration, which is used as a ballast gas. As one might expect, methane that acts as an inert in the temperature range between SOR and EOR together with helium was not included in kinetic model. As a matter of fact, auto-ignition temperature of methane in air is around 600°C [101]. This value is very far away from our temperature range in both lab-rig reactor and industrial EO reactors. Regarding to outlet gas concentrations, ethylene oxide yields rarely exceed the maximum validity value in some experiments but it mostly lies between 1-1.2% on average. For the EO values lying beyond the range, extrapolation was used by sticking to the calibration regression equation which has superior degree of statistical accuracy ($R^2=0.99940$). Moreover, the values to be extrapolated are fairly close to the values in EO validity range. Discounting the higher EO yields obtained from high pressure experiments that are supposed to be erroneous, the maximum non-reconciled and reconciled EO values are 3.83% and 4.41%, respectively.

DoE statistical design strategies are used to either establish a preferred rate mechanism for the reaction, which involves selecting several models based on multiple assumptions and then conducting experimental runs to discriminate various models or to obtain precise parameter estimations in the preferred model by trying all candidates one

by one [102]. As an alternative approach in this study, the first strategy will be used. In order to aim for optimal experimentation, the essential point will be to select feasible experimental regions for the factors of interest. Therefore, prior knowledge about the process at hand plays a crucial role in selecting the right factors for investigation for an efficient means of determining the intrinsic kinetic parameters of the catalyst.

Table 3.3. Validity range of reactor inlet components.

Validity Range	Feed Concentrations				
	C₂H₄	O₂	CH₄	CO₂	EO
Max	35	16	66.67	11	1.23
Min	5	1.33	53	2	0.15
Validity Range	GC Measurements in Peak Area				
	C₂H₄	O₂	CH₄	CO₂	EO
Max	3051.52	1113.47	3185.64	983.94	70.76
Min	442.34	95.72	2397.77	205.75	9.4

As an alternative approach in this study, the first strategy will be used. In order to aim for optimal experimentation, the essential point will be to select feasible experimental regions for the factors of interest. Therefore, prior knowledge about the process at hand plays a crucial role in selecting the right factors for investigation for an efficient means of determining the intrinsic kinetic parameters of the catalyst. The D-optimal design criterion was chosen and allows for minimization of the determinant of the inverse of the variance-covariance matrix and is therefore a commonly preferred criterion. D-optimal design is an appropriate experimental design approach because the bench-scale reactor system includes a coupling of both mixture and process variables, which include five feed gas compositions (ethylene, oxygen, methane, carbon dioxide, and vinyl chloride) and the reactor temperature summing to a total of six adjustable factor variables [103-107].

Many catalyst investigation studies have relied on design of experiments (DoE) approaches. Akıttı et al. performed a sequential design strategy for selecting experimental runs to obtain model discrimination and precise parameter estimation for the simulation study of the propylene oxidation kinetics using the joint design criterion

(JDC) [102]. Another remarkable study that directly relates to this one is that conducted by Petrov et al. [108], who applied sequential experimental design in order to do kinetic model discrimination and parameter estimation based on the data collected from uninhibited EO oxidation experiments using a Ag catalyst. Sjoblom et al. [109] used a D-optimal design approach in Modde 6.0 in a NO_x storage and reduction system with varying engine design parameters such as cycle time, injection time, bypass time, total injected amount, and injection rate. Federico et al. [110] constructed a model-based design of experiments (MbDoE) procedure for designing optimal experiment sets in an effort to discriminate competing kinetic models and improve estimation of kinetic parameters. Similarly, Sethapokin et al. [111] performed an investigation on a reactor model of the phthalic anhydride production using fractional design coupled with central composite design (CCD) in Comsol Multiphysics 3.5.

Table 3.4. Factor variables used in D-Optimal Design in Modde Pro.

Name	Units	Type	Settings
Temperature	°C	Quantitative	219 to 255
CO ₂	Fraction	Formulation	0.021 to 0.0618
C ₂ H ₄	Fraction	Formulation	0.0713 to 0.666
O ₂	Fraction	Formulation	0.0181 to 0.2304
CH ₄	Fraction	Formulation	0.0418 to 0.6633
VCM/He	Fraction	Formulation	0 to 0.2

In the determination of the experiments in set #1 within the scope of D-optimal design, the Modde Pro software (free trial) was used. Table 3.4 shows mixture factor variables at a scale of 1:100 with exception of temperature (process variable), which is shown in its actual value used in experiments. Input flow rates of the gas components are just multiplication of scaled values with total flow rate of 75 sccm. Replicates in set #1 were determined automatically using Modde Pro, which are close to mid-value experiment (2b0) performed in other experiments. In addition, run order approach was modified in accordance to our system since we cannot perform experiments in random order. The two main reasons for this limitation is that first VCM levels should be increased in an ascending order in order to fully ensure that experiments with very low or zero VCM do not follow experiments where high levels of VCM were used and

second adjustments in VCM levels take at least 7–8 hours to take effect on repeatable EO yields. In contrast, the case of using a constant VCM amount in sequential experiments, but different compositions and/or temperatures takes only 4–5 hours to show effect on EO yields.

The range study in Table C.2 allows determination of the constraints, which are generally linear and therefore easier to manage. Non-linear constraints; however, pose more difficulties in optimization when using statistical softwares. There are some ways to cope with these problems associated with non-linear constraints such as using ready-built statistical softwares. In this project, linear constraints such as the upper limits of the mass flow rate, lower and upper limits of the output gas compositions based on the real plant reactor SOR and EOR conditions are taken into account in the range study. Nevertheless, some of the non-linear and hard-to-predict factors (e.g. flammability limits) could be neither included in the range study nor in the Modde Pro software. Flammability limit violations could happen either insufficiently elimination of mass and heat transfer limitations or lack of concentration in the mixture of which component (e.g. methane) primarily has the function in removing the heat of reaction. Moreover, VCM also adjusts the severity of reaction by passivating more particularly the total oxidation.

CHAPTER 4

RESULTS AND DISCUSSION

4.1 Characterization Results for Ethylene Oxide Catalyst

It is known that the some catalyst properties need to know in order to use model-based approach in the lab-rig reactor. All characterization tests are done by using fresh catalyst. Powder-like samples are used in XRD, helium pycnometer and tapped density measurement while pellet samples are used in SEM, mercury porosimetry, nitrogen adsorption and helium pycnometer. To point out, powder-like catalyst and inert mixture is used in the lab-rig reactor whereas catalyst pellet has been using in the industrial reactor.

Some of the properties are required for lab-rig reactor model whereas some (effective thermal conductivity, tortuosity and permeability coefficient) are only performed for using in the industrial reactor model because of the fact that these properties are only considered in plant-scale operation unlike lab-rig reactor where grinded catalyst is used. Governing physical properties in the kinetic modeling of the catalyst pellet dealing with the global reaction rate are different from the ones in crushed catalyst particles that are generally used in determination of intrinsic reaction rate [94].

Pellet radius is taken as grinded particle radius which has a geometric average of 110 μm . Effective thermal conductivity of the grinded pellet particles is very low [112]. Therefore, it was taken as 1 apart from actual pellet material which was found by using semi-empirical equations. Pellet emissivity (chosen as default value of 0.8) is not a key parameter for ethylene oxide reactor because radiative heat transfer is negligible below 300°C [113]. For inert pellet section, properties of silicon carbide (SiC), which is the inert material in catalyst mixture, are taken into account. Therefore, bulk density and specific heat capacity of SiC are taken as 3160 kg/m^3 and 675 J/kg.K, respectively [114].

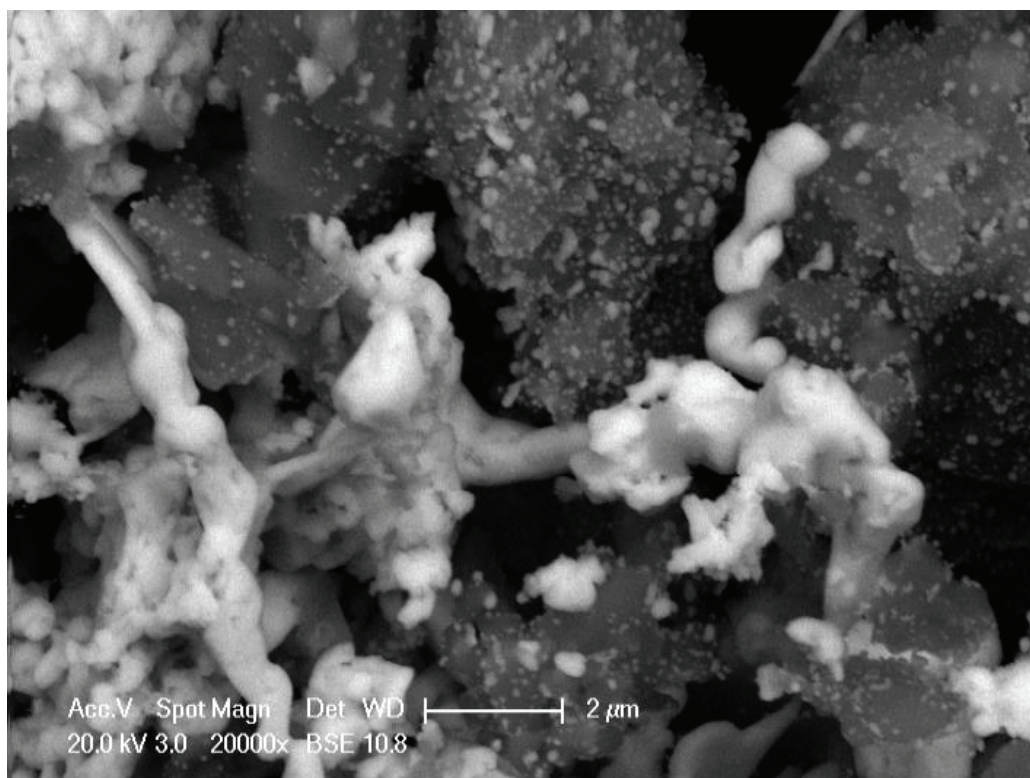


Figure 4.1. SEM image of fresh Ag/Al₂O₃ catalyst pellet.

It is started from Scanning Electron Microscope (SEM) owing to the fact that surface characterization of the catalyst gives insights into active material distribution and surface morphology. It appears that two different fragments are intermingled in a way that no certain layer is formed on the surface. Active silver particles are diffused into aluminum oxide crystals by the help of incipient wetness impregnation which is the most common technique in the preparation of heterogeneous catalysts. Therefore, it could be fathomed from SEM image that catalyst is not coated by a stacked of an active layer.

The pellet type that is required to be specified in AML: FBCR (Figure 3.5) should be “whole pellet” instead of “coated pellet”. The geometric shape of the catalyst is a hollow cylinder. Another qualitative ramification could be that average particle diameter is higher than 50 nm proving that catalyst is not counted as microporous material and more close to macroporous structure, which will further be proved more concretely by porosity analyses (nitrogen adsorption and mercury porosimetry). These results are fairly consistent with the literature [5, 29, 115].

Table 4.1. Elemental analysis of the catalyst.

Elements	Mass percentage (%)
Ag	15.12
Al	82.44
Px	0.181
Si	0.139
Ca	0.125

Elemental analysis of the catalyst was done in X-ray Fluorescence Spectrometer (XRF). As can be shown in Table 4.1, the catalyst includes considerable amount of aluminum (c.a 82-83%) which followed by silver with a content of c.a 14-15% by mass. Rest of the elements (Px, Si and Ca) are originated from internal desiccants that are used for keeping the humidity at certain levels throughout the catalyst life.

Table 4.2. Results of the Hanawalt Index based on Powder Diffraction File (PDF).

Material	Maximum d-space values			Source
α -Al ₂ O ₃	1.6	2.08	2.54	Analysis
	1.6	2.09	2.55	PDF
Ag	2.35	2.04	1.23	Analysis
	2.36	2.04	1.23	PDF

The phase identification results of the sample which is in the form of powder are shown in Table 4.2. D-values of the catalyst, which are the spacing of the lattice planes and strongly depend on wavelength and line position ($2\Theta_{\text{beam}}$) are found due to the XRD analysis. By using Hanawalt index through Powder Diffraction File (PDF, supplied by International Centre for Diffraction Data) that contains over 300,000 diffraction patterns, three strongest d-space values (d_1 , d_2 and d_3) of the sample coupled with their relative intensities (I/I_1) are matched with the ones in PDF in an attempt to find a best overlapping pattern. Indices in d-space values show the degree of the intensity (n_{doi}). It could be a time-saving action to analyze the catalyst by XRF in advance of XRD because of the fact that it would have been known which elements would be searched in

PDF [116-118]. As a result of this analysis, it is found that fresh catalyst has two main crystal structures: Corundum ($\alpha\text{-Al}_2\text{O}_3$) and elemental silver. Corundum serves as a support material for active silver particles.

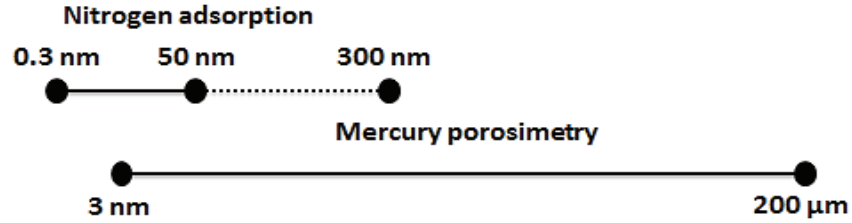


Figure 4.2. Pore size scale related with measurement technique
(Source: Adapted from [28, 119]).

$$r_K = \frac{-2 * \gamma(N_2) * V_m(N_2)}{R * T_b(N_2) * \ln(P(N_2)/P_0(N_2))} \quad (4.1)$$

r_K : Kelvin radius of the pore

$V_m(N_2)$: Molar volume of liquid nitrogen ($34.7 \text{ cm}^3/\text{mol}$)

$\gamma(N_2)$: Surface tension of nitrogen at its boiling point (8.85 ergs/cm^2 at 77K)

R : Gas constant ($8.314 * 10^7 \text{ ergs/deg/mol}$)

$T_b(N_2)$: Boiling point of nitrogen (77K)

$P(N_2)/P_0(N_2)$: Relative pressure of nitrogen

$$r_{\text{Washburn}} = \frac{-2 * \gamma_{Hg} * \cos \theta_{Hg}}{P_{Hg}} \quad (4.2)$$

r_{Washburn} : Radius of the pore where mercury intrudes

γ_{Hg} : Surface tension of mercury (480 mNm^{-1})

θ_{Hg} : Contact angle of mercury on the surface of a solid sample (140°)

P_{Hg} : *Applied pressure for the liquid mercury to enter a pore*

Porous solid materials and powders are classified into three groups with respect to their pore size: Microporous, mesoporous and macroporous materials. It is very essential to use appropriate instrumental method in order to get accurate volume measurements.

As illustrated in Figure 4.2, nitrogen adsorption is not capable to measure materials that have greater than 50 nm in pore size. Upper limit of nitrogen adsorption could be extended up to 300 nm but there is a miscalculation risk for pore volume over 50 nm which is critical limit. That's why it is advised to cross-check the volume measurement by using mercury porosimetry beyond this limit (shown as dash line). Due to the fact that $\ln(P/P_0)$ part of the Kelvin equation (4.1) used by nitrogen adsorption approaches to zero at large operation pressure and this gives rise to fail to determine pore diameter with respect to P/P_0 step changes. In case of using nitrogen porosimetry at large pores (>50 nm), P would inevitably decrease in comparison with saturated vapor pressure (P_0) at plane surface and therefore nitrogen evaporates which results in changing pore size distribution. That's why Washburn's equation (4.2) is used in determination of total porosity and volume. In both equations, it is assumed that pores are cylindrical in shape [28, 119-120].

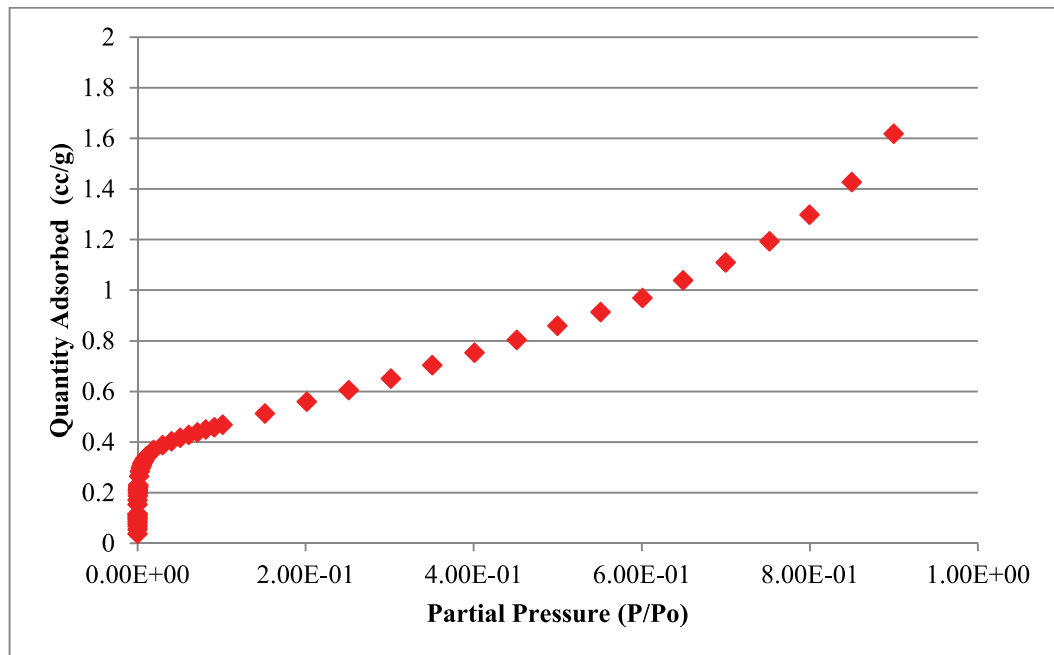


Figure 4.3. Multipoint BET analysis of the pellet.

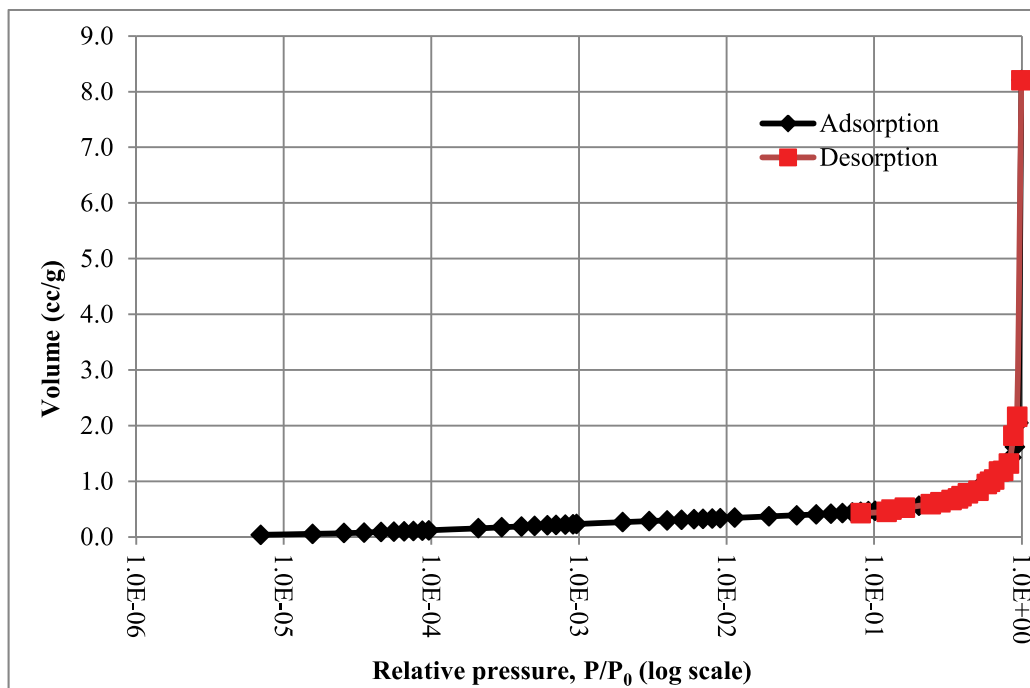


Figure 4.4. Full adsorption-desorption curve of the pellet by using nitrogen adsorption.

Before passing through mercury porosimetry, nitrogen adsorption was used in order to find surface area of the pellet coupled with micro and meso pore volumes nevertheless it is known that they are negligible with a priori knowledge. In Figure 4.3, it is deduced that the governing isotherm is Type II in which materials have nonporous or macroporous.

Multipoint BET surface area was found as $0.615 \text{ m}^2/\text{g}$, which is also consistent with previous studies. Specific mesopore volume of the pellet is determined as 0.01379 cc/g by applying Barrett-Joyner-Halenda (BJH) method whereas specific micropore volume is found as $7.926 \times 10^{-4} \text{ cc/g}$ by using Harvath-Kawazoe (HK) method. These two methods were chosen in an appropriate way according to type of the pore structure [120-121]. As can be inferred from these results, specific mesopore volume is almost two orders of magnitude higher specific micropore volume and has some contribution in total. However, these specific pore volumes are in minuscule amount comparing to macropore volume.

Full adsorption-desorption test was done to find micro and meso volume of the pellet. It is clearly observed that there is no hysteresis loop in the desorption part of the Figure 4.4. Hysteresis, which is known as the delayed condensation attributed to metastability of multilayer adsorption followed by capillary condensation, mostly

occurred in mesoporous materials due to the presence of non-uniform pore geometry and swelling and shrinkages effects throughout the filling process [122-124].

Table 4.3. Helium pycnometer results for pellet and powder samples.

Pellet	True volume (cc)	0.1719
	Sample mass (g)	0.7509
	True density (ρ_s)(g/cc)	4.3682
Powder	True volume (cc)	0.7936
	Sample mass (g)	3.4028
	True density (ρ_s)(g/cc)	4.2878

There are many density types in the literature such as tapped density, bulk density, apparent density and so forth [28, 120]. In this study, bulk and skeletal (true) density were calculated by the help of instruments. As a rule of thumb, as increasing the fidelity of the volume measurement method from volume displacement to helium pycnometer, it is obtained more accurate volume which in turn gives rise to the fact that density would decrease.

For the same material, bulk density is absolutely lower than skeletal density. Before starting to mercury porosimetry, it is essential that it requires finding out the skeletal volume which would be used as an input in mercury instrument for volume calculations. For this reason, helium pycnometer was performed at first. Helium pycnometer is the most accurate way in identification of the very minute pores because helium is capable to fill thoroughly and swiftly in the smallest pore spaces [125]. In Table 4.3, true density measurements are shown for pellet and powder samples. As seen, they are very close to each other because of the fact that all pores and as well as the void spaces even if they are occluded are detected and excluded in volume determination.

Mercury porosimetry is the most critical characterization technique particularly for macroporous particles in determination of accurate volume and porosity coupled with average pore size diameter. In the beginning of the analysis at zero pressure, the bulk density of the pellet was measured as 1.48 g/cc on the basis of mercury displacement. Having a non-wetting characteristic of the mercury makes the mercury

porosimetry as an indispensable tool in measuring bulk density in an accurate manner regardless of the type of porous structure [126].

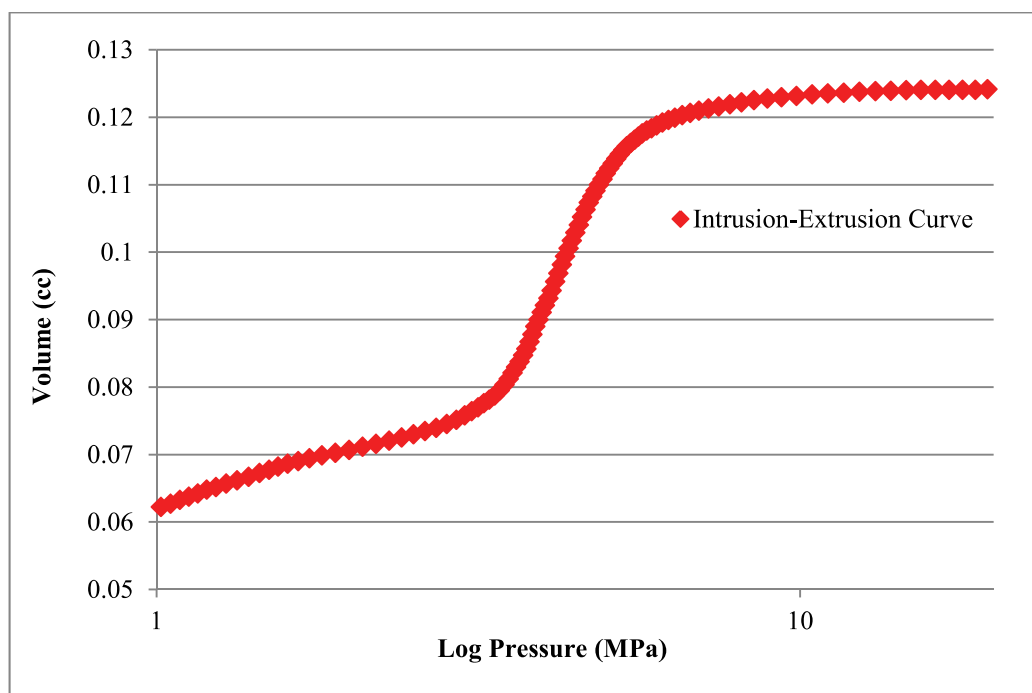


Figure 4.5. Intrusion-extrusion curve of the pellet obtained from mercury porosimetry at 40.000 psi (275.8 MPa).

It is apparently deduced from intrusion-extrusion curve in Figure 4.5 that the galloping mercury intrusion is decelerating around 10 MPa. More precisely, there is no even small amount of increase in volume intrusion after 20.40 MPa. Thus, total specific macroporous volume is found as 0.1811cc/g, which is order of magnitude higher than specific mesoporous volume discovered by BJH method in nitrogen adsorption. Total porosity is calculated as 0.268 from the ratio of total intruded volume and sample bulk volume.

Pore size distribution is also another important outcome of the mercury porosimetry as shown in Figure 4.6 where mercury intruded into pores was normalized with respect to the pore diameters. That's why, normalized volume (cc/g) was used in the y-axis. From this graph, it is easily realized that the average pore size diameter, which is in macroporous scale (>50 nm) is determined as 538 nm. This result is another explicit evidence of the type of porosity of the catalyst.

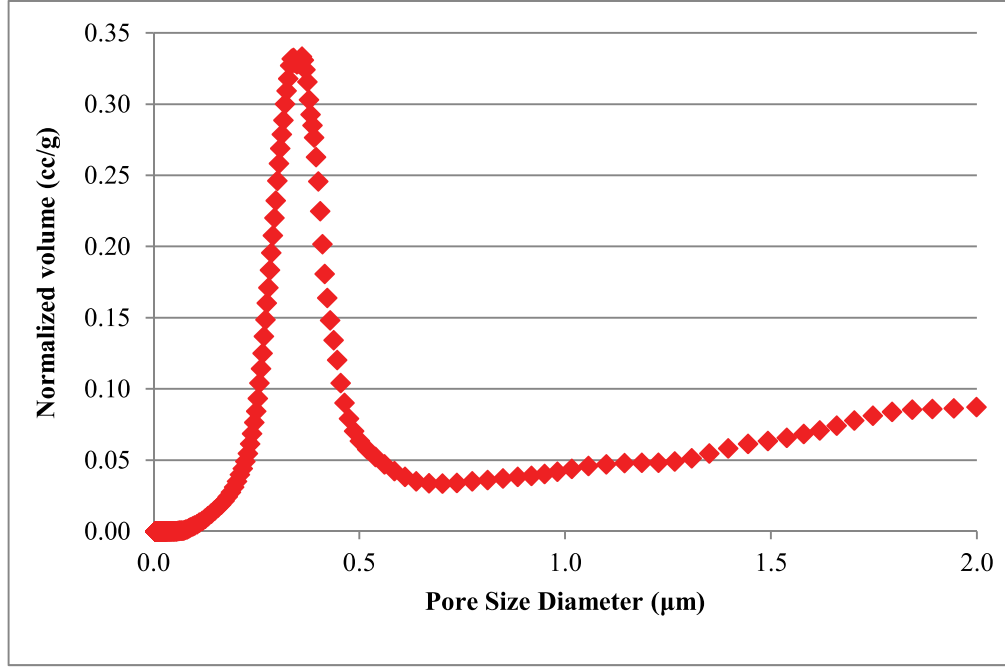


Figure 4.6. Pore size distribution of the pellet taken from mercury porosimetry.

In addition to skeletal and true density, tapped density is also another useful density type which was used for mass transfer limitation calculations in our study. Tapped density, which was found as 1.57 g/cc, was determined by using a graduated cylinder that has an ID of 0.9 cm (same as lab-rig reactor) and catalyst mixture of 2g. Calculated tapped density is also used instead of theoretical bulk density in bed void fraction calculation as shown in Appendix B. This is assumed to be more accurate because bulk density of SiC strongly depends on many parameters such as production type, materials and seed orientation. Maximum reported bulk density is 1.86 g/cm³ in the literature. The bulk density range lies between 0.5-1.86 g/cm³ while particle density of SiC is 3.21 g/cm [127-128]. Therefore, there is no specific bulk density value for SiC.

$$\tau = [2.23 - (1.13 * v_{mp} * \rho_{mp})] * (0.92 * \gamma_{sf})^{1+\varepsilon_{sf}} \quad (4.3)$$

$$\gamma = \frac{4 * v_{mp}}{A_{BET} * d_{mean}} \quad (4.4)$$

τ :	<i>Tortuosity</i>
v_{mp} :	<i>Total specific pore volume (from mercury porosimetry)</i>
ρ_{mp} :	<i>Pellet bulk density (from mercury porosimetry)</i>
γ_{sf} :	<i>Pore shape factor</i>
ε_{sf} :	<i>Exponent of pore shape factor(1 for cylindrical shape)</i>
A_{BET} :	<i>Specific BET surface area</i>
d_{mean} :	<i>Average pore size diameter (from mercury porosimetry)</i>

Tortuosity for chemical porous media is an effective unit that compares the average length of a chemical's diffusive pathway with straight-line length [129]. Tortuosity, which is the strong function of particle porosity could be experimentally measured as well as calculated in an empirical way. Macroporous structures generally have relatively high tortuosity values than micro and mesoporous materials [130-131]. Carniglia developed a couple of extremely useful and realistic equations (4.3-4.4) for cylindrical paths that have been using in the software tools of mercury porosimetry instruments at the present time. The values obtained from these equations are very compatible with the ones that are calculated from diffusion measurement experiments [120, 126, 132] Tortuosity factor was empirically calculated as 7.8 from the equations of 4.3-4.4 by using the results obtained from mercury porosimetry and nitrogen adsorption.

$$k_{pc} = \frac{\epsilon_p^3 * d_{mean}^2}{32 * \tau * (1 - \epsilon_p)^2} \quad (4.5)$$

k_{pc} : *Permeability coefficient*

\bar{d} : *Average pore size diameter (from mercury porosimetry)*

ϵ_p : *Porosity (from mercury porosimetry)*

τ : *Tortuosity*

Permeability, which is the one of the effective transport parameters for multicomponent gas transport in the porous media of the catalyst as well as tortuosity, is a measure of gas flow through porous material in order to find out the pressure gradient across the pore cross-sectional area [133-134]. Permeability highly depends on structural parameters (i.e. textural parameters) of the catalyst like porosity, pore size diameter and tortuosity as described in equation (4.5) [120]. Put it differently, if the permeability is known as a function of these parameters, pressure drop calculation could be conducted in intraparticle diffusion phenomena for industrial reactor modeling. From the point of the catalyst design perspective, pore size characteristics or porosity could be tailored by using a known or target permeability. Therefore, permeability is an important parameter not only for model-based process design but also model-based product design [135-137]. From equation (4.5), permeability coefficient for our catalyst pellet was found as 4.16×10^{-17} .

$$\frac{k_{eff}}{k_m} = 1 + \frac{3 * \vartheta_{fp}}{\left(\frac{k_{fp} + 2 * k_m}{k_{fp} - k_m}\right) - \vartheta_{fp}} \quad (4.6)$$

k_{eff} : Effective thermal conductivity of the pellet

k_m : Thermal conductivity of composite matrix (corundum)

k_{fp} : Thermal conductivity of filler particles (silver)

ϑ_{fp} : Volume fraction of the filler particles in the composite material

Effective thermal conductivity, which is one of the critical thermal properties of the composite materials, could be determined by using either Laser Flash Analysis (LFA) or composition-based prediction techniques [138-139]. Catalyst pellet is considered as a ceramic material which contains silver particles in the corundum matrix [140]. In the literature, modeling techniques could give a realistic prediction for thermal conductivity in comparison with experimental studies. In case of the fact that composition of the pellet is quantitatively known and has a silver amount that is lower than 25% in the composite matrix (corundum), Maxwell equation (4.6) is selected as a predictive model in which filling material (silver particles) has no thermal interaction amongst themselves [141-143]. Volumetric fractions of filling material (6.36%) and

composite matrix (93.64%) are calculated by using XRF results from Table 4.1 and density of the components at 250°C are retrieved from literature which is average process temperature both for lab-rig and industrial reactor. It is assumed that density of the corundum does not change with temperature until the target process temperature of 250 °C [144]. Thermal conductivities of the components (k_l and k_m) at 250 °C are taken from literature [145-146] as 409 and 17.36 W/m.K, respectively. As a result, effective thermal conductivity of the pellet was calculated as 20.457 W/m.K.

$$C_{p,pellet} = 0.1512 * C_{p,Ag} + 0.8244 * C_{p,cor} \quad (4.7)$$

Last property of interest is heat capacity of the pellet, which could be found by using either differential scanning calorimetry (DSC) or predictive model by using mass fractions of the components in the matrix [147-149]. Apart from effective thermal conductivity, heat capacity of the composite material is directly found by using individual heat capacities of the components and their mass fractions in a mixture model as a more straightforward and robust method. Heat capacities of silver and corundum (Al_2O_3) at 250°C were taken as 255.36 and 1061.14 J/kg.K, respectively [150-151]. Pellet heat capacity was thereupon calculated from equation (4.7) as 913.41 J/kg.K.

As catalyst is aging, it is readily seen that some process indicators have been changing in a discernible manner such as reactor temperature, EO selectivity, outlet carbon dioxide level and amount of steam production. Among these indicators, EO selectivity only decreases whereas the remainders increase as drawing closer to the catalyst change-over period. Therefore, providing that type of catalyst is the same as the previous catalyst life cycle, the deactivation pattern could be easily tracked by the help of utilizing data retrieved from process historian database. By the same fashion, retrospective data could be used for monitoring catalyst health which gives valuable information to process engineer when to have to change catalyst in presence of current operating conditions.

Commercial catalyst that was exposed to several characterization techniques for reactor modeling purpose has different status throughout its life (c.a 4 yrs). In addition to these, deactivation pattern recognition study was conducted in order to reveal what kind of stages catalyst has. In this regard, the data obtained from the end of run period (EOR) of ex-batch of catalyst and the start of run (SOR) period of recent batch of

catalyst coupled with more recent data investigated from the point of machine learning perspective.

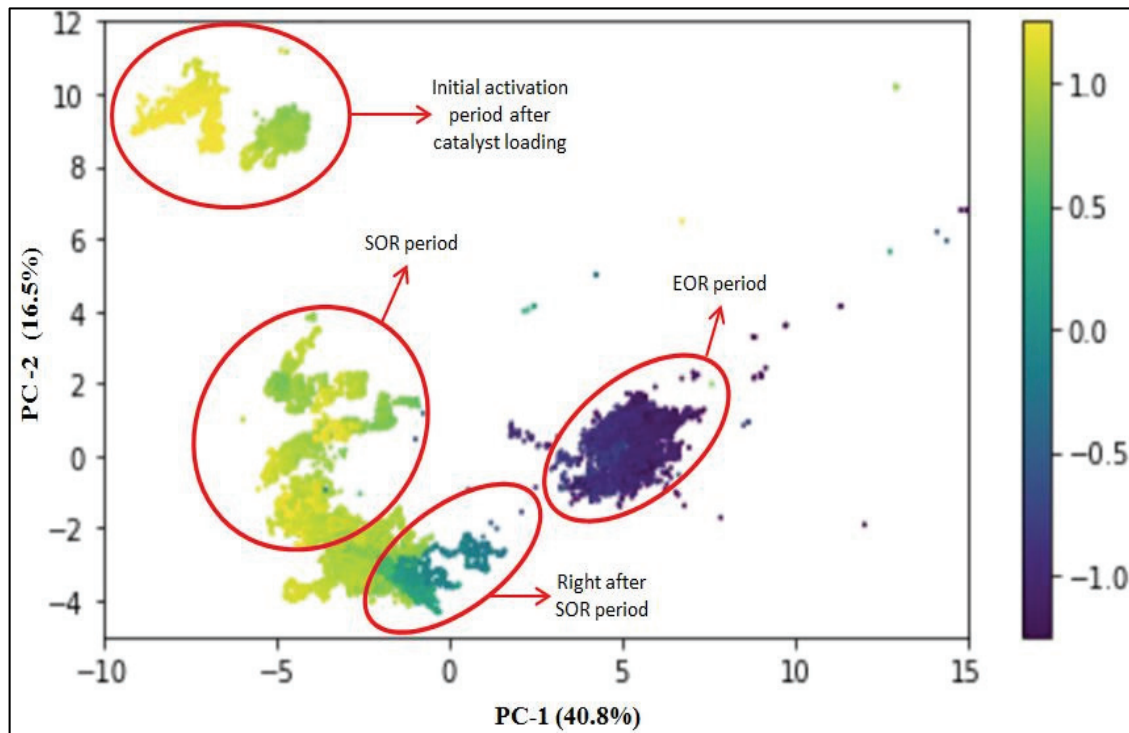


Figure 4.7. Catalyst deactivation pattern visualization by using PCA and SVR.

As can be seen from Figure 4.7, the transition periods of the catalyst are well visualized by using Principal Component Analysis (PCA) and Support Vector Machine (SVR) which are most commonly used data exploratory and classification techniques [152]. Complete stage differentiation was obtained from this data analysis part of the catalyst characterization. It is clearly seen that catalyst acts as a different behavior in the period called initial activation right after the catalyst loading. This period is required to squeeze a maximum benefit from catalyst and lasted for c.a 2 months.

From the modeling point of view, the model that is constructed for industrial reactor is built on SOR period in which catalyst is considered as a fresh catalyst (i.e. activity loss is negligible). For this reason, it is very important to figure out which portion of the historian data belongs to which certain periods. Another deduction from this analysis, there should be determined a catalyst activation procedure for the lab-rig reactor for each catalyst loading. Moreover, there is a distinctive shift in the catalyst deactivation status from SOR to EOR as expected in the big picture.

To do the data analysis, scikit-learn library (decomposition, preprocessing, pipeline, model_selection and svm) from Python 3 was utilized [153]. Firstly, predictors (sensor variables) related to the reactor were retrieved from database. Then the dataset is splitted into the subsets of training (75%) and test (25%). Dimension of the dataset that is used is 720x56. In total, there are 56 features. Each of them were preprocessed which means that subsets are normalized and scaled. After that, PCA decomposition (i.e. dimensionality reduction) was applied in order to reveal potential patterns within the data and in order for capturing 95% of the variance. This is achieved by finding orthonormal directions which maximizes the variance, followed by projection of the data on these directions. After dimensionality reduction, 95% of the variance refers to 14 components out of 56. Explained variances by two main principal components (PC-1 and PC-2) are 40.8% and 16.5%, respectively.

Classification between SOR and EOR periods was accomplished by using linear support vector machine regression (LSVR) in a binary target scale. In this 2D dataset representation, the beginning of the SOR period was shown as “1” whereas the ending of the EOR period was denoted as “-1”. This situation was also illustrated in color scale in Figure 4.7.

4.2 Preliminary Kinetic Experiments

In advance of embarking on the kinetic experiments itself, there is an important part that has to be fulfilled called as preliminary kinetic experiments, which enables that experimental results will be free from faulty and misleading situations. As a matter of fact, it is undeniable that experimental data contain some sorts of errors (e.g., random and gross errors) by its very nature. From this perspective, given that optimum preparatory conditions are determined, the underlying data which is hidden into the raw data could be readily refined from measurement errors by deploying advanced statistical methods. Kinetic data should be merely dependent on macroscopic variables of the reactor such as temperature, reactant concentration, space velocity and so forth. Hence, it would be attained to the point that observed kinetic rate equals to intrinsic kinetic rate which is the main objective of the kinetic tests, where effectiveness factor is assumed to be zero.

Preliminary kinetic experiments that have been done within the context of this study are mainly divided into four parts:

- 1- *Elimination of heat transfer limitations*
- 2- *Foundation of plug flow criteria*
- 3- *Elimination of mass transfer (intraphase&interphase) limitations*
- 4- *Catalyst activation, stability tests and case-specific system checks*

Achieving to isothermal conditions as much as possible plays a critical role in the system that has multiple reaction pathways like in ethylene oxide reactor. Nevertheless model-based approach is used and therefore it could be handled such kind of complex circumstances, there is no point to increase the complexity of the system. In this regard, some preemptive precautions were taken for mitigating temperature gradients. First, catalyst amount in the mixture does not exceed 10% in total. This provides satisfactory dilution during the reaction which is highly exothermic. Inert and catalyst particles (SiC) have same particle size distribution which lies between 150-300 μm . This minimized the bed voidage and accordingly maintained the close proximity amongst catalyst and inert particles. It was chosen SiC as an inert material which has excellent heat insulating performance. Two different mixture gas tubes (VCM and EO) that are sporadically used in the experiments were prepared with helium as a diluent gas (i.e.ballast gas), which has high thermal conductivity [112].

$$Bi_h = \frac{R_{solid}}{R_{fluid}} = \frac{h_f * L_{c,particle}}{\lambda_f} \quad (4.8)$$

Bi_h : *Biot heat number*

h_f : *Heat transfer coefficient of the fluid ($\text{W} * \text{K}^{-1} * \text{m}^{-2}$)*

$L_{c,particle}$: *Characteristic length of the solid particle (m)*

λ_f : *Thermal conductivity of the fluid phase ($\text{W} * \text{m}^{-1} * \text{K}^{-1}$)*

R_{solid} : *Heat resistance inside the solid*

R_{fluid} : *Heat resistance on the surface*

Elimination of external heat transfer is also conceptually important to consider because of the fact that external fluid layer (gas phase) has relatively lower thermal conductivity than catalyst (solid phase). Once the same procedure is set for mass transfer limitation and carried out perfectly, external heat transfer would be eliminated or minimized to a negligible extent as well. The foundation of plug flow criteria (L/d_p or d_t/d_p) as described in equations (4.9) and (4.10) also plays crucial role in this step. Biot heat number (Bi_h) in equation (4.8), which is a dimensionless number indicating the extent of external heat transfer limitation in gas-solid catalytic environment, is mostly smaller than 1. In our case, biot number lies between 0.5-1 with reference to lab-rig model results which points out that the dominant thermal resistance rule over the film layer in comparison with catalyst particle which is supposed to be isothermal. In laboratory experiments, internal heat transfer gradient is always lower than external heat transfer gradient due to the small particle size unlike industrial operations [5, 154].

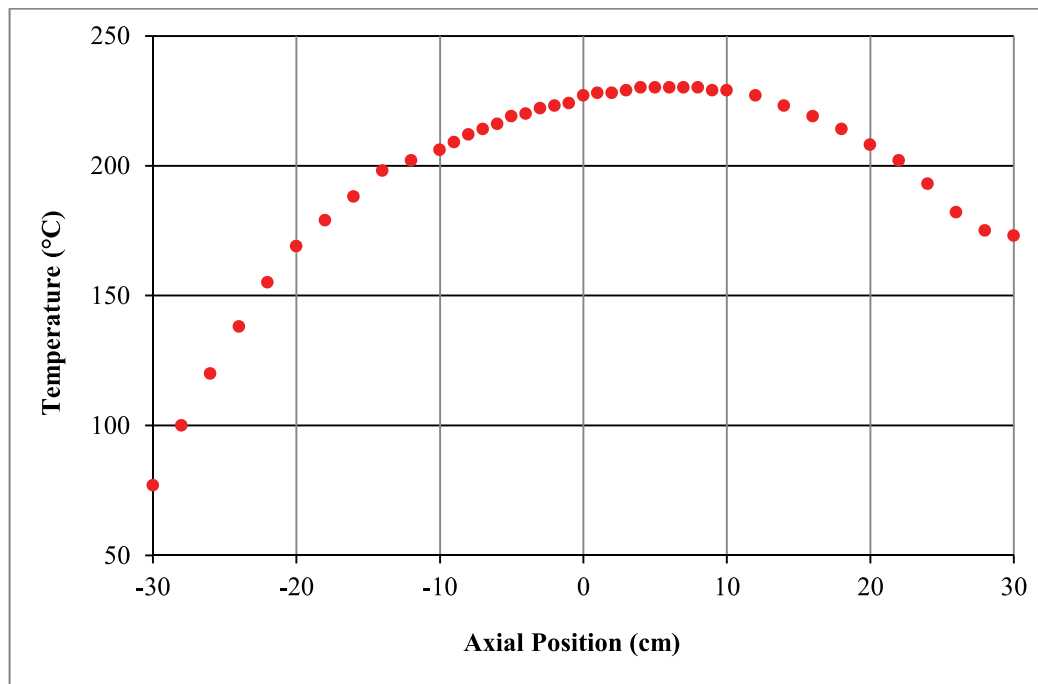


Figure 4.8. Temperatures from reactor mid-section ($x = 0$) at steady-state conditions.

Dealing with determination of the isothermal zone (± 5) alongside the reactor, after several successive trials, the setpoints of TIC-1 and TIC-2 were increased to 280 °C and 180 °C respectively. Once the system reached steady states temperatures, the temperature profile along the reactor axial direction was recorded. It is seen from Figure

4.8 that the area between $x = 0-10$ cm (above TIC-2) is near isothermal region it is best to work with the catalyst bed in this region. Superposition at $x=10$ refers to the edge of the lower part of the quartz wool. These constant temperatures have been determined for a blank (non-reactive) reactor filled with inert particles.

$$\frac{d_t}{d_p} > 10 \quad (4.9)$$

$$\frac{L}{d_p} > 50 \quad (4.10)$$

d_t : Reactor diameter (9 mm)

d_p : Catalyst particle diameter (212 μm)

L : Catalyst bed length (20 mm)

Establishment of the plug flow requirements is another important point to consider. Ideal flow is a demanded criterion in order for attaining reliable ramification from kinetic data. As described in equations (4.9) and (4.10), there are two important inequalities to be fulfilled [94, 155-156]. In our system, d_t/d_p and L/d_p ratios are determined as 42.4 and 94.34, respectively. The minimum value of L/d_p is also calculated as 17.563 by using Reynold number and average ethylene conversion (Appendix B). Therefore, it was assumed that uniform velocity governs over the cross section area of the reactor. For this reasons, radial temperature and concentration gradients as well as axial dispersion in the reactor are assumed to be negligible [112, 155].

The limiting reagent in the lab-rig reaction system is oxygen whose average conversion range falls within the band of 30-40% which is very close to the industrial conditions. Conversion of limiting reagent in the integral reactor are generally much higher than that of differential reactor (c.a <10%). Put it differently, it is in the vicinity of industrial conditions. However, this does not give rise to a complex situation for our case thanks to the model-targeted experimentation approach that will be applied by using gPROMS. Otherwise, it would be turned out to be a challenging impediment in making a quantitative analysis.

The lab-rig reactor behaves in a non-adiabatic fashion due to the continuous heat removal as in industrial reactor. Regarding to isothermality, it could be said that it is close to isothermal conditions but does not perfectly obey to isothermality criteria because of having higher conversion values.

For the sake of proving the plug flow assumption for the lab-rig reactor, it is decided to determine hydrodynamic entrance region based on fluid dynamics, which is utilized as an indicator whether velocity distribution is fully-developed or not [157-158]. With this mind, transport and physical properties of the gas mixture (viscosity and density) and Reynold number of the flow regime were calculated based on the moderate temperature (250°C) of planned experiments.

In density calculations, ideal gas law, which is applicable for those processes that are operating at low pressure and high temperature, is used [114] whereas viscosity values were interpolated between the temperatures of 500 and 600K [159]. Moreover, pressure drop calculation was done in order to confirm whether particle size brings about any pressure drop alongside the catalyst bed. Volumetric flow rates of the components are measured at 25°C and 14.696 psi by mass flow controllers. Hence, temperature compensated flow adjustments were performed in total volumetric flow rate (75 sccm) according to catalyst bed temperature of 250 °C which was chosen for sample calculation steps.

Almost all experiments were done at atmospheric pressure. It is assumed that inlet gas volumetric fractions are same as molar fractions. Deviations from standart condition (0°C and 1atm) are neglected. The results are in concordance with the outcomes of lab-rig reactor modeling study given in the section of 4.6. Calculation steps are appended in Appendix B. It is inferred from the results that flow regime is Darcy flow because Reynold number was found as 0.41 (<1) [160-161]. Accordingly, length of the hydrodynamic entrance region ($L_{h,laminar}$) for laminar flow regime was calculated as 0.019 cm which is very lower than catalyst bed length (2cm). So, it is clearly stated that interstitial velocity does not change alongside the catalyst bed which means that the governing flow pattern is the plug flow.

Péclet number, which is the ratio of convective transport rate to diffusive transport rate, is another important dimensionless parameter even in the lab-scale environment. Péclet number is calculated as 6.69 by using the formula that includes Reynold number, particle diameter and catalyst length and is particularly for laboratory reactors [112], which is a portent of neglecting axial dispersion. This calculation is a

validation of being well-established plug flow criteria dealing with tube diameter and catalyst length [155].

$$\eta(\text{Effectiveness factor}) = \frac{\text{global rate}}{\text{intrinsic rate}} \quad (4.11)$$

Other very critical criteria in kinetic experimentation are to eliminate mass transfer limitations between gas phase and catalyst pellet unlike homogeneous catalytic media in which all reaction components including catalysts stay in one common phase. As a rule of thumb, reactions are limited by either chemical kinetics or thermodynamic equilibrium which is not present in ethylene oxide process. That's why chemical kinetics is the only pillar of interest so it should be determined very accurately in lab-rig reactor.

There are two fundamental phenomena having influence on intrinsic reaction rate: Mass transfer phenomena and chemical kinetics. If any of these becomes slower than the other one, the slower one determines the governing phenomena. The former is not a wanted situation which makes the kinetic data acquisition difficult. If not decoupled, the kinetic model would eventuate with falsified kinetics and therefore does not reflect the reality.

Effectiveness factor as shown in Equation (4.11), which is generally used for porous catalytic media, shows how much deviation exists between global kinetic rate and intrinsic kinetic rate. It is highly recommended for kinetic experimentation that global rate should be as much as close to intrinsic rate. In other words, effectiveness factor ought to be equal to 1 in such circumstances [5, 155, 162-163].

Surface layer surrounding the catalyst as shown in Figure 4.9 is the source of the external mass transfer limitations whereas internal mass transfer limitations are dealing with pore diffusions (forward and reverse) inside the pores. The extent of both limitations is dependent on size of the particle apart from the fact that increasing the flow rate solely ends up with diminishing the external mass flow rate. However, regarding to increasing the flow rate, this could result in a challenging issue when the upper limit of the mass flow controllers are not so high, which is for the very reason in our lab-rig reactor system. This is the minor reason of opting for decreasing catalyst particle size other than increasing total flow rate.

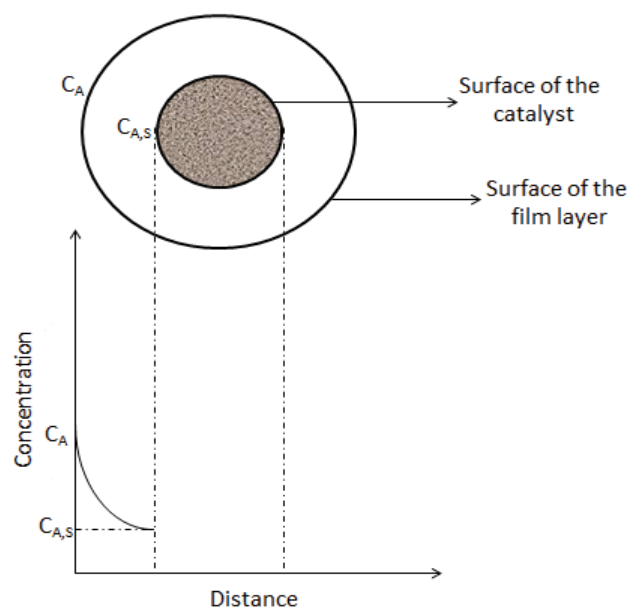


Figure 4.9. Concentration profile through the film (Source: [155]).

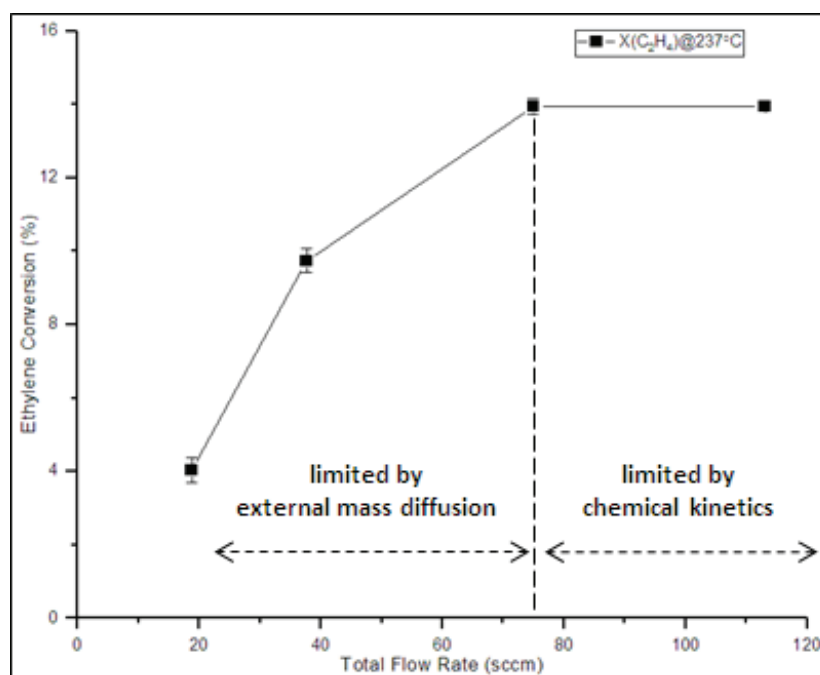


Figure 4.10. Influence of flow rate on conversion at a constant space velocity (GHSV).

Two types of limitations are experimentally investigated and further analysis was done by observing the conversion and ultimately pressure drop calculation was performed with respect to the results of the internal mass transfer limitation experiments. Upon investigation of external mass transfer limitations, constant space velocity was determined by using bed and physical properties of the mixture as tabulated in Table B.2 (Appendix B). Catalyst amount was changed from 0.05g to 0.3g with catalyst volume in the bed by keeping constant gas-hourly space velocity (GHSV) at 0.981s^{-1} . It is apparently observed from Figure 4.10 that ethylene conversion is almost keeping on constant after the vicinity of 75 sccm. Before this region, catalytic process is limited by external mass transfer diffusion. Thus, this critical region is taken into account in determination of total flow rate at the stage of design of experiments. All mass transfer limitation experiments were conducted at 250°C . Regarding to error analysis, standard error of mean of each experiment relating to external and internal mass transfer limitations was calculated in obedience to the formula consisting of standard deviation and sample size coupled with t-distribution coefficient based on 95% confidence interval (Appendix B).

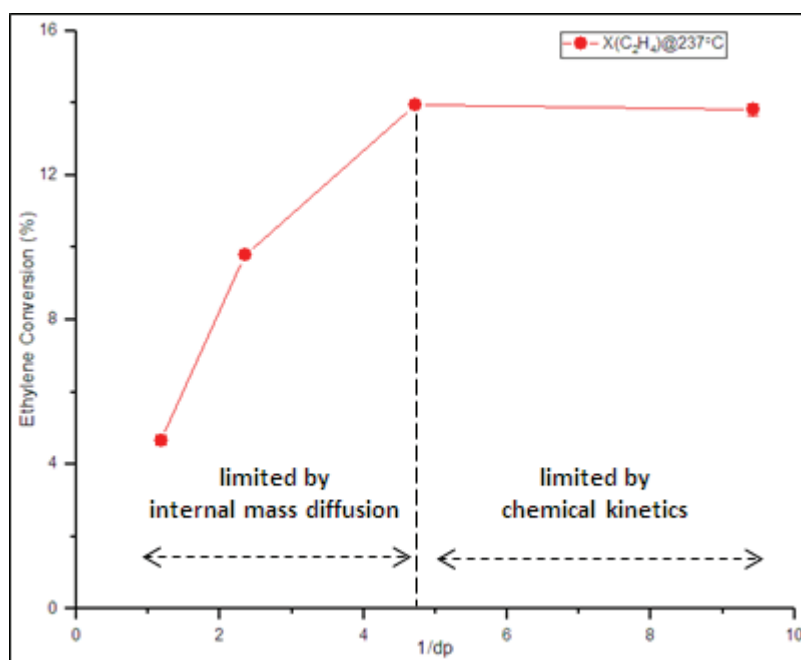


Figure 4.11. Influence of catalyst particle diameter on conversion at a constant space velocity.

Like external mass transfer limitation experiments, gas-hourly space velocity was kept constant at 0.981s^{-1} with the difference of changing particle diameter from $106\text{ }\mu\text{m}$ to $850\text{ }\mu\text{m}$. The key indicator parameter is ethylene conversion. In Figure 4.11, increasing particle diameter did not have an influence on conversion until the particle diameter exceeded the critical region of $300\text{--}400\text{ }\mu\text{m}$. Therefore, it was opted for those particles that have the geometric average of $212\text{ }\mu\text{m}$ after being elected the grinded catalyst particles by using laboratory sieve shaker [52]. Inert catalyst particles in the same range were also chosen accordingly. Lastly, pressure drop calculation (Appendix B) was performed by using the Carman-Kozeny equation which is appropriate for those porous bed configurations that have lower Reynolds number (i.e <1) and porosity that is lower than 0.5 [164]. Our porosity value is 0.511 which is very close to 0.5 . That's why; it is assumed that this small difference is negligible. Pressure drop across the solely catalyst bed was found as 96.07 Pa . It could be extended to whole bed including the inert sections above and below the catalyst bed. Whole bed length is thrice times longer than catalyst bed. Due to the fact that pressure drop is directly proportional with bed length, pressure drop across all the bed turns out to be 288.21 Pa approximately thereby neglecting particle size deviations in the inert beds. Consequently, calculated pressure drop is very low. This indicates that bed configuration and particle diameter is well-structured.

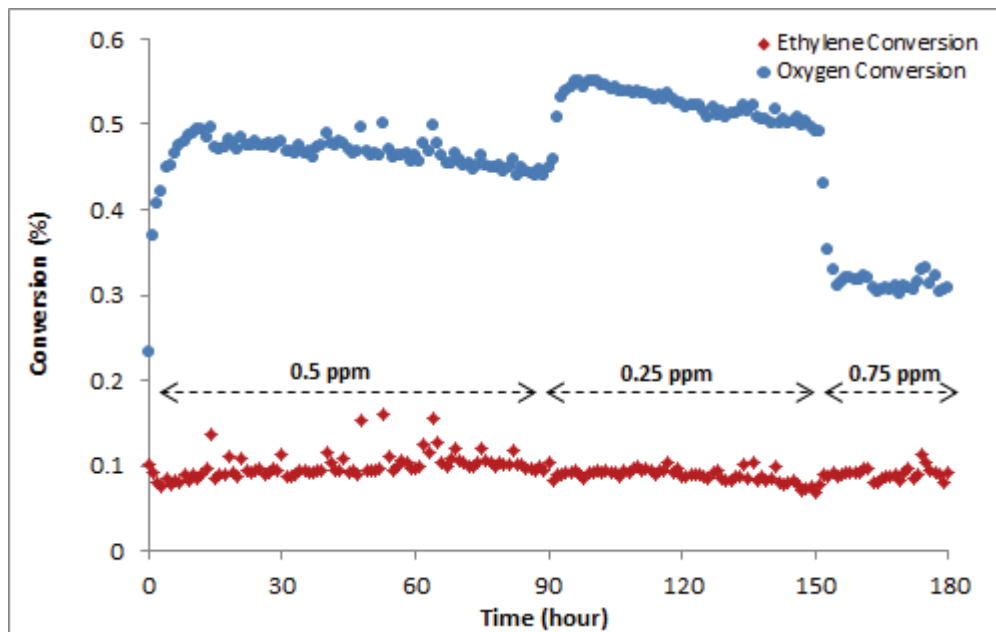


Figure 4.12. Conversion patterns with respect to VCM step changes during stability test.

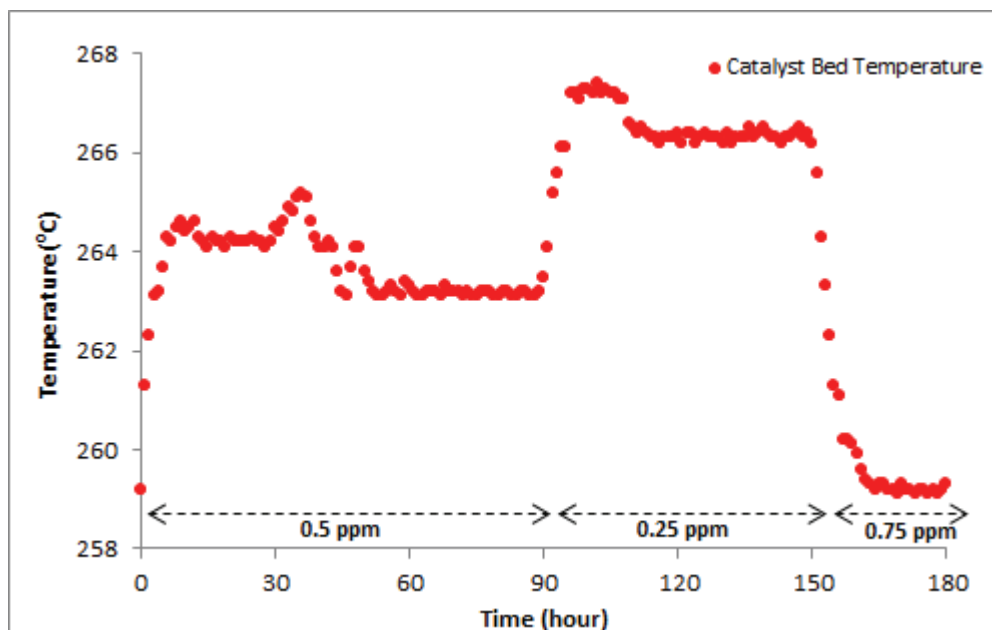


Figure 4.13. Catalyst bed temperature pattern with respect to VCM step changes during stability test.

Lastly, case-specific analyses were done such as catalyst activation, stability tests and CO₂ co-feed experiments. There are many *modi operandi* to get the catalyst activated as mentioned in literature [19, 23, 46, 57]. Literature review part of the thesis touches on different methods of catalyst activation for ethylene oxide reaction which is a type of oxidation process. For hydrogenation reactions, catalysts have to be reduced before being used. Therefore, unlike hydrogenation catalysts, activation was considered satisfactory by exposing the catalyst to a 20 sccm pure oxygen stream for 6 h at a bed temperature of 250°C. Duration of the activation process is quite compatible with the literature.

On the other hand, the main objective of the stability test is that it allows us for monitoring of reaction temperature, reactant conversions, product selectivities and yields over a longer period of time in the presence of a moderator such as VCM. Nevertheless it is known that industrial catalyst has long life expectancy up to 5 yrs, it is good to know that grinded particles would experience any activity loss during the long duration of operation. Stability tests are generally carried out at high temperatures for investigating thermal stability and resistance to sintering owing to the fact that it is likely to occur sintering process at relatively high temperatures which is the main reason

of the deactivation for ethylene oxide catalyst [165]. In our case, stability tests are performed for about 3 days.

As seen in Figure 4.12, first stability test was carried out at different VCM step changes (0.25-0.50-0.75 ppm) by monitoring conversions of ethylene and oxygen during the course of the catalyst stability test. Activated catalyst was used. Along with the reactant feeds of 25% ethylene, 7% O₂, and balance CH₄, vinyl chloride monomer (VCM) was fed to the reactor to moderate the catalyst activity. VCM was fed at 0.5 ppm for the initial 90 hours, later fed at 0.25 ppm between 90–150 hours, and finally fed at 0.75 ppm between 150–180 hours. This VCM was fed from the tube having a 5 ppm concentration in a balance He gas at a flow rate of 8 sccm, which was included into the total reactor feed flow rate of 80 sccm. It can be observed from Figure 4.12., that VCM plays an important role in the O₂ conversion. This inverse relationship is due to the fact that VCM competitively binds to the active sites and thereby lowering the reaction rate and favoring the ethylene epoxidation reaction. Thus, with higher VCM concentrations, the combustion reaction is reduced resulting in lower O₂ conversions. By contrast, ethylene conversion remains relatively constant throughout the course of the stability test and is independent of the VCM concentrations and O₂ conversions.

Figure 4.13 shows that the catalyst bed temperature increases with varied VCM concentration in the feed. With lower VCM concentrations, the combustion reaction is favored, which has a higher heat of reaction and thus results in increased temperatures and visa versa. Other aim of the activated catalyst experiment was to observe the catalyst behavior at higher steady-state temperatures. The reaction exothermic temperatures reached 260–270 °C during this experiment.

As inferred from Figure 4.14., lowering the VCM concentration from 0.5 ppm to 0.25 ppm results in a higher production of CO₂ (i.e. lowering the selectivity of EO by favoring the combustion reaction). Increasing the VCM concentration from 0.25 ppm to 0.75 ppm has the opposite effect and sharply decreases the CO₂ production and as well as EO production. These initial observations suggest that at higher VCM concentrations (>> 0.5 ppm), VCM has a strong inhibiting effect lowering the EO production by 25% to an average concentration of 1.56%. Therefore, it is necessary to investigate an optimum VCM level in order to obtain higher EO selectivities while maintaining desirable EO yields. This pattern is very similar with industrial operations regardless of the degrees of scale in operations which is only affecting on the VCM amounts in ppm. This is always a dynamic optimization case throughout the catalyst life [45].

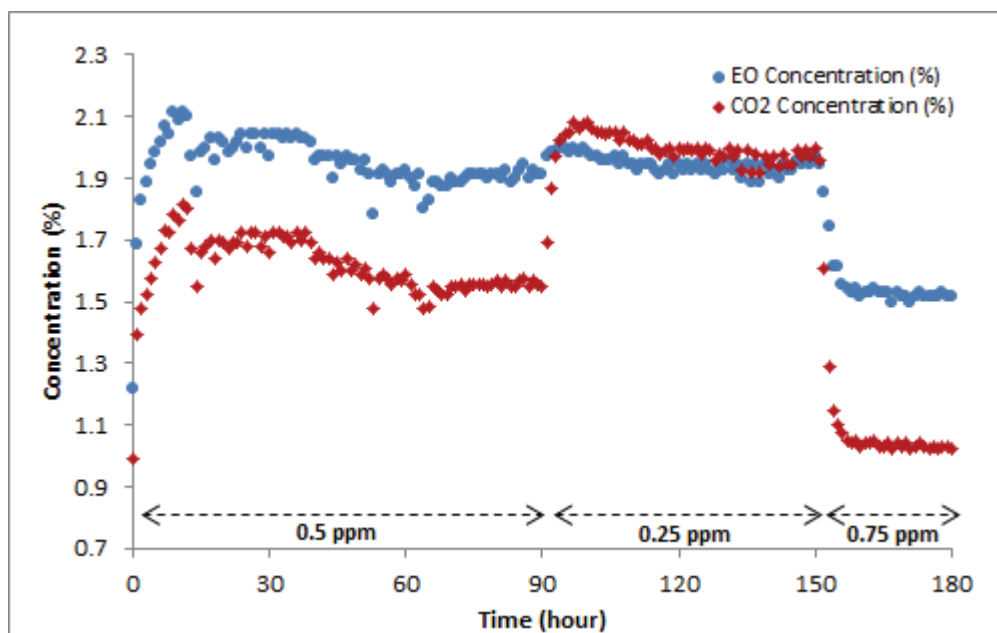


Figure 4.14. Product concentration patterns with respect to VCM step changes during stability test.

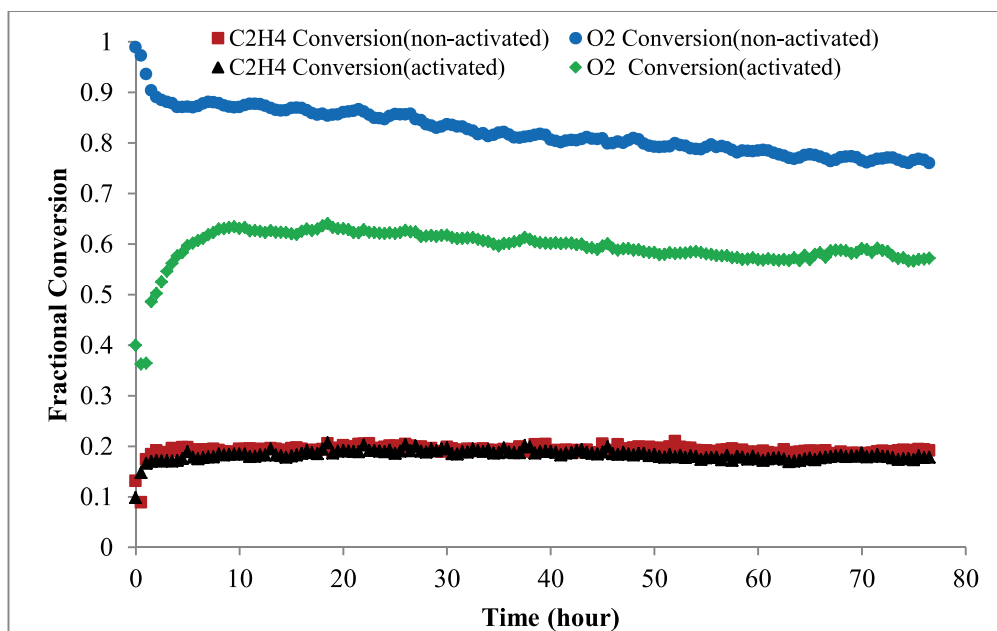


Figure 4.15. Conversion patterns at constant VCM with activated and non-activated catalyst during stability test.

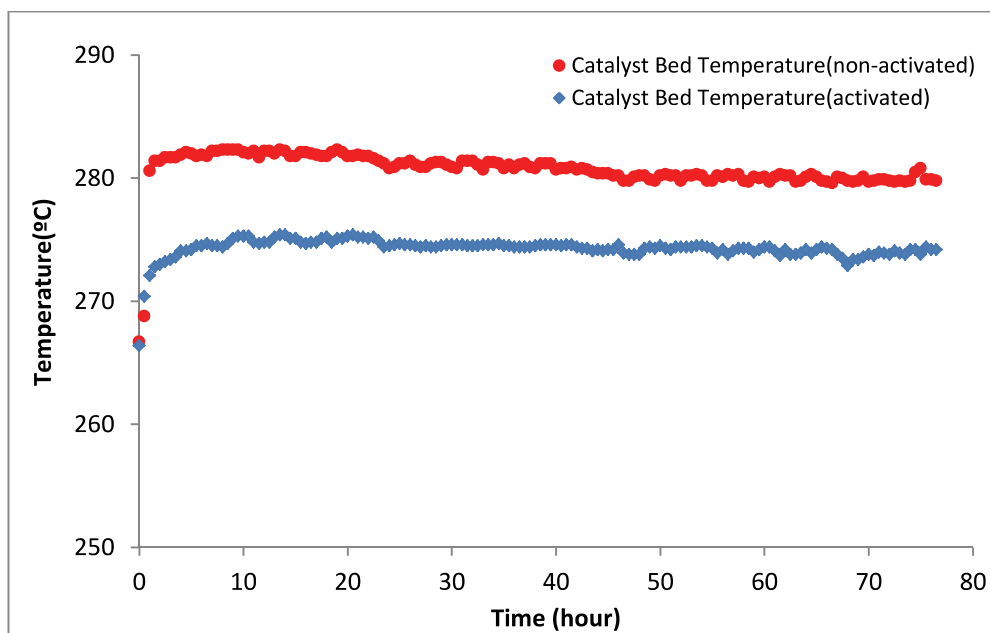


Figure 4.16. Catalyst bed temperatures at constant VCM with activated and non-activated catalyst during stability test.

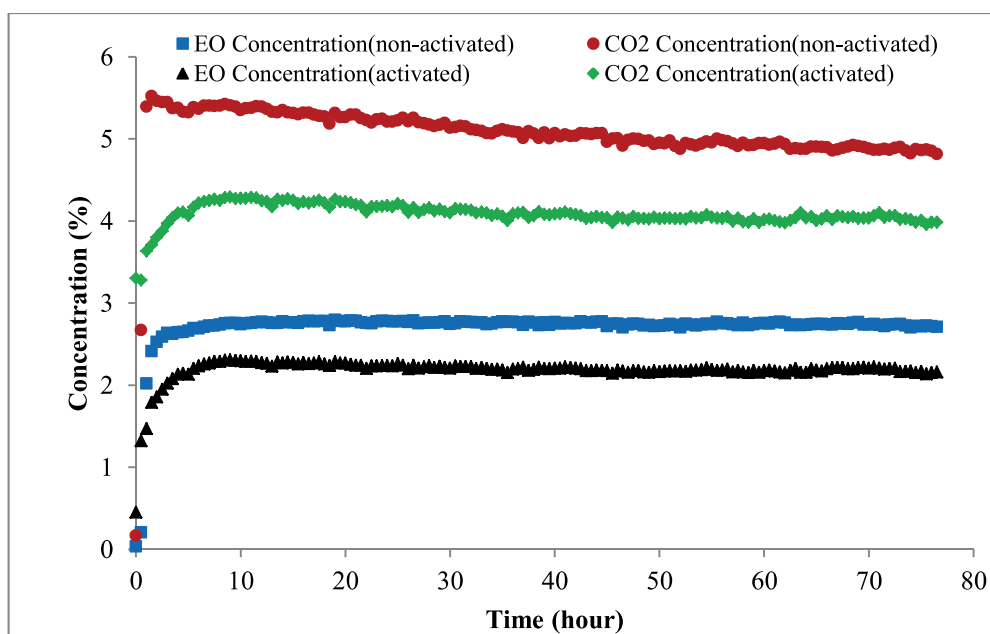


Figure 4.17. Product concentrations at constant VCM with activated and non-activated catalyst during stability test.

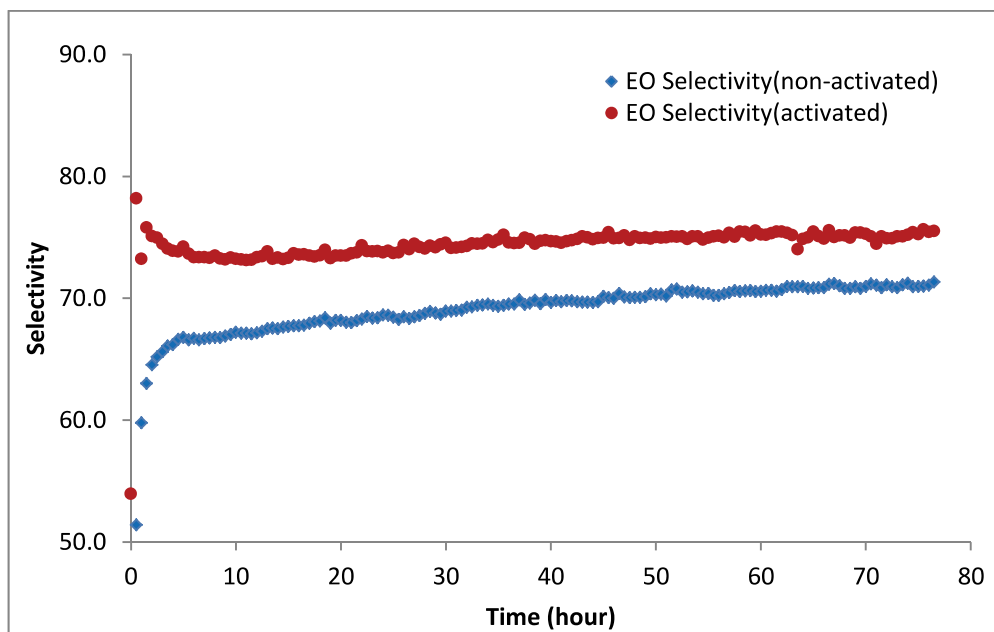


Figure 4.18. EO selectivities during the course of the catalyst stability tests obtained for each hour.

Table 4.4. Experimental conditions for the second stability test at constant VCM.

Inlet Gases	Concentration (%)	Feed Flow Rate (sccm)
Ethylene	26.88	21.5
Oxygen	6.88	5.5
Methane	53.75	43
CO ₂	2.50	2
He/VCM	10.00 (VCM: 0.5 ppm)	8
He/EO	0.00	0
Total	100.00	80.00

Due to an internal software defect in the mass flow controller of He/VCM, flow rates were fluctuated during the experiments resulting in varied concentrations of VCM fed to the reaction. The observed fluctuation is about $\pm 1\%$ of the set value, which is higher than guaranteed accuracy value of 0.4%.

After MFC had been fixed, second stability test were performed at a constant VCM concentration of 0.5 ppm by using activated and non-activated catalyst. Experimental conditions for both the activated and non-activated catalyst tests were kept the same as shown in Table 4.4. Activation was done by exposing the catalyst to a 20-sccm pure oxygen stream for 6 h at a bed temperature of 260.5 °C with the setpoint temperature for both the reactor inlet and furnace set to 255 °C. Figure 4.15 indicates that the activation status of the catalyst only has an effect on the oxygen conversion, which is 38% higher when using the non-activated catalyst than when using the activated catalyst. Figure 4.16 shows that steady-state catalyst bed temperatures when using the non-activated catalyst were 6.45 °C higher than when the activated catalyst is used. The bed temperature difference between activated and non-activated catalyst explicitly shows that applied activation procedure works well. Moreover, it can be observed in Figure 4.17 that CO₂ concentrations at the reactor outlet are higher by 24% when using the non-activated catalyst in comparison to when the activated catalyst is used. Thus, EO concentrations, overall, are higher when the non-activated catalyst is used, which is due to the increased conversions of reactants. Nevertheless, EO selectivity is lowered by 7.7% when using the non-activated catalyst as shown in Figure 4.18 due to the reaction pathway favoring epoxidation rather than combustion. Apart from this issue, it is not expected that selectivity will be same or close to the industrial conditions at the start-of-run period due to the use of grinded catalyst particles. Catalyst selectivity, which is the issue for industrial reactor modeling is not a focal point for kinetic experimentation.

Lastly, CO₂ co-feed experiments were conducted in order to check the general system accuracy and compare the results with literature. In these experiments, three different furnace set temperatures were used such as 220°C, 230°C and 240°C. For this reason, in Figures 18-21, discrete changes in reaction parameters are readily noticeable. Regarding to experimental conditions as shown in Table 4.5, VCM moderator was not used and CO₂ feed was compensated by decreasing methane flow rate. Moreover, non-activated catalyst was used in both experiments.

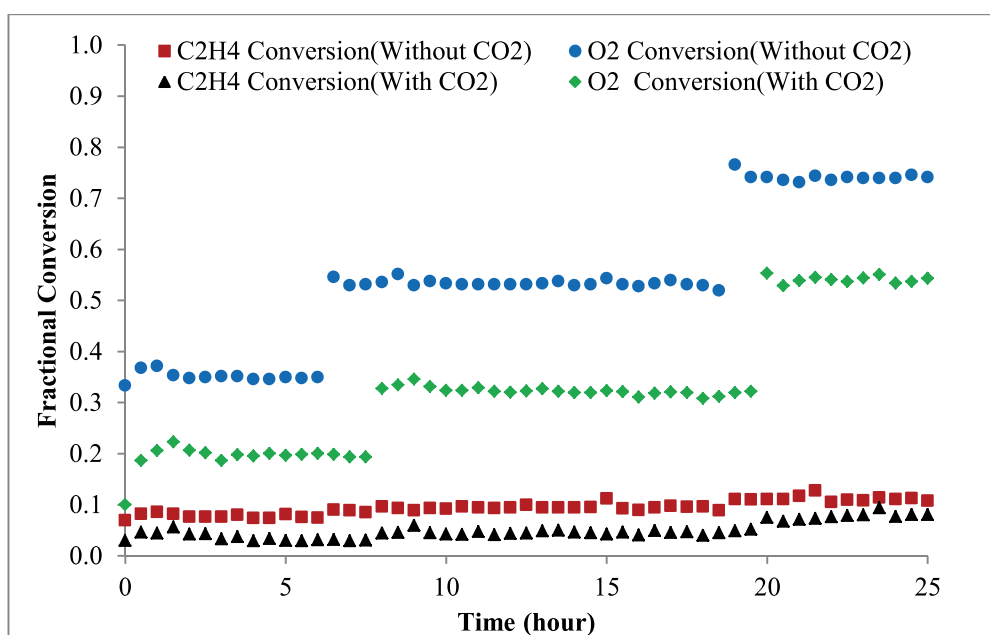


Figure 4.19. Conversion patterns at discrete furnace set temperatures (220°C-230°C-240°C) during the course of the experiments with/without CO₂ obtained for each hour.

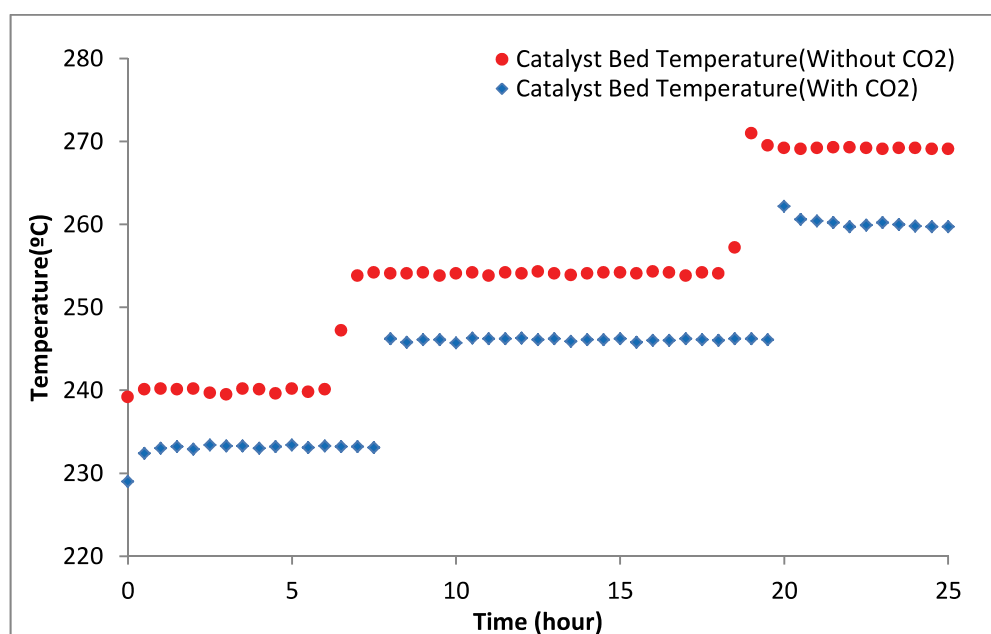


Figure 4.20. Catalyst bed temperatures at discrete furnace set temperatures (220°C-230°C-240°C) during the course of the experiments with/without CO₂ obtained for each hour.

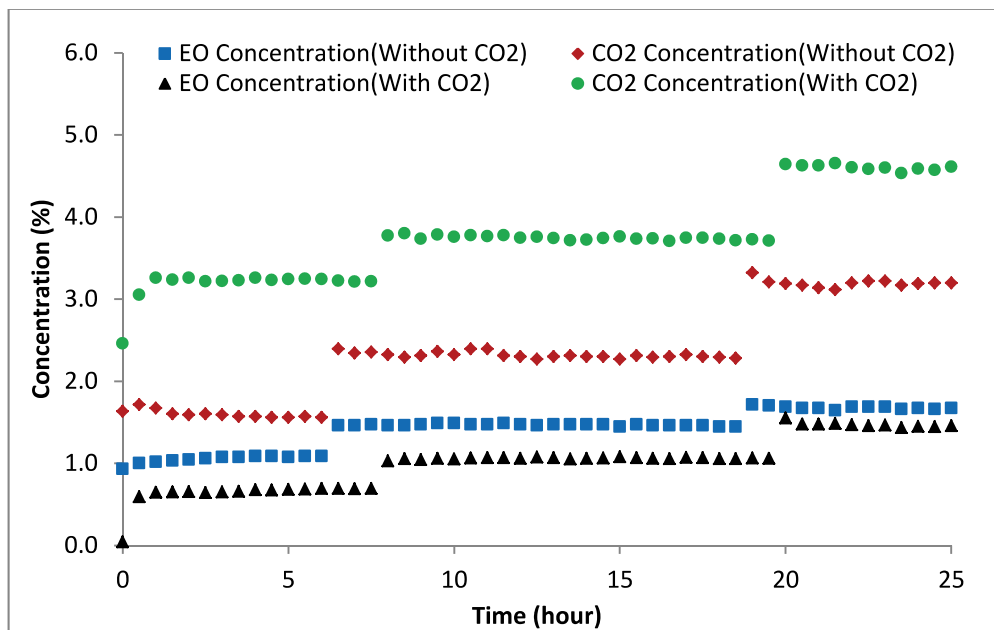


Figure 4.21. Product concentrations at discrete furnace set temperatures (220°C-230°C-240°C) during the course of the experiments with/without CO₂ obtained for each hour.

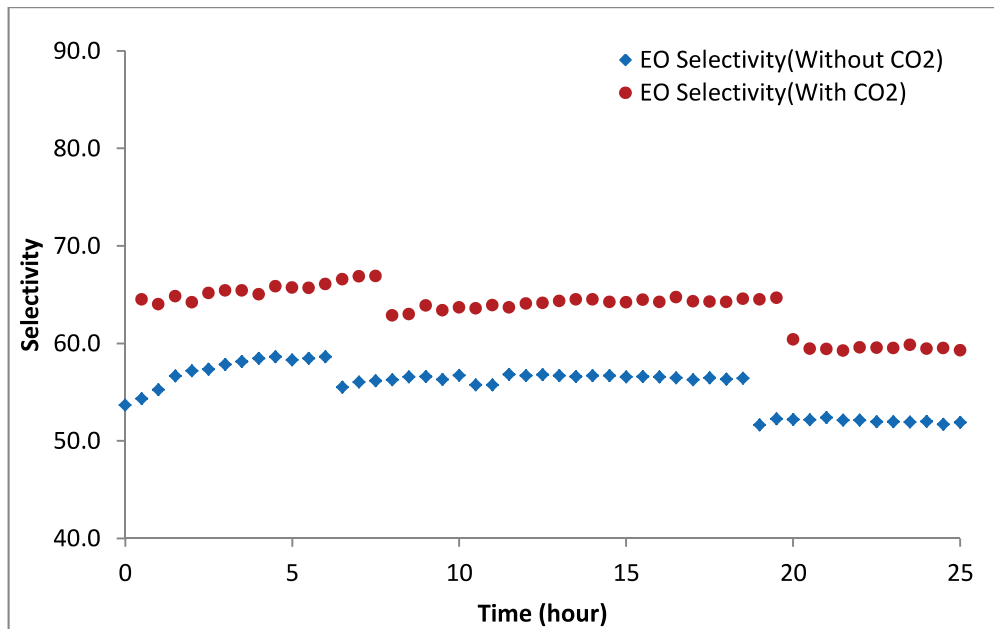


Figure 4.22. EO selectivities at discrete furnace set temperatures (220°C-230°C-240°C) during the course of the experiments with/without CO₂ obtained for each hour.

Table 4.5. Experimental conditions with/without CO₂ co-feed experiments.

Feed	Without CO ₂		With CO ₂	
	Concentration (%)	Flow Rate (sccm)	Concentration (%)	Flow Rate (sccm)
Ethylene	25.0	18.0	25.0	18.0
Oxygen	6.9	5.0	6.9	5.0
Methane	68.1	49.0	65.6	47.2
CO ₂	0.0	0.0	2.5	1.8
He/VCM	0.0	0.0	0.0	0.0
He/EO	0.0	0.0	0.0	0.0
Total	100.0	72.0	100.0	72.0

As observed from Figures 4.20, catalyst bed temperatures are 3.5% higher for experiments without CO₂ co-feed, which shows that CO₂ suppresses catalyst activity by surpassing total oxidation. In a similar manner, it can be deduced from Figure 4.19 that oxygen conversion is much higher in the experiments without CO₂ co-feed. In addition, ethylene conversion is only slightly higher in the experiments without CO₂ co-feed. Therefore, it can be concluded that CO₂ does indeed have a strong effect on the oxygen conversion. As can also be seen in Figure 4.21, EO yield is lower in the presence of CO₂ co-feed because of the inhibitory effect of CO₂.

In these experiments, an optimization study on the quantity of CO₂ co-feed was not conducted. The inlet CO₂ amount was set to 2.5% based on average values obtained from industrial plant data at the start-of-run period of operation. Based on the results, it can be seen that CO₂ plays a reverse role in the effects on EO and CO₂ formation. The inhibitory effects of CO₂ are clearly not the same for the epoxidation and combustion reactions. On top of that it was also found that the total oxidation is inhibited to a greater extent than the partial oxidation reaction. In other words, at all inlet levels of CO₂, selectivity towards EO would be higher than when no CO₂ was used as shown in Figure 4.22, however, the yield in EO does not necessarily increase. This tendency proves yet again that our catalyst testing set-up and GC calibration are functioning properly on the grounds that results are in line with literature [38]. From the theoretical point of view, the CO₂ amount in the industrial reactor inlet should not exceed 0.2% in

order to maintain reactor efficiency. However, it is practically hard to achieve such a low level unless high efficient CO₂ absorbing system including robust solvent and appropriate process design is preferred to use.

4.3 Design of Experiments

In total, 171 unique experiments were executed (Appendix C). Experiments are designed inside the sets. Each new loading with a fresh catalyst refers to a specific set or combined set. Put it differently, once a loading was done, many experiments were performed within approximately 20 days because it is known that catalyst has a long life expectancy up to 4 years. Notwithstanding this situation, catalyst deactivation was also investigated in lab-rig reactor. To do so, a specifically selected experiment derived from the maximum and minimum values of reactor compositions obtained from SOR and EOR conditions was repeated during the course of the each set. Moreover, the process conditions (concentration and temperature) of this experiment were kept constant among all experiments in order for monitoring the variations between loadings. In the experimental design, the flammability limit will be disregarded due to the elimination of heat transfer limitations. In the case that a thermal runaway is observed after a set point change, the reactor will be cooled down.

The experiments dealing with stability tests carried out with activated catalyst prior to the planned experiments were also added to the experimental domain. These loadings were denoted as 0a and 0b. Apart from these loadings, there are seven loadings in total. Till the catalyst loading #4, the amount of the catalyst used in the reactor was 0.1 g. After then, it was increased to 0.2 g and remained same.

The experimental plan is divided into five sets of experiments (as shown in the Table C.1). All but set #1 was calculated using Excel Solver where the upper and lower limits of flow rates provided by the manufacturer of mass flow controllers and the plant process conditions based on the SOR and EOR conditions were set as constraints. All experiments were performed using activated catalyst (i.e. exposed to a pure oxygen (O₂) stream for a minimum of 6 hours prior to commencing the experiment). In all experiments, except for those in set #0 and set #2, total feed gas flow rates were set to 75 sccm.

When taking all experiments in the grand scheme of things, the majority of the experiments were executed by using OFAT approach aside from the experiments in Set#1 (cat.loading#2&3) which are based on D-optimal design in view of the fact that it is explicitly to be untangled the relationships among temperature and reactant compositions by adapting OFAT method. These set of experiments are based on the fact that it is changed one or two variables simultaneously while keeping constant other variables. For example, the ethylene to oxygen ratio is fixed at different values while changing ethylene and oxygen values. Generally, this is the most frequently used technique in kinetic experimentations. Thanks to this method, the effects of total flow rate and pressure in combination with bed temperature, reactant compositions and moderator (VCM) concentration are experimentally investigated. Bed temperature is adjusted by furnace set temperature. It was found that there are some offset values between set and bed temperatures resulting from the small but not negligible physical distance between reactor wall and tip of the furnace thermocouple. In an average reaction severity based on compositions, furnace set point temperatures of 219, 237 and 250°C approximately refer to the 230, 250 and 265°C, respectively. Exact value of temperature at the center of the catalyst bed for each experiment is used in model-based approach.

Some of experiments (46 out of 171) were done without using VCM moderator. This helped the kinetic model train for the effect of VCM. The maximum VCM amount that could be allowable in lab-rig reactor due to the constraint on both VCM/He gas mixture tube and total gas flow rate is 1 ppm. In the industrial reactor, VCM is converted into the chlorine by products such as ethyl chloride (EC), methyl chloride (MC), ethylene dichloride (EDC) and allyl chloride (AC). All these components are acting as moderator. On top of that, recycle gas stream contains chlorinated components in the range between 1.6-2.0 ppm. Total amount of reactor inlet chlorine components increase up to 3-3.5 ppm by adding continuously fresh VCM in order to compensate chlorine lost through absorbing tower and process purge. Total cycling chlorine content is intentionally being increased towards EOR period. Like temperature increase, this is also a process strategy for meeting EO yield that is strongly dependent on deactivation phenomena of the catalyst. Nevertheless there is no considerable pressure variation in the industrial reactor which is operating at the very narrow range between 15.5-16.5 barg, influence of pressure effects up to 10 barg also was investigated within catalyst loading #7 in Set 3&4&5. For these reasons, in the stage of the industrial reactor

modeling for SOR period, conventional data with higher chlorine content and higher pressure will be used in the parameter estimation steps for reactor scale-up parameters (i.e. coolant side heat transfer coefficient for reactor inlet and outlet, catalyst activity for main and side reactions, linear and constant terms for coolant pressure, turbulent flow term for process pressure and process feed temperature adjustment term) in order to adjust the kinetic model with reference to reconciled historian process data.

In the industrial reactor, the main control variables for reactor operation are coolant pressure (directly related to coolant temperature) and I-Factor (Inhibitor-Factor) which is manipulated by adjusting VCM injection rate. I- factor is an empirical equation defined as:

$$I - \text{Factor} = \frac{[EC] + [VCM] + 2 \cdot [EDC] + \frac{1}{3} \cdot [MC] + \frac{1}{6} \cdot [AC]}{\%C_2H_4 + (\%C_2H_6 \cdot 85)} \quad (4.12)$$

The concentrations of chlorine components as shown in equation (4.12) are in molar ppm and ethylene and ethane is in molar %, all measured at outlet of the reactor A and B. The concentration of EDC and AC are negligible and they are not considered in the formula used in DCS. I-factor, which is a critical indicator empirically characterizing the total chloride effect on the catalyst surface is monitored in the plant and controlled by advanced process control layer. Nominator of the formula elucidates the effective chlorine impact for each chlorinated components whereas the denominator shows the sweeping degree of ethylene and ethane concentrations having significant influence on chlorine compounds on the surface of the catalyst. In the industrial model, for the sake of simplicity, all the components in the nominator will be considered as VCM owing to the fact they are acting in a particular way. This is the reason why it was found unnecessary that rest of the chlorine components take separately in the design of experiments.

In optimal design performance evaluation, there are three common criteria: G-efficiency, normalized logdet ($X'X$) with respect to total number of model terms (p) and runs and condition number. G-efficiency compares the efficiency of a D-optimal design that of a fractional factorial design. G-efficiency at the 100% is the upper limit and designates that a fractional factorial design was obtained. The recommended range for the G-efficiency in D-optimal design lies between 60–70%. The condition number is the

ratio of the largest to smallest singular value of X (i.e. the design matrix). In other words, it is a measure of sphericity. Here, a value of unity is the ideal limit and denotes orthogonal design in coded factor variables. From the alternative design candidates, the final design is the one that has the closest normalized logdet (normlogdet) to zero [103]. In our design, chosen optimal experiments of 32 runs out of 275 runs have quite good agreement with three of the above-mentioned criteria as shown in Table C.3 in the Appendix C section. G-efficiency was 67.35% within the recommended range. The normlogdet was -0.394, which is close to zero and this design has the lowest condition number of 16.49.

As shown in Tables C.1 within the loading #2 and 3 relating to Set#1, there remained 31 executed experiments out of 32 which are automatically generated based on a D-optimal design. On the grounds that thermal runaway occurred in the last experiment of catalyst loading #2 which results in early termination of the experiment. This event attributed to the lack of concentration in methane (8.26%) and absence of VCM (0 ppm). The most important deduction that could be made from the experiments in Set#1 is that DoE approach should not be directly applied to the reaction system regardless of having substantial priori knowledge on the process. However, 31 out of 32 experiments had been carried out with no trouble, albeit some sort of inconveniences and these experiments were used in the parameter estimations.

4.4 Data Reconciliation and Experimental Analysis

Data reconciliation (DR) of the GC measurements was also necessary for lab-rig reactor like industrial reactor. This necessity stems from the fact that mass and energy balances are not always consistent due to errors in instrumental measurements. These types of errors are often referred to as gross errors [166]. Random errors follow normal distribution and generally least of squares method is satisfactory to weed them out from the data set. Nevertheless, gross errors which are attributed to instrument failure, calibration errors, leaks or human intervention do not follow a statistical distribution. In most cases, statistical hypothesis testing methods (e.g., Global Test, Bonferroni Test, Generalized Likelihood Ratio Test) are practiced to detect gross errors. In particular, DR is an established standard for on-line real time optimization. Inlet and outlet compositions of the reactor should obey to the rules of material and energy balance.

Most importantly, the material balance is a sine qua non for the accuracy of the following steps [167-171].

For laboratory experiments, data reconciliation sequential steps that are excel-based were developed in a custom manner. Sample calculation for one GC trial belonging to the 33rd experiment in catalyst loading #4 is shown in the Appendix D. These steps are explained as below:

1. Correction factor design for changes in moles that is based on two terms:

The molar volume of the product gas is somewhat less than that of the feed gas due to the fact that moles are not conserved in the reaction system. For this reason, it is required to calculate the dry-basis volume shrinkage factor. The first term accounts for the changes in the EO concentration. Since moles are not conserved, where 1.5 moles of reactant is converted to 1 mole of EO in the partial oxidation reaction. The second term accounts for water that is unable to measure in the GC but calculated from the amount of CO₂ produced in the total oxidation reaction instead. The calculated water amount serves as the basis for the dry-basis calculations.

2. Calculation CH₄ outlet molar fraction and GC concentration sum: It is based on the CH₄ fraction in the inlet and the correction for changes in moles based on step 1. By using reconciled CH₄ molar concentration regarding to overall molar change in the reaction system, concentration sum of outlet GC components (%) recalculated by taking helium gas into account. Nevertheless helium is not detected in the GC due to the fact that it is concomitantly carries gas, it has a diluting effect which in turn gives rise to change GC throughput concentrations.

3. Execution of carbon balance: Calculations are based on inlet and outlet fractions corrected for changes in moles based on step 1. There are 2 moles of C per mole of C₂H₄ and 1 mole of C per mole of CO₂. The difference between the corrected outlet and inlet moles are calculated. In this stage, the unmeasured trace amounts of byproducts including carbon (e.g., formaldehyde, acetaldehyde) were not taken into consideration.

4. Calculation of reconciled C₂H₄, EO, and CO₂ concentrations: Molar concentrations of these three gases are corrected based on the carbon balance in step 3. It must be noted that step 1 uses the original EO and CO₂ outlet

concentrations measured directly from the GC system and have not yet been reconciled. These values are reconciled by repeating steps 1–4 using an iterative procedure in order to bring the error in the carbon balance to zero. It is apparently seen that the procedure with three iterations in total is satisfactory as long as carbon balance error is considerably minimized.

- 5. Normalization:** In this step, normalization, which is widely used in chromatographic analysis, was applied to methane by using the reconciled concentrations of the carbonaceous components [172]. CH₄ molar concentrations in the GC outlet are normalized to CH₄-free fraction consisting of final C₂H₄, EO, CO₂, and O₂ compositions coupled with total helium molar concentration in order to sum up to 100%. Final compositions except O₂ are calculated with regard to the second iteration whose reconciled composition values make carbon balance error zero in the third iteration. Final concentration of oxygen is calculated by using the ratio of reconciled and nonreconciled ethylene for the reason that oxygen balance is not applied to O₂ measurements.
- 6. Calculation of conversions and component-based errors:** C₂H₄ and O₂ conversions are calculated based on the inlet and consolidated outlet composition values in step 5. After being calculated conversions, correction factors based on molar changes are multiplied with reconciled ethylene and oxygen compositions. Eventually, error analysis was done in order for comparing with reconciled and non-reconciled concentration of the components.

For the sake of comparison of reconciled experimental data, it was delved into the effects of seven unique criteria on conversion and selectivity under the similar circumstances. These are catalyst amount, ethylene over oxygen ratio, CO₂ and VCM feed concentrations, total flow rate, center point experiment for monitoring catalyst maturity and total reactor pressure. In addition to these criteria, ethylene oxide conversion was also investigated. It is important to note that there observed water accumulation that is knocked down in the pot right below the reactor after each reactor demounting. Therefore it is assumed that very low amount water reached to GC along side the pipeline down the reactor. Another import point to notice is that recorded catalyst bed temperatures are also taken into account in the lab-rig reactor model. However, in figures, furnaces set temperatures are reported. All related figures are in

Appendix E. Apart from these, uncertainty between catalyst loadings was calculated with respect to small sample size confidence interval of 95% in Table 4.8.

Table 4.6. Error analysis based on standard experiment between catalyst loadings.

Standard experiment with unique identifier	Ethylene conversion	Oxygen conversion	EO/CO₂ selectivity
4_1	6.47	35.90	67.85
6_1	7.70	41.62	65.56
7_1	7.49	41.72	65.48
Calculation of standard error of mean			
Mean	7.22	39.75	66.30
Standard deviation	0.66	3.33	1.35
Sample size	3	3	3
t-dist coeff ($\alpha_{st}=0.05$)	4.30	4.30	4.30
Standart error of mean	1.65	8.28	3.35

According to the results in Table 4.8 which are belonging to the first experiments of catalyst loadings with same conditions, ethylene conversion has the lowest standard error of mean among other key process indicators. As is the analysis in Table 4.8, unique identifies (e.g., 4_1, 6_1, 7_1) which are the combinations of catalyst loading# and experiment# are used in gPROMS in order to define each experiment of each loading.

The most underlying information hidden in Table 4.8 is that the catalyst activity is changing significantly with every loading of the catalyst. Similar situation was observed in the literature as well [57, 95]. For this reason, initial activity parameter (catalyst_activity_ref) that is peculiar to each catalyst loading is created. This parameter is also dependent on the type of reaction mechanisms (main and side reactions) which in turn evolved as a brand new parameter entitled by catalyst_activity_ref_per_reaction in gPROMS custom model environment. However, this variable was only used in the estimations for plant reactor, where the activity will be estimated separately for the main reaction and side reaction whereas the other kinetic parameters will be fixed to their optimal estimates. Therefore, regarding to the kinetics based on lab model, these

variables were fixed to 1 since the aim is to estimate the rate constants (adsorption and kinetic) and activation energies rather than estimating catalyst activity for each reaction. Each of catalyst loading is set as a variable inside catalyst activity in lab reactor model. Nested if/else conditional statements in the model are then used in order for assigning correct value to catalyst activity that would multiply the reaction rate. In this regard, the activity of catalyst loading#1 was fixed to 1 which means that activity parameters for other loadings are relative to this specific loading. All in all, this method would allow us to estimate the catalyst activities for different catalyst loadings separately. Moreover, apart from their intrinsic functions, these parameters are the basis of deactivation model (i.e catalyst maturity monitoring) for lab-rig reactor.

Two different catalyst amounts have been used throughout the experiments. Catalyst of 0.1g was used before catalyst loading#4 afterwards catalyst amount increased to 0.2 g in the catalyst loadings of #4-7. In Figure E.1, it is seen that ethylene and oxygen conversion are both increasing with catalyst amount but in almost all ethylene over oxygen ratios except the one for 4.95, percent change in oxygen conversion is much higher than that of ethylene conversion which could be attributed to unparallel consumption of oxygen in total oxidation. On the other hand, there is no significant change in EO/CO₂ selectivity due to catalyst increase.

Table E.2 shows how much ethylene and oxygen conversions have changed with temperature at different fixed C₂H₄/O₂ ratios. The aim of this change is to reveal temperature dependencies that are unique to various ratios (ethylene to oxidizer) in broader range than in the industrial process so as to use them for kinetic model determination. At higher ethylene concentrations in the ratio, ethylene conversion is gradually tend to decrease whereas oxygen conversion is increasing to some extent which is very near to maximum detected C₂H₄/O₂ ratio in the industrial reactor during Start-of-Run (SOR) period in Table C.2 then it bounces back from a peak value. The similar trend also observed in the percent change of oxygen conversion in Table E.1. This fashion could be explained by the lack of oxidizer with respect to ethylene and attributed to the loss of optimum mixing ratio between ethylene and oxygen. In our experiments, inlet oxygen concentration is corresponding to 6.30% at the lowest C₂H₄/O₂ ratio while the oxygen concentration in the lab-reactor inlet is set to 2.33% at the highest C₂H₄/O₂ ratio. As a matter of fact, the most frequently encountered C₂H₄/O₂ ratio in the industrial reactor inlet for SOR timeframe which is deemed to be optimum mixing proportion is in the range between 3.5-4.5% which leads to the nominal ethylene

and oxygen conversion that are 9-10% and 30-40%, respectively. Ethylene conversion also decreases because of the fact that temperature increase is not able to compensate it due to the decrease in oxygen. Aside from these facts, it does not find any reasonable and comparable relationships for EO/CO₂ selectivity within the context of the alleged criteria like the one in Table E.1 (b). Middle point furnace set temperature (237 °C) is not included into this comparison on the grounds that related in a multitude of experiments are not conducted at the same conditions like others.

As can be seen from Figure E.3 and E.4, CO₂ feed in the reactor inlet apparently affects on both conversion and selectivity parameters. Ethylene and oxygen conversion are decreasing because of the inhibition effect of CO₂ which does not have equal influence on main and side reactions. Inhibition rate of total oxidation is higher than partial oxidation reaction. For this reason, EO/CO₂ is increasing with introducing more CO₂ into the reactor. At very low furnace set temperatures (219 °C), it observed that percent absolute change in conversions is much higher than other temperatures (237 and 250°C).

Another critical experimental factor is vinyl chloride monomer (VCM) as a reaction moderator which is introduced into the reactor in ppm levels. In our study, five different VCM concentrations were used as shown in Figure E.5 and E.6. At all temperature levels with increasing VCM concentration from 0 to 1 ppm, ethylene and oxygen conversion are both lowering whereas EO/CO₂ selectivity is increasing. Percent changes in conversions are decreasing with increasing temperature while that of selectivity is increasing. At the inlet of the plant reactor, VCM is not found in a single form as explained before. Therefore, the amount of total chlorine compounds in ppm should be the main basis for industrial reactor model. In the lab-reactor, we were able to increase VCM up to 1 ppm whilst total inlet of chlorine components is about 2.5-3 ppm. This situation is the one of the reason of why kinetic model derived from lab-data could not be directly scaled to the industrial reactor. The reaction rates need to be adjusted based on the plant data.

Regarding to flow rate variation from 65 sccm to 85 sccm as shown in Figure E.7, it is not regarded any significant change in neither conversions nor selectivity values. When it comes to mentioning about catalyst maturity, the experiments (i.e. center point experiment) that have same standard conditions were executed at some certain time intervals for each catalyst loading. Figure E.8 implies that catalyst activity is not being maintained during the course of the experiments for catalyst loading#4.

This could not be counted as a deactivation phenomena in real terms because EO/CO₂ selectivity is increasing in Figure E.8 (b) whereas ethylene and oxygen conversions are both decreasing and on the top of that this happens exceptionally in an agile manner in the lab rig reactor. Normally, deactivation of the commercial catalyst is very sluggish occurrence in the industrial plant that extends over a 4-year period of time.

Total reactor pressure was also investigated by increasing the temperature up to 10 barg as illustrated in Figure E.9. As it is known from literature [19, 61], pressure has some effects on conversion and selectivity even if not as substantial as compositions because the reaction is not reversible. In our case, nevertheless the initial observed pattern leans toward to increase conversion and selectivities together up to 4 barg as anticipated in contrast to the study done by Kestenbaum et al. [173], after that it is not obtained reasonable values beyond 4 barg. O₂ composition measurements are not consistent with EO and CO₂ measurement. Put it differently, measured O₂ at the outlet of the reactor is too high for the amount of EO and CO₂ produced. In line with this unexpected trend, standard error of means increased abnormally. Notwithstanding being failed to pinpoint the main cause, this erroneous fashion could be attributed to the accumulation of oxygen inside the molsieve column in GC because of the sudden increase in oxygen level. High pressure experiments are not repeated due to the fact that pressure effect could also be taken into account at the stage of the reactor modeling by using industrial data having high pressure. Needless to say, pressure in the industrial reactor of our interest is keeping at a very narrow band (15.5-16.5 barg). As a result; all the experiments that will be utilized in parameter estimations were carried out in atmospheric pressure.

Last of all, effect of temperature was examined upon ethylene oxide conversion in order to construct the kinetic model for ethylene oxide combustion which is designated as “side reaction_2” in the further sections. Figure E.10 tells us that side reaction_2 becomes more significant at higher temperature. The recorded average catalyst bed temperatures that are corresponding to furnace set temperatures are 249.1, 257.1, 267.9, 278.6 and 289.5 °C in an ascending order. In the close vicinity of 260 °C in bed temperature, percent change in EO conversion doubled which approximately ended up with 5.7% conversion. After 260 °C, conversion exponentially starts to increase with temperature. For this reason, neglecting EO conversion at higher temperature is not a good assumption from the modeling point of view for those who want to get a robust kinetic model that is applicable over a wide range of temperature.

In order to decouple the EO conversion in GC from the conversion due to ethylene feed, experiments as part of this purpose were designed without fresh ethylene feed. In addition to this, EO conversion experiments are conducted without VCM and CO₂ inlet flow so as to achieve higher EO conversions because the EO gas tube only contains EO of 1.23% with the helium ballast. Therefore, it requires getting concentrated EO inlet stream without decreasing the total flow rate.

4.5 Parameter Estimation and Kinetic Model Discrimination

As was well known in the literature, parameter estimation, which is a sort of optimization problem, is a prerequisite to discriminate the model candidates in order for using the most promising one in the industrial scale model. This stage not always ends up with one superior model if some of candidates turn out to be very close kinetic parameters from the point of statistical view. The most underlying challenges in parameter estimation are the computational capabilities of the solver and statistical accuracy of the parameters which in turn overcoming of these would make the objective function lead to global optimum. Total number of parameters to be estimated that is definitely dependent on a case is a critical decision maker in choosing the most appropriate software [82]. In our case, we obliged to estimate up to 48 parameters while setting few of them at a fixed value in certain instances. This is the one of the reasons why we used gPROMS in this project.

Parameter estimation in gPROMS is based on the maximum likelihood estimation (MLE) algorithm in equation (4.13) as shown below [97]:

$$\Phi = \frac{N_{meas}}{2} \ln(2\pi) + \frac{1}{2} \min_{\theta_{s,m}} \left\{ \sum_{l=1}^{NE} \sum_{m=1}^{NV_l} \sum_{t=1}^{NM_{lm}} \left[\ln(\sigma_{lmt}^2) + \frac{(\tilde{z}_{lmt} - z_{lmt})^2}{\sigma_{lmt}^2} \right] \right\} \quad (4.13)$$

where;

Φ : *Objective function*

N_{meas} : *Total number of measurements taken during all the experiments*

$\theta_{s,m}$: *Set of model parameters to be estimated*

NE : *Number of experiments performed*

- NV_l : Number of variables measured in the l^{th} experiment
- NM_{lm} : Number of measurements of the m^{th} variable in the l^{th} experiment
- σ_{lmt}^2 : Variance of the t^{th} measurement of variable m in experiment l
- \tilde{z}_{lmt} : t^{th} measured value of variable m in experiment l
- z_{lmt} : t^{th} predicted (model) value of variable m in experiment l

The maximum likelihood estimation (MLE) method aims to find the most probable parameters that maximize the likelihood function, which is the probability for a certain probability density function (pdf). This approach is essentially the reverse of what is accomplished in ordinary least squares estimation (OLE). MLE is considered to be a more powerful technique than OLE due to its lower asymptotic error and generalizability for regression when the appropriate pdf is chosen. gPROMS uses the Gaussian distribution as a pdf [174-175]. In our reactor system, the standard deviations of gas components are not equivalent. For this reason, the weighted least squares objective function is preferred over the normal least squares objective function in the cost function of the objective function. Uncertainty that belongs to known measurements can be regarded as the variance of measurements. Sensors are devices that take experimental measurements and the source of the uncertainty of the measurement is directly related to the measurement technique of the sensor. Many times, sensors typically measure more than one variable. For example, the thermal conductivity detector (TCD), which is a sensor in the GC system, measures multiple components streaming into the GC column.

Table 4.7. Variance models in gPROMS [97].

Variance model	Mathematical Expression
Constant variance	$\sigma = \omega$
Constant relative variance	$\sigma = \omega \cdot (z + \varepsilon)$
Heteroscedastic variance	$\sigma = \omega \cdot (z + \varepsilon)^\nu$
Linear variance	$\sigma = \alpha \cdot z + \beta + \varepsilon$

The residual error is the difference between the values measured experimentally and the values predicted from the model. The errors of the measurements are assumed to be statistically independent and normally distributed with a mean of zero. Variance

models are used for the formulation of the residuals as mathematical descriptions, which are intrinsic to the system. gPROMS uses four different variance models as shown in Table 4.7.

$$\sigma^2 = \sigma^2(z_{mp}, B) \quad (4.14)$$

where z_{mp} is the model prediction of the measured quantity and B is a set of parameters (4.14), which contains omega/alpha and gamma/beta parameters.

The objective function (Φ) that is used in parameter estimation as shown in equation (4.13) is solved by a nonlinear sequential quadratic programming solver (NLPSQP) which is one of the solver in mixed integer nonlinear programming (MINLP) provided by gPROMS. This solver uses four tolerances to decide whether or not a local optimal solution has been reached. These tolerances include the feasibility, complementary, Taylor, and optimization tolerances. The algorithm continues until all the tolerances are satisfied and then terminates to give the optimum values for the estimated parameters [97].

It is of great importance when or when not to eliminate model terms or parameters. There are three main criteria in the evaluation of model terms that are used in gPROMS. Once such a sound consensus for these three is formed, it is concluded that estimated parameters are statistically significant. The so-called three criteria are listed and explained as follows:

1. If a 95% t-value for an estimated parameter is greatly below the reference t-value, this indicates that the available data from these experiments may not be sufficient for the determination of that parameter. However, if the value is only slightly below the reference t-value, then the estimated parameter is considered acceptable.
2. If final value of the estimated parameter is significantly larger than its standard deviation, then the estimated parameter is considered acceptable.
3. In the correlation matrix, the off-diagonal elements close to 1 or -1 indicate a strong correlation between two parameters. In the correlation matrix, elements close to 0 are desired.

Table 4.8. Variance models and parameters that are used in parameter estimations.

Sensor Group #	Sensor Variable	Variance Model Type	Model Parameters		
			α	β (mol%)	ω (%)
1	Flowsheet.outlet_composition("CO2")	Linear	0.02	0.05	-
2	Flowsheet.outlet_composition("ETHYLENE OXIDE")	Linear	0.03	0.02	-
3	Flowsheet.outlet_composition("ETHYLENE")	Linear	0.02	0.1	-
4	Flowsheet.outlet_composition("OXYGEN")	Linear	0.03	0.1	-
5	Flowsheet.conversion(1,"ETHYLENE")	Constant	-	-	100
6	Flowsheet.conversion(1,"OXYGEN")	Constant	-	-	100
7	Flowsheet.outlet_composition("ETHYLENE OXIDE")	Linear	0.06	0.04	-

In Table 4.8, variance parameters that are used for the parameter estimation sets are shown. There are two types of variance models in our case: Linear variance model and constant variance. The linear variance model (LVM) was chosen as a variable model for outlet GC concentrations of interest excluding methane because the residual term (ϵ) is assumed to be independent from the actual measured value. Therefore, the model providing for the error term in LVM is well-defined and a decoupled function, which is more appropriate with the GC calibration approach than the constant relative variance model (CRVM), in which the error in all measurements is directly proportional to magnitude of measured values. In the former model, the alpha (constant relative term) and beta (constant term) parameters are added into the variance model parameters to be estimated. In LVM, beta terms are generally fixed at a value of 0.05% mol as deemed by best practice. The beta values in LVMs are just fixed terms in the linear dependencies to protect the weighted contribution of low concentrations to go considerably high values which is more likely to happen in CRVM. Variance parameters are defined separately for each gas component in the experimental set. Alpha terms are found by constructing GC calibration model in gPROMS whereas beta terms are heuristically determined.

Table 4.9. Control and measured variable for experimental entities in gPROMS.

Control Variables	
Variable Name	Control Type
Flowsheet.catalyst_loading_no	Time-invariant
Flowsheet.mass_of_catalyst	Time-invariant
Flowsheet.bed_temperature("10 mm")	Piecewise-constant
Flowsheet.inlet_flow_rate("CO2")	Piecewise-constant
Flowsheet.inlet_flow_rate("ETHYLENE")	Piecewise-constant
Flowsheet.inlet_flow_rate("ETHYLENE OXIDE")	Piecewise-constant
Flowsheet.inlet_flow_rate("HELIUM")	Piecewise-constant
Flowsheet.inlet_flow_rate("METHANE")	Piecewise-constant
Flowsheet.inlet_flow_rate("OXYGEN")	Piecewise-constant
Flowsheet.inlet_flow_rate("VCM-He")	Piecewise-constant
Flowsheet.inlet_pressure	Piecewise-constant
Measured Variables	
Flowsheet.conversion(1,"ETHYLENE")	
Flowsheet.conversion(1,"OXYGEN")	
Flowsheet.outlet_composition("CO2")	
Flowsheet.outlet_composition("ETHYLENE OXIDE")	
Flowsheet.outlet_composition("ETHYLENE")	
Flowsheet.outlet_composition("OXYGEN")	

The function of ethylene and oxygen conversions in Table 4.8 is just for monitoring because of the fact that it is desired to give less weight to the EO measurements which have larger errors in comparison with others. That's why constant variance model is used by setting the lowercase omega parameter to 100%. The reason why there exist two different EO outlet compositions is about having different standard deviations throughout the experiments. Because capillary columns in gas chromatography were exchanged with the new ones after the catalyst loading #5 owing to the fact that column bleeding trouble bursted. This fact gives rise to some changes in areas which in turn there are some minor changes in all compositions but ethylene oxide in calibration that were definitely taken into consideration.

It should be defined the status of the experimental conditions and the experimental control strategy which are essential for executing parameter estimations. In our experimental domain, the process and composition values were changed in a dynamic manner for each catalyst loading as does in perturbation activities for the models used in model-based advanced process control layers where process parameters are changed by the help of systematic step size manipulations. Put it differently, each catalyst loading consist of many sub-experiments. For this reason, it would be better to sort all the experiments for each catalyst loading with regard to the elapsed unit time which could be done in dynamic initial conditions in gPROMS rather steady-state initial conditions. There are three types of experimental control strategies in gPROMS: Time-invariant control, piecewise constant control and piecewise linear control. The first provides a single or constant value for a quantity which will be the same for the duration of experiment. This type control could be used both for steady-state and dynamic conditions. The second one is piecewise constant control which enables to be entered multiple variable values for a quantity that is desired to be hold a different constant value for specified time intervals throughout the experiment. The third one is for the case that value of the quantity changes linearly during a specified time frame between a start and final values. The last two are suitable for dynamic conditions.

As can be seen from Table 4.9, control types of catalyst loading number and mass of catalyst are set as time-invariant whereas inlet flow rates of reactant and inert gases and process parameters (temperature and pressure) were exposed to change during the course of the each loading which necessitates that control type should be piecewise-constant. In addition to this, key measured variables of interest are conversions of

ethylene and oxygen and outlet composition values of the main reaction components (i.e, ethylene, oxygen, carbon dioxide and ethylene oxide).

In the literature review part (Table 2.1), kinetic models from the past to present were investigated. Ethylene oxide kinetic experiments could be done either with lean or rich oxygen inlet concentrations in the direction of the goal of the project. With this mind, models that were constructed under the rich oxygen conditions were eliminated on the grounds that our intention is to create a model for our process which is working at lean inlet oxygen conditions. This provided us with good initial conditions in the very early stage of the parameter estimations. So, eight different kinetic model candidates were defined to be tested as illustrated in Appendix (Table F.1). 6 kinetic models out of 8 are extended version of the kinetic models that exist in the literature. The reason of the extension of the models is based on (i) adding kinetic constants for VCM moderator, (ii) side reaction for ethylene oxide oxidation (iii) making the models similar in conformity of the postulation of considering the fact that main and side reactions take place at different active sites and (iv) adding CO₂ adsorption kinetic constant term into the denominator. Because we conducted kinetic experiments particularly for discovering VCM adsorption kinetics in order to embed it into the structure of model candidates. Furthermore, EO oxidation experiments performed for determining the kinetics of side reaction₂. For these reasons, the common features for all kinetic models but Petrov et al. are that they all have EO oxidation kinetics with a separate model expression named as r_3 , VCM adsorption kinetics and different catalytic active sites with regard to main and side reaction₁ and lastly CO₂ adsorption term. Model taken from Petrov et al. was used as it is. One of them has been newly generated as a hybrid model by taking Westerterp₁ as a basis. That's why it was entitled as modified Westerterp_{1a}.

Adsorption constants of ethylene, oxygen, carbon dioxide, water and ethylene oxide were included in all models of Westerterp et al. but model (1) which was further modified by adding the missing oxygen adsorption term into denominator under the name of model (1a). Originally, models of Salmi et al. and Petrov et al. are founded on ethylene and oxygen adsorptions. In our study, Salmi's model was extended with adding CO₂ adsorption constant term. Gu et al. takes adsorption of CO₂ and co-adsorption of O₂ into account whereas Gan et al. consider adsorption of oxygen and co-adsorption of O₂ and CO₂. In regard to the VCM effects, Petrov et al. contemplated the effects of DCE as a kind of reverse reaction in the numerator of the model. Gu et al. takes the VCM effect in a separate term that is multiplied with the denominator of the kinetic model

equations. Other models do not include effect of moderator. Therefore, we added a competitive adsorption term of VCM.

Designation of the model terms regarding to the oxygen in Table F.1 was not implemented in accordance with the adsorption form of the oxygen such as associative or dissociative oxygen. In this regard, it was completely stick to the assumptions that had been made by the authors in the original studies.

Regarding to the issue of catalytic active site, all kinetic models except the ones constructed by Westerterp et al. did not use different adsorption kinetic constants for each reaction which means that main reaction and side reaction₁ occur on the same catalyst site. However, this assumption is not reflecting the reality. For this reason, we extended all kinetic models but the model of Petrov et al. by adding different adsorption kinetic constants for two types of the reactions as well. Same adsorption kinetic constants as main reaction or side reaction₁ are used for that of side reaction₂. Rate equation for EO oxidation in the Petrov's model is defined as the same adsorption kinetic constants as side reaction₁. For the models of Gan et al., Gu et al. and Westerterp et al. (model 3), adsorption kinetic constants of side reaction₂ are same as side reaction₁. In the rest of the four models (i.e, Salmi et al., Westerterp et al. (model 1, 1a and 2)) adsorption constants of the main reaction are used for that of side reaction₂.

According to many articles issued by Van Santen et al [43, 176], single-site Langmuir-Hinshelwood (L-H) was highly unlikely because the C₂H₄ molecule is very likely to bind to two sites before reacting with surface oxygen. Eley-Rideal (E-R) mechanisms were of very low probability with respect to Langmuir-Hinshelwood mechanisms because of the probability of a gas phase molecule directly striking a surface-adsorbed molecule and then producing a product on the surface was extremely rare. The promoters can also have effects on the surface mechanisms; however, because it is not practical to model the surface reactions involving the trace amount of surface promoters, it is better to model based on the known parameters such as C₂H₄ and oxygen adsorption mechanisms and simply perform empirical corrections by including their weights into denominator of the rate equations as we did.

If the catalyst is pure Ag like our case, then the possibility of an E-R mechanism can be eliminated. Thus, if the surface is Ag₂O, then the silver surface is already completely oxidized and even if the possibility is rare, an E-R mechanism involving gas phase ethylene striking surface-bound oxygen atoms of the Ag₂O can still

occur. The possibility of the E-R mechanism whereby C_2H_4 binds to the surface and afterwards reacts with O_2 in the gas phase could be also eliminated due to the very low odds.

In dissociative adsorption of O_2 , the gas molecule may first bind to the surface molecularly. After some time, this molecular can then dissociate into two separate atoms. This dissociative adsorbed O_2 mechanism can only occur in a L-H mechanism. In an E-R mechanism, the surface is completely saturated with oxygen and gas phase ethylene directly reacts with these surface-bound oxygen atoms. It must be noted that the molecular (associative) adsorption of O_2 is quite rare (most often favoring dissociative adsorption) just like the probability of the Eley-Rideal mechanism. There is a possibility of sub-surface oxygen taking place in reactions; however, the likelihood of these interactions is much less common than those involving surface oxygens. Such sub-surface oxygens have a tendency to change the energy of the surface lattices.

Dissociative and molecular mechanisms can include both adsorption – desorption and surface reactions collectively, thus to mention that a surface reaction occurs via single-site or dual-site mechanisms may result in confusion if one considers these mechanisms as being adsorption – desorption alone. Surface reaction rate mechanisms need to be derived considering that the surface reaction can also involve single and dual-sites mechanisms.

The reason why many adsorption – desorption mechanisms require multiple sites is that these additional sites allow for easier dissociation of the bound molecules where fewer sites would not have been able to break the bonds due to high energy barriers. Multiple site mechanisms often allow for the formation of an oxometallic cycle (OMC) on the surface. Many times, this intermediate is formed for reactions where the reactants are large molecules (e.g. long HC chains), which require multiple sites. Such is also the case of EO formation from C_2H_4 and O_2 .



In a single-site surface reaction mechanism of the L-H type, two species, A and B, typically bind to adjacent sites. However, when a reaction occurs, one species

combines with the other species on its site leaving a single vacant site behind. Once a product, AB, forms on the occupied site, this species then desorb from site, leaving behind that site vacant as well. In a dual-site surface reaction mechanism of the L-H type, two species, A and B, typically bind to adjacent sites. Then they react forming the surface adsorbed product, AB, which is bound to two sites. Upon desorption, this AB desorbs from the two sites leaving them both vacant. Single and dual site surface reactions can be depicted in the reaction equations (4.15-4.16).

As a result, the models derived by using dual-site L-H mechanisms like Westerterp et al. yields much better statistical fits than E-R mechanism (Petrov et al.) as it happened in our study. As a rule of thumb, if the reaction system to be used in a well-structured kinetic model is specified with many proven process indicators such as product concentrations and VCM moderator, it is inevitable that the obtained model could be more reliable. It is noteworthy that most rate models are not fitted directly from first-principle expressions, but rather are empirically corrected when they would use for modeling large-scale unit operations.

$$k = k_0 * \exp(-E/RT) \quad (4.17)$$

$$k = k_{ref} * \exp\left(-\frac{E}{R} * \left(\frac{1}{T} - \frac{1}{T_{ref}}\right)\right) \quad (4.18)$$

One last manipulation attempted in the model was to re-parameterize the Arrhenius equation (as shown above) in order to independently estimate the two parameters, k_0 and E . Therefore, conventional Arrhenius equation (4.17) was converted into equation (4.18) which is reparameterized version of it. Since k_0 and E are highly dependent on one another as shown in the first equation (4.17), their correlation cannot be ignored. This is not desirable when seeking the true relationship and thus re-parameterization is generally applied to set apart these parameters in the Arrhenius equation. Reference temperature is generally taken to be the average temperature of the data set of interest [177-182]. T_{ref} was set to 250°C for our case.

$$-\frac{d\alpha}{dt} = k_{d_0} * e^{(-E_d/RT)} * (\alpha_0 - \alpha_\infty)^2 \quad (4.19)$$

On the subject of catalyst maturation, three different mechanisms were tested throughout the study. These are i) Based on cumulative production of EO and CO₂, plus poisoning by VCM ii) Based on sintering with same rate for all reactions and iii) Based on sintering with different rate for each reactions. The third approach gave statistically best result which means that there is significant difference in the deactivation rate for the main reaction and the side reaction. Because of the fact that selectivity is significantly increasing during the course of the each catalyst loading while conversion is decreasing, this tendency is explained as some kind of catalyst maturing. However, these changes in activity and selectivity could be only described by the catalyst decay which is only function of time, which is present in the sintering model as shown in equation (4.19) [45]. The effect of temperature and terminal activity, which is normally also present in sintering model, was not confirmed by the parameter estimation. The values for the temperature dependent parameter either went to 0 or were estimated with poor confidence which gives rise to the fact that deactivation model has two parameters in gPROMS: i) ACT.K_D_SINTERING (“MAIN REACTION”) ii) ACT.K_D_SINTERING (“SIDE_REACTION_1”) . These parameters are in the notation of gPROMS language. The second one is always higher than the first one. The activity of side reaction_2 is assumed to be the same as activity of the main reaction. However, this situation could not be interpreted that the mechanism of the deactivation in the lab data is sintering on the grounds that this is not a deactivation of the catalyst.

When it comes to parameter estimation for kinetic model discrimination, step by step procedure was followed by using subsets of experiments. Regarding to the works dealing with data-loading from excel to gPROMS Process Builder and outlier detection, gPROMS Formulated Products Utilities is utilized for the sake of ease of operation. We used all experiments except high pressure ones due to the erroneous behavior. There are 5 sequential steps as follows:

- **Step 1:** Experiments at 0 ppm of VCM and same feed compositions were chosen (in Table F.2 in the Appendix). The rationale in here is that the kinetics does not need to account for effect of VCM and the reaction order with respect to reactants and adsorbing components. As such, rate constants for the two reactions and activation energy for the two reactions were estimated assuming main reaction and only one side reaction leading to CO₂.
- **Step 2:** VCM adsorption constants and their temperature dependencies were found by the help of subset of experiments in Table F.3.

- **Step 3:** Experiments at 0 ppm of VCM and varied feed composition were chosen as illustrated in Table F.4. This allowed us to distinguish how various kinetic models could predict the yields for variable ethylene over oxygen ratio. In this step, first stage discrimination was done.
- **Step 4:** All experiments were included and adsorption constants of CO₂ were estimated.
- **Step 5:** All experiments in catalyst loading #6 and 7 with EO feed were included. In this step, it was decided whether denominator part of the EO oxidation rate equation is taking place on the same sites as the main reaction or the side reaction₁. Moreover, rate constants and temperature dependencies of EO oxidation were estimated in this step.

In Table 4.10, the quality of fits which are based on root mean square error (RMSE) of each four gas components shows that models from Westerterp et al. are fitting the experimental data better. This proves that two reactions should assume to take place at different active sites. As a result, kinetic models of Gan et al., Gu et al. and Petrov et al. were eliminated in this stage.

In the second stage of the discrimination process, step 4 and 5 were carried out. One more kinetic model generated entitled as “Westerterp et al. model (1a)”. In these last two steps, some mixed subsets were tested and further eliminations were executed in order to achieve the best-fit model.

Subset of experiments particularly belonging to catalyst loading 1, 4 and 6, which shows variations in feed CO₂ compositions at different furnace temperatures, was identified. These were used in finding out the adsorption rate constants and temperature dependencies for CO₂. This was repeated for each of the remaining kinetic mechanisms. As a result, the kinetic mechanisms of Westerterp et al. (model 3) were eliminated due to poor fits.

Subset of experiments from catalyst loading 6 and 7 were used to identify the influences of feed EO compositions at different furnace temperatures. In the vast majority of these experiments, ethylene feed was not introduced into the reaction system on purpose. These were used to find rate constant and temperature dependencies for the side reaction of EO oxidation. This action was again repeated for each of the remaining kinetic mechanisms. The structure of EO further oxidation took similar form with the existing main and side reaction.

Table 4.10. Results of the model discrimination at the first stage (i.e, in steps 1-3).

Kinetic Model	RMSE - CO₂	RMSE -C₂H₄	RMSE - EO	RMSE -O₂	RMSE Overall
Gan et al.	0.247	0.164	0.12	0.237	0.768
Gu et al.	0.19	0.165	0.125	0.259	0.739
Petrov et al.	0.212	0.161	0.11	0.36	0.843
Salmi et al.	0.2	0.152	0.125	0.229	0.706
Westerterp et al. - model 1	0.127	0.132	0.076	0.235	0.57
Westerterp et al. - model 2	0.141	0.132	0.074	0.251	0.597
Westerterp et al. - model 3	0.141	0.134	0.085	0.225	0.584

Table 4.11. Results of the model discrimination at the second stage (i.e, in steps 4-5).

Kinetic model	RMSE - CO₂	RMSE -C₂H₄	RMSE -EO	RMSE -O₂	RMSE Overall
Salmi et al.	0.237	0.306	0.121	0.348	1.012
Westerterp et al. - model 1	0.166	0.307	0.095	0.314	0.882
Westerterp et al. - model 2	0.212	0.318	0.097	0.306	0.933
Westerterp et al. - model 1a	0.156	0.304	0.106	0.346	0.912

Investigations identified that the most suitable denominator of the EO oxidation reaction was that of the main reaction. In line with this issue, reaction order of the side reaction₂ was assumed to be same as that of main reaction for all four remaining kinetic models tested in the second stage that includes reaction order terms (n_j or α_j and β_j). For this reason, the reaction order of main reaction and side reaction₁ were only estimated as seen in Table F.5 which belongs to the best fit model.

From Table 4.11, even though all models showed promising predictions to the measurements, it is clearly shown that models from Westerterp et al. are again most promising kinetic models as in the results of the first discrimination step. It can be concluded that all models predicted significantly larger adsorption of VCM for the side reaction, suggesting small effect of VCM on the main reaction and thus improving selectivity. Among models of Westerterp et al, the one that has the lowest RMSE is Westerterp et al._model 1 which has overall RMSE of 0.882. Parity charts of the main reactor outlet components are illustrated in Figure F.1-4 in the Appendix. Parity chart shows how predicted outlet gas concentration is far away from the experimental measurement. The data used in parity chart is also used in RMSE, which is also an important statistical indicator as described in equation (4.20). The model with less RMSE portends to the fact that its parameters fit much better than others from the statistical point of view.

$$RMSE = \sqrt{\sum_{i=1}^n \frac{(m_i - p_i)^2}{n_{RMSE}}} \quad (4.20)$$

$$n_{RMSE} = \text{total \# of experiments in use}$$

Regarding to apparent activation energies in Table F.5, it is seen that three of them are higher than critical limit of interphase activation energy which is about 20kJ/mol [94]. Activation energies of partial oxidation, total oxidation and ethylene oxide oxidation that were found in this study are 88kJ/mol, 64.5 kJ/mol and 107 kJ/mol, respectively.

4.6 Lab-Rig Reactor Modeling

Owing to the fact that model-targeted experimentation approach is used throughout the study, reactor model is modeled in gPROMS in order to run parameter estimations over this first-principle model.

First of all, inlet and outlet reaction components are specified in Multiflash. There are eight gas components in the reaction system. Seven of them are inlet gases whereas water is only a byproduct produced as a result of total oxidation. Therefore, the dominant phase in the reaction system regarding to feed and product concentrations is gas phase except for the fact that there is a small amount of water which is trapping in the pot after the reactor.

$$a_i = a_{ci} * (1 + \kappa_i (1 - \sqrt{T/T_{ci}}))^2 \quad (4.21)$$

$$\kappa_i = 0.48 + 1.574 * \omega_i - 0.176 * \omega_i^2 \quad (4.22)$$

ω_i = *acentric factor*

Cubic equation of states are most demanded in refinery and petrochemical applications because these type of equation of states require limited pure component data and are robust. Thanks to the cubic equation of state, equation of state parameters can be fitted to reproduce both the saturated vapor pressure using an existing databank correlation and the saturated liquid density at 298K or $T_r=0.7$ by using Peneloux method. There are two type of cubic EOS that is most frequently used: Peng-Robinson (PR) and Redlich-Kwong-Soave (RKS). In equations (4.21-4.22), equation of states parameters relating to RKS EOS are shown. In this study, we used advanced RKS which is improved by Peneloux correction in which “a” parameter in RKS is fitted to vapour pressure by using the Van der Waals 1-fluid mixing rules [100].

The SuperTRAPP method is a predictive extended corresponding states model where propane as a reference fluid is used. It could be predicted viscosity and thermal conductivity of petroleum fluids and well-defined components over a wide range of thermodynamic states from the dilute gas to the dense fluid. SuperTRAPP method was used in our model [100].

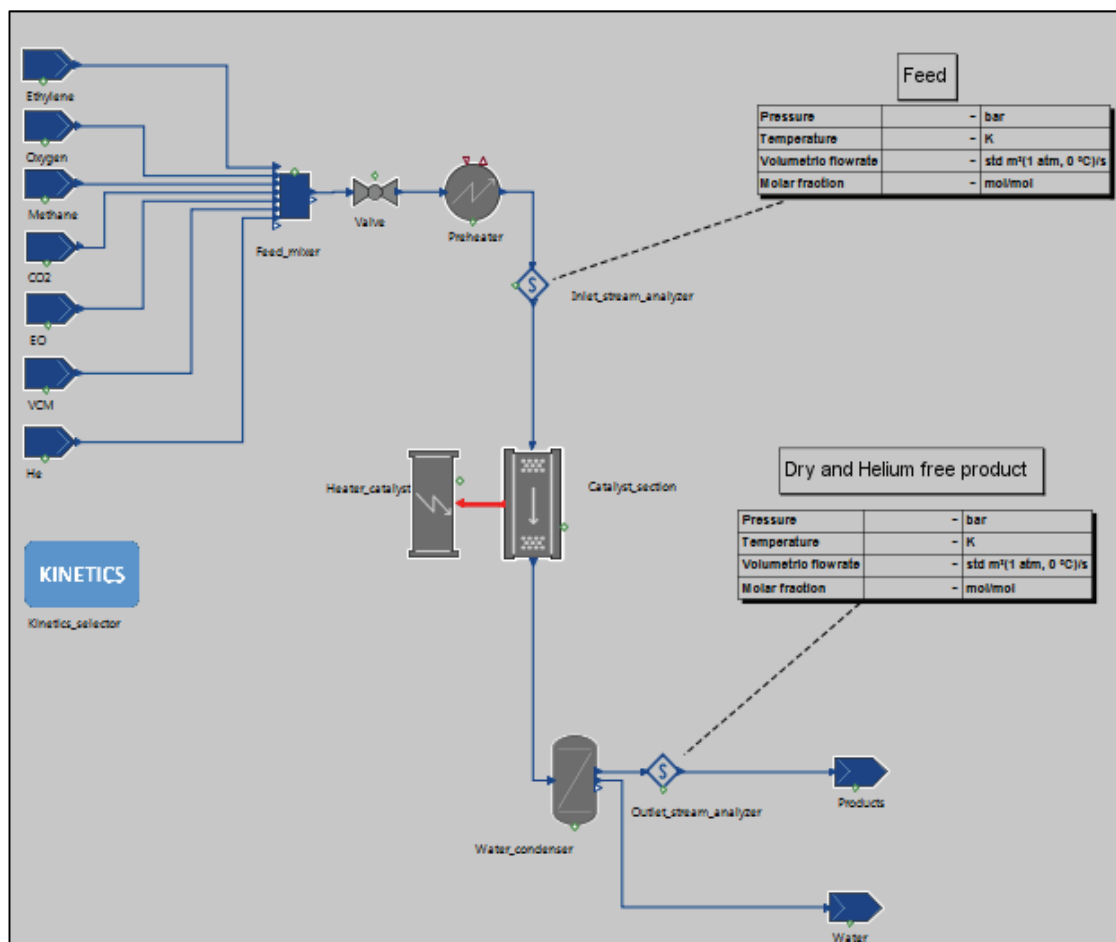


Figure 4.23. Lab-rig reactor system model in gPROMS Process Builder.

Phase Gas

Diffusivity calculation From Fuller method

Gas phase

☒ Bulk component METHANE

☒ Reference pressure 1.0 bar

☒ Reference temperature 298.15 K

☒ Reference mass fraction ☐ Uniform for entire array ☒ Per element

Components	OXYGEN	0.079
	METHANE	0.299
	ETHYLENE	0.262
	CO2	0.12
	ETHYLENE OXIDE	0.018
	VINYL CHLORIDE	0
	WATER	0
	HELIUM	0

kg/kg

☒ Diffusion volumes

Components	OXYGEN	16.3
	METHANE	25.14
	ETHYLENE	41.04
	CO2	26.9
	ETHYLENE OXIDE	47.15
	VINYL CHLORIDE	78.4
	WATER	10.73
	HELIUM	16

Figure 4.24. Diffusion specifications for lab-rig reactor.

The overview of the model in gPROMS Process Builder is shown in Table 4.23. In the AML: FBCR library, there are many built-in reactor types. If required, it is possible to manipulate the built-in templates by using custom model language. We used “Catalyst pellets section 1D” model in gPROMS where gas or liquid flows through the fixed bed including solid catalyst pellet. Hence, there are two phases in the catalyst bed which make our model axially distributed considering separate conservation equations for fluid and catalyst. This approach is better than the pseudo-homogeneous model where both phases have the same temperature. Because there is a consequential interphase transport resistance which gives rise to notable dissimilarity in both phase temperatures. Lumped model is used for catalyst pellet because of the fact that crushed catalyst is used which makes the effectiveness factor equal to 1 (i.e, neglecting intra-particle mass transfer limitations) [97, 183].

In regard to diffusivity calculations for gas phase in Figure 4.24, Fuller method, which is based on experimental studies, is used for diffusion volumes and binary diffusion coefficients of the gases [184]. For this reason, physical property package is not used in this regard. Reference temperature and pressure for diffusion calculations are specified as 25°C and 1 bar. Most abundant component in our system is methane. That’s why it was determined as bulk component which is used to obtain a single Schmidt (Sc) number in mass balances and in diffusion equations. Reference mass fractions are defined for the calculation of mean diffusion coefficient to attain a single particle-fluid boundary layer thickness.

Heat transfer coefficient specification	Specified	
Temperature profile	Constant	
Temperature specification	Specified	
<input checked="" type="checkbox"/> Heat transfer coefficient	1000	W m ⁻² K ⁻¹
<input type="checkbox"/> Temperature	260	°C

Figure 4.25. Coolant specifications for lab-rig reactor.

Lab-rig reactor is non-adiabatic non-isothermal so mass and energy balance equations are solved in the direction of flow (i.e, 1D tube model). As being in small size

and having high heat transfer to the outside environment, reactor is close to the isothermal operation conditions.

Regarding to heat transfer, the heat is exchanged through the reactor tube wall. In general, the essential requirements as cooling/heating specifications for reactors are either wall temperature profile or coolant/heating temperature coupled with coolant heat transfer coefficient (h_c). For the sake of the ease of equation oriented approach in gPROMS, h_c is fixed with the assumption of uniform profile of coolant temperature and then single point bed temperature (center of the catalyst bed) is entered instead of specifying coolant temperature. That's why we used fixed coolant as heater type in the model as demonstrated in Figure 4.25. The model then solves for the coolant temperature. Coolant term that is used here is outside media because there is no any real coolant flow in order to cool down the reactor. All that is needed for the coolant from the modeling point of view are a temperature and heat transfer coefficient outside the tube.

In the lab-rig reactor model, one-dimensional heterogeneous mathematical model is used. The assumptions dealing with the model development are summarized as below:

- Steady-state operation
- Non-adiabatic reaction system
- Very close to isothermal conditions
- Advanced RKS is used as an equation of state model.
- Concentration and temperature gradients in radial direction is negligible.
- 1D distributed flow is considered.
- Intraparticle mass transfer is neglected by using lumped pellet model (i.e, effectiveness factor is equal to 1).
- Axial dispersion (concentration and heat) is neglected due to uniform fluid velocity in the axial direction.
- Axial heat conduction is taken into account.
- Radiation is negligible
- Constant bed porosity for axial and radial directions
- Verified plug flow pattern along the bed

Bed porosity calculation		Mass of catalyst ▼
Reactor geometry		
<input checked="" type="checkbox"/> Catalyst section length	20	mm ▼
<input checked="" type="checkbox"/> Bed radius	4.5	mm ▼
<input checked="" type="checkbox"/> Thermo-well radius	1.5	mm ▼
<input checked="" type="checkbox"/> Number of tubes	1	
Bed properties		
<input type="checkbox"/> Catalyst volumetric fraction	0.1/2.0	- ▼
<input type="checkbox"/> Catalyst mass per tube	0.1	g ▼

Figure 4.26. General settings in Catalyst_pellets_section_1D.

Bed porosity in the model (Figure 4.26) is calculated from mass of catalyst and catalyst volumetric fraction based on the below-stated formula (4.23). Volume of catalyst is an extensive property that is dependent on the catalyst mass. Catalyst section volume is calculated by considering catalyst section length, bed radius coupled with thermo-well radius which is physically reaching out up to the tip of the upper edge of the quartz wool. Therefore, the loss of volume due to thermo-well radius should be considered in calculation of catalyst section volume.

$$\varphi_{cat} = \frac{V_{c,b}}{\left(\frac{\pi * d_t^2 * L}{4}\right) * (1 - \epsilon_b)} \quad (4.23)$$

φ_{cat} : Volumetric fraction of the catalyst

$V_{c,b}$: Volume of catalyst in the bed

ϵ_b : Bed porosity

d_t : Inner tube diameter

L : Length of the catalyst bed

Mass and energy conservation equations for gas and solid phase that are valid for our case under these assumptions are shown in 4.24-4.27. Similar balance equations were studied in the literature [71, 183, 185].

Mass and energy balance equations for the gas phase

$$k_{f_i} * a_v * (C_i - C_{i_s}) + \frac{\partial(v_f * C_i)}{\partial z} = 0 \quad (4.24)$$

$$-v_f * \rho_f * C_{p_f} * \frac{\partial T}{\partial z} + h_f * a_v * (T_s - T) + \frac{4}{d_t} * U * (T_\infty - T) + \lambda_f * \frac{\partial^2 T}{\partial z^2} = 0 \quad (4.25)$$

Mass and energy balance equations for the solid phase

$$k_{f_i} * a_v * (C_i - C_{i_s}) + \eta * \rho_s * (1 - \epsilon_b) * \sum_{j=1}^M a_j * (-r_i) = 0 \quad (4.26)$$

$$h_f * a_v * (T - T_s) + \eta * \rho_s * \sum_{j=1}^M r_j * a_j * (-\Delta H_{rxn,j}) + \lambda_s * \frac{\partial^2 T}{\partial z^2} = 0 \quad (4.27)$$

$$i = 1, 2, 3 \dots N$$

$N = \text{Total \# of reaction components}$

$$j = 1, 2, 3 \dots M$$

$M = \text{Total \# of reactions}$

Boundary conditions

$$@z = 0 \quad C_i = C_{i,0}; \quad T = T_0$$

$$@z = L \quad \frac{\partial T}{\partial z} = 0$$

Initial conditions

$$C_i = C_{i,0}; \quad T = T_0$$

Number of discretization points used in the axial distribution domain of the model is 20. This means that partial differential equations in the mass and energy balance equations for gas and solid phases are solved with discretisation of the distributed equations with respect to all spatial domains, which reduces the problem to the solution of a set of DAEs. Various finite difference methods are used for discretization. First order backward finite difference method is used for convective terms while central finite difference method is used for conduction terms.

As a mathematical solver, DAEBDF (Differential-Algebraic Equations Backward Differentiation Formulae), which is based on variable time step and variable order backward differentiation formulae, is used in gPROMS. This solver is designed to cope with large, sparse systems of equations where variable values are restricted to specified lower and upper bounds. DAEBDF can handle situations in which some of the partial derivatives of the equations with respect to the variables are available analytically while the rest must be approximated. In gPROMS models, almost all partial derivatives are computed analytically from expressions derived using symbolic manipulations. Efficient finite difference approximations are used for this purpose. This solver automatically adjusts each time step taken so that the following criterion (4.28) is satisfied [97]:

$$\sqrt{\frac{1}{N_d} * \sum_{n=1}^{N_d} \left(\frac{\epsilon_{l,n}}{a_{tol} + r_{tol} * |\Lambda_n|} \right)^2} \leq 1 \quad (4.28)$$

where:

N_d = Number of differential variables in the problem

$\epsilon_{l,n}$ = Solver's estimate for the local error in the n^{th} differential variable

Λ_n = Current value of the n^{th} differential variable

a_{tol} = Absolute error tolerance

r_{tol} = Relative error tolerance

Heat transfer	On - Heat from connection ▼	
Radial heat transfer medium	Solid ▼	
<input checked="" type="checkbox"/> Axial heat conduction	On ▼	
Wall geometry		
<input checked="" type="checkbox"/> Tube wall thickness	2	mm ▼
Wall properties		
<input checked="" type="checkbox"/> Tube wall thermal conductivity	16	$\text{W m}^{-1} \text{K}^{-1}$ ▼
<input checked="" type="checkbox"/> Tube wall specific heat capacity	2000	$\text{J kg}^{-1} \text{K}^{-1}$ ▼
<input checked="" type="checkbox"/> Tube wall density	7000	kg/m^3 ▼
<input checked="" type="checkbox"/> Tube wall emissivity	0.9	
Bed-wall heat transfer		
<input checked="" type="checkbox"/> Dynamic contribution	DeWasch-Froment ▼	
<input checked="" type="checkbox"/> Dynamic contribution adjustable factor	10.0	
<input checked="" type="checkbox"/> Static contribution	Constant ▼	
<input checked="" type="checkbox"/> Constant static contribution	300	$\text{W m}^{-2} \text{K}^{-1}$ ▼
Effective bed conductivity		
<input checked="" type="checkbox"/> Dynamic contribution	DeWasch-Froment ▼	
<input checked="" type="checkbox"/> Dynamic contribution adjustable factor	10	
<input checked="" type="checkbox"/> Static contribution	Constant ▼	
<input checked="" type="checkbox"/> Constant static contribution	2.0	$\text{W m}^{-1} \text{K}^{-1}$ ▼

Figure 4.27. Heat transfer parameter specifications in lab-rig reactor model.

$$\lambda_{rs}^e = \lambda_{rs0}^e + \lambda_{rs,d}^e \quad (4.29)$$

$$\alpha_{ws}^e = \alpha_{ws0}^e + \alpha_{ws,d}^e \quad (4.30)$$

λ_{rs}^e : *Effective bed heat conductivity*

λ_{rs0}^e : *Static term of the effective bed heat conductivity*

$\lambda_{rs,d}^e$: *Dynamic term of the effective bed heat conductivity*

α_{ws}^e : *Overall effective bed – wall heat transfer coefficient (used in 1D bed models)*

α_{ws0}^e : *Static term of the effective bed – wall heat transfer coefficient*

$\alpha_{ws,d}^e$: *Dynamic term of the effective bed – wall heat transfer coefficient*

AML: FBCR uses two sorts of effective transport formulation in calculating heat flux in radial direction. One is lambda effective transport and the other one is alpha effective transport. These concepts are formulated with two different equations (4.29-4.30) all of which have static and dynamic contributions. Static contribution involves with the heat transfer in the hypothetical situation of zero flow whereas dynamic contribution only takes hydrodynamic effects into consideration.

Parameters and methods relating to heat transfer section are illustrated in Figure 4.27. Because of the fact that crushed catalyst is used in our reactor, correlations that are used in heat transfer section do not play crucial roles in the model. It is assumed that heat transfer in the bed is fast and therefore it is very close to isothermal conditions. For this reason, dynamic contribution adjustable factors for bed-wall heat transfer (CatalystBed.Alp_w_s1) and effective bed conductivity (CatalystBed.Lam_r_s1), which have both a factor of 1 as default, were set to 10 in order to make the heat transfer fast. No any correlation was used for static contribution terms in bed-wall heat transfer and effective bed conductivity which were fixed at constant values of 300 and 2 Wm⁻²K⁻¹, respectively. DeWash-Froment method was used for the prediction of dynamic contribution of bed-wall heat transfer and effective bed conductivity.

Correlations (DeWasch-Froment) dealing with dynamic term contributions that are used for the calculation of effective bed-wall heat transfer coefficient and effective bed conductivity, are shown as below (4.31-4.32):

$$Nu_w^f = A_\alpha * Re_p * \frac{0.01340}{\lambda_f/d_t} * \left(\frac{Pr}{Pr_{air}} \right)^{\frac{1}{3}} \quad (4.31)$$

Nu_w^f : Nusselt number for bed – wall heat transfer – dynamic term

Re_p : Reynolds number for packed bed

Pr : Prandtl number for the fluid

A_α : User

– specified adjustable factors for dynamic term of the effective bed

$$Pe_r = \frac{1}{0.002908} * \lambda_f * Pr_{air} * \left[1 + 0.46 * \left(\frac{d_{pl}}{d_t} \right)^2 \right] \quad (4.32)$$

Pe_r : Peclet number for radial mass transfer

d_{pl} : Equivalent pellet diameter of a sphere with the same surface area

d_t : Hydraulic or inner diameter of the tube

λ_f : Thermal conductivity of the fluid

One-dimensional models of packed beds with heat transfer in AML:FBCR use an overall heat transfer coefficient which is calculated from the effective bed conductivity and bed-wall heat transfer coefficient correlations. The bed properties model for one-dimensional beds also includes a prediction of bed centre temperature based on an overall heat transfer coefficient ($J \ s^{-1} \ m^{-2} \ K^{-1}$) between tube wall temperature and centre bed temperature, rather than on bed average temperature as α_w^0 . In our lab-rig model, centre bed temperature which refers to the distance of “10 mm” from top of the catalyst bed (i.e, “0 mm” refers to the top of the catalyst section).

Catalyst bed of 20 mm height was discretized into 20 units. By using Dixon correlation as shown in equation (4.33), other points along the bed were calculated accordingly.

$$\alpha_w^0 = \alpha_{ws}^e * \frac{Bi_d^4 + 24 * Bi_d^3 + 240 * Bi_d^2 + 1152 * Bi_d + 2304}{16 * (Bi_d^2 + 6 * Bi_d + 12)^2} \quad (4.33)$$

where:

α_w^0 : Overall effective bed – wall heat transfer coefficient, with respect to center bed temperature

α_{ws}^e : Overall effective bed – wall heat transfer coefficient (used in 1D bed models)

Bi_d : Biot number for Dixon correlation

Biot number in here is formulated as follows:

$$Bi_d = \frac{\alpha_{ws}^e * d_t}{2 * \lambda_{rs}^e} \quad (4.34)$$

Bulk reactions	Off
Partial enthalpy calculation	Ideal mixture
Additional user specified parameters	Off
<hr/>	
Flow resistance	
<input checked="" type="checkbox"/> Pressure drop equation	Ergun
<input checked="" type="checkbox"/> Pressure drop coefficient A	1.0
<input checked="" type="checkbox"/> Pressure drop coefficient B	1.0
<hr/>	
Heat and mass transfer between pellet and bulk fluid	
<input checked="" type="checkbox"/> Solid-fluid transfer correlation	Hougen
<input checked="" type="checkbox"/> Mass transfer coefficient adjustable factor	1
<input checked="" type="checkbox"/> Heat transfer coefficient adjustable factor	1
<hr/>	
Specify below only if 'Constant' option is selected for the solid-fluid transfer	
<input checked="" type="checkbox"/> Mass transfer coefficient	0.1 m/s
<input checked="" type="checkbox"/> Heat transfer coefficient	200.0 W m ⁻² K ⁻¹

Figure 4.28. Flow resistance and fluid-to-solid heat and mass transfer specifications.

Regarding to pressure drop in a packed bed, Ergun equation (4.35), which is specified with two adjustable factors relating to laminar and turbulent flow terms is chosen in gPROMS. These two terms are used in the adjustments relating to flow regime by the help of the equation-oriented approach in gPROMS. All specifications pertaining to flow resistance and fluid-to-solid heat and mass transfer are demonstrated in Figure 4.28.

$$f = \frac{1 - \varepsilon_b}{\varepsilon_b^3} * \left[A_f * 150 * \frac{(1 - \varepsilon_b)}{Re_p} + B_f * 1.75 \right] \quad (4.35)$$

f : Friction factor

ε_b : Bed void fraction

A_f : User – specified adjustable factors for laminar flow term of the pressure drop equation

B_f : User – specified adjustable factors for turbulent flow term of the pressure drop equation

Re_p : Reynolds number for packed bed

Catalyst bed models in the AML: FBCR module consider fluid-to-particle interfacial heat and mass transfer resistance. The heat transfer resistance in the bed is described using the fluid-solid heat transfer coefficient (h_f) and the mass transfer resistance using the fluid-solid mass transfer coefficient (k_f). In this model, Hougen correlation, which is based on Colburn j-factor analogy, is used. This correlation (4.36), related dimensionless numbers (4.37-4.40) and Colburn criteria based on Reynold number (4.41) are shown as below:

j_D : Colburn j – factor for mass transfer

j_H : Colburn j – factor for heat transfer

$$j_D = \frac{Sh_p}{Re_p * Sc^{1/3}} = \frac{Nu_p}{Re_p * Pr^{1/3}} = j_H \quad (4.36)$$

$$Sh_p(\text{Sherwood number for packed bed}) = \frac{d_p * k_f}{D_e} \quad (4.37)$$

$$Re_p(\text{Reynold number for packed bed}) = \frac{d_p * \rho_f * v_f}{\mu_f} \quad (4.38)$$

$$Nu_p(\text{Nusselt number for fluid – solid heat transfer}) = \frac{h_f * d_p}{\lambda_f} \quad (4.39)$$

$$Pr(\text{Prandtl number for the fluid}) = \frac{\mu_f * C_{p,f}}{\lambda_f} \quad (4.40)$$

$$j_D = \begin{cases} 1.66 * Re_p^{-0.51}, & Re_p < 190 \\ 0.983 * Re_p^{-0.41}, & Re_p > 190 \end{cases} \quad (4.41)$$

In Appendix G, the patterns regarding to reaction rates (mol/kg_catalyst-s) of main and side reactions are shown in Figures G.1-3. The chosen experiment has a unique identifier of 4_4 which is center point experiment (2b0) belonging to the catalyst loading #4. According to results, it is observed that the reaction rates of main and side reaction_1 are higher at the very early stages of the catalyst bed. This reduction in the reaction rates along the bed could be attributed to the product concentrations in the bed. Reaction rate of side reaction_2 is gradually increasing along side the bed. When it comes to comparing the order of magnitudes of reaction rates, average reaction rate of main reaction ($2.76 * 10^{-3}$) is 2.4 times higher than side reaction_1 ($1.12 * 10^{-3}$) which is 136.7 times greater than side reaction_2 ($8.19 * 10^{-6}$). Figures G.4-8 show temperature and concentration profiles along side the catalyst bed in axial direction. As one might expect that molar fractions of ethylene oxide and carbon dioxide are both increasing whereas ethylene and oxygen concentrations are decreasing along the bed. Temperature is slightly increasing due to exothermic nature of the reactions and reaches its maximum at the center of the bed.

CHAPTER 5

CONCLUSION

Within the context of all tasks done throughout the thesis, a custom kinetic model for commercial ethylene oxide catalyst in EO/EG plant, which is the main objective, was obtained. To attain this, custom catalyst testing system for ethylene oxide reaction was established and commissioned. The way that we took for achieving our goal was to implement a model-based experimentation approach by using gPROMS Process Builder which enabled us a custom modeling environment for discriminating kinetic model candidates.

To find out the necessary information to be populated in AML: FBCR, catalyst characterization was carried out. Moreover, machine learning methods were used to truly understand the catalyst behavior in the long run which is analogous with its journey from Start-of-Run (SOR) to End-of-Run (EOR) in the industrial plant. Prerequisites of kinetic experimentation such as heat transfer limitations, intraphase&interphase mass transfer limitations, establishment of plug-flow criterion, determination of catalyst activation method and stability tests were successfully accomplished.

Experiments to be used in parameter estimations were designed by using one-factor at a time approach and D-optimal criterion in such a way to capture all crucial relationships between process parameters and reactor inlet concentrations. Effects of product concentrations and VCM as a chlorine source were also investigated. Experiments particularly on ethylene oxide oxidation were performed. High pressure experiments were done but not included into parameter estimations due to the unidentified faulty results. Data reconciliation method was developed for the executed experiments in the lab-rig reactor.

According to the experimental results, it is explicitly observed from initial catalyst activity parameters that catalyst activity of each loading is not identical. On the top of that EO/CO₂ selectivity is increasing whereas ethylene conversion is decreasing, thereby changing catalyst behaviour in the same way during the course of each loading. This was mathematically modeled with conventional catalyst deactivation function; this

was not an actual deactivation phenomenon in theoretical sense nevertheless. That's why it is concluded that this behavior is sort of catalyst maturing that could be seen in the transition period from high activity region to high selectivity one.

Two-staged discrimination approach was used by following a sequence consisting of uniquely-organized experiments in subsets. Kinetic models taken from literature were extended and modified. Among eight kinetic models that were tested, the ones (1, 1(a) and 2) derived from Westerterp et al. show the best statistical fits. Model (1) was chosen as the best kinetic model in terms of root mean square errors with respect to main reaction components. Besides, the denominator of the main reaction in the rate equation was used as that of ethylene oxide oxidation in the sense that the denominator of partial oxidation reaction was found more statistically significant than that of total oxidation.

“Catalyst pellets section 1D” heterogeneous model in AML: FBCR was used in compliance with model-targeted experimentation approach. Parameter estimations were conducted under the guidance of this model. As such, optimization upon kinetic model parameters was provided in accordance with first-principle model equations with heedful assumptions. As is to be expected, main reaction rate has the most dominant rate in order of magnitude among the other two.

In the further studies, this kinetic model will be used as a slave model in order for modeling multitubular industrial ethylene oxide reactors in gPROMS Process Builder. There are three caveats that are required to consider in modeling the plant reactor as a master model. One is the deactivation issue which could not be predicted in lab-rig reactor model and therefore need to be estimated on the basis of the real plant data encompassing the SOR period. Second is the operation pressure which is not atmospheric in the industrial reactor. The third is the total amount of chlorine components introducing the reactor which is almost three times higher than lab-rig reactor system. All things considered, kinetic rate equations based on lab-rig reactor should be rectified by using adjustment factors in contemplation of these notices of certain points without changing kinetic and adsorption constants that were estimated in this study.

REFERENCES

1. Tarafder, A.; Lee, B. C. S.; Ray, A. K.; Rangaiah, G. P., Multiobjective optimization of an industrial ethylene reactor using a nondominated sorting genetic algorithm. *Industrial & Engineering Chemistry Research* 2005, 44 (1), 124-141.
2. Zakkour, P.; Cook, G. *CCS Industry Roadmap – High Purity CO₂ Sources: Final Draft Sectoral Assessment*; Carbon Counts Company (UK) Ltd, 2010.
3. Keyvanloo, K.; Sedighi, M.; Towfighi, J., Genetic algorithm model development for prediction of main products in thermal cracking of naphtha: Comparison with kinetic modeling. *Chemical Engineering Journal* 2012, 209, 255-262.
4. ICIS Ethylene oxide. www.icis.com/subscriber/plants-and-projects/ (accessed 29/08/2017).
5. *Handbook of Heterogeneous Catalysis*. Second, Completely Revised and Enlarged Edition ed.; Wiley-VCH Weinheim, Germany, 2008; Vol. 1-8, p 4270.
6. Carucci, J. R. H.; Halonen, V.; Eränen, K.; Wärnå, J.; Ojala, S.; Huuhtanen, M.; Keiski, R.; Salmi, T., Ethylene Oxide Formation in a Microreactor: From Qualitative Kinetics to Detailed Modeling. *Ind. Eng. Chem. Res.* 2010, 49, 10897–10907.
7. *Applied Industrial Catalysis*. 1st ed.; Academic Press Inc: USA, 1983; Vol. 1, p 304.
8. Nawaz, Z., Heterogeneous Reactor Modeling of an Industrial Multitubular Packed-Bed Ethylene Oxide Reactor. *Chemical Engineering & Technology* 2016, 39 (10), 1845-1857.
9. Rase, H. F., *Handbook of Commercial Catalysts: Heterogeneous Catalysts*. CRC Press: USA, 2000; p 501.
10. Lockemeyer, J. R.; Yeates, R. C. Process for preparing a catalyst, the catalyst, and a use of the catalyst US 20050222462A1, Oct.6,2005.
11. Rase, H. F., *Fixed-Bed Reactor Design and Diagnostics: Gas Phase Reactions*. Butterworth Publishers: USA, 1990.
12. Nikačević, N. M.; Huesman, A. E. M.; Van den Hof, P. M. J.; Stankiewicz, A. I., Opportunities and challenges for process control in process intensification. *Chemical Engineering and Processing: Process Intensification* 2012, 52, 1-15.
13. Bäumler, C.; Z.Urban; M.Matzopoulos, Enhanced methods optimize ownership costs for catalysts. *Hydrocarbon Processing* June 2007, 71-78.
14. Rebsdatt, S.; Mayer, D., Ethylene Oxide. In *Ullmann's Encyclopedia of Industrial Chemistry*, 2001.

15. Dever, J. P.; George, K. F.; Hoffman, W. C.; Soo, H., Ethylene Oxide. In *Kirk Othmer Encyclopedia of Chemical Technology*, 2004; Vol. 10, pp 632-673.
16. Clarke, P. *APIC May 2017*; pci Wood Mackenzie: 2017.
17. Santen, R. A. v.; Niemantsverdriet, J. W., *Chemical Kinetics and Catalysis*. Springer Science+Business Media New York, 1995; p 280.
18. Satterfield, C. N., *Heterogeneous Catalysis in Industrial Practice*. 2nd ed.; Krieger Publishing Company: Malabar, Florida, 1996; p 554.
19. Kursawe, A. Partial Oxidation of Ethene to Ethylene Oxide in Microchannel Reactors. TU Chemnitz, Chemnitz, 2009.
20. Chorkendorff, I.; Niemantsverdriet, J. W., *Concepts of Modern Catalysis and Kinetics*. Wiley-VCH: Weinheim, 2003; p 452.
21. Morbidelli, M.; Gavrilidis, A.; Varma, A., *Catalyst Design: Optimal Distribution of Catalyst in Pellets, Reactors, and Membranes*. Cambridge University Press: New York, 2001; p 227.
22. Özbek, M. O.; van Santen, R. A., The Mechanism of Ethylene Epoxidation Catalysis. *Catalysis Letters* 2013, 143 (2), 131-141.
23. Lafarga, D.; Al-Juaied, M. A.; Bondy, C. M.; Varma, A., Ethylene Epoxidation on Ag-Cs/ α -Al₂O₃ Catalyst: Experimental Results and Strategy for Kinetic Parameter Determination. *Ind. Eng. Chem. Res.* 2000, 39, 2148-2156.
24. Hagen, J., *Industrial Catalysis : A Practical Approach*. Third Completely Revised and Enlarged ed.; Wiley-VCH: Weinheim, Germany, 2015; p 544.
25. Crampton, A. S.; Rötzer, M. D.; Ridge, C. J.; Yoon, B.; Schweinberger, F. F.; Landman, U.; Heiz, U., Assessing the concept of structure sensitivity or insensitivity for sub-nanometer catalyst materials. *Surface Science* 2016, 652, 7-19.
26. Ozbek, M. O.; Onal, I.; van Santen, R. A., Why silver is the unique catalyst for ethylene epoxidation. *Journal of Catalysis* 2011, 284 (2), 230-235.
27. Stegelmann, C., Microkinetic analysis of transient ethylene oxidation experiments on silver. *Journal of Catalysis* 2004, 226 (1), 129-137.
28. Bartholomew, C. H.; Farrauto, R. J., *Fundamentals of Industrial Catalytic Processes*. Second ed.; John Wiley & Sons, Inc: Hoboken, New Jersey, 2005; p 966.
29. Macleod, N.; Keel, J. M.; Lambert, R. M., The effects of catalyst aging under industrial conditions: ethylene oxide conversion over Ag-Cs/ α -Al₂O₃ catalysts. *Catalysis letters* 2003, 86 (1), 51-56.

30. Boskovic, G.; Wolf, D.; Brückner, A.; Baerns, M., Deactivation of a commercial catalyst in the epoxidation of ethylene to ethylene oxide—basis for accelerated testing. *Journal of Catalysis* 2004, 224 (1), 187-196.
31. Peschel, A. Model-based design of optimal chemical reactors. Max Planck Institute, Shaker Verlag, Aachen, 2012.
32. Baratti, R.; Gavriilidis, A.; Morbidelli, M.; Varma, A., Optimization of a nonisothermal nonadiabatic fixed-bed reactor using dirac-type silver catalysts for ethylene epoxidation. *Chemical engineering science* 1994, 49 (12), 1925-1936.
33. TP-410, Flow of Fluids Through Valves, Fittings and Pipe. 2009 ed.; Paper, C. T., Ed. Crane Co.: USA, 2009.
34. Peschel, A.; Jörke, A.; Sundmacher, K.; Freund, H., Optimal reaction concept and plant wide optimization of the ethylene oxide process. *Chemical Engineering Journal* 2012, 207-208, 656-674.
35. Kingsley, H. A.; Cleland, F. A. Ethylene oxide production by controlled oxidation of ethylene in the presence of the methane Jan.28,1964.
36. Papavassiliou, V.; Wagner, M. L., Ballast gas for heat transfer control in fixed-bed reactors. *Chemical engineering science* 1999, 54 (15-16), 3683-3689.
37. Eliyas, A.; Petrov, L., Modelling of the inhibiting effect of carbon dioxide on the selective oxidation of ethene over silver catalyst. *Applied Catalysis* 1990, 62 (1), 11-21.
38. Schouten, E.; Borman, P.; Westerterp, K., Influence of reaction products on the selective oxidation of ethene. *Chemical Engineering and Processing: Process Intensification* 1996, 35 (2), 107-120.
39. Liu, W.; Eliyas, A.; Petrov, L., Influence of feed water vapour on the selective oxidation of ethylene over silver catalyst. *Applied Catalysis* 1990, 61 (1), 265-274.
40. Force, E. L.; Bell, A. T., The relationship of adsorbed species observed by infrared spectroscopy to the mechanism of ethylene oxidation over silver. *Journal of Catalysis* 1975, 40 (3), 356-371.
41. Force, E. L.; Bell, A. T., Infrared spectra of adsorbed species present during the oxidation of ethylene over silver. *Journal of Catalysis* 1975, 38 (1-3), 440-460.
42. Grant, R. B.; Lambert, R. M., A single crystal study of the silver-catalysed selective oxidation and total oxidation of ethylene. *Journal of Catalysis* 1985, 92 (2), 364-375.
43. Van Santen, R. A.; Kuipers, H. P. C. E., The Mechanism of Ethylene Epoxidation. 1987; pp 265-321.

44. Stegelmann, C.; Schiødt, N. C.; Campbell, C. T.; Stoltze, P., Microkinetic modeling of ethylene oxidation over silver. *Journal of Catalysis* 2004, 221 (2), 630-649.
45. Zhou, X.-G.; Yuan, W.-K., Optimization of the fixed-bed reactor for ethylene epoxidation. *Chemical Engineering and Processing: Process Intensification* 2005, 44 (10), 1098-1107.
46. Klugherz, P. D.; Harriott, P., Kinetics of ethylene oxidation on a supported silver catalyst. *AIChE Journal* 1971, 17 (4), 856-866.
47. Metcalf, P. L.; Harriott, P., Kinetics of silver-catalyzed ethylene oxidation. *Industrial & Engineering Chemistry Process Design and Development* 1972, 11 (4), 478-484.
48. Petrov, L.; Eliyas, A.; Shopov, D., A kinetic model of steady state ethylene epoxidation over a supported silver catalyst. *Applied catalysis* 1985, 18 (1), 87-103.
49. Petrov, L.; Eliyas, A.; Shopov, D., Kinetics of ethylene oxidation over a silver catalyst in the presence of dichloroethane. *Applied catalysis* 1986, 24 (1), 145-161.
50. Eliyas, A.; Petrov, L.; Shopov, D., Ethylene oxide oxidation over a supported silver catalyst: II. Kinetics of inhibited oxidation. *Applied catalysis* 1988, 41, 39-52.
51. Petrov, L.; Eliyas, A.; Maximov, C.; Shopov, D., Ethylene oxide oxidation over a supported silver catalyst: I. Kinetics of uninhibited oxidation. *Applied catalysis* 1988, 41, 23-38.
52. Ghazali, S.; Park, D.; Gau, G., Kinetics of ethylene epoxidation on a silver catalyst. *Applied Catalysis* 1983, 6 (2), 195-208.
53. Park, D. W.; Gau, G., Ethylene epoxidation on a silver catalyst: unsteady and steady state kinetics. *Journal of Catalysis* 1987, 105 (1), 81-94.
54. Stoukides, M.; Pavlou, S., Ethylene oxidation on silver catalysts: effect of ethylene oxide and of external transfer limitations. *Chemical Engineering Communications* 1986, 44 (1-6), 53-74.
55. Al-Saleh, M.; Al-Ahmadi, M.; Shalabi, M., Kinetic study of ethylene oxidation in a Berty reactor. *The Chemical Engineering Journal* 1988, 37 (1), 35-41.
56. Westerterp, K.; Ptasiński, K., Safe design of cooled tubular reactors for exothermic, multiple reactions; parallel reactions—II: The design and operation of an ethylene oxide reactor. *Chemical engineering science* 1984, 39 (2), 245-252.
57. Borman, P. C.; Westerterp, K. R., An Experimental Study of the Kinetics of the Selective Oxidation of Ethene over a Silver on α -Alumina Catalyst. *Industrial & engineering chemistry research* 1995, 34 (1), 49-58.

58. Borman, P.; Westerterp, K., An experimental study of the selective oxidation of ethene in a wall cooled tubular packed bed reactor. *Chemical engineering science* 1992, 47 (9), 2541-2546.
59. Gan, L.; Wang, H.-s.; Zhu, B.-c.; Xu, M.-s.; Wang, Z.-l., Global kinetics and deactivation of silver catalyst for ethylene oxide synthesis. *Journal of Chemical Industry and Engineering-China*- 2001, 52 (11), 969-973.
60. Gu, Y.; Gao, Z.; Jin, J., Kinetic models for ethylene oxidation to ethylene oxide. *Petrochem. Technol* 2003, 32, 838-840.
61. Salmi, T.; Hernández Carucci, J.; Roche, M.; Eränen, K.; Wärnå, J.; Murzin, D., Microreactors as tools in kinetic investigations: Ethylene oxide formation on silver catalyst. *Chemical Engineering Science* 2013, 87, 306-314.
62. Russo, V.; Kilpiö, T.; Hernandez Carucci, J.; Di Serio, M.; Salmi, T. O., Modeling of microreactors for ethylene epoxidation and total oxidation. *Chemical Engineering Science* 2015, 134, 563-571.
63. Perzon, H. A Simulation Model of a reactor for Ethylene Oxide production. Lund University, 2015.
64. Gudekar, K. G. Modeling, control, and optimization of fixed bed reactors. Texas Tech University, 2002.
65. Iordanidis, A. A. Mathematical Modeling of Catalytic Fixed Bed Reactors. University of Twente, 2002.
66. Peschel, A.; Karst, F.; Freund, H.; Sundmacher, K., Analysis and optimal design of an ethylene oxide reactor. *Chemical Engineering Science* 2011, 66 (24), 6453-6469.
67. Aryana, S.; Ahmadi, M.; Gomes, V. G.; Romagnoli, J. A.; Ngian, K., Modelling and Optimisation of an Industrial Ethylene Oxide Reactor. *Chemical Product and Process Modeling* 2009, 4 (1).
68. Galan, O.; Gomes, V. G.; Romagnoli, J.; Ngian, K. F., Selective Oxidation of Ethylene in an Industrial Packed-Bed Reactor: Modelling, Analysis and Optimization. *International Journal of Chemical Reactor Engineering* 2009, 7 (1).
69. Vandervoort, A.; Thibault, J.; Gupta, Y. P., Multi-Objective Optimization of an Ethylene Oxide Reactor. *International Journal of Chemical Reactor Engineering* 2011, 9 (1).
70. Rahimpour, M. R.; Shayanmehr, M.; Nazari, M., Modeling and Simulation of an Industrial Ethylene Oxide (EO) Reactor Using Artificial Neural Networks (ANN). *Industrial & Engineering Chemistry Research* 2011, 50 (10), 6044-6052.
71. Bayat, M.; Hamidi, M.; Dehghani, Z.; Rahimpour, M. R., Dynamic optimal design of an industrial ethylene oxide (EO) reactor via differential evolution algorithm. *Journal of Natural Gas Science and Engineering* 2013, 12, 56-64.

72. Zahedi, G.; Lohi, A.; Mahdi, K. A., Hybrid modeling of ethylene to ethylene oxide heterogeneous reactor. *Fuel Processing Technology* 2011, 92 (9), 1725-1732.
73. Luo, N.; Du, W.; Ye, Z.; Qian, F., Development of a Hybrid Model for Industrial Ethylene Oxide Reactor. *Industrial & Engineering Chemistry Research* 2012, 51 (19), 6926-6932.
74. Lahiri, S. K.; Khalfe, N., Process modeling and optimization of industrial ethylene oxide reactor by integrating support vector regression and genetic algorithm. *The Canadian Journal of Chemical Engineering* 2009, 87 (1), 118-128.
75. Kugelstadt, T. *The RS-485 Design Guide*; 2016.
76. Pantelides, C. C.; Nauta, M.; Matzopoulos, M.; Grove, H. In *Equation-oriented process modelling technology: recent advances & current perspectives*, 5th Annual TRC-Idemitsu Workshop, 2015.
77. Shin, S. B.; Han, S. P.; Lee, W. J.; Im, Y. H.; Chae, J. H.; Lee, D. I.; Lee, W. H., Optimize terephthaldehyde reactor operations. *Hydrocarbon Processing* April 2007, 83-90.
78. Rodríguez, H. M.; Cano, A.; Matzopoulos, M., Improve engineering by whole-plant design optimization. *Hydrocarbon Processing* December 2010, 43-49.
79. Hukkanen, E. J.; Rangitsch, M. J.; Witt, P. M., Non-Adiabatic Multitubular Fixed-Bed Catalytic Reactor Model Coupled with Shell-Side Coolant CFD Model. *Industrial & Engineering Chemistry Research* 2013, 52 (44), 15437-15446.
80. Mendoza, D. F.; Palacio, L. M.; Graciano, J. E.; Riascos, C. A.; Vianna Jr, A. S.; Le Roux, G. C., Real-time optimization of an industrial-scale vapor recompression distillation process. Model validation and analysis. *Industrial & Engineering Chemistry Research* 2013, 52 (16), 5735-5746.
81. Tanvir, M.; Mujtaba, I., Optimisation of design and operation of MSF desalination process using MINLP technique in gPROMS. *Desalination* 2008, 222 (1-3), 419-430.
82. Tijl, P. Assessment of the parameter estimation capabilities of gPROMS and ASPEN Custom Modeler, using the Sec-Butyl-Alcohol stripper kinetics case study. Eindhoven Technical University, Amsterdam, July 2005.
83. Berreni, M.; Wang, M., Modelling and dynamic optimization of thermal cracking of propane for ethylene manufacturing. *Computers & Chemical Engineering* 2011, 35 (12), 2876-2885.
84. Seitz, G. Global nonlinear optimization and optimal control for applications in pulp and paper industry. Ulm university, September 2009.

85. Kiss, A. A.; Bildea, C. S.; Grievink, J., Dynamic modeling and process optimization of an industrial sulfuric acid plant. *Chemical Engineering Journal* 2010, 158 (2), 241-249.
86. Meidanshahi, V.; A. Adams, T., Integrated Design and Control of Semicontinuous Processes Using Mixed Integer Nonlinear Dynamic Optimization. In *12th International Symposium on Process Systems Engineering and 25th European Symposium on Computer Aided Process Engineering*, 2015; Vol. 37, pp 1181-1186.
87. Lunze, J.; Lamnabhi-Lagarrigue, F., *Handbook of Hybrid Systems Control: Theory, Tools, Applications*. Cambridge University Press: New York, 2009; p 565.
88. Georgiadis, M. C.; Banga, J. R.; Pistikopoulos, E. N., *Dynamic Process Modeling*. Wiley-VCH 2011; Vol. 7.
89. Song, D., Kinetic Model Development for Dehydration of 2,3-Butanediol to 1,3-Butadiene and Methyl Ethyl Ketone over an Amorphous Calcium Phosphate Catalyst. *Ind. Eng. Chem. Res.* 2016, 55 (45), 11664-11671.
90. S.Z.Abbas; V.Dupont; T.Mahmud, Kinetics study and modelling of steam methane reforming process over a NiO/Al₂O₃ catalyst in an adiabatic packed bed reactor. *International Journal of Hydrogen Energy* 2016, 42 (5), 2889-2903.
91. Shin, S. B.; Skau, K. I.; Menon, M.; Maroor, S.; Spatenka, S., A modelling approach to kinetics study and novel monolith channel design for selective catalytic reduction (SCR) applications. *Chemical Engineering Research and Design* 2019, 142, 412-428.
92. Davis, M. E.; Davis, R. J., *Fundamentals of Chemical Reaction Engineering*. McGraw-Hill: 2003; p 368.
93. Wolf, D.; Höhenberger, M.; Baerns, M., External Mass and Heat Transfer Limitations of the Partial Oxidation of Methane over a Pt/MgO Catalyst Consequences for Adiabatic Reactor Operation. *Ind. Eng. Chem. Res.* 1997, 36 (8), 3345–3353.
94. Perego, C.; Peratello, S., Experimental methods in catalytic kinetics. *Catalysis Today* 1999, 52, 133-145.
95. Schouten, E. P. S.; Borman, P. C.; Westerterp, K. R., Determination of the kinetics of ethene epoxidation. *Chemical Engineering and Processing* 1996, 35, 43-55.
96. Berty, J. M., *Experiments in catalytic reaction engineering*. Elsevier: 1999; Vol. 124, p 267.
97. gPROMS ProcessBuilder Documentation 1.2.0. Process Systems Enterprise Limited: 2017.
98. Martín, M. M., *Introduction to Software for Chemical Engineers*. CRC Press: 2015; p 586.

99. User Guide for Multiflash for Windows 6.1. Infochem/KBC Advanced Technologies ltd: 2015.
100. User Guide for Models and Physical Properties (Multiflash Version 6.1). Infochem/KBC Advanced Technologies plc: 2016.
101. Robinson, C.; Smith, D. B., The auto-ignition temperature of methane. *Journal of Hazardous Materials* 1984, 8, 199-203.
102. T. T. Akıttı, J.; Bircumshaw, L. D.; Eckert, R. E., Sequential design including initial experimental runs for a kinetic study of propylene oxidation. *The Canadian Journal of Chemical Engineering* 1997, 75.
103. Umetrics *Modde Pro Help*, 11.0.1; Sartorius Stedim Biotech: 2018.
104. Montgomery, D. C., *Design and Analysis of Experiments*. 8 ed.; Wiley: 2013.
105. Lazić, Ž. R., *Design of Experiments in Chemical Engineering: A Practical Guide*. Wiley-VCH: 2004.
106. Goos, P.; Jones, B., *Optimal Design of Experiments: A Case Study Approach*. Wiley: 2011.
107. Mason, R. L., *Statistical Design and Analysis of Experiments with Applications to Engineering and Science*. Wiley-Interscience: 2003.
108. Petrov, L. A.; Eliyas, A. E.; Maximov, C. S., Difficulties in the application of sequential design to kinetic model discrimination and parameter estimation. *Ind. Eng. Chem. Res.* 1991, 30, 639-645.
109. Sjöblom, J.; Papadakis, K.; Creaser, D.; Odenbrand, C. U. I., Use of experimental design in development of a catalyst system. *Catalyst Today* 2005, 100, 243-248.
110. Galvanin, F.; Cao, E.; Al-rifai, N.; Dua, V.; Gavrilidis, A., Optimal design of experiments for the identification of kinetic models of methanol oxidation over silver catalyst. *Chimica Oggi-Chemistry Today* 2015, 33 (3).
111. Sethapokin, P.; Kunatippapong, S.; Lothongkum, A. W., Estimation of kinetic parameters for the reactor model of the phthalic anhydride production by the design of experiments. *Journal of Industrial and Engineering Chemistry* 2015, 24, 51-58.
112. Dautzenberg, F. M., Ten Guidelines for Catalyst Testing. In *Characterization and Catalyst Development*, Steven A. Bradley; Mark J. Gattuso; Bertolacini, R. J., Eds. American Chemical Society: 1989; Vol. 411, pp 99-119.
113. Charles G. Hill, J., *An Introduction to Chemical Engineering Kinetics & Reactor Design* John Wiley & Sons: 1977.

114. Perry, R. H.; Green, D. W., *Perry's Chemical Engineers' Handbook*. 7 ed.; McGraw-Hill: 1999.
115. Reijen, J. E. v. d.; Kanungo, S.; Welling, T. A. J.; Versluijs-Helder, M.; Nijhuis, T. A.; Jong, K. P. d.; Jongh, P. E. d., Preparation and particle size effects of Ag/ α -Al₂O₃ catalysts for ethylene epoxidation. *Journal of Catalysis* 2017, 356, 65-74.
116. Waseda, Y.; Matsubara, E.; Shinoda, K., *X-Ray Diffraction Crystallography*. Springer: 2011.
117. Cullity, B. D.; Stock, S. R., *Elements of X-Ray Diffraction*. 3 ed.; Pearson: 2014.
118. ICDD: The International Centre for Diffraction Data. www.icdd.com (accessed 25.03.2019).
119. Westermarck, S. Use of Mercury Porosimetry and Nitrogen Adsorption in Characterization of the Pore Structure of Mannitol and Microcrystalline Cellulose Powders, Granules and Tablets. University of Helsinki, Finland, 2000.
120. Lowell, S.; Shields, J. E.; Thomas, M. A.; Thommes, M., *Porous Solids and Powders: Surface Area, Pore Size and Density*. Springer Science+Business Media, LLC: 2004.
121. Autosorb-1 Gas Sorption System Manual. Instruments, Q., Ed. Boynton Beach, U.S.A.
122. Haynes, J. M., Pore size analysis according to the Kelvin equation. *Matériaux et Constructions* 1973, 6 (33).
123. Conner, W. C.; Cevallos-Candau, J. F.; Weist, E. L.; J. Pajares; Mendioroz, S.; Cortés, A., Characterization of Pore Structure: Porosimetry and Sorption. *Langmuir* 1986, 2, 151-154.
124. Sing, K., The use of nitrogen adsorption for the characterisation of porous materials. *Colloids and Surfaces* 2001, 187-188, 3-9.
125. Operating Manual for Ultrapyc 1200e. Instruments, Q., Ed. Boynton Beach, Florida, 2017.
126. Mercury Intrusion Pore Size Analyzer Operating Manual. Instruments, Q., Ed. Boynton Beach, Florida, 2015.
127. Gerhardt, R., *Properties and Applications of Silicon Carbide*. InTech: Croatia, 2011; p 535.
128. Mills, W. <https://www.washingtonmills.com/history-of-silicon-carbide/sic-properties/> (accessed 06.04.2019).

129. Ghanbarian, B.; Hunt, A. G.; Ewing, R. P.; Sahimi, M., Tortuosity in Porous Media: A Critical Review. *Soil Science Society of America Journal* 2013, 77, 1461-1477.
130. Wang, C.-T.; Smith, J. M., Tortuosity factors for diffusion in catalyst pellets. *AIChE Journal* 1983, 29 (1), 132-136.
131. Sharma, R. K.; Cresswell, D. L., Effective diffusion coefficients and tortuosity factors for commercial catalysts. *Ind. Eng. Chem. Res.* 1991, 30, 1428-1433.
132. Carniglia, S. C., Construction of the tortuosity factor from porosimetry. *Journal of Catalyst* 1986, 102, 401-418.
133. Čapek, P.; Hejtmánek, V.; Šolcová, O., Permeation of gases in industrial porous catalysts. *Chemical Engineering Journal* 2001, 81, 281-285.
134. Wijngaarden, R. J.; Kronberg, A.; Westerterp, K. R., *Industrial Catalysis-Optimizing Catalysts and Processes*. Wiley-VCH: 1998.
135. Čapek, P.; Veselý, M.; Hejtmánek, V., On the measurement of transport parameters of porous solids in permeation and Wicke-Kallenbach cells. *Chemical Engineering Science* 2014, 118, 192-207.
136. Gómez-Martín, A.; Orihuela, M. P.; Becerra, J. A.; Martínez-Fernández, J.; J. Ramírez-Rico, Permeability and mechanical integrity of porous biomorphic SiC ceramics for application as hot-gas filters. *Materials and Design* 2016, 107, 450-460.
137. Walowski, G., Assessment of gas permeability coefficient of porous materials. *Journal of Sustainable Mining* 2017, 16 (2), 55-65.
138. Lattimer, B. Y.; Goodrich, T. W.; Chodak, J.; Cain, C., Properties of composite materials for modeling high temperature response. *International Conference on Composite Materials-17* 2009.
139. Tritt, T. M., *Thermal Conductivity-Theory, Properties and Applications*. Kluwer Academic/Plenum Publishers: 2004.
140. Carter, C. B.; Norton, M. G., *Ceramic Materials: Science and Engineering*. 2 ed.; Springer: 2013.
141. Xu, Y.; Yamazaki, M., Prediction of thermal conductivity of composite materials. In *Challenges of Power Engineering and Environment*, Cen, K.; Chi, Y.; Wang, F., Eds. Zhejiang University Press/Springer: 2007; Vol. 1, pp 897-902.
142. Xu, J.; Gao, B.; Du, H.; Kang, F., A statistical model for effective thermal conductivity of composite materials. *International Journal of Thermal Sciences* 2016, 104, 348-356.

143. Pietrak, K.; Wiśniewski, T. S., A review of models for effective thermal conductivity of composite materials. *Journal of Power Technologies* 2015, 95 (1), 14-24.
144. Janz, G. J., *Thermodynamic and transport properties for molten salts : correlation equations for critically evaluated density, surface tension, electrical conductance, and viscosity data*. American Institute of Physics: 1988; Vol. 17, p 309.
145. Touloukian, Y. S.; Powell, R. W.; Ho, C. Y.; Klemens, P. G. *Thermophysical properties of matter - the TPRC data series. Thermal conductivity - metallic elements and alloys*; 1970.
146. Touloukian, Y. S., *Thermophysical Properties of High Temperature Solid Materials*. 1 ed.; Macmillan: 1967; Vol. 5.
147. Xing, J.; Radovic, M.; Muliana, A., Thermal properties of BaTiO₃/Ag composites at different temperatures. *Composites Part B: Engineering* 2016, 90, 287-301.
148. Rivière, L.; Causse, N.; Lonjon, A.; Dantras, É.; Lacabanne, C., Specific heat capacity and thermal conductivity of PEEK/Ag nanoparticles composites determined by Modulated-Temperature Differential Scanning Calorimetry. *Polymer Degradation and Stability* 2016, 127, 98-104.
149. Chung, D. D. L., *Composite Materials: Science and Applications*. 2 ed.; Springer: 2010.
150. Smith, D. R.; Fickett, F. R., Low-temperature properties of silver. *Journal of Research of the National Institute of Standards and Technology* 1995, 100 (2), 119-171.
151. Furukawa, G. T.; Douglas, T. B.; McCoskey, R. E.; Ginnings, D. C., Thermal properties of aluminum oxide from 0° to 1,200° K. *Journal of Research of the National Bureau of Standards* 1956, 57 (2), 67-82.
152. Brereton, R. G., *Chemometrics for Pattern Recognition*. Wiley: 2009; p 504.
153. scikit-learn-Machine Learning in Python: Documentation of scikit-learn 0.20.3. <https://scikit-learn.org/stable/index.html> (accessed 25.03.2019).
154. L.Bergman, T.; Lavine, A. S., *Fundamentals of Heat and Mass Transfer*. 8 ed.; Wiley: 2017.
155. Schmal, M., *Chemical Reaction Engineering: Essentials, Exercises and Examples*. CRC Press: 2014; p 677.
156. Delgado, J. M. P. Q., A critical review of dispersion in packed beds. *Heat Mass Transfer* 2006, 42, 279-310.
157. Geankoplis, C. J., *Transport Processes and Separation Process Principles*. 4 ed.; Pearson Education: 2003; p 1056.

158. Sparrow, E. M.; Lin, S. H.; Lundgren, T. S., Flow development in the hydrodynamic entrance region of tubes and ducts. *Physics of Fluids* 1964, 7 (3), 338-347.
159. Albright, L. F., *Albright's Chemical Engineering Handbook*. CRC Press: 2009.
160. Dybbs, A.; Edwards, R. V., A new look at porous media fluid mechanics - Darcy to turbulent. In *Fundamentals of Transport Phenomena in Porous Media*, Bear, J.; Corapcioglu, M. Y., Eds. Martinus Nijhoff Publishers: 1984; pp 199-256.
161. Balhoff, M.; Mikelić, A.; Wheeler, M. F., Polynomial Filtration Laws for Low Reynolds Number Flows Through Porous Media. *Transp Porous Med* 2010, 81, 35-60.
162. Fogler, H. S., *Elements of Chemical Reaction Engineering*. 5 ed.; Prentice Hall: 2016.
163. Klaewkla, R.; Arend, M.; Hoelderich, W. F., A Review of Mass Transfer Controlling the Reaction Rate in Heterogeneous Catalytic Systems. In *Mass Transfer: Advanced Aspects*, 2012 ed.; Nakajima, H., Ed. InTech: 2011; pp 667-684.
164. Rushton, A.; Ward, A. S.; Holdich, R. G., *Solid-Liquid Filtration and Separation Technology*. Wiley-VCH: 1996; p 538.
165. Petrov, L., Problems and Challenges About Accelerated Testing of the Catalytic Activity of Catalysts. In *Principles and Methods for Accelerated Catalyst Design and Testing*, Derouane, E. G.; Parmon, V.; Lemos, F.; Ribeiro, F. R., Eds. Springer Science+Business Media Dordrecht: 2002; Vol. 69, pp 13-69.
166. Tamhane, A. C.; Mah, R. S. H., Data Reconciliation and Gross Error Detection in Chemical Process Networks. *Technometrics* 1985, 27 (4), 409-422.
167. Knopf, F. C., *Modeling, Analysis and Optimization of Process and Energy Systems*. John Wiley & Sons: Hoboken, New Jersey, 2012; p 462.
168. Romagnoli, J. A.; Sánchez, M. C., *Data Processing and Reconciliation for Chemical Process Operations*. Academic Press: USA, Vol. 2, p 270.
169. Narasimhan, S.; Jordache, C., *Data reconciliation & Gross Error Detection: An Intelligent Use of Process Data*. Gulf Publishing Company: USA, 2000; p 405.
170. Özyurt, D. B.; Pike, R. W., Theory and practice of simultaneous data reconciliation and gross error detection for chemical processes. *Computers and Chemical Engineering* 2004, 28, 381-402.
171. Prata, D. M.; Schwaab, M.; Lima, E. L.; Pinto, J. C., Simultaneous robust data reconciliation and gross error detection through particle swarm optimization for an industrial propylene reactor. *Chemical Engineering Science* 2010, 65, 4943-4954.

172. Crowe, C. M., Data Reconciliation-progress and challenges *J.Proc.Cont.* 1996, 6 (2/3), 89-98.
173. Kestenbaum, H.; Oliveira, A. L. d.; Schmidt, W.; Schüth, F.; Ehrfeld, W.; Gebauer, K.; Löwe, H.; Richter, T., Synthesis of ethylene oxide in a catalytic microreactor system. In *Studies in Surface Science and Catalysis*, Corma, A.; Melo, F. V.; S.Mendioroz; J.L.G.Fierro, Eds. Elsevier Science B.V.: 2000; Vol. 130, pp 2741-2746.
174. Aldrich, J., R.A.Fisher and the Making of Maximum Likelihood 1912-1922. *Statistical Science* 1997, 12 (3), 162-176.
175. Myung, I. J., Tutorial on maximum likelihood estimation. *Journal of Mathematical Psychology* 2003, (47), 90-100.
176. Sachtler, W. M. H.; Backx, C.; Santen, R. A. V., On the mechanism of ethylene epoxidation. *Catalysis Reviews-Science and Engineering* 1981, 23 (1-2), 127-149.
177. Rawlings, J. B.; Ekerdt, J. G., *Chemical Reactor Analysis and Design Fundamentals*. 2 ed.; Nob Hill Publishing, LLC: Madison, Wisconsin, 2013; p 633.
178. Schwaab, M.; Pinto, J. C., Optimum reference temperature for reparameterization of the Arrhenius equation. Part 1: Problems involving one kinetic constant. *Chemical Engineering Science* 2007, 62, 2750-2764.
179. Schwaab, M.; Lemos, L. P.; Pinto, J. C., Optimum reference temperature for reparameterization of the Arrhenius equation. Part 2: Problems involving multiple reparameterizations. *Chemical Engineering Science* 2008, 63, 2895-2906.
180. Klička, R.; Kubáček, L., Statistical properties of linearization of the Arrhenius equation via the logarithmic transformation. *Chemometrics and Intelligent Laboratory Systems* 1997, 39, 69-75.
181. Lira, T. S.; Santos, K. G.; Murata, V. V.; Ganesella, M.; Barrozo, M. A. S., The use of nonlinearity measures in the estimation of kinetic parameters of sugarcane bagasse pyrolysis. *Chem. Eng. Technol.* 2010, 33 (10), 1699-1705.
182. Triyono, Correlation between preexponential factor and activation energy of isoamylalcohol hydrogenolysis on platinum catalysts. *Indonesian Journal of Chemistry* 2004, 4 (1), 5.
183. Hayes, R. E.; Mmbaga, J. P., *Introduction to Chemical Reactor Analysis*. 2 ed.; CRC Press: 2013; p 528.
184. Fuller, E. N.; Schettler, P. D.; Giddings, J. C., A new method for prediction of binary gas-phase diffusion coefficients. *Industrial & Engineering Chemistry* 1966, 58 (5), 18-27.

185. Abbas, S. Z.; Dupont, V.; Mahmud, T., Kinetics study and modelling of steam methane reforming process over a NiO/Al₂O₃ catalyst in an adiabatic packed bed reactor. *International Journal of Hydrogen Energy* 2017, 42 (5), 2889-2903.
186. Carr, N. L.; Kobayashi, R., Viscosity of hydrocarbon gases under pressure. *Journal of Petroleum Technology* 1954, 6 (10).
187. Pushnov, A. S., Calculation of average bed porosity. *Chemical and Petroleum Engineering* 2006, 42 (1), 14-17.

APPENDIX A

GC CALIBRATION RESULTS

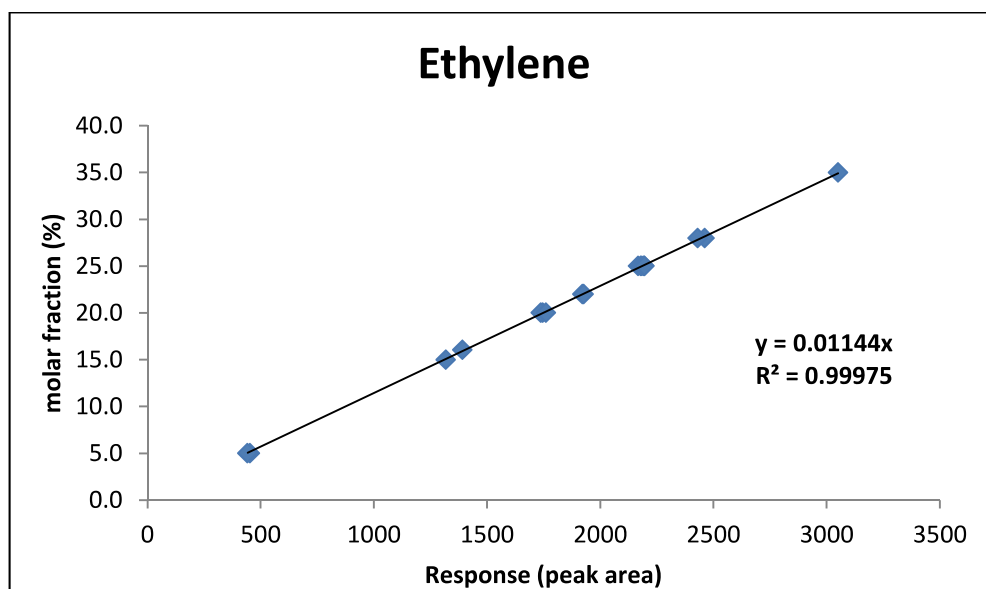


Figure A.1. Calibration curve for ethylene.

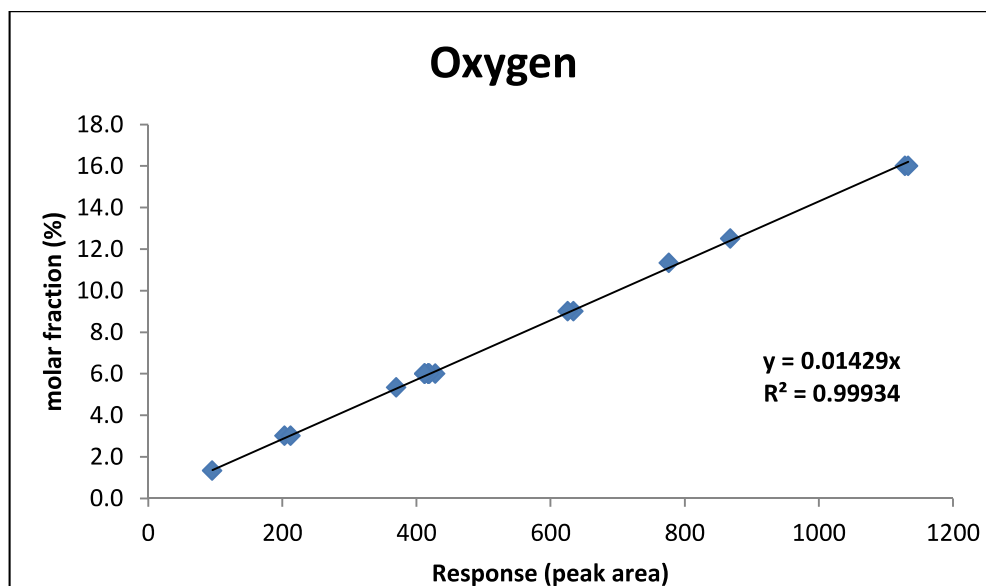


Figure A.2. Calibration curve for oxygen.

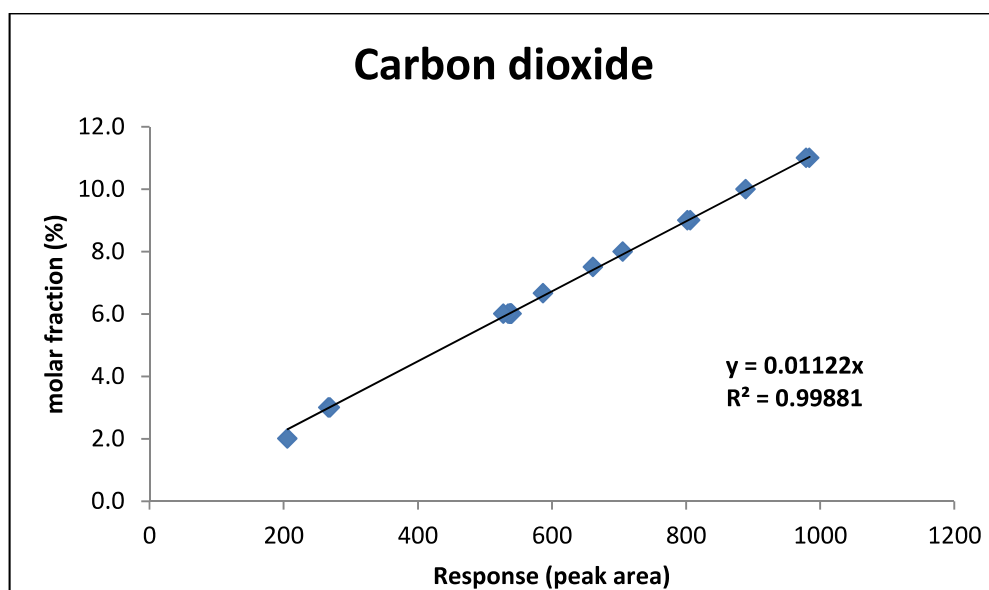


Figure A.3. Calibration curve for carbon dioxide.

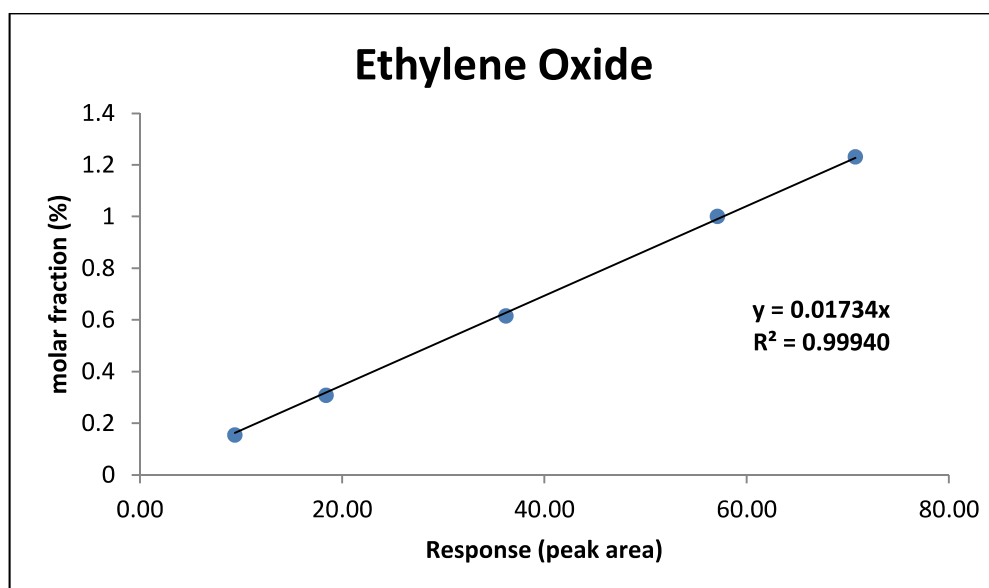


Figure A.4. Calibration curve for ethylene oxide

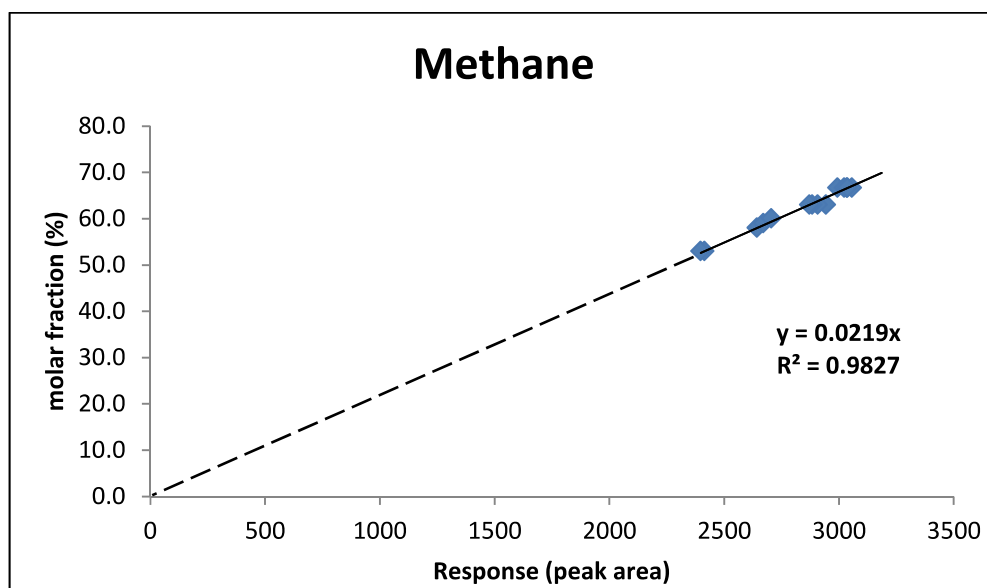


Figure A.5. Calibration curve for methane.

APPENDIX B

CALCULATION OF PLUG FLOW CRITERIA AND MASS TRANSFER LIMITATIONS

$$Q_{in}^{C_2H_4} = 17.06 \text{ sccm}, Q_{in}^{O_2} = 4.33 \text{ sccm}, Q_{in}^{CH_4} = 43.01 \text{ sccm}, Q_{in}^{CO_2} = 3.11 \text{ sccm}$$

$$Q_{in}^{He} = 7.50 \text{ sccm}$$

$$Q_T = 75.0 \text{ sccm} = 75.0 \text{ cm}^3/\text{min}$$

$$x_i = \frac{Q_{in}^i}{Q_T}, i = \text{reactor inlet gases}, x_i = \text{mole fraction of } i\text{th gas component}$$

$$MW_{C_2H_4} = 28 \text{ g/mol}, MW_{O_2} = 32 \text{ g/mol}, MW_{CH_4} = 16 \text{ g/mol}, MW_{CO_2} = 44 \text{ g/mol}$$

$$MW_{He} = 4 \text{ g/mol}$$

$$MW_{mix} = \sum_i^n x_i * MW_i, i = \text{reactor inlet gases}, n = \text{total \# of components}$$

$$y_i = x_i * \frac{MW_i}{MW_{mix}}, y_i = \text{mass fraction of } i\text{th gas component}$$

Table B.1. Some of the important properties of the feed gases.

Feed gas	x (mol fraction)	y (mass fraction)	MW (molecular weight)	Density (g/cm ³ , @250°C and 1 atm)	Viscosity (Pa.s, @250°C and 1 atm)
Ethylene	0.2274	0.3246	28	6.48E-04	1.68E-05
Oxygen	0.0577	0.0942	32	7.34E-04	3.16E-05
Methane	0.5735	0.468	16	3.69E-04	1.76E-05
Carbon dioxide	0.0414	0.0928	44	1.02E-03	2.48E-05
Helium	0.1	0.0204	4	8.83E-04	2.93E-05

Mixture density is calculated as follows:

$$\rho_{f,p} = \sum_i^n (\rho_i * x_i), i = \text{reactor inlet gases}$$

$$\text{For } T_1 = 288.7K \text{ and } T_2 = 523.15K$$

$$\rho_{2,@523.15K} = \rho_{1,@60^\circ F}$$

$$* \frac{T_1}{T_2} \text{ (Temperature compensation for density based on IGM)}$$

$$\rho_{2,@523.15K} = \rho_{f,p} = 5.31 * 10^{-4} g/cm^3 = 0.531 kg/m^3$$

Mixture viscosity is found from the formula as follows [186]:

$$\mu_{f,p} = \frac{\sum_i^n \mu_i * x_i * \sqrt{MW_i}}{\sum_i^n x_i * \sqrt{MW_i}}$$

$$\mu_{f,p} = 1.94 * 10^{-5} Pa.s$$

Volumetric flow rate is adjusted as follows:

$$\text{For } T_1 = 298.15K \text{ and } T_2 = 523.15K$$

$$Q_T = Q_{1,@298.15K}$$

$$Q_{2,@523.15K} = Q_{1,@298.15K}$$

$$* \frac{T_1}{T_2} \text{ (Temperature compensation for density based on IGM)}$$

$$Q_{2,@523.15K} = 75.0 \frac{cm^3}{min} * \frac{298.15K}{523.15K}$$

$$Q'_T = Q_{2,@523.15K} = 131.6 sccm$$

Porosity calculation [187]:

$$\epsilon_{b,p} = 1 - \frac{\rho_b(SiC)}{\rho_p(SiC)} = 1 - \frac{1570 kg/m^3}{3210 kg/m^3}$$

$$\epsilon_{b,p} = 0.511$$

Superficial velocity calculation:

$$v_{f,p} = \frac{Q'_T}{A} = \frac{Q'_T}{\pi * d_t^2 / 4} = \frac{131.6 cm^3/min}{0.636 cm^2}$$

$$v_{f,p} = 206.92 \text{ cm/min} = 3.45 \text{ cm/s} = 0.0345 \text{ m/s}$$

Interstitial velocity calculation:

$$v_{is} = \frac{v_{f,p}}{\epsilon_{b,p}} = \frac{3.45 \text{ cm/s}}{0.511}$$

$$v_{is} = 6.75 \text{ cm/s} = 0.0675 \text{ m/s}$$

Reynold number calculation in packed bed:

$$G' = v_{f,p} * \rho_{f,p} = 0.0345 \text{ m/s} * 0.531 \text{ kg/m}^3$$

$$G' = 0.0183 \frac{\text{kg}}{\text{m}^2 * \text{s}}$$

$$Re_{p,p} = \frac{d_p * G'}{(1 - \epsilon_{b,p}) * \mu_{f,p}} = \frac{(2.12 * 10^{-4} \text{ m}) * (0.0183 \frac{\text{kg}}{\text{m}^2 * \text{s}})}{(1 - 0.511) * (1.94 * 10^{-5} \text{ Pa.s})}$$

$$Re_{p,p} = 0.41 < 1 \text{ (Darcy Flow)}$$

Hydrodynamic entrance region calculation:

$$L_{h,laminar} = 0.05 * Re_{p,p} * d_t = 0.05 * (0.41) * (0.9 \text{ cm})$$

$$L_{h,laminar} = 0.019 \text{ cm} \ll 2 \text{ cm (L, catalyst mixture bed length)}$$

Therefore, the governing flow type is plug flow.

Pressure drop calculation in porous media across the fixed bed by using Carman-Kozeny equation [164]:

- $Re_{p,p}$ is lower than 1 (Darcy flow) and porosity is very close to 0.5

-Specific surface area (a_v) is calculated from $6/d_p$ (based on spherical particle)

-Kozeny constant (K) is taken as 5 for fixed bed.

$$\Delta P = \frac{K * \mu_{f,p} * v_{f,p} * L * (1 - \epsilon_{b,p})^2 * a_v^2}{\epsilon_{b,p}^3}$$

$$\Delta P = \frac{180 * (1.94 * 10^{-5} \text{ Pa.s}) * 0.0345 \text{ m/s} * 0.02 \text{ m} * (1 - 0.511)^2}{(2.12 * 10^{-4} \text{ m})^2 * (0.511)^3}$$

$$\Delta P = 96.07 \text{ Pa} = 9.48 * 10^{-4} \text{ atm}$$

Péclet number calculation [112]:

$$Pe_z = 0.087 * Re_{p,p}^{0.23} * \frac{L}{d_p}$$

$$Pe_z = 6.69$$

Gas-hourly space velocity (GHSV) calculation:

$$GHSV = \frac{Q_T}{V_{c,b}} = \frac{Q_T}{\frac{m_{c,b}}{\rho_{s,p}}}$$

$$\rho_{s,p} = 1.57 \text{ g/cm}^3$$

Q_T : Total volumetric flow rate (sccm)

$V_{c,b}$: Catalyst mixture volume in the bed (cm^3)

$m_{c,b}$: Total catalyst mixture mass (g)

$\rho_{s,p}$: Catalyst mixture density calculated by tapped density measurement (gcm^{-3})

L : Height of the catalyst bed (cm)

ST : Space time (s)

d_p : Particle size of the catalyst (μm)

Table B.2. Interphase (external) mass transfer limitation experiments.

Catalyst (g)	SiC (g)	$m_{c,b}$ (g)	$V_{c,b}$ (cm^3)	L (cm)	Q_T (cm^3/min)	GHSV (1/s)	ST (s)	Ethylene Conversion
0.05	0.45	0.50	0.318	0.50	18.835	0.9857	1.0145	4.03
0.1	0.90	1.00	0.637	1.00	37.685	0.9861	1.0141	9.73
0.2	1.80	2.00	1.274	1.99	75.000	0.9813	1.0191	13.95
0.3	2.70	3.00	1.911	2.99	113.070	0.9862	1.0140	13.93

Table B.3. Intraphase (internal) mass transfer limitation experiments.

Catalyst (g)	SiC (g)	m _{c,b} (g)	V _{c,b} (cm ³)	L (cm)	Q _T (cm ³ /min)	GHSV (1/s)	ST (s)	d _p (μm)	Ethylene Conversion
0.2	1.80	2.00	1.274	2.0	75.0	0.9813	1.0191	850	4.66
0.2	1.80	2.00	1.274	2.0	75.0	0.9813	1.0191	425	9.80
0.2	1.80	2.00	1.274	2.0	75.0	0.9813	1.0191	212	13.95
0.2	1.80	2.00	1.274	2.0	75.0	0.9813	1.0191	106	13.81

$$SE = \frac{\sigma_{ex}}{\sqrt{n_{se}}} * t_{\alpha_{st}, n-1}$$

SE: Standard error of mean

$$\alpha_{st} = 0.05$$

n_{se}: number of experiment used for standard error calculation

σ_{ex}: standard deviation of each experiment

APPENDIX C

EXPERIMENTAL DOMAIN AND EXPERIMENTAL DESIGN CONSIDERATIONS

Table C.1. Experiments that are used for kinetic model determination

Cat. Load. #	Set Name	Exp. Name	Exp. #	Cat. Amt(g)	Flow Rates (sccm)							C ₂ H ₄ /O ₂ ratio	p (barg)	Total flow (sccm)	Concentrations (%)				
					C ₂ H ₄	O ₂	CH ₄	CO ₂	EO (in He)	He	VCM (in He)				C ₂ H ₄	O ₂	CO ₂	EO	VCM (ppm)
0a	0	1	1	0.1	20.0	5.5	46.5	0.0	0.0	0.0	8.0	0	80.0	25.0	6.9	0.0	0.0	0.5	58.1
	0	2	2	0.1	20.0	5.5	50.0	0.0	0.0	0.0	4.0	0	79.5	25.2	6.9	0.0	0.0	0.3	62.9
	0	3	3	0.1	20.0	5.5	42.5	0.0	0.0	0.0	12.0	0	80.0	25.0	6.9	0.0	0.0	0.8	53.1
0b	0	1	1	0.1	21.5	5.5	43.0	2.0	0.0	0.0	8.0	0	80.0	26.9	6.9	2.5	0.0	0.5	53.8
	2	0a	1	0.1	17.1	4.3	47.3	3.1	0.0	3.2	0.0	0	75.0	22.7	5.8	4.1	0.0	0.0	63.1
	2	0b	2	0.1	17.1	4.3	47.3	3.1	0.0	3.2	0.0	0	75.0	22.7	5.8	4.1	0.0	0.0	63.1
	2	0c	3	0.1	17.1	4.3	47.3	3.1	0.0	3.2	0.0	0	75.0	22.7	5.8	4.1	0.0	0.0	63.1
	2	2b0	4	0.1	17.1	4.3	43.0	3.1	0.0	0.0	7.5	0	75.0	22.7	5.8	4.1	0.0	0.5	57.4
1	2	2b1	5	0.1	11.5	2.9	50.0	3.1	0.0	0.0	7.5	0	75.0	15.3	3.9	4.1	0.0	0.5	66.7
	2	2b2	6	0.1	30.7	7.8	25.8	3.1	0.0	0.0	7.5	0	75.0	41.0	10.4	4.1	0.0	0.5	34.5
	2	2b3	7	0.1	50.0	12.7	1.7	3.1	0.0	0.0	7.5	0	75.0	66.7	16.9	4.1	0.0	0.5	2.3
	2	1a	8	0.1	17.1	4.3	44.5	1.6	0.0	0.0	7.5	0	75.0	22.7	5.8	2.1	0.0	0.5	59.4
	2	1b	9	0.1	17.1	4.3	44.5	1.6	0.0	0.0	7.5	0	75.0	22.7	5.8	2.1	0.0	0.5	59.4
	2	1c	10	0.1	17.1	4.3	44.5	1.6	0.0	0.0	7.5	0	75.0	22.7	5.8	2.1	0.0	0.5	59.4
	2	2a	11	0.1	17.1	4.3	43.0	3.1	0.0	0.0	7.5	0	75.0	22.7	5.8	4.1	0.0	0.5	57.4
	2	2c	12	0.1	17.1	4.3	43.0	3.1	0.0	0.0	7.5	0	75.0	22.7	5.8	4.1	0.0	0.5	57.4

(Cont.on next page)

Table C.1 (Cont.)

1	2	3a	13	0.1	17.1	4.3	41.5	4.6	0.0	0.0	7.5	3.9	0	75.0	22.7	5.8	6.2	0.0	0.5	55.3
	2	3b	14	0.1	17.1	4.3	41.5	4.6	0.0	0.0	7.5	3.9	0	75.0	22.7	5.8	6.2	0.0	0.5	55.3
	2	3c	15	0.1	17.1	4.3	41.5	4.6	0.0	0.0	7.5	3.9	0	75.0	22.7	5.8	6.2	0.0	0.5	55.3
	2	2b0	16	0.1	17.1	4.3	43.0	3.1	0.0	0.0	7.5	3.9	0	75.0	22.7	5.8	4.1	0.0	0.5	57.4
	2	4a	17	0.1	12.7	4.3	47.4	3.1	0.0	0.0	7.5	2.9	0	75.0	16.9	5.8	4.1	0.0	0.5	63.2
	2	4b1	18	0.1	10.7	3.7	50.0	3.1	0.0	0.0	7.5	2.9	0	75.0	14.3	4.9	4.1	0.0	0.5	66.7
	2	4b2	19	0.1	29.4	10.0	25.0	3.1	0.0	0.0	7.5	2.9	0	75.0	39.2	13.3	4.1	0.0	0.5	33.3
	2	4b3	20	0.1	48.1	16.3	0.0	3.1	0.0	0.0	7.5	2.9	0	75.0	64.1	21.8	4.1	0.0	0.5	0.0
	2	4c	21	0.1	12.7	4.3	47.4	3.1	0.0	0.0	7.5	2.9	0	75.0	16.9	5.8	4.1	0.0	0.5	63.2
	2	5a	22	0.1	21.4	4.3	38.7	3.1	0.0	0.0	7.5	4.9	0	75.0	28.5	5.8	4.1	0.0	0.5	51.6
	2	5b1	23	0.1	12.0	2.4	50.0	3.1	0.0	0.0	7.5	5.0	0	75.0	16.0	3.2	4.1	0.0	0.5	66.7
	2	5b2	24	0.1	31.0	6.3	27.1	3.1	0.0	0.0	7.5	5.0	0	75.0	41.3	8.3	4.1	0.0	0.5	36.2
	2	5b3	25	0.1	50.0	10.1	4.3	3.1	0.0	0.0	7.5	5.0	0	75.0	66.7	13.5	4.1	0.0	0.5	5.7
	2	5c	26	0.1	21.4	4.3	38.7	3.1	0.0	0.0	7.5	4.9	0	75.0	28.5	5.8	4.1	0.0	0.5	51.6
	2	2b0	27	0.1	17.1	4.3	43.0	3.1	0.0	0.0	7.5	3.9	0	75.0	22.7	5.8	4.1	0.0	0.5	57.4
2	1	1	1	0.1	50.0	1.4	22.1	1.6	0.0	0.0	0.0	36.8	0	75.0	66.6	1.8	2.1	0.0	0.0	29.5
	1	2	2	0.1	50.0	17.3	3.1	4.6	0.0	0.0	0.0	2.9	0	75.0	66.6	23.0	6.2	0.0	0.0	4.2
	1	3	3	0.1	19.3	1.4	49.7	4.6	0.0	0.0	0.0	14.2	0	75.0	25.7	1.8	6.2	0.0	0.0	66.3
	1	4	4	0.1	6.4	17.3	49.7	1.6	0.0	0.0	0.0	0.4	0	75.0	8.5	23.0	2.1	0.0	0.0	66.3
	1	14	5	0.1	26.4	10.7	34.7	3.2	0.0	0.0	0.0	2.5	0	75.0	35.2	14.3	4.3	0.0	0.0	46.3
	1	16	6	0.1	50.0	1.4	19.1	4.6	0.0	0.0	0.0	36.8	0	75.0	66.6	1.8	6.2	0.0	0.0	25.4
3	1	18	1	0.1	22.3	1.4	49.7	1.6	0.0	0.0	0.0	31.6	0	75.0	29.8	1.8	2.1	0.0	0.0	66.3
	1	23	2	0.1	20.2	17.3	32.9	4.6	0.0	0.0	0.0	7.1	0	75.0	27.0	23.0	6.2	0.0	0.0	43.8

(Cont. on next page)

Table C.1 (Cont.)

3	1	24	3	0.1	5.3	17.3	49.1	3.3	0.0	0.0	0.0	0.0	14.9	0	75.0	7.1	23.0	4.4	0.0	0.0	65.4
	1	28	4	0.1	25.3	9.2	29.6	3.0	0.0	0.0	7.9	9.7	0	0	75.0	33.7	12.3	4.1	0.0	0.5	39.5
	1	5	5	0.1	5.3	17.3	32.7	4.6	0.0	0.0	15.0	7.1	0	0	75.0	7.1	23.0	6.2	0.0	1.0	43.7
	1	6	6	0.1	7.3	1.4	49.7	1.6	0.0	0.0	15.0	31.6	0	0	75.0	9.8	1.8	2.1	0.0	1.0	66.3
	1	8	7	0.1	46.0	9.3	3.1	1.6	0.0	0.0	15.0	2.0	0	0	75.0	61.3	12.4	2.1	0.0	1.0	4.2
	1	11	8	0.1	35.1	1.4	18.9	4.6	0.0	0.0	15.0	4.1	0	0	75.0	46.8	1.8	6.2	0.0	1.0	25.2
	1	13	9	0.1	36.0	17.3	3.1	3.6	0.0	0.0	15.0	0.9	0	0	75.0	48.0	23.0	4.8	0.0	1.0	4.2
	1	19	10	0.1	5.3	1.4	48.7	4.6	0.0	0.0	15.0	10.5	0	0	75.0	7.1	1.8	6.2	0.0	1.0	64.9
	1	28	11	0.1	25.3	9.2	29.6	3.0	0.0	0.0	7.9	9.7	0	0	75.0	33.7	12.3	4.1	0.0	0.5	39.5
	1	20	12	0.1	50.0	1.4	7.1	1.6	0.0	0.0	15.0	4.5	0	0	75.0	66.6	1.8	2.1	0.0	1.0	9.5
	1	21	13	0.1	5.3	17.3	35.8	1.6	0.0	0.0	15.0	22.7	0	0	75.0	7.1	23.0	2.1	0.0	1.0	47.7
	1	22	14	0.1	35.0	17.3	3.1	4.6	0.0	0.0	15.0	0.7	0	0	75.0	46.6	23.0	6.2	0.0	1.0	4.2
	1	27	15	0.1	50.0	4.3	3.1	2.6	0.0	0.0	15.0	1.2	0	0	75.0	66.6	5.8	3.5	0.0	1.0	4.2
	1	12	16	0.1	5.3	1.4	49.7	3.9	0.0	0.0	14.6	12.7	0	0	75.0	7.1	1.8	5.2	0.0	1.0	66.3
	1	7	17	0.1	42.0	17.3	3.1	1.6	0.0	0.0	11.0	2.0	0	0	75.0	56.0	23.0	2.1	0.0	0.7	4.2
	1	28	18	0.1	25.3	9.2	29.6	3.0	0.0	0.0	7.9	9.7	0	0	75.0	33.7	12.3	4.1	0.0	0.5	39.5
	1	25	19	0.1	5.3	8.0	49.7	1.6	0.0	0.0	10.4	31.6	0	0	75.0	7.1	10.6	2.1	0.0	0.7	66.3
	1	10	20	0.1	50.0	1.4	9.1	4.6	0.0	0.0	10.0	2.0	0	0	75.0	66.6	1.8	6.2	0.0	0.7	12.1
	1	15	21	0.1	23.3	17.3	25.8	2.8	0.0	0.0	5.8	9.3	0	0	75.0	31.0	23.0	3.7	0.0	0.4	34.5
	1	28	22	0.1	25.3	9.2	29.6	3.0	0.0	0.0	7.9	9.7	0	0	75.0	33.7	12.3	4.1	0.0	0.5	39.5
	1	26	23	0.1	50.0	12.3	3.1	4.6	0.0	0.0	5.0	0.7	0	0	75.0	66.6	16.4	6.2	0.0	0.3	4.2
	1	9	24	0.1	5.3	10.6	49.7	4.6	0.0	0.0	4.6	10.7	0	0	75.0	7.1	14.2	6.2	0.0	0.3	66.3
	1	28	25	0.1	25.3	9.2	29.6	3.0	0.0	0.0	7.9	9.7	0	0	75.0	33.7	12.3	4.1	0.0	0.5	39.5

(Cont.on next page)

Table C.1 (Cont.)

4	2	0b	1	0.2	17.1	4.3	47.3	3.1	0.0	3.2	0.0	3.9	0	75.0	22.7	5.8	4.1	0.0	0.0	63.1
	2	0a	2	0.2	17.1	4.3	47.3	3.1	0.0	3.2	0.0	3.9	0	75.0	22.7	5.8	4.1	0.0	0.0	63.1
	2	0c	3	0.2	17.1	4.3	47.3	3.1	0.0	3.2	0.0	3.9	0	75.0	22.7	5.8	4.1	0.0	0.0	63.1
	2	2b0	4	0.2	17.1	4.3	43.0	3.1	0.0	0.0	7.5	3.9	0	75.0	22.7	5.8	4.1	0.0	0.5	57.4
	2	1c	5	0.2	17.1	4.3	44.5	1.6	0.0	0.0	7.5	3.9	0	75.0	22.7	5.8	2.1	0.0	0.5	59.4
	2	2c	6	0.2	17.1	4.3	43.0	3.1	0.0	0.0	7.5	3.9	0	75.0	22.7	5.8	4.1	0.0	0.5	57.4
	2	3c	7	0.2	17.1	4.3	41.5	4.6	0.0	0.0	7.5	3.9	0	75.0	22.7	5.8	6.2	0.0	0.5	55.3
	2	4c	8	0.2	12.7	4.3	47.4	3.1	0.0	0.0	7.5	2.9	0	75.0	16.9	5.8	4.1	0.0	0.5	63.2
	2	5c	9	0.2	21.4	4.3	38.7	3.1	0.0	0.0	7.5	4.9	0	75.0	28.5	5.8	4.1	0.0	0.5	51.6
	2	7c	10	0.2	19.5	2.3	42.5	3.1	0.0	0.0	7.5	8.4	0	75.0	26.0	3.1	4.1	0.0	0.5	56.7
	2	8c	11	0.2	17.1	6.3	41.0	3.1	0.0	0.0	7.5	2.7	0	75.0	22.7	8.4	4.1	0.0	0.5	54.7
	2	9c	12	0.2	17.1	4.3	46.8	3.1	0.0	0.0	3.8	3.9	0	75.0	22.7	5.8	4.1	0.0	0.3	62.3
	2	10c	13	0.2	17.1	4.3	39.3	3.1	0.0	0.0	11.3	3.9	0	75.0	22.7	5.8	4.1	0.0	0.8	52.4
	2	11c	14	0.2	17.1	4.3	35.5	3.1	0.0	0.0	15.0	3.9	0	75.0	22.7	5.8	4.1	0.0	1.0	47.3
	2	2b0	15	0.2	17.1	4.3	43.0	3.1	0.0	0.0	7.5	3.9	0	75.0	22.7	5.8	4.1	0.0	0.5	57.4
	2	2b1	16	0.2	11.5	2.9	50.0	3.1	0.0	0.0	7.5	3.9	0	75.0	15.3	3.9	4.1	0.0	0.5	66.7
	2	2b2	17	0.2	30.7	7.8	25.8	3.1	0.0	0.0	7.5	3.9	0	75.0	41.0	10.4	4.1	0.0	0.5	34.5
	2	2b3	18	0.2	50.0	12.7	1.7	3.1	0.0	0.0	7.5	3.9	0	75.0	66.7	16.9	4.1	0.0	0.5	2.3
	2	1b	19	0.2	17.1	4.3	44.5	1.6	0.0	0.0	7.5	3.9	0	75.0	22.7	5.8	2.1	0.0	0.5	59.4
	2	3b	20	0.2	17.1	4.3	41.5	4.6	0.0	0.0	7.5	3.9	0	75.0	22.7	5.8	6.2	0.0	0.5	55.3
	2	4b1	21	0.2	10.7	3.7	50.0	3.1	0.0	0.0	7.5	2.9	0	75.0	14.3	4.9	4.1	0.0	0.5	66.7
	2	4b2	22	0.2	29.4	10.0	25.0	3.1	0.0	0.0	7.5	2.9	0	75.0	39.2	13.3	4.1	0.0	0.5	33.3
	2	4b3	23	0.2	48.1	16.3	0.0	3.1	0.0	0.0	7.5	2.9	0	75.0	64.1	21.8	4.1	0.0	0.5	0.0

(Cont.on next page)

Table C.1 (Cont.)

4	2	5b1	24	0.2	12.0	2.4	50.0	3.1	0.0	0.0	7.5	5.0	0	75.0	16.0	3.2	4.1	0.0	0.5	66.7
	2	5b2	25	0.2	31.0	6.3	27.1	3.1	0.0	0.0	7.5	5.0	0	75.0	41.3	8.3	4.1	0.0	0.5	36.2
	2	5b3	26	0.2	50.0	10.1	4.3	3.1	0.0	0.0	7.5	5.0	0	75.0	66.7	13.5	4.1	0.0	0.5	5.7
	2	7b1	27	0.2	12.9	1.5	50.0	3.1	0.0	0.0	7.5	8.4	0	75.0	17.2	2.0	4.1	0.0	0.5	66.7
	2	7b2	28	0.2	31.4	3.7	29.2	3.1	0.0	0.0	7.5	8.4	0	75.0	41.9	5.0	4.1	0.0	0.5	39.0
	2	7b3	29	0.2	50.0	6.0	8.4	3.1	0.0	0.0	7.5	8.4	0	75.0	66.7	7.9	4.1	0.0	0.5	11.3
	2	8b1	30	0.2	10.5	3.9	50.0	3.1	0.0	0.0	7.5	2.7	0	75.0	14.0	5.2	4.1	0.0	0.5	66.7
	2	8b2	31	0.2	28.8	10.6	25.0	3.1	0.0	0.0	7.5	2.7	0	75.0	38.4	14.2	4.1	0.0	0.5	33.3
	2	8b3	32	0.2	47.0	17.4	0.0	3.1	0.0	0.0	7.5	2.7	0	75.0	62.7	23.1	4.1	0.0	0.5	0.0
	2	2b0	33	0.2	17.1	4.3	43.0	3.1	0.0	0.0	7.5	3.9	0	75.0	22.7	5.8	4.1	0.0	0.5	57.4
	2	9b	34	0.2	17.1	4.3	46.8	3.1	0.0	0.0	3.8	3.9	0	75.0	22.7	5.8	4.1	0.0	0.3	62.3
	2	10b	35	0.2	17.1	4.3	39.3	3.1	0.0	0.0	11.3	3.9	0	75.0	22.7	5.8	4.1	0.0	0.8	52.4
	2	11b	36	0.2	17.1	4.3	35.5	3.1	0.0	0.0	15.0	3.9	0	75.0	22.7	5.8	4.1	0.0	1.0	47.3
	2	12	37	0.2	19.3	4.9	48.7	3.5	0.0	0.0	8.5	3.9	0	85.0	22.7	5.8	4.1	0.0	0.5	57.3
	2	13	38	0.2	18.2	4.6	45.9	3.3	0.0	0.0	8.0	3.9	0	80.0	22.7	5.8	4.1	0.0	0.5	57.4
	2	14	39	0.2	15.9	4.0	40.1	2.9	0.0	0.0	7.0	3.9	0	70.0	22.7	5.8	4.1	0.0	0.5	57.3
	2	15	40	0.2	14.8	3.8	37.3	2.7	0.0	0.0	6.5	3.9	0	65.0	22.7	5.8	4.1	0.0	0.5	57.3
	2	1a	41	0.2	17.1	4.3	44.5	1.6	0.0	0.0	7.5	3.9	0	75.0	22.7	5.8	2.1	0.0	0.5	59.4
	2	2a	42	0.2	17.1	4.3	43.0	3.1	0.0	0.0	7.5	3.9	0	75.0	22.7	5.8	4.1	0.0	0.5	57.4
	2	3a	43	0.2	17.1	4.3	41.5	4.6	0.0	0.0	7.5	3.9	0	75.0	22.7	5.8	6.2	0.0	0.5	55.3
	2	4a	44	0.2	12.7	4.3	47.4	3.1	0.0	0.0	7.5	2.9	0	75.0	16.9	5.8	4.1	0.0	0.5	63.2
	2	5a	45	0.2	21.4	4.3	38.7	3.1	0.0	0.0	7.5	4.9	0	75.0	28.5	5.8	4.1	0.0	0.5	51.6
	2	7a	46	0.2	19.5	2.3	42.5	3.1	0.0	0.0	7.5	8.4	0	75.0	26.0	3.1	4.1	0.0	0.5	56.7

(Cont.on next page)

Table C.1 (Cont.)

4	2	8a	47	0.2	17.1	6.3	41.0	3.1	0.0	0.0	7.5	2.7	0	75.0	22.7	8.4	4.1	0.0	0.5	54.7
	2	9a	48	0.2	17.1	4.3	46.8	3.1	0.0	0.0	3.8	3.9	0	75.0	22.7	5.8	4.1	0.0	0.3	62.3
	2	10a	49	0.2	17.1	4.3	39.3	3.1	0.0	0.0	11.3	3.9	0	75.0	22.7	5.8	4.1	0.0	0.8	52.4
	2	11a	50	0.2	17.1	4.3	35.5	3.1	0.0	0.0	15.0	3.9	0	75.0	22.7	5.8	4.1	0.0	1.0	47.3
	2	2b0	51	0.2	17.1	4.3	43.0	3.1	0.0	0.0	7.5	3.9	0	75.0	22.7	5.8	4.1	0.0	0.5	57.4
5	2	2b0	1	0.2	17.1	4.3	43.0	3.1	0.0	0.0	7.5	3.9	0	75.0	22.7	5.8	4.1	0.0	0.5	57.3
	3&4	3	2	0.2	17.1	4.3	14.7	3.1	28.4	0.0	7.5	3.9	0	75.0	22.7	5.8	4.1	0.5	0.5	19.5
	2	9b	3	0.2	17.1	4.3	46.8	3.1	0.0	0.0	3.8	3.9	0	75.0	22.7	5.8	4.1	0.0	0.3	62.3
	2	10b	4	0.2	17.1	4.3	39.3	3.1	0.0	0.0	11.3	3.9	0	75.0	22.7	5.8	4.1	0.0	0.8	52.3
	2	11b	5	0.2	17.1	4.3	35.5	3.1	0.0	0.0	15.0	3.9	0	75.0	22.7	5.8	4.1	0.0	1.0	47.3
6	2	12	6	0.2	19.3	4.9	48.7	3.5	0.0	0.0	8.5	3.9	0	85.0	22.7	5.8	4.1	0.0	0.5	57.4
	2	13	7	0.2	18.2	4.6	45.9	3.3	0.0	0.0	8.0	3.9	0	80.0	22.7	5.8	4.1	0.0	0.5	57.4
	3&4&5	1	1	0.2	17.1	4.3	43.0	3.1	0.0	7.5	0.0	3.9	0	75.0	22.7	5.8	4.1	0.0	0.0	57.3
	3&4&5	2	2	0.2	0.0	4.3	20.7	0.0	50.0	0.0	0.0	0.0	0	75.0	0.0	5.8	0.0	0.8	0.0	27.6
	3&4&5	3	3	0.2	17.1	4.3	43.0	0.0	0.0	10.6	0.0	3.9	0	75.0	22.7	5.8	0.0	0.0	0.0	57.3
7	3&4&5	4	4	0.2	17.1	4.3	33.6	0.0	20.0	0.0	0.0	3.9	0	75.0	22.7	5.8	0.0	0.3	0.0	44.8
	3&4&5	1	5	0.2	17.1	4.3	43.0	3.1	0.0	7.5	0.0	3.9	0	75.0	22.7	5.8	4.1	0.0	0.0	57.3
	3&4&5	1	1	0.2	17.1	4.3	43.0	3.1	0.0	7.5	0.0	3.9	0	75.0	22.7	5.8	4.1	0.0	0.0	57.3
	3&4&5	2	2	0.2	0.0	4.3	20.7	0.0	50.0	0.0	0.0	0.0	0	75.0	0.0	5.8	0.0	0.8	0.0	27.6
	3&4&5	3	3	0.2	0.0	4.3	20.7	0.0	50.0	0.0	0.0	0.0	0	75.0	0.0	5.8	0.0	0.8	0.0	27.6
7	3&4&5	4	4	0.2	0.0	4.3	20.7	0.0	50.0	0.0	0.0	0.0	0	75.0	0.0	5.8	0.0	0.8	0.0	27.6
	3&4&5	5	5	0.2	0.0	4.3	20.7	0.0	50.0	0.0	0.0	0.0	0	75.0	0.0	5.8	0.0	0.8	0.0	27.6
	3&4&5	6	6	0.2	0.0	8.7	16.3	0.0	50.0	0.0	0.0	0.0	0	75.0	0.0	11.5	0.0	0.8	0.0	21.8

(Cont. on next page)

Table C.1 (Cont.)

7	3&4&5	7	7	0.2	0.0	13.0	12.0	0.0	50.0	0.0	0.0	0.0	0.0	0	75.0	0.0	17.3	0.0	0.8	0.0	16.0
	3&4&5	8	8	0.2	0.0	4.3	13.2	0.0	50.0	7.5	0.0	0.0	0.0	0	75.0	0.0	5.8	0.0	0.8	0.0	17.6
	3&4&5	9	9	0.2	0.0	4.3	13.2	0.0	50.0	0.0	7.5	0.0	0.0	0	75.0	0.0	5.8	0.0	0.8	0.5	17.6
	3&4&5	2	10	0.2	0.0	4.3	20.7	0.0	50.0	0.0	0.0	0.0	0.0	0	75.0	0.0	5.8	0.0	0.8	0.0	27.6
	3&4&5	10	11	0.2	8.5	4.3	12.1	0.0	50.0	0.0	0.0	0.0	2.0	0	75.0	11.4	5.8	0.0	0.8	0.0	16.2
	3&4&5	11	12	0.2	17.1	4.3	3.6	0.0	50.0	0.0	0.0	0.0	3.9	0	75.0	22.7	5.8	0.0	0.8	0.0	4.8
	3&4&5	6	13	0.2	0.0	8.7	16.3	0.0	50.0	0.0	0.0	0.0	0.0	0	75.0	0.0	11.5	0.0	0.8	0.0	21.8
	3&4&5	7	14	0.2	0.0	13.0	12.0	0.0	50.0	0.0	0.0	0.0	0.0	0	75.0	0.0	17.3	0.0	0.8	0.0	16.0
	3&4&5	2	15	0.2	0.0	4.3	20.7	0.0	50.0	0.0	0.0	0.0	0.0	0	75.0	0.0	5.8	0.0	0.8	0.0	27.6
	3&4&5	3	16	0.2	0.0	4.3	20.7	0.0	50.0	0.0	0.0	0.0	0.0	0	75.0	0.0	5.8	0.0	0.8	0.0	27.6
	3&4&5	2	17	0.2	0.0	4.3	20.7	0.0	50.0	0.0	0.0	0.0	0.0	0	75.0	0.0	5.8	0.0	0.8	0.0	27.6
	3&4&5	4	18	0.2	0.0	4.3	20.7	0.0	50.0	0.0	0.0	0.0	0.0	0	75.0	0.0	5.8	0.0	0.8	0.0	27.6
	3&4&5	5	19	0.2	0.0	4.3	20.7	0.0	50.0	0.0	0.0	0.0	0.0	0	75.0	0.0	5.8	0.0	0.8	0.0	27.6
	3&4&5	23	20	0.2	0.0	4.3	20.7	0.0	50.0	0.0	0.0	0.0	0.0	0	75.0	0.0	5.8	0.0	0.8	0.0	27.6
	3&4&5	2	21	0.2	0.0	4.3	20.7	0.0	50.0	0.0	0.0	0.0	0.0	0	75.0	0.0	5.8	0.0	0.8	0.0	27.6
	3&4&5	10	22	0.2	8.5	4.3	12.1	0.0	50.0	0.0	0.0	0.0	2.0	0	75.0	11.4	5.8	0.0	0.8	0.0	16.2
	3&4&5	11	23	0.2	17.1	4.3	3.6	0.0	50.0	0.0	0.0	0.0	3.9	0	75.0	22.7	5.8	0.0	0.8	0.0	4.8
	3&4&5	8	24	0.2	0.0	4.3	13.2	0.0	50.0	7.5	0.0	0.0	0.0	0	75.0	0.0	5.8	0.0	0.8	0.0	17.6
	3&4&5	9	25	0.2	0.0	4.3	13.2	0.0	50.0	0.0	7.5	0.0	0.0	0	75.0	0.0	5.8	0.0	0.8	0.5	17.6
	3&4&5	2	26	0.2	0.0	4.3	20.7	0.0	50.0	0.0	0.0	0.0	0.0	0	75.0	0.0	5.8	0.0	0.8	0.0	27.6
	3&4&5	1	27	0.2	17.1	4.3	43.0	3.1	0.0	7.5	0.0	0.0	3.9	0	75.0	22.7	5.8	4.1	0.0	0.0	57.3
	3&4&5	2b0	28	0.2	17.1	4.3	43.0	3.1	0.0	0.0	7.5	0.0	3.9	0	75.0	22.7	5.8	4.1	0.0	0.5	57.4
	3&4&5	12	29	0.2	30.7	7.8	25.8	3.1	0.0	0.0	7.5	3.9	3.9	0	75.0	41.0	10.4	4.1	0.0	0.5	34.5

(Cont.on next page)

Table C.1 (Cont.)

7	3&4&5	13	30	0.2	50.0	12.7	1.7	3.1	0.0	0.0	7.5	3.9	0	75.0	66.7	16.9	4.1	0.0	0.5	2.3
	3&4&5	14	31	0.2	17.1	4.3	43.0	3.1	0.0	0.0	7.5	3.9	2	75.0	22.7	5.8	4.1	0.0	0.5	57.4
	3&4&5	15	32	0.2	30.7	7.8	25.8	3.1	0.0	0.0	7.5	3.9	2	75.0	41.0	10.4	4.1	0.0	0.5	34.5
	3&4&5	16	33	0.2	50.0	12.7	1.7	3.1	0.0	0.0	7.5	3.9	2	75.0	66.7	16.9	4.1	0.0	0.5	2.3
	3&4&5	17	34	0.2	17.1	4.3	43.0	3.1	0.0	0.0	7.5	3.9	4	75.0	22.7	5.8	4.1	0.0	0.5	57.4
	3&4&5	18	35	0.2	30.7	7.8	25.8	3.1	0.0	0.0	7.5	3.9	4	75.0	41.0	10.4	4.1	0.0	0.5	34.5
	3&4&5	19	36	0.2	50.0	12.7	1.7	3.1	0.0	0.0	7.5	3.9	4	75.0	66.7	16.9	4.1	0.0	0.5	2.3
	3&4&5	20	37	0.2	17.1	4.3	43.0	3.1	0.0	0.0	7.5	3.9	6	75.0	22.7	5.8	4.1	0.0	0.5	57.4
	3&4&5	21	38	0.2	30.7	7.8	25.8	3.1	0.0	0.0	7.5	3.9	6	75.0	41.0	10.4	4.1	0.0	0.5	34.5
	3&4&5	22	39	0.2	50.0	12.7	1.7	3.1	0.0	0.0	7.5	3.9	6	75.0	66.7	16.9	4.1	0.0	0.5	2.3
	3&4&5	23	40	0.2	17.1	4.3	43.0	3.1	0.0	0.0	7.5	3.9	8	75.0	22.7	5.8	4.1	0.0	0.5	57.4
	3&4&5	24	41	0.2	30.7	7.8	25.8	3.1	0.0	0.0	7.5	3.9	8	75.0	41.0	10.4	4.1	0.0	0.5	34.5
	3&4&5	25	42	0.2	50.0	12.7	1.7	3.1	0.0	0.0	7.5	3.9	8	75.0	66.7	16.9	4.1	0.0	0.5	2.3
	3&4&5	26	43	0.2	17.1	4.3	43.0	3.1	0.0	0.0	7.5	3.9	10	75.0	22.7	5.8	4.1	0.0	0.5	57.4
	3&4&5	27	44	0.2	30.7	7.8	25.8	3.1	0.0	0.0	7.5	3.9	10	75.0	41.0	10.4	4.1	0.0	0.5	34.5
	3&4&5	28	45	0.2	50.0	12.7	1.7	3.1	0.0	0.0	7.5	3.9	10	75.0	66.7	16.9	4.1	0.0	0.5	2.3
	3&4&5	1	46	0.2	17.1	4.3	43.0	3.1	0.0	7.5	0.0	3.9	0	75.0	22.7	5.8	4.1	0.0	0.0	57.3

Table C.2. Range values of industrial ethylene oxide reactor taken from different operational periods (SOR and EOR).

End of run (EOR)			Start of run (SOR)			Mid values		
Reactor Inputs								
	Min	Max		Min	Max		EOR	SOR
C ₂ H ₄ (%)	24.8	28.5	C ₂ H ₄ (%)	19.2	26.8	C ₂ H ₄ (%)	26.7	23
O ₂ (%)	7.2	8.4	O ₂ (%)	5.1	7.1	O ₂ (%)	7.8	6.1
CO ₂ (%)	3	4.7	CO ₂ (%)	2.1	2.7	CO ₂ (%)	3.9	2.4
C ₂ H ₄ /O ₂	3	3.9	C ₂ H ₄ /O ₂	2.7	5.3	C ₂ H ₄ /O ₂	3.5	4
Reactor Outputs								
	Min	Max		Min	Max		EOR	SOR
C ₂ H ₄ (%)	22.7	26.3	C ₂ H ₄ (%)	16.9	26	C ₂ H ₄ (%)	24.5	21.5
O ₂ (%)	4.4	5.4	O ₂ (%)	3.1	4.7	O ₂ (%)	4.9	3.9
CO ₂ (%)	4.2	6.2	CO ₂ (%)	2.8	4.4	CO ₂ (%)	5.2	3.6
C ₂ H ₄ /O ₂	4.2	5.9	C ₂ H ₄ /O ₂	3.6	8.4	C ₂ H ₄ /O ₂	5.1	6
Others								
	Min	Max		Min	Max		EOR	SOR
Fresh VCM(kg)	0.2	0.5	Fresh VCM(kg)	0.3	0.7	Fresh VCM(kg)	0.4	0.5
Temperature	239	266	Temperature	227	257	Temperature	253	242

Table C.3. Optimal design summary and performance criteria.

Objective	Optimization (RSM)	
Process model	Quadratic	
Mixture model	Quadratic	
Design	D-Optimal	
Runs in design	27	
Center points	5	
Replicates	0	
N = actual runs	32	
Maximum runs	12000	
Constraints	No	
Candidate set		
Extreme vertices	50	
Edge points	204	
Centroids of high dim. surfaces	21	
Total runs	275	
D-Optimal		
Potential terms	Cubic	
Number of inclusions	0	
Constraints	No	
Selected design number	14	
Design statistics	G-efficiency	67.4
	log(Det. of X'X)	21.8
	Norm. log(Det. of X'X)	-0.394
	Condition number	16.5

APPENDIX D

SAMPLE CALCULATIONS FOR MOLAR-BASED DATA RECONCILIATION

GC measurements for reactor outlet water-free nonreconciled composition

$$X_{out_0}^{C_2H_4} = 21.14\%, X_{out_0}^{O_2} = 4.14\%, X_{out_0}^{C_2H_4O} = 1.09\%, X_{out_0}^{CO_2} = 4.73\%, X_{out_0}^{CH_4} = 55.59\%$$

$$X_{out_0}^{He} = 10\%$$

Initial non-reconciled GC sum

$$\sum_{i=1}^{NC} X_{out_0}^i (mol\%) = 96.69 \text{ (water-free)}$$

$i = C_2H_4, O_2, C_2H_4O, CO_2 \text{ and } CH_4$

Reactor inlet concentrations

$$Q_{in}^{C_2H_4} = 17.06 \text{ sccm}, Q_{in}^{O_2} = 4.33 \text{ sccm}, Q_{in}^{C_2H_4O/He} = 0, Q_{in}^{CO_2} = 3.11 \text{ sccm}$$

$$Q_{in}^{CH_4} = 43.01 \text{ sccm}$$

$$Q_{in}^{VCM/He} = 7.5 \text{ sccm}, Q_{in}^{He} = 0$$

$$Q_{in}^{total} = 75 \text{ sccm}$$

$$\begin{aligned} X_{in}^{C_2H_4} (mol\%) &= \frac{100 * Q_{in}^{C_2H_4}}{(Q_{in}^{C_2H_4} + Q_{in}^{O_2} + Q_{in}^{CH_4} + Q_{in}^{CO_2} + Q_{in}^{C_2H_4O/He} + Q_{in}^{VCM/He} + Q_{in}^{He})} \\ &= 22.74 \end{aligned}$$

$$X_{in}^{O_2} (mol\%) = \frac{100 * Q_{in}^{O_2}}{(Q_{in}^{C_2H_4} + Q_{in}^{O_2} + Q_{in}^{CH_4} + Q_{in}^{CO_2} + Q_{in}^{C_2H_4O/He} + Q_{in}^{VCM/He} + Q_{in}^{He})} = 5.77$$

$$X_{in}^{CO_2} (mol\%) = \frac{100 * Q_{in}^{CO_2}}{(Q_{in}^{C_2H_4} + Q_{in}^{O_2} + Q_{in}^{CH_4} + Q_{in}^{CO_2} + Q_{in}^{C_2H_4O/He} + Q_{in}^{VCM/He} + Q_{in}^{He})}$$

$$= 4.14$$

$$X_{in}^{CH_4} (mol\%) = \frac{100 * Q_{in}^{CH_4}}{(Q_{in}^{C_2H_4} + Q_{in}^{O_2} + Q_{in}^{CH_4} + Q_{in}^{CO_2} + Q_{in}^{C_2H_4O/He} + Q_{in}^{VCM/He} + Q_{in}^{He})}$$

$$= 57.35$$

$$X_{in}^{He} (mol\%) = \frac{100 * (Q_{in}^{He} + 0.9877 * Q_{in}^{C_2H_4O/He} + 0.99995 * Q_{in}^{VCM/He})}{(Q_{in}^{C_2H_4} + Q_{in}^{O_2} + Q_{in}^{CH_4} + Q_{in}^{CO_2} + Q_{in}^{C_2H_4O/He} + Q_{in}^{VCM/He} + Q_{in}^{He})}$$

$$= 9.9995$$

$$X_{in}^{C_2H_4} = 22.74\%, X_{in}^{O_2} = 5.77\%, X_{in}^{C_2H_4O} = 0, X_{in}^{CO_2} = 4.14\%, X_{in}^{CH_4} = 57.35\%$$

$$X_{in}^{He} \cong 10\%$$

1st Iteration

$$Correction\ Factor(CF_1) = 1 - 0.5 * \left(\frac{X_{out_0}^{C_2H_4O} - X_{in}^{C_2H_4O}}{100} \right) - \left(\frac{X_{out_0}^{CO_2} - X_{in}^{CO_2}}{100} \right) = 0.989$$

$$X_{out_1}^{CH_4*} (mol\%) = \frac{X_{in}^{CH_4}}{CF_1} = 58.01$$

$$\sum_{i=1}^{NC} X_{out_1}^i (mol\%) = 99.10$$

$$Error\ in\ outlet\ CH_4(\%) = 100 * \frac{(X_{out_1}^{CH_4*} - X_{out_0}^{CH_4})}{X_{out_0}^{CH_4}} = 4.35$$

Carbon balance error (CBE)

$$CBE_1(\%) = \frac{[(2X_{out_0}^{C_2H_4} + 2X_{out_0}^{C_2H_4O} + X_{out_0}^{CO_2}) * (CF_1) - (2 * X_{in}^{C_2H_4} + 2 * X_{in}^{C_2H_4O} + X_{in}^{CO_2})]}{(2 * X_{in}^{C_2H_4} + 2 * X_{in}^{C_2H_4O} + X_{in}^{CO_2})}$$

$$* 100 = -1.99$$

$$X_{out_1}^{C_2H_4*} (mol\%) = \frac{X_{out_0}^{C_2H_4}}{(1 + CBE_1)} = 21.57, X_{out_1}^{C_2H_4O*} (mol\%) = \frac{X_{out_0}^{C_2H_4O}}{(1 + CBE_1)} = 1.11$$

$$X_{out_1}^{CO_2*} (mol\%) = \frac{X_{out_0}^{CO_2}}{(1 + CBE_1)} = 4.83$$

2nd Iteration

$$\begin{aligned} Correction\ Factor(CF_2) &= 1 - 0.5 * \left(\frac{X_{out_1}^{C_2H_4O*} * CF_1 - X_{in}^{C_2H_4O}}{100} \right) - \left(\frac{X_{out_1}^{CO_2*} - X_{in}^{CO_2}}{100} \right) \\ &= 0.988 \end{aligned}$$

$$X_{out_2}^{CH_4*} (mol\%) = \frac{X_{in}^{CH_4}}{CF_2} = 58.03$$

$$\sum_{i=1}^{NC} X_{out_2}^i (mol\%) = 99.68$$

$$Error\ in\ outlet\ CH_4(\%) = 100 * \frac{(X_{out_2}^{CH_4*} - X_{out_0}^{CH_4})}{X_{out_0}^{CH_4}} = 4.40$$

Carbon balance error (CBE)

$$\begin{aligned} CBE_2(\%) &= \frac{[(2X_{out_1}^{C_2H_4} + 2X_{out_1}^{C_2H_4O} + X_{out_1}^{CO_2}) * (CF_2) - (2 * X_{in}^{C_2H_4} + 2 * X_{in}^{C_2H_4O} + X_{in}^{CO_2})]}{(2 * X_{in}^{C_2H_4} + 2 * X_{in}^{C_2H_4O} + X_{in}^{CO_2})} \\ &* 100 = -0.05 \end{aligned}$$

$$X_{out_2}^{C_2H_4*} (mol\%) = \frac{X_{out_1}^{C_2H_4}}{(1 + CBE_2)} = 21.58, X_{out_2}^{C_2H_4O*} (mol\%) = \frac{X_{out_1}^{C_2H_4O}}{(1 + CBE_2)} = 1.11$$

$$X_{out_2}^{CO_2*} (mol\%) = \frac{X_{out_1}^{CO_2}}{(1 + CBE_2)} = 4.83$$

3rd Iteration

$$\begin{aligned} Correction\ Factor(CF_3) &= 1 - 0.5 * \left(\frac{X_{out_2}^{C_2H_4O*} * CF_2 - X_{in}^{C_2H_4O}}{100} \right) - \left(\frac{X_{out_2}^{CO_2*} - X_{in}^{CO_2}}{100} \right) \\ &= 0.988 \end{aligned}$$

$$X_{out_3}^{CH_4^*} (mol\%) = \frac{X_{in}^{CH_4}}{CF_3} = 58.03$$

$$\sum_{i=1}^{NC} X_{out_3}^i (mol\%) = 99.69$$

$$Error \text{ in outlet } CH_4(\%) = 100 * \frac{(X_{out_3}^{CH_4^*} - X_{out_0}^{CH_4})}{X_{out_0}^{CH_4}} = 4.40$$

Carbon balance error (CBE)

$$CBE_3(\%) = \frac{[(2X_{out_2}^{C_2H_4} + 2X_{out_2}^{C_2H_4O} + X_{out_2}^{CO_2}) * (CF_3) - (2 * X_{in}^{C_2H_4} + 2 * X_{in}^{C_2H_4O} + X_{in}^{CO_2})]}{(2 * X_{in}^{C_2H_4} + 2 * X_{in}^{C_2H_4O} + X_{in}^{CO_2})} \\ * 100 = 0$$

GC measurements for reactor outlet water-free reconciled composition

$$X_{out_3}^{C_2H_4*} (mol\%) = X_{out_2}^{C_2H_4*} = 21.58$$

$$X_{out_3}^{O_2*} (mol\%) = \frac{X_{out_0}^{O_2} * X_{out_3}^{C_2H_4*}}{X_{out_0}^{C_2H_4}} = 4.22$$

$$X_{out_3}^{C_2H_4O*} (mol\%) = X_{out_2}^{C_2H_4O*} = 1.11$$

$$X_{out_3}^{CO_2*} (mol\%) = X_{out_2}^{CO_2*} = 4.83$$

$$X_{out_4}^{CH_4*} (mol\%) = 100 - (X_{out_3}^{C_2H_4*} + X_{out_3}^{O_2*} + X_{out_3}^{C_2H_4O*} + X_{out_3}^{CO_2*} + X_{out_0}^{He}) = 58.26\%$$

$$Final Error in outlet CH_4(\%) = 100 * \frac{(X_{out_4}^{CH_4*} - X_{out_0}^{CH_4})}{X_{out_0}^{CH_4}} = 4.80$$

$$Final Error in outlet C_2H_4(\%) = 100 * \frac{(X_{out_3}^{C_2H_4*} - X_{out_0}^{C_2H_4})}{X_{out_0}^{C_2H_4}} = 2.08$$

$$Final Error in outlet O_2(\%) = 100 * \frac{(X_{out_3}^{O_2*} - X_{out_0}^{O_2})}{X_{out_0}^{O_2}} = 1.93$$

$$Final Error in outlet CO_2(\%) = 100 * \frac{(X_{out_3}^{CO_2*} - X_{out_0}^{CO_2})}{X_{out_0}^{CO_2}} = 2.11$$

$$Final Error in outlet C_2H_4O(\%) = 100 * \frac{(X_{out_3}^{C_2H_4O*} - X_{out_0}^{C_2H_4O})}{X_{out_0}^{C_2H_4O}} = 1.83$$

Final Reconciled GC sum (water-free)

$$\sum_{i=1}^{NC} X_{out_3}^{i*} (mol\%) = 100.00$$

Ethylene conversion

$$Conversion (\%) = \frac{\left(X_{in}^{C_2H_4} - X_{out_3}^{C_2H_4*} * CF_3 \right)}{X_{in}^{C_2H_4}} * 100 = 6.24$$

Oxygen conversion

$$Conversion (\%) = \frac{\left(X_{in}^{O_2} - X_{out_3}^{O_2*} * CF_3 \right)}{X_{in}^{O_2}} * 100 = 27.74$$

APPENDIX E

FIGURES UPON RECONCILED EXPERIMENTAL DATA

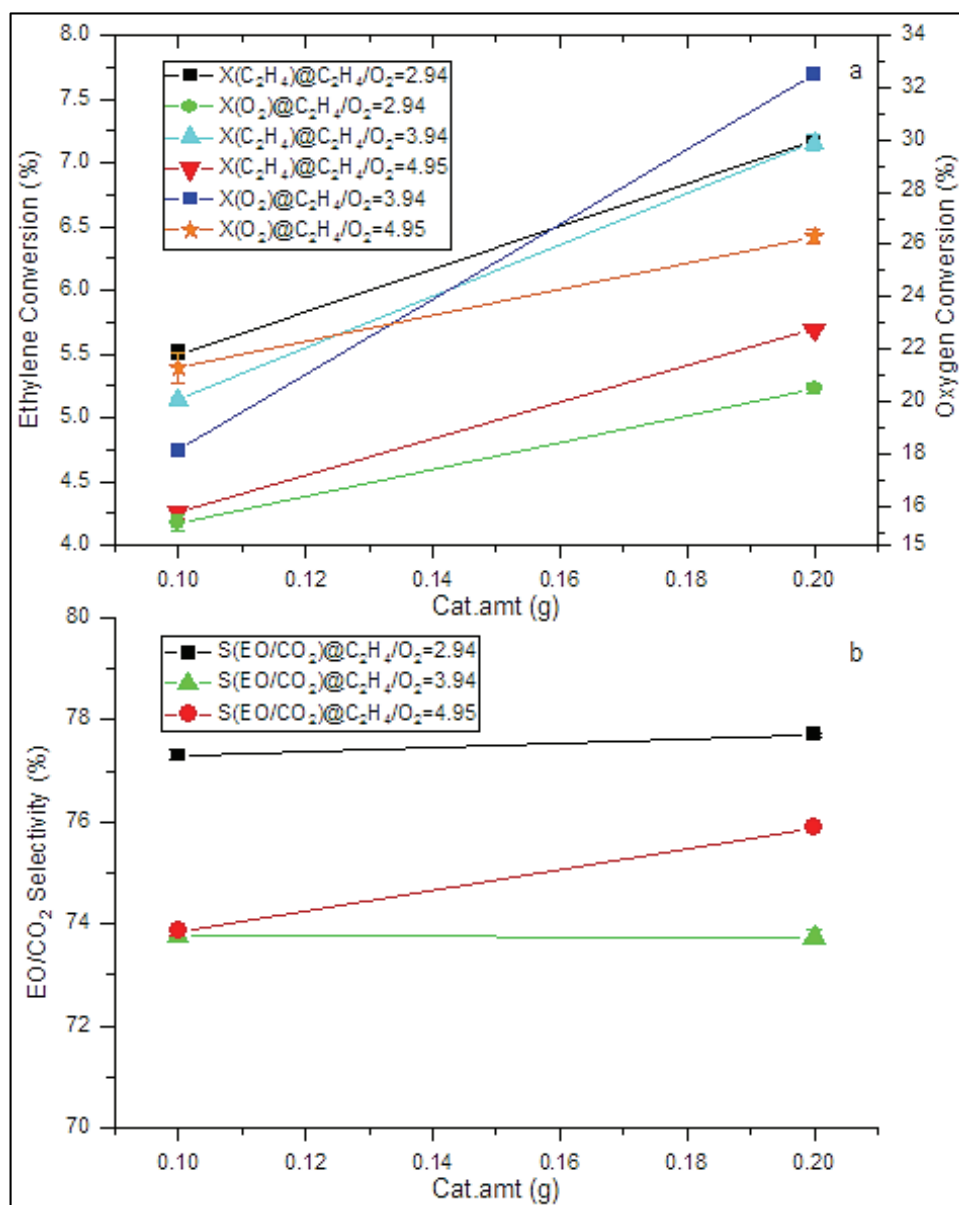


Figure E.1. Changes in ethylene and oxygen conversions (a) and EO/CO₂ selectivity (b) at two different catalyst amounts (0.1 and 0.2g) and three different C₂H₄/O₂ ratios (2.94, 3.94 and 4.95)

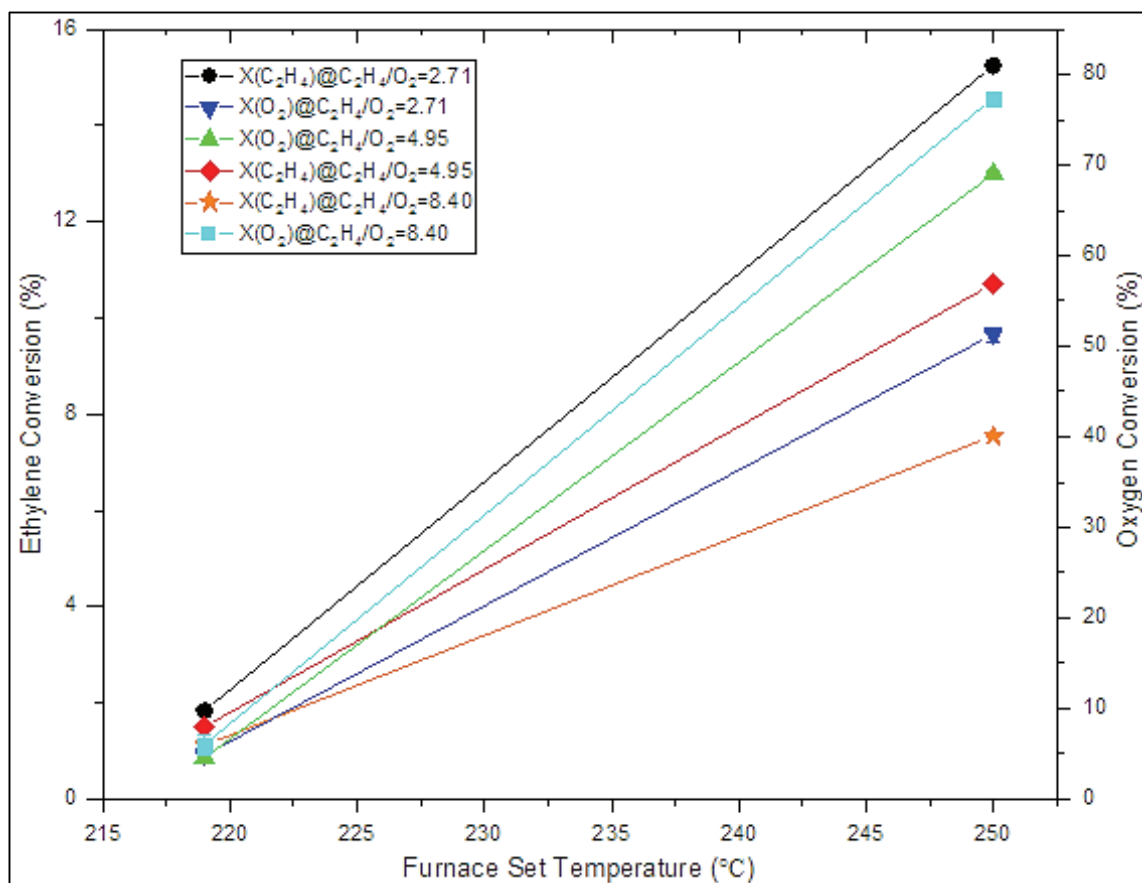


Figure E.2. Changes in ethylene and oxygen conversions at two different temperatures (219 and 250°C) and C₂H₄/O₂ ratios (2.71, 4.95 and 8.40).

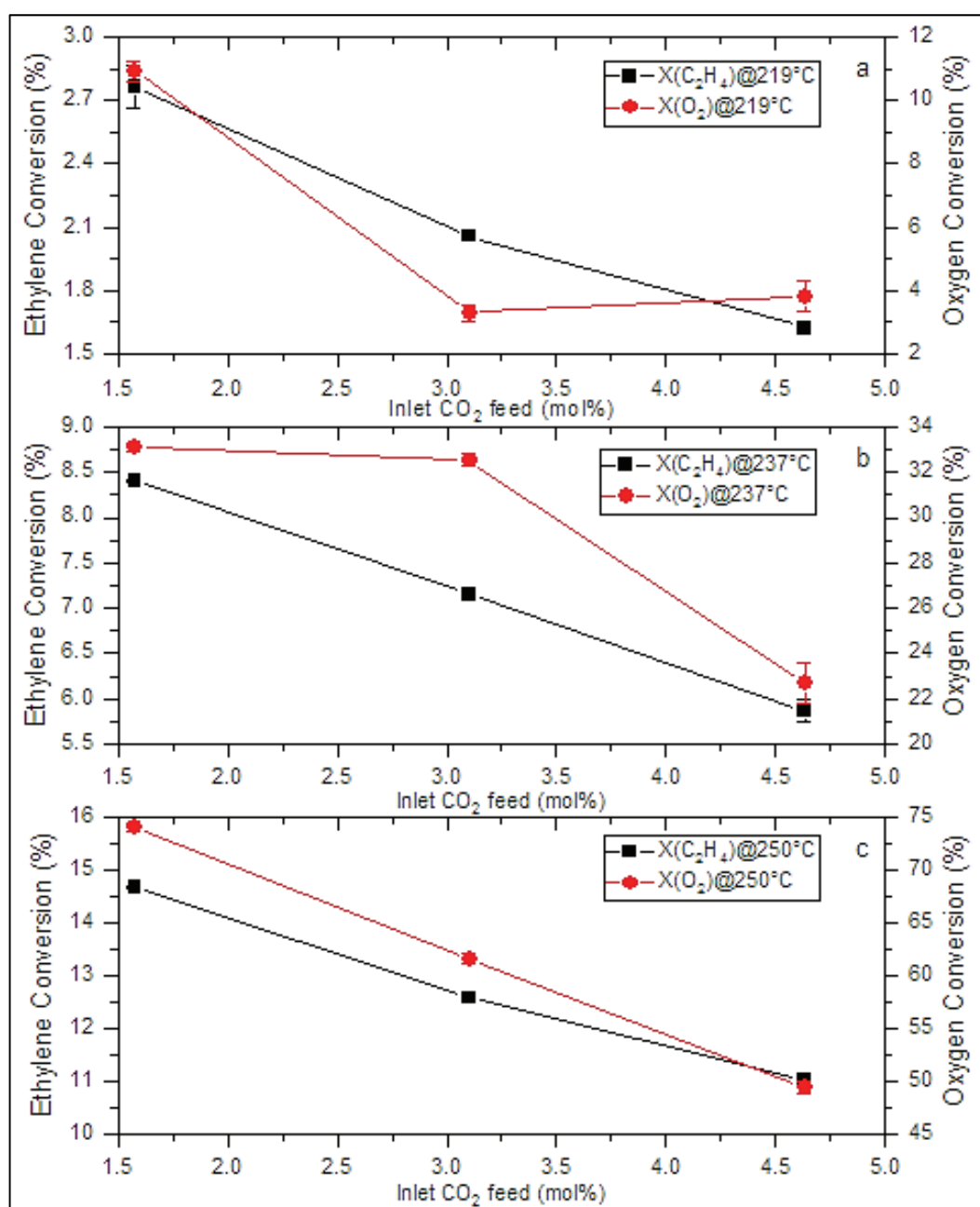


Figure E.3. Changes in ethylene and oxygen conversions at three different inlet CO₂ feed molar concentrations (1.58, 3.11 and 4.64%) with different temperatures of 219 °C (a), 237 °C (b), and 250 °C (c).

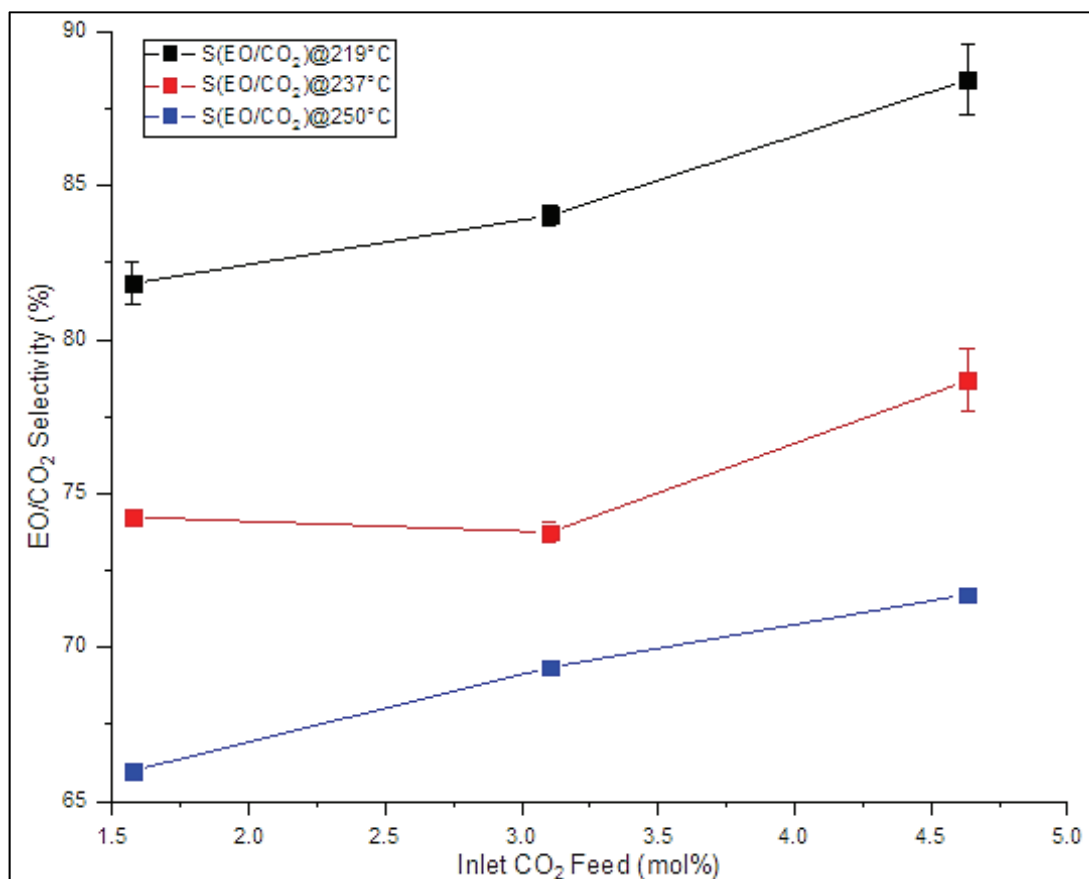


Figure E.4. Changes in EO/CO₂ selectivity at three different molar inlet concentrations of CO₂ feed (1.58, 3.11 and 4.64%) with different temperatures of 219, 237, and 250 °C.

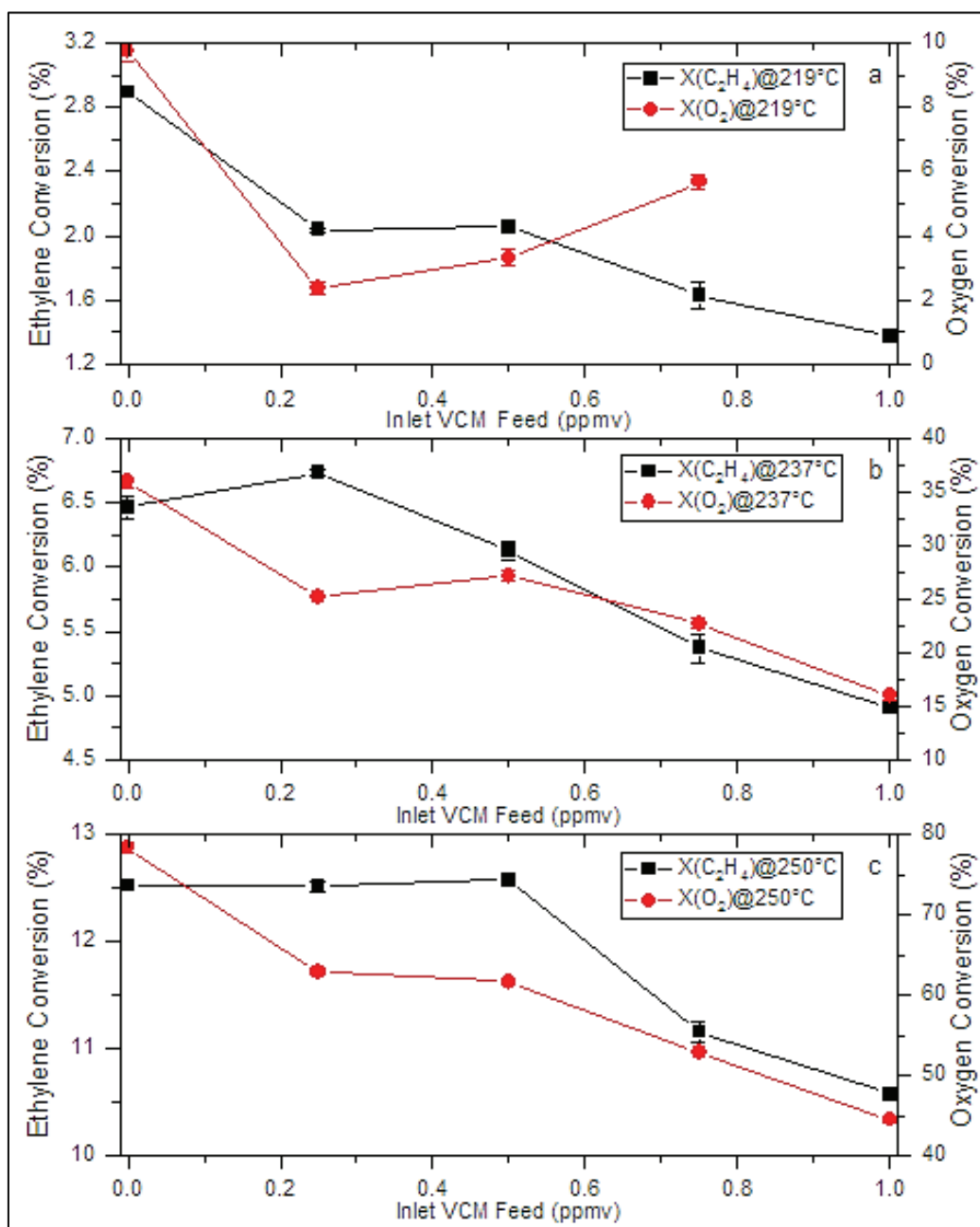


Figure E.5. Changes in ethylene and oxygen conversions at five different inlet concentrations of VCM feed (0, 3.75, 7.5, 11.25 and 15.0 ppmv) with different temperatures of 219 °C (a), 237 °C (b), and 250 °C (c).

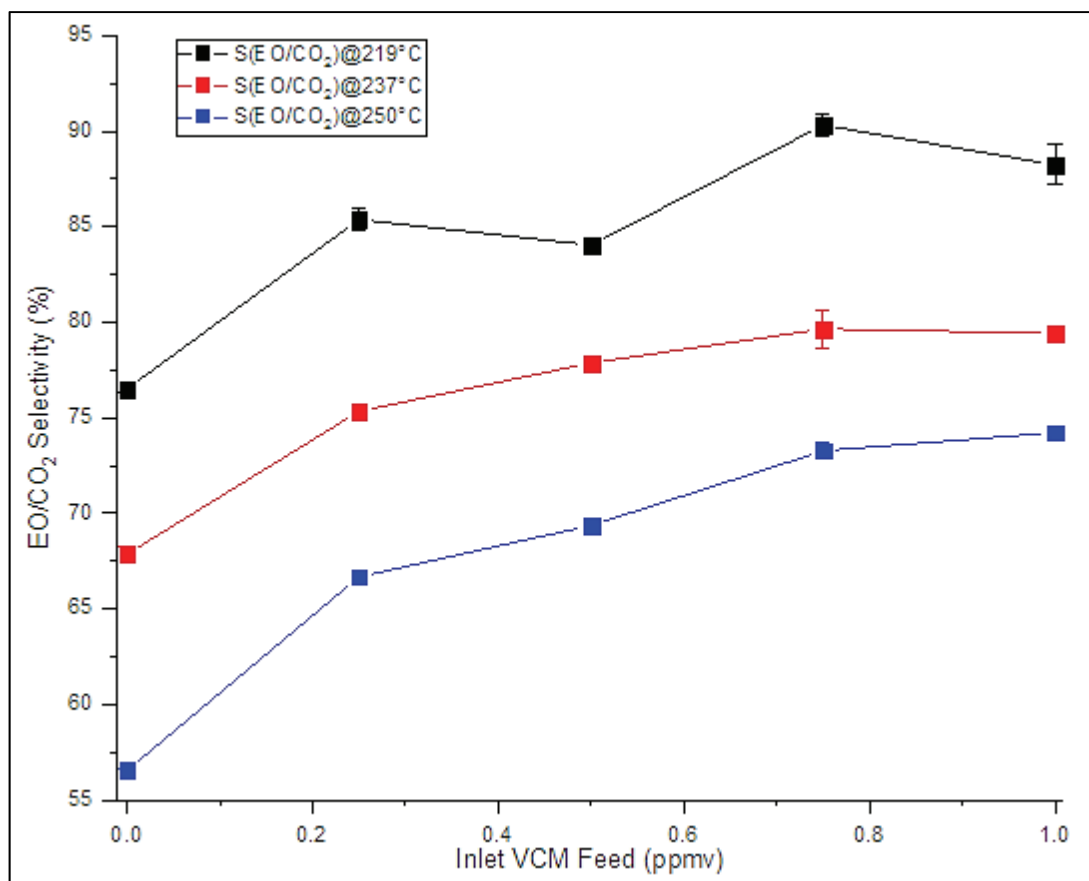


Figure E.6. Changes in EO/CO₂ selectivity at five different inlet concentrations of VCM feed (0, 3.75, 7.5, 11.25 and 15.0 ppmv) with different temperatures of 219, 237 °C and 250 °C (c).

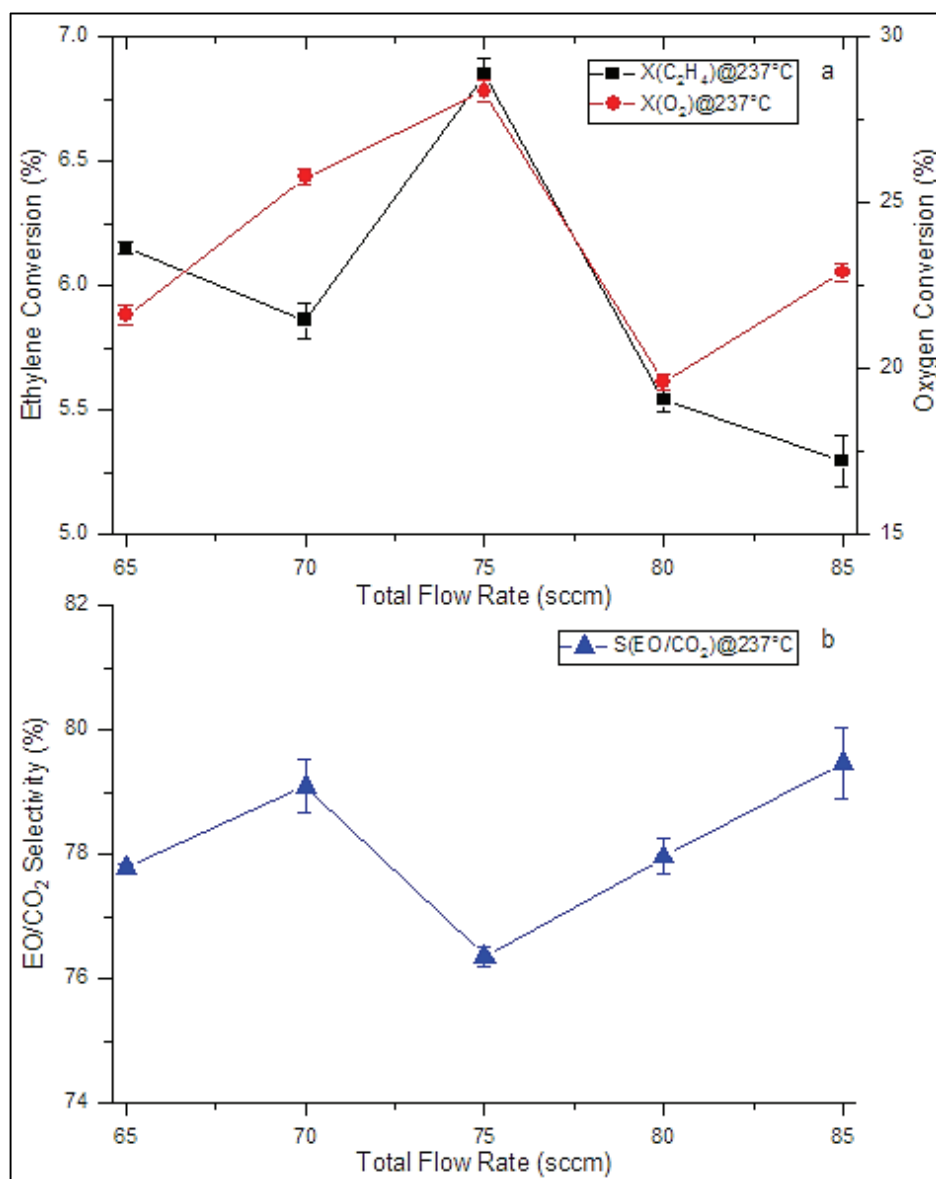


Figure E.7. Changes in ethylene and oxygen conversions (a) and EO/CO₂ selectivity (b) at five different total flow rates (65, 70, 75, 80 and 85 sccm).

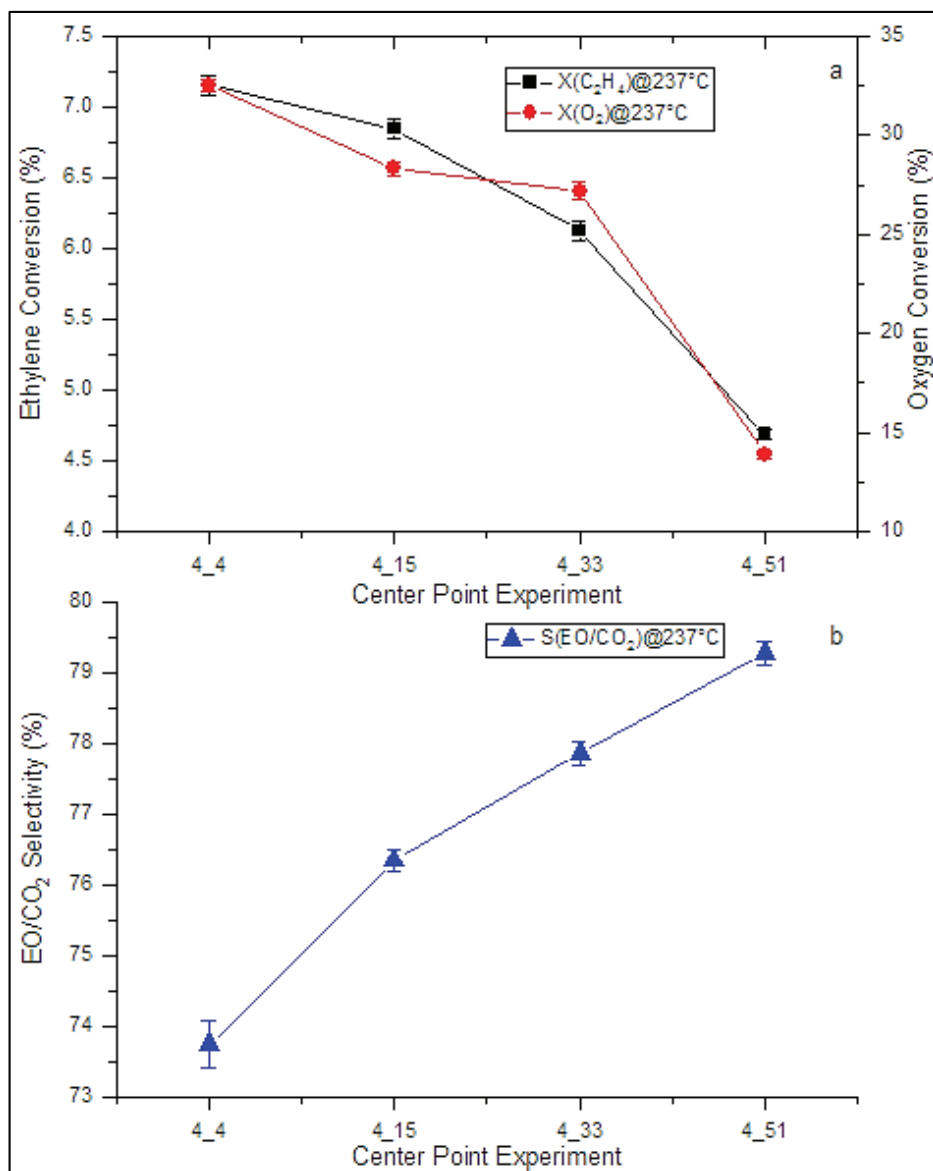


Figure E.8. Changes in ethylene and oxygen conversions (a) and EO/CO₂ selectivity (b) at five same center point experiments executed different times at the same catalyst loading (#4).

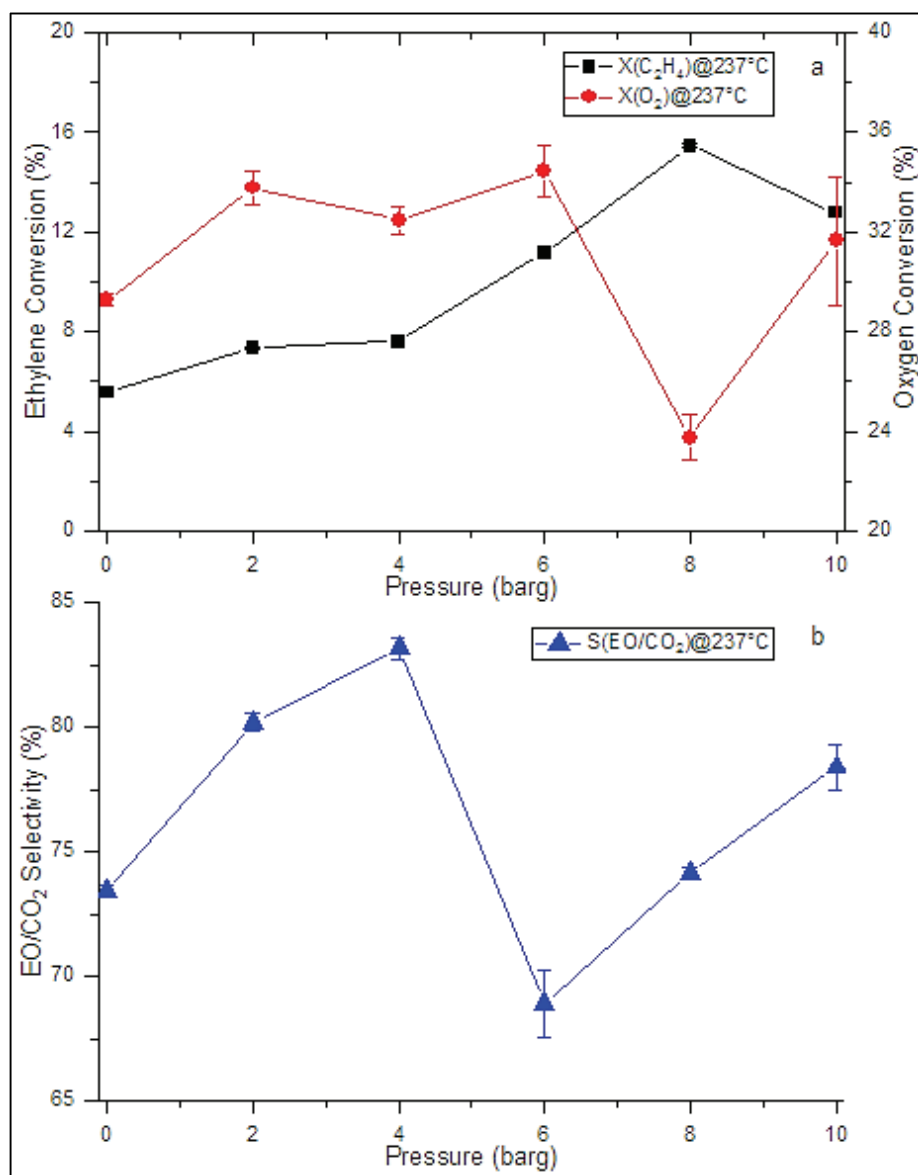


Figure E.9. Changes in ethylene and oxygen conversions (a) and EO/CO₂ selectivity (b) at six different reactor pressures (0, 2, 4, 6, 8 and 10 barg).

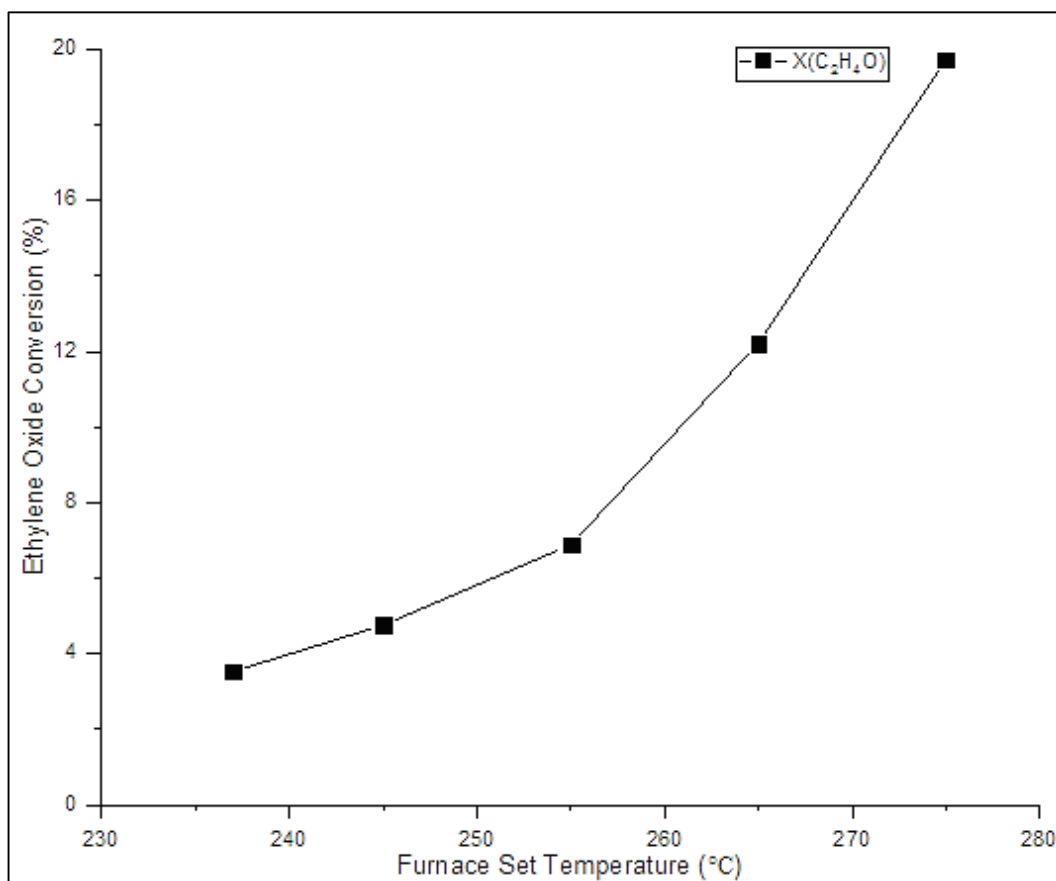


Figure E.10. Changes in ethylene oxide conversion at five different temperatures (237, 245, 255, 265 and 275°C).

APPENDIX F

TESTED KINETIC MODEL CANDIDATES, EXPERIMENTS USED IN PARAMETER ESTIMATION STEPS AND STATISTICAL EVALUATION FOR BEST- FITTED MODEL

Table F.1.1. All kinetic model candidates used in model discrimination steps.

Kinetic models that were tested	Reference
$r_1 = \frac{k_{r1} * P_{O_2} * P_{C_2H_4}}{1 + K_{O_{21}} * P_{O_2} + K_{CO_{21}} * P_{O_2}^{0.5} * P_{CO_2} + K_{VCM_1} * P_{VCM}}$	Extended Gan et al.
$r_2 = \frac{k_{r2} * P_{O_2}^{0.5} * P_{C_2H_4}}{1 + K_{O_{22}} * P_{O_2} + K_{CO_{22}} * P_{O_2}^{0.5} * P_{CO_2} + K_{VCM_2} * P_{VCM}}$	
$r_3 = \frac{k_{r3} * P_{O_2}^{0.5} * P_{C_2H_4O}}{1 + K_{O_{22}} * P_{O_2} + K_{CO_{22}} * P_{O_2}^{0.5} * P_{CO_2} + K_{VCM_2} * P_{VCM}}$	
$r_1 = \frac{(k_1 * \exp(-E_1/RT) * P_{C_2H_4} * P_{O_2})}{(1 + K_{CO_{21}} * \exp(\Delta H_{CO_{21}}/RT) * P_{CO_2} + K_{O_{21}} * \exp(\Delta H_{O_{21}}/RT) * P_{O_2}^{0.5} * P_{H_2O}) * (1 + e_1 * \exp(E_1/RT) * C_{VCM})}$	Extended Gu et al.
$r_2 = \frac{(k_2 * \exp(-E_2/RT) * P_{C_2H_4} * P_{O_2}^{0.75})}{(1 + K_{CO_{22}} * \exp(\Delta H_{CO_{22}}/RT) * P_{CO_2} + K_{O_{22}} * \exp(\Delta H_{O_{22}}/RT) * P_{O_2}^{0.5} * P_{H_2O}) * (1 + e_2 * \exp(E_2/RT) * C_{VCM})}$	
$r_3 = \frac{(k_3 * \exp(-E_3/RT) * P_{C_2H_4O} * P_{O_2}^{0.75})}{(1 + K_{CO_{22}} * \exp(\Delta H_{CO_{22}}/RT) * P_{CO_2} + K_{O_{22}} * \exp(\Delta H_{O_{22}}/RT) * P_{O_2}^{0.5} * P_{H_2O}) * (1 + e_2 * \exp(E_2/RT) * C_{VCM})}$	

(Cont.on next page)

Table F.1 (Cont.)

$r_1 = \frac{k_1 * P_{C_2H_4} * P_{O_2} - k_2 * P_{C_2H_4} * P_{O_2} * P_{VCM}^{k_7}}{1 + k_5 * P_{O_2} + k_6 * P_{C_2H_4}}$	Petrov et al.
$r_2 = \frac{k_3 * P_{C_2H_4} * P_{O_2} - k_4 * P_{C_2H_4} * P_{O_2} * P_{VCM}^{k_8}}{1 + k_5 * P_{O_2} + k_6 * P_{C_2H_4}}$	
$r_3 = \frac{k_3 * P_{C_2H_4O} * P_{O_2} - k_4 * P_{C_2H_4O} * P_{O_2} * P_{VCM}^{k_8}}{1 + k_5 * P_{O_2} + k_6 * P_{C_2H_4O}}$	
$r_1 = \frac{k_1 * C_{C_2H_4} * C_{O_2}^{\alpha_1}}{(1 + K_{C_2H_4} * C_{C_2H_4} + K_{O_2} * C_{O_2}^{\beta_1} + K_{CO_2} * C_{CO_2} + K_{VCM_1} * C_{VCM})^2}$	Extended Salmi et al.
$r_2 = \frac{k_2 * C_{C_2H_4} * C_{O_2}^{\alpha_2}}{(1 + K_{C_2H_4} * C_{C_2H_4} + K_{O_2} * C_{O_2}^{\beta_2} + K_{CO_2} * C_{CO_2} + K_{VCM_2} * C_{VCM})^2}$	
$r_3 = \frac{k_3 * C_{C_2H_4O} * C_{O_2}^{\alpha_3}}{(1 + K_{C_2H_4} * C_{C_2H_4} + K_{O_2} * C_{O_2}^{\beta_3} + K_{CO_2} * C_{CO_2} + K_{VCM_1} * C_{VCM})^2}$	
$r_1 = \frac{k_{r_1} * K_{C_2H_4} * P_{C_2H_4} * P_{O_2}^{n_1}}{1 + K_{C_2H_4} * P_{C_2H_4} + K_{CO_2} * P_{CO_2} + K_{H_2O_1} * P_{H_2O} + K_{C_2H_4O_1} * P_{C_2H_4O} + K_{VCM_1} * P_{VCM}}$	Extended Westerterp et al. Model (1)
$r_2 = \frac{k_{r_2} * K_{C_2H_4} * P_{C_2H_4} * P_{O_2}^{n_2}}{1 + K_{C_2H_4} * P_{C_2H_4} + K_{CO_2} * P_{CO_2} + K_{H_2O_2} * P_{H_2O} + K_{C_2H_4O_2} * P_{C_2H_4O} + K_{VCM_2} * P_{VCM}}$	
$r_3 = \frac{k_{r_3} * K_{C_2H_4O} * P_{C_2H_4O} * P_{O_2}^{n_3}}{1 + K_{C_2H_4} * P_{C_2H_4} + K_{CO_2} * P_{CO_2} + K_{H_2O_1} * P_{H_2O} + K_{C_2H_4O_1} * P_{C_2H_4O} + K_{VCM_1} * P_{VCM}}$	

(Cont. on next page)

Table F.1 (Cont.)

$r_1 = \frac{k_{r_1} * K_{C_2H_4} * P_{C_2H_4} * K_{O_2}^{0.5} * P_{O_2}^{r_1}}{1 + K_{C_2H_4} * P_{C_2H_4} + \sqrt{K_{O_2} * P_{O_2} + K_{CO_2} * P_{CO_2} + K_{H_2O} * P_{H_2O} + K_{C_2H_4O_1} * P_{C_2H_4O_1} + K_{VCM_1} * P_{VCM_1} + K_{VCM_2} * P_{VCM_2}}}$	Modified Westerterp et al. Model (1a)
$r_2 = \frac{k_{r_2} * K_{C_2H_4} * P_{C_2H_4} * K_{O_2}^{0.5} * P_{O_2}^{r_2}}{1 + K_{C_2H_4} * P_{C_2H_4} + \sqrt{K_{O_2} * P_{O_2} + K_{CO_2} * P_{CO_2} + K_{H_2O} * P_{H_2O} + K_{C_2H_4O_1} * P_{C_2H_4O_1} + K_{VCM_1} * P_{VCM_1} + K_{VCM_2} * P_{VCM_2}}}$	
$r_3 = \frac{k_{r_3} * K_{C_2H_4O_1} * P_{C_2H_4O_1} * K_{O_2}^{0.5} * P_{O_2}^{r_3}}{1 + K_{C_2H_4} * P_{C_2H_4} + \sqrt{K_{O_2} * P_{O_2} + K_{CO_2} * P_{CO_2} + K_{H_2O} * P_{H_2O} + K_{C_2H_4O_1} * P_{C_2H_4O_1} + K_{VCM_1} * P_{VCM_1} + K_{VCM_2} * P_{VCM_2}}}$	
$r_1 = \frac{k_{r_1} * K_{C_2H_4} * P_{C_2H_4} * K_{O_2} * P_{O_2}}{(1 + K_{C_2H_4} * P_{C_2H_4} + K_{CO_2} * P_{CO_2} + K_{H_2O} * P_{H_2O} + K_{C_2H_4O_1} * P_{C_2H_4O_1} + K_{VCM_1} * P_{VCM_1} + K_{VCM_2} * P_{VCM_2})^2}$	Extended Westerterp et al. Model (2)
$r_2 = \frac{k_{r_2} * K_{C_2H_4} * P_{C_2H_4} * K_{O_2} * P_{O_2}}{(1 + K_{C_2H_4} * P_{C_2H_4} + K_{CO_2} * P_{CO_2} + K_{H_2O} * P_{H_2O} + K_{C_2H_4O_1} * P_{C_2H_4O_1} + K_{VCM_1} * P_{VCM_1} + K_{VCM_2} * P_{VCM_2})^2}$	
$r_3 = \frac{k_{r_3} * K_{C_2H_4O_1} * P_{C_2H_4O_1} * K_{O_2} * P_{O_2}}{(1 + K_{C_2H_4} * P_{C_2H_4} + K_{CO_2} * P_{CO_2} + K_{H_2O} * P_{H_2O} + K_{C_2H_4O_1} * P_{C_2H_4O_1} + K_{VCM_1} * P_{VCM_1} + K_{VCM_2} * P_{VCM_2})^2}$	

(Cont. on next page)

Table F.1 (Cont.)

$r_1 = \frac{k_{r_1} * K_{C_2H_4} * P_{C_2H_4} * \sqrt{K_{O_2} * P_{O_2}}}{(1 + K_{C_2H_4} * P_{C_2H_4} + \sqrt{K_{O_2} * P_{O_2}} + K_{CO_2} * P_{CO_2} + K_{H_2O} * P_{H_2O} + K_{C_2H_4O} * P_{C_2H_4O} + K_{VCM} * P_{VCM})^2}$	Extended Westerterp et al. Model(3)
$r_2 = \frac{k_{r_2} * K_{C_2H_4} * P_{C_2H_4} * \sqrt{K_{O_2} * P_{O_2}}}{(1 + K_{C_2H_4} * P_{C_2H_4} + \sqrt{K_{O_2} * P_{O_2}} + K_{CO_2} * P_{CO_2} + K_{H_2O} * P_{H_2O} + K_{C_2H_4O} * P_{C_2H_4O} + K_{VCM} * P_{VCM})^2}$	
$r_3 = \frac{k_{r_3} * K_{C_2H_4O} * P_{C_2H_4O} * \sqrt{K_{O_2} * P_{O_2}}}{(1 + K_{C_2H_4} * P_{C_2H_4} + \sqrt{K_{O_2} * P_{O_2}} + K_{CO_2} * P_{CO_2} + K_{H_2O} * P_{H_2O} + K_{C_2H_4O} * P_{C_2H_4O} + K_{VCM} * P_{VCM})^2}$	

Table F.2. Experiments used for parameter estimations in step 1.

Cat. Load.#	Set Name	Exp. Name	Exp. #	Cat. (g)	Flow Rates (sccm)							C ₂ H ₄ /O ₂	P (kg cm ⁻² g)	Total flow	Concentrations (%)					
					C ₂ H ₄	O ₂	CH ₄	CO ₂	EO (in He)	He	VCM (in He)				C ₂ H ₄	O ₂	CO ₂	EO	VCM (ppm)	CH ₄
1	2	0a	1	0.1	17.1	4.3	47.3	3.1	0	3.2	0	3.9	0	75.0	22.7	5.8	4.1	0	0	63.1
1	2	0b	2	0.1	17.1	4.3	47.3	3.1	0	3.2	0	3.9	0	75.0	22.7	5.8	4.1	0	0	63.1
1	2	0c	3	0.1	17.1	4.3	47.3	3.1	0	3.2	0	3.9	0	75.0	22.7	5.8	4.1	0	0	63.1
4	2	0b	1	0.2	17.1	4.3	47.3	3.1	0	3.2	0	3.9	0	75.0	22.7	5.8	4.1	0	0	63.1
4	2	0a	2	0.2	17.1	4.3	47.3	3.1	0	3.2	0	3.9	0	75.0	22.7	5.8	4.1	0	0	63.1
4	2	0c	3	0.2	17.1	4.3	47.3	3.1	0	3.2	0	3.9	0	75.0	22.7	5.8	4.1	0	0	63.1

Table F.3. Experiments used for parameter estimations in step 2.

Cat. Load. #	Set Name	Exp. Name	Exp. #	Cat. (g)	Flow Rates (sccm)							C ₂ H ₄ /O ₂	p (kg cm-cm-2g)	Total flow	Concentrations (%)					
					C ₂ H ₄	O ₂	CH ₄	CO ₂	EO (in He)	He	VCM (in He)				C ₂ H ₄	O ₂	CO ₂	EO	VCM (ppm)	CH ₄
1	2	0a	1	0.1	17.1	4.3	47.3	3.1	0	3.2	0.0	3.9	0	75.0	22.7	5.8	4.1	0	0.0	63.1
	2	0b	2	0.1	17.1	4.3	47.3	3.1	0	3.2	0.0	3.9	0	75.0	22.7	5.8	4.1	0	0.0	63.1
	2	0c	3	0.1	17.1	4.3	47.3	3.1	0	3.2	0.0	3.9	0	75.0	22.7	5.8	4.1	0	0.0	63.1
	2	2b0	4	0.1	17.1	4.3	43.0	3.1	0	0.0	7.5	3.9	0	75.0	22.7	5.8	4.1	0	0.5	57.4
	2	2a	11	0.1	17.1	4.3	43.0	3.1	0	0.0	7.5	3.9	0	75.0	22.7	5.8	4.1	0	0.5	57.4
	2	2c	12	0.1	17.1	4.3	43.0	3.1	0	0.0	7.5	3.9	0	75.0	22.7	5.8	4.1	0	0.5	57.4
	2	2b0	16	0.1	17.1	4.3	43.0	3.1	0	0.0	7.5	3.9	0	75.0	22.7	5.8	4.1	0	0.5	57.4
	2	2b0	27	0.1	17.1	4.3	43.0	3.1	0	0.0	7.5	3.9	0	75.0	22.7	5.8	4.1	0	0.5	57.4
4	2	0b	1	0.2	17.1	4.3	47.3	3.1	0	3.2	0.0	3.9	0	75.0	22.7	5.8	4.1	0	0.0	63.1
	2	0a	2	0.2	17.1	4.3	47.3	3.1	0	3.2	0.0	3.9	0	75.0	22.7	5.8	4.1	0	0.0	63.1
	2	0c	3	0.2	17.1	4.3	47.3	3.1	0	3.2	0.0	3.9	0	75.0	22.7	5.8	4.1	0	0.0	63.1
	2	2b0	4	0.2	17.1	4.3	43.0	3.1	0	0.0	7.5	3.9	0	75.0	22.7	5.8	4.1	0	0.5	57.4
	2	2c	6	0.2	17.1	4.3	43.0	3.1	0	0.0	7.5	3.9	0	75.0	22.7	5.8	4.1	0	0.5	57.4
	2	9c	12	0.2	17.1	4.3	46.8	3.1	0	0.0	3.8	3.9	0	75.0	22.7	5.8	4.1	0	0.3	62.3
	2	10c	13	0.2	17.1	4.3	39.3	3.1	0	0.0	11.3	3.9	0	75.0	22.7	5.8	4.1	0	0.8	52.4
	2	11c	14	0.2	17.1	4.3	35.5	3.1	0	0.0	15.0	3.9	0	75.0	22.7	5.8	4.1	0	1.0	47.3

(Cont.on next page)

Table F.3 (Cont.)

4	2	2b0	15	0.2	17.1	4.3	43.0	3.1	0	0.0	7.5	3.9	0	75.0	22.7	5.8	4.1	0	0.5	57.4
	2	2b0	33	0.2	17.1	4.3	43.0	3.1	0	0.0	7.5	3.9	0	75.0	22.7	5.8	4.1	0	0.5	57.4
	2	9b	34	0.2	17.1	4.3	46.8	3.1	0	0.0	3.8	3.9	0	75.0	22.7	5.8	4.1	0	0.3	62.3
	2	10b	35	0.2	17.1	4.3	39.3	3.1	0	0.0	11.3	3.9	0	75.0	22.7	5.8	4.1	0	0.8	52.4
	2	11b	36	0.2	17.1	4.3	35.5	3.1	0	0.0	15.0	3.9	0	75.0	22.7	5.8	4.1	0	1.0	47.3
	2	2a	42	0.2	17.1	4.3	43.0	3.1	0	0.0	7.5	3.9	0	75.0	22.7	5.8	4.1	0	0.5	57.4
	2	9a	48	0.2	17.1	4.3	46.8	3.1	0	0.0	3.8	3.9	0	75.0	22.7	5.8	4.1	0	0.3	62.3
	2	10a	49	0.2	17.1	4.3	39.3	3.1	0	0.0	11.3	3.9	0	75.0	22.7	5.8	4.1	0	0.8	52.4
	2	11a	50	0.2	17.1	4.3	35.5	3.1	0	0.0	15.0	3.9	0	75.0	22.7	5.8	4.1	0	1.0	47.3
	2	2b0	51	0.2	17.1	4.3	43.0	3.1	0	0.0	7.5	3.9	0	75.0	22.7	5.8	4.1	0	0.5	57.4
	2	2b0	1	0.2	17.1	4.3	43.0	3.1	0	0.0	7.5	3.9	0	75.0	22.7	5.8	4.1	0	0.5	57.3
	2	9b	3	0.2	17.1	4.3	46.8	3.1	0	0.0	3.8	3.9	0	75.0	22.7	5.8	4.1	0	0.3	62.3
5	2	10b	4	0.2	17.1	4.3	39.3	3.1	0	0.0	11.3	3.9	0	75.0	22.7	5.8	4.1	0	0.8	52.3
	2	11b	5	0.2	17.1	4.3	35.5	3.1	0	0.0	15.0	3.9	0	75.0	22.7	5.8	4.1	0	1.0	47.3

Table F.4. Experiments used for parameter estimations in step 3.

Cat. Load. #	Set Name	Exp. Name	Exp. #	Cat. (g)	Flow Rates (sccm)							C ₂ H ₄ /O ₂	p (kg cm ⁻²)	Total flow	Concentrations (%)					
					C ₂ H ₄	O ₂	CH ₄	CO ₂	EO (in He)	He	VCM (in He)				C ₂ H ₄	O ₂	CO ₂	EO	VCM (ppm)	CH ₄
1	2	0a	1	0.1	17.1	4.3	47.3	3.1	0	3.2	0	3.9	0	75.0	22.7	5.8	4.1	0	0	63.1
	2	0b	2	0.1	17.1	4.3	47.3	3.1	0	3.2	0	3.9	0	75.0	22.7	5.8	4.1	0	0	63.1
	2	0c	3	0.1	17.1	4.3	47.3	3.1	0	3.2	0	3.9	0	75.0	22.7	5.8	4.1	0	0	63.1
2	1	1	1	0.1	50.0	1.4	22.1	1.6	0	0.0	0	36.8	0	75.0	66.6	1.8	2.1	0	0	29.5
	1	2	2	0.1	50.0	17.3	3.1	4.6	0	0.0	0	2.9	0	75.0	66.6	23.0	6.2	0	0	4.2
	1	3	3	0.1	19.3	1.4	49.7	4.6	0	0.0	0	14.2	0	75.0	25.7	1.8	6.2	0	0	66.3
	1	4	4	0.1	6.4	17.3	49.7	1.6	0	0.0	0	0.4	0	75.0	8.5	23.0	2.1	0	0	66.3
	1	14	5	0.1	26.4	10.7	34.7	3.2	0	0.0	0	2.5	0	75.0	35.2	14.3	4.3	0	0	46.3
	1	16	6	0.1	50.0	1.4	19.1	4.6	0	0.0	0	36.8	0	75.0	66.6	1.8	6.2	0	0	25.4
3	1	18	1	0.1	22.3	1.4	49.7	1.6	0	0.0	0	31.6	0	75.0	29.8	1.8	2.1	0	0	66.3
	1	23	2	0.1	20.2	17.3	32.9	4.6	0	0.0	0	7.1	0	75.0	27.0	23.0	6.2	0	0	43.8
	1	24	3	0.1	5.3	17.3	49.1	3.3	0	0.0	0	14.9	0	75.0	7.1	23.0	4.4	0	0	65.4
4	2	0b	1	0.2	17.1	4.3	47.3	3.1	0	3.2	0	3.9	0	75.0	22.7	5.8	4.1	0	0	63.1
	2	0a	2	0.2	17.1	4.3	47.3	3.1	0	3.2	0	3.9	0	75.0	22.7	5.8	4.1	0	0	63.1
	2	0c	3	0.2	17.1	4.3	47.3	3.1	0	3.2	0	3.9	0	75.0	22.7	5.8	4.1	0	0	63.1

Table F.5. Parameter estimation results of the best-fitted kinetic model (Westerterp et al., model (1)).

Parameter	Optimal Estimate	90%	95%	99%	95% t-value	Standard Deviation
FLWSHEET.CATALYST_ACTIVITY_REF(2)	6.73E-01	1.61E-02	1.91E-02	2.52E-02	3.51E+01	9.77E-03
FLWSHEET.CATALYST_ACTIVITY_REF(3)	3.97E-01	5.74E-03	6.84E-03	8.99E-03	5.80E+01	3.49E-03
FLWSHEET.CATALYST_ACTIVITY_REF(4)	5.81E-01	5.38E-03	6.41E-03	8.43E-03	9.05E+01	3.27E-03
FLWSHEET.CATALYST_ACTIVITY_REF(5)	7.68E-01	1.15E-02	1.37E-02	1.80E-02	5.60E+01	6.99E-03
FLWSHEET.CATALYST_ACTIVITY_REF(6)	7.30E-01	2.02E-02	2.41E-02	3.17E-02	3.03E+01	1.23E-02
FLWSHEET.CATALYST_ACTIVITY_REF(7)	5.75E-01	8.94E-03	1.07E-02	1.40E-02	5.40E+01	5.44E-03
FLWSHEET.CATALYST_ACTIVITY_REF_0(1)	1.00E+00	4.84E-02	5.77E-02	7.58E-02	1.74E+01	2.94E-02
FLWSHEET.CATALYST_ACTIVITY_REF_0(2)	9.73E-01	1.12E-02	1.34E-02	1.76E-02	7.27E+01	6.83E-03
CATALYST_ACTIVITY_TERMINAL("MAIN_REACTION")	0.00E+00	Optimal value at bounds				
CATALYST_ACTIVITY_TERMINAL("SIDE_REACTION_1")	0.00E+00	Optimal value at bounds				
E_D_SINTERING("MAIN_REACTION")	0.00E+00	Optimal value at bounds				
E_D_SINTERING("SIDE_REACTION_1")	0.00E+00	Optimal value at bounds				
K_D("MAIN_REACTION")	0.00E+00	Value fixed by user				
K_D("SIDE_REACTION_1")	0.00E+00	Value fixed by user				
K_D_2("MAIN_REACTION")	0.00E+00	Value fixed by user				
K_D_2("SIDE_REACTION_1")	0.00E+00	Value fixed by user				
K_D_SINTERING("MAIN_REACTION")	4.16E-04	8.98E-05	1.07E-04	1.41E-04	3.89E+00	5.46E-05
K_D_SINTERING("SIDE_REACTION_1")	8.25E-03	3.46E-04	4.12E-04	5.42E-04	2.00E+01	2.10E-04
Activation energy ("MAIN_REACTION")	8.80E+04	2.81E+03	3.35E+03	4.41E+03	2.63E+01	1.71E+03
Activation energy ("SIDE_REACTION_1")	6.45E+04	1.69E+03	2.01E+03	2.64E+03	3.21E+01	1.02E+03
Activation energy ("SIDE_REACTION_2")	1.07E+05	1.11E+04	1.32E+04	1.74E+04	8.08E+00	6.74E+03
E_ADS("CO2, MAIN_REACTION")	6.71E+04	Value fixed by user				

(Cont.on next page)

Table F.5 (Cont.)

E_ADS("CO2, SIDE_REACTION_1")	9.35E+04	Value fixed by user	6.23E+03	8.19E+03	3.48E+00	3.18E+03
E_ADS("ETHYLENE, MAIN_REACTION")	2.17E+04	5.23E+03				
E_ADS("ETHYLENE, SIDE_REACTION_1")	0.00E+00	Optimal value at bounds				
E_ADS("ETHYLENE OXIDE, MAIN_REACTION")	0.00E+00	Value fixed by user				
E_ADS("ETHYLENE OXIDE, SIDE_REACTION_1")	0.00E+00	Value fixed by user				
E_ADS("VINYL CHLORIDE, MAIN_REACTION")	8.89E+04	Value fixed by user				
E_ADS("VINYL CHLORIDE, SIDE_REACTION_1")	4.21E+04	Value fixed by user				
E_ADS("WATER, MAIN_REACTION")	1.97E+04	Value fixed by user				
E_ADS("WATER, SIDE_REACTION_1")	2.85E+04	Value fixed by user				
K_ADS_TREF("CO2, MAIN_REACTION")	8.14E+01	Value fixed by user				
K_ADS_TREF("CO2, SIDE_REACTION_1")	3.61E+02	Value fixed by user				
K_ADS_TREF("ETHYLENE, MAIN_REACTION")	2.25E+01	8.55E-01	1.02E+00	1.34E+00	2.20E+01	5.20E-01
K_ADS_TREF("ETHYLENE, SIDE_REACTION_1")	4.46E+01	2.50E+00	2.98E+00	3.92E+00	1.50E+01	1.52E+00
K_ADS_TREF("ETHYLENE OXIDE, MAIN_REACTION")	9.00E+01	Value fixed by user				
K_ADS_TREF("ETHYLENE OXIDE, SIDE_REACTION_1")	4.88E+01	Value fixed by user				
K_ADS_TREF("VINYL CHLORIDE, MAIN_REACTION")	1.34E+01	Value fixed by user				
K_ADS_TREF("VINYL CHLORIDE, SIDE_REACTION_1")	7.81E+01	Value fixed by user				
K_ADS_TREF("WATER, MAIN_REACTION")	3.41E+01	Value fixed by user				
K_ADS_TREF("WATER, SIDE_REACTION_1")	2.84E+01	Value fixed by user				
Rate constant at T_ref ("MAIN_REACTION")	3.46E-02	8.21E-04	9.78E-04	1.29E-03	3.54E+01	4.99E-04
Rate constant at T_ref ("SIDE_REACTION_1")	2.11E-02	1.12E-03	1.33E-03	1.75E-03	1.59E+01	6.80E-04
Rate constant at T_ref ("SIDE_REACTION_2")	9.82E-04	1.07E-04	1.28E-04	1.68E-04	7.70E+00	6.51E-05
N("MAIN_REACTION")	4.13E-01	5.63E-03	6.70E-03	8.81E-03	6.16E+01	3.42E-03
N("SIDE_REACTION_1")	3.77E-01	1.12E-02	1.34E-02	1.76E-02	2.82E+01	6.82E-03
				Reference t-value (95%):		
				1.645E+00		

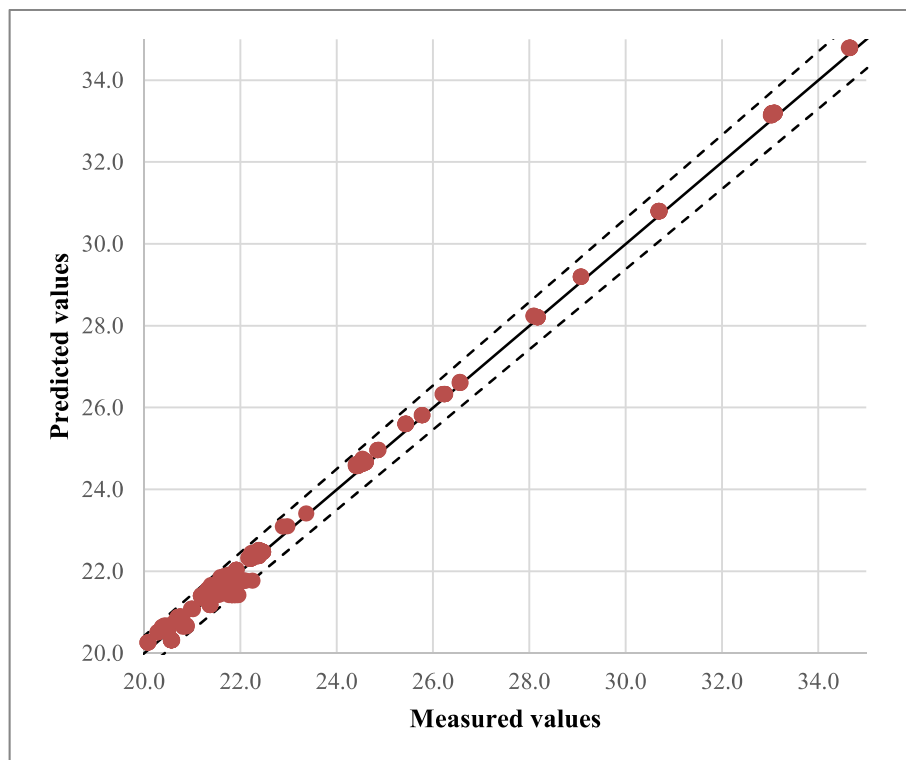


Figure F.1. Parity chart of reactor outlet ethylene composition for Westerterp et al._model (1).

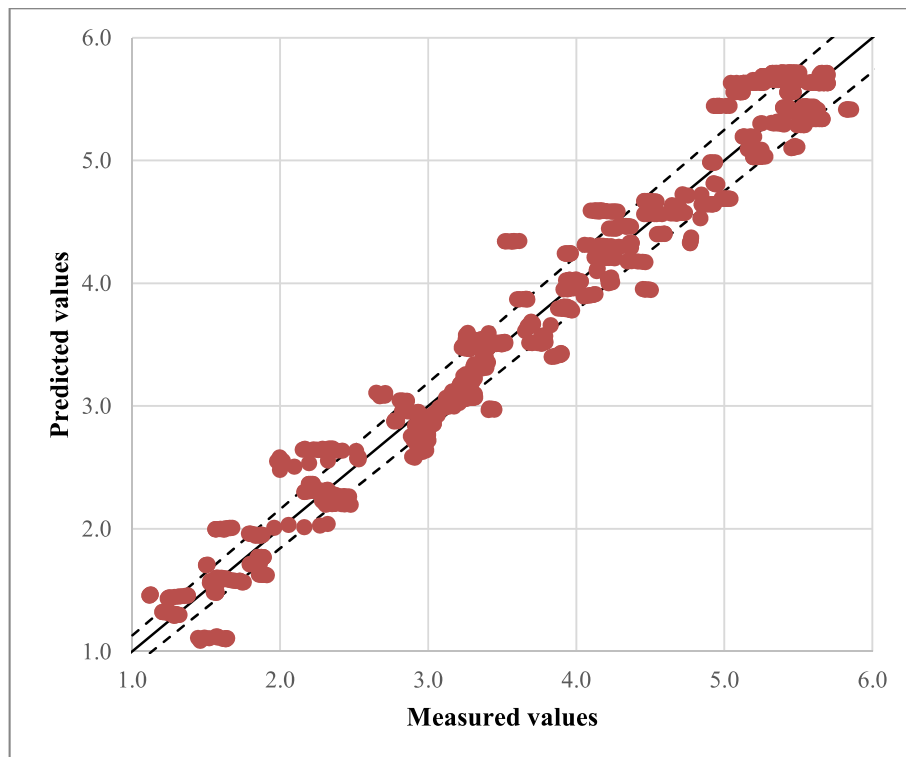


Figure F.2. Parity chart of reactor outlet oxygen composition for Westerterp et al._model (1).

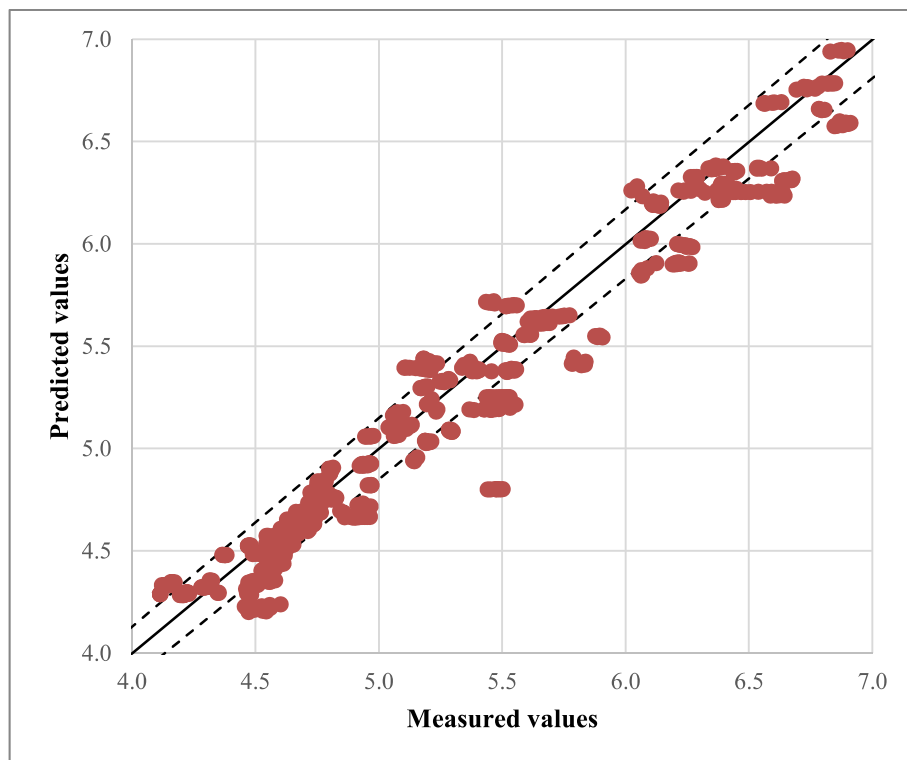


Figure F.3. Parity chart of reactor outlet CO₂ composition for Westerterp et al._model (1).

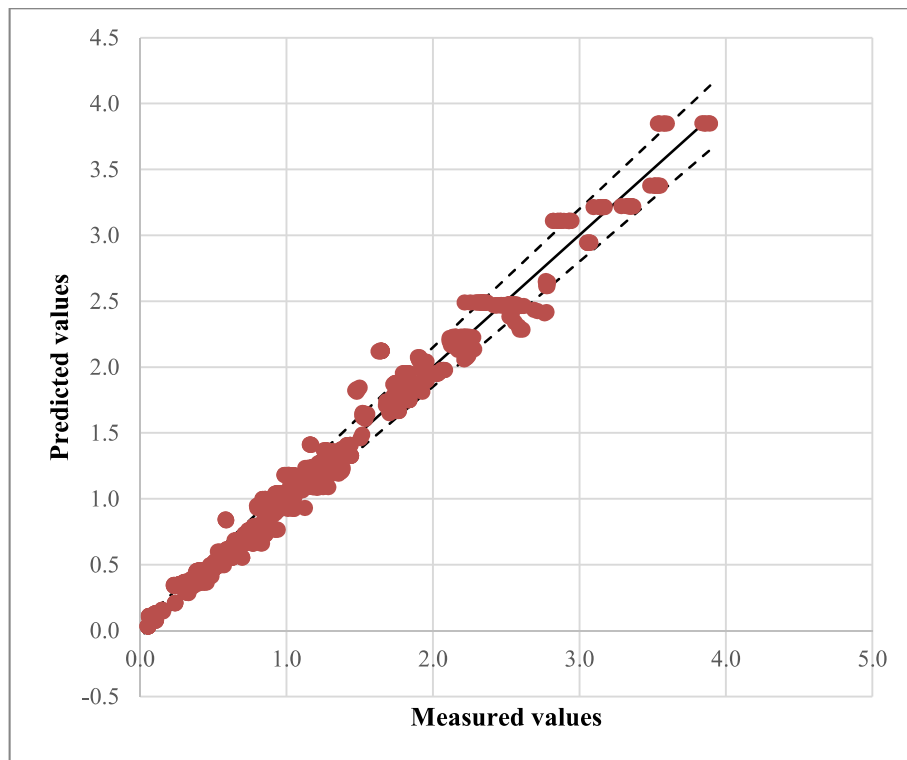


Figure F.4. Parity chart of reactor outlet EO composition for Westerterp et al._model (1).

APPENDIX G

CHANGES IN REACTION RATES AND COMPOSITIONS ALONG THE BED

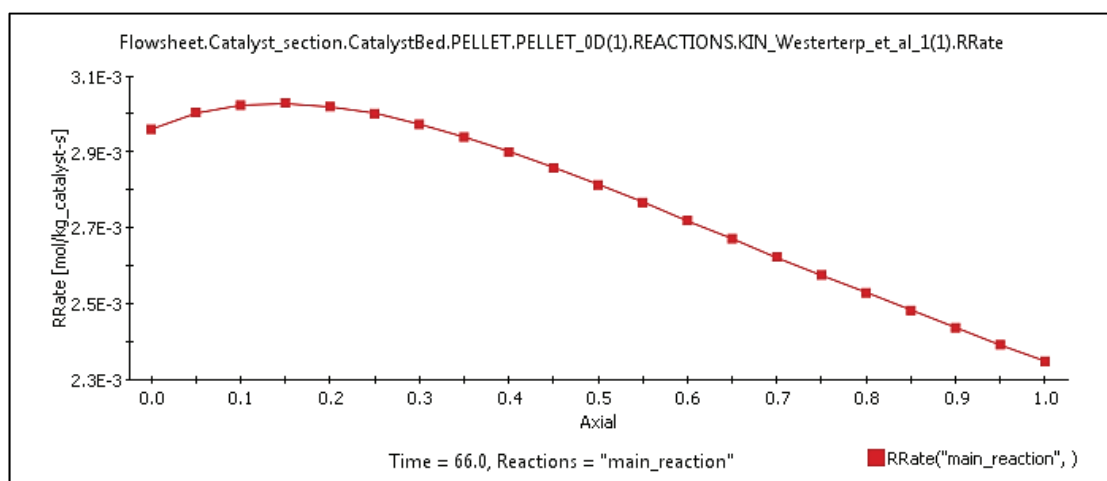


Figure G.1. Change in main reaction rate along with the catalyst bed in the axial direction.

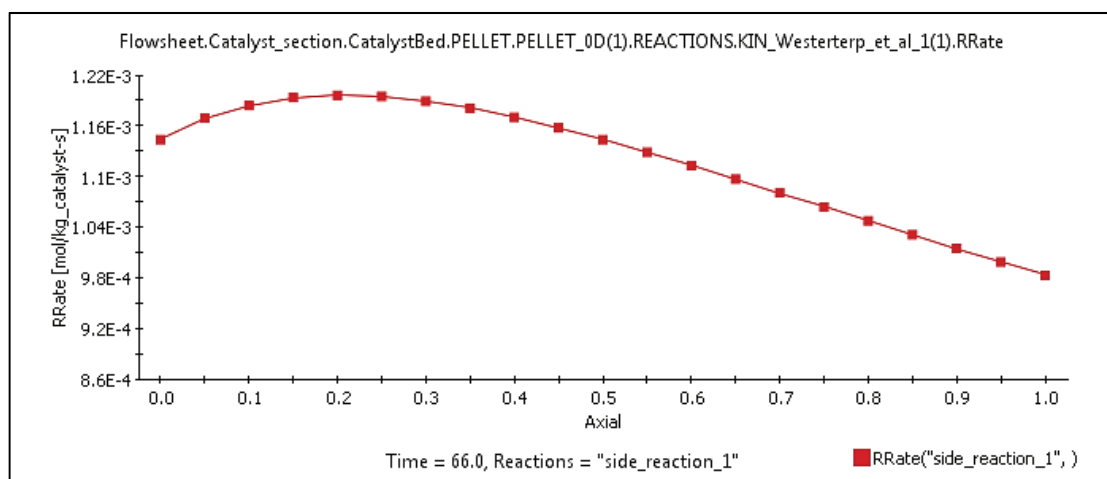


Figure G.2. Change in side reaction_1 rate along with the catalyst bed in the axial direction.

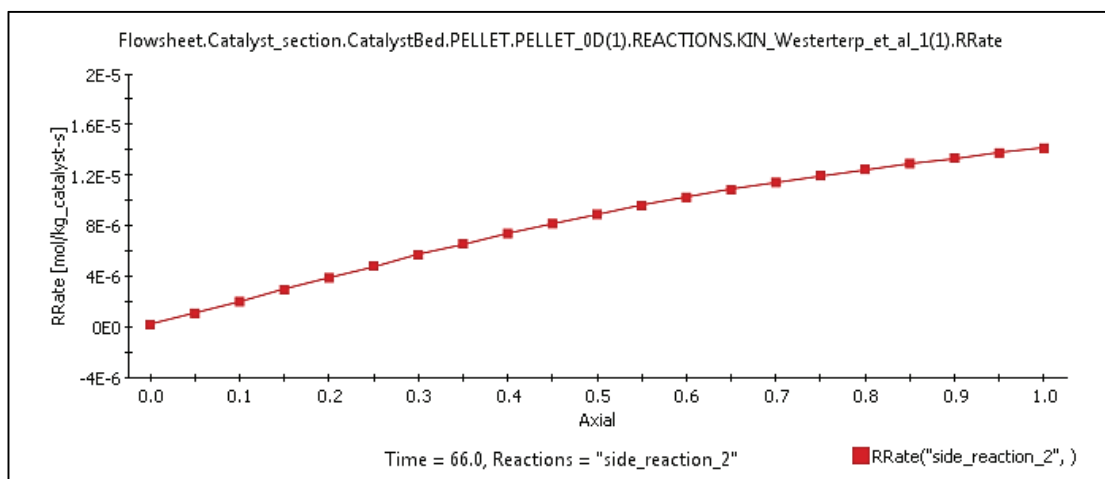


Figure G.3. Change in side reaction_2 rate along with the catalyst bed in the axial direction.

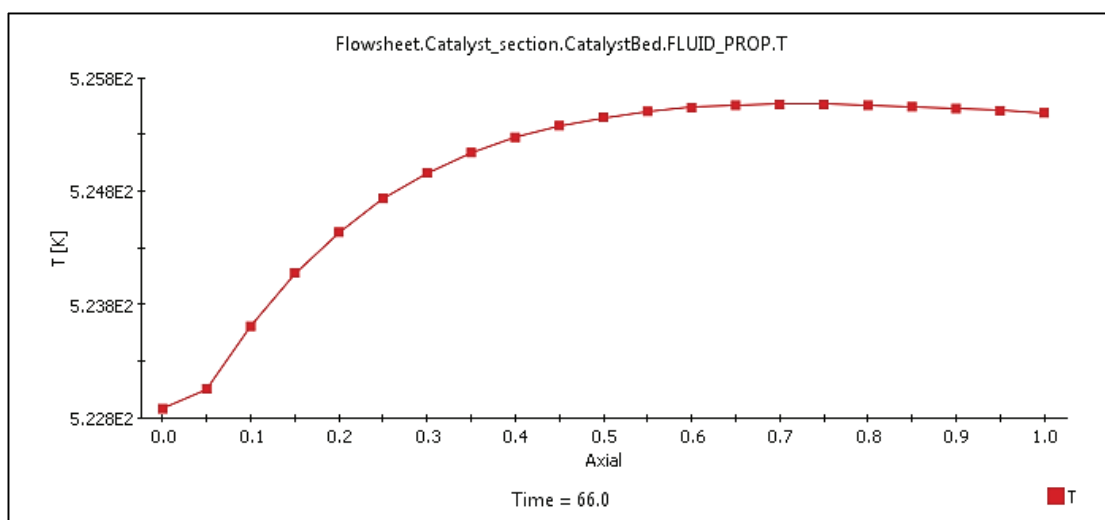


Figure G.4. Change in bed temperature along with the catalyst bed in the axial direction.

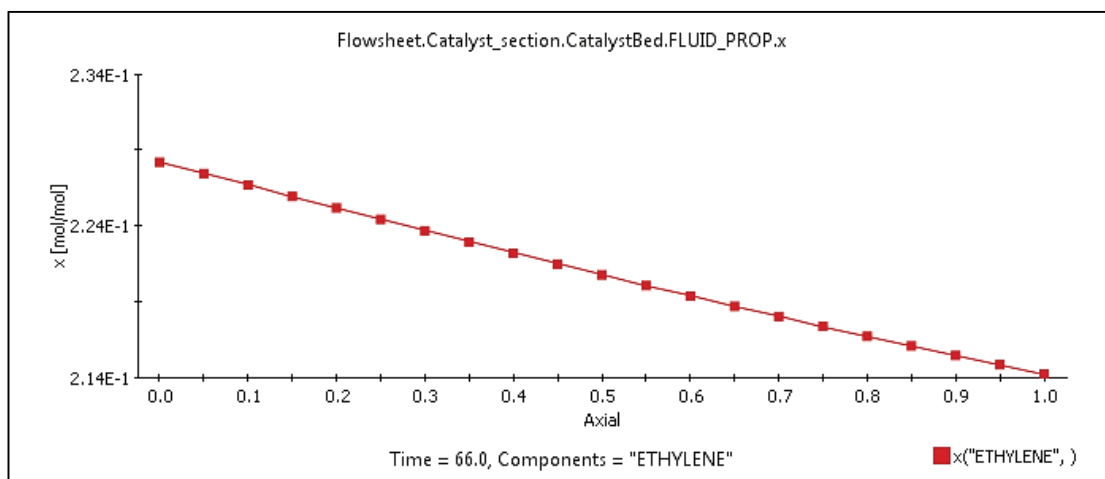


Figure G.5. Change in ethylene concentration along with the catalyst bed in the axial direction.

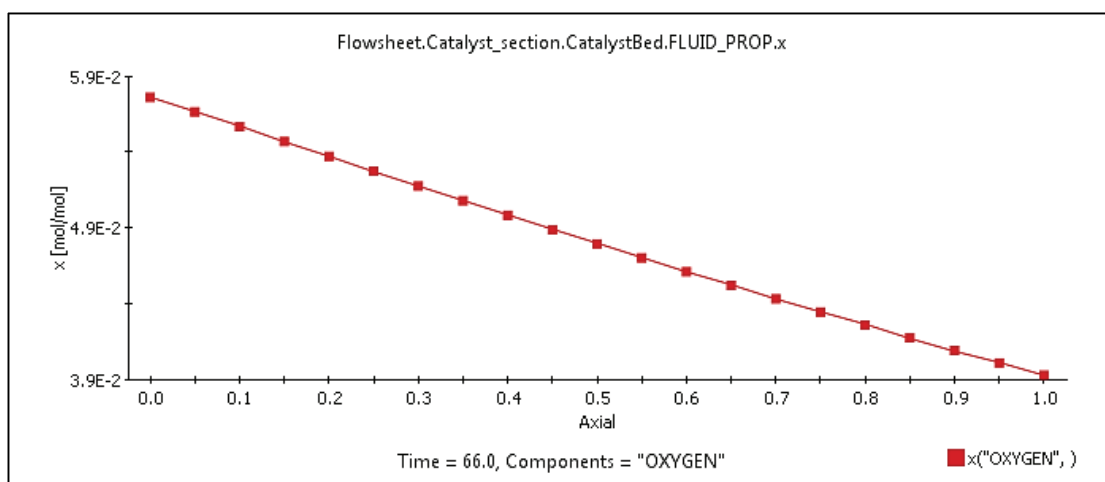


Figure G.6. Change in oxygen concentration along with the catalyst bed in the axial direction.

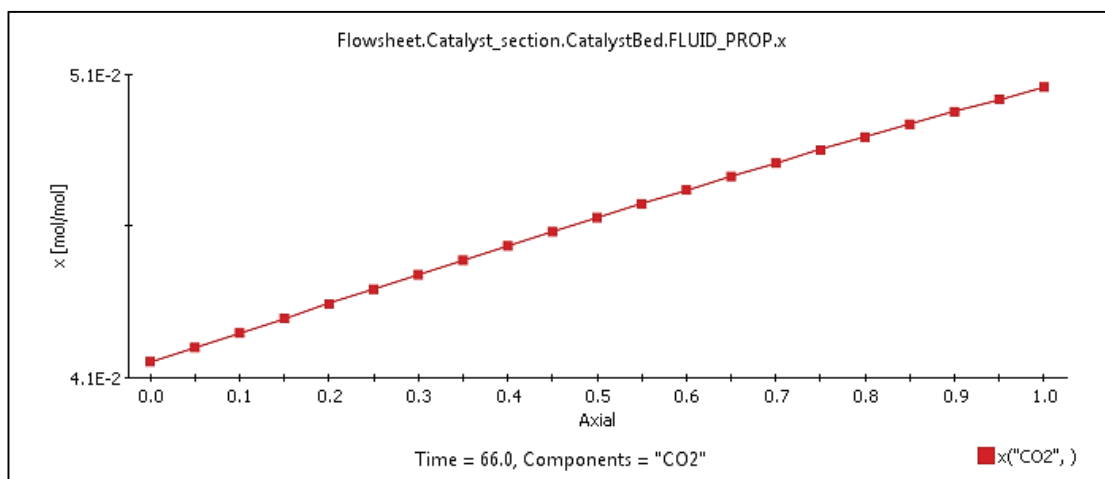


Figure G.7. Change in carbon dioxide concentration along with the catalyst bed in the axial direction.

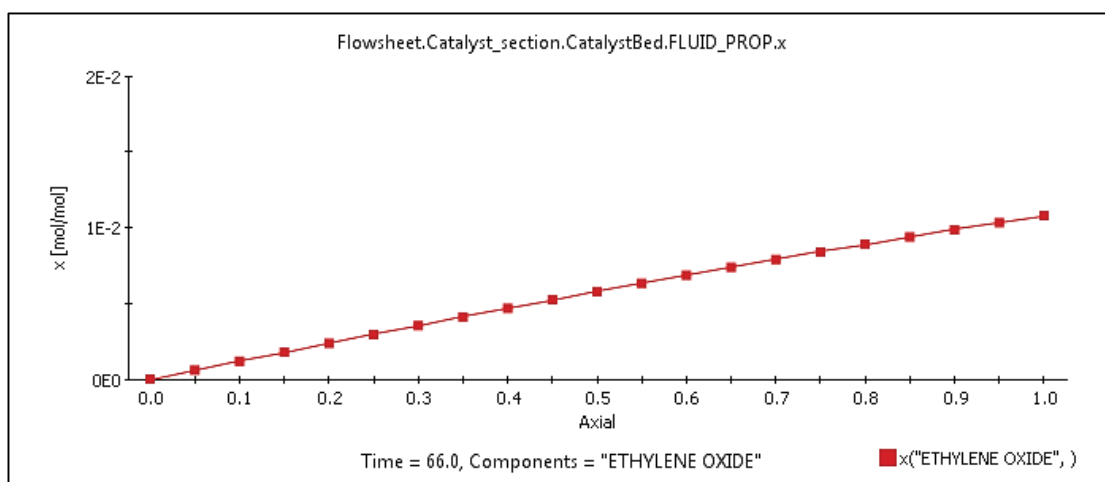


Figure G.8. Change in ethylene oxide concentration along with the catalyst bed in the axial direction.